Wolfram H. Geissler

Seismic and Petrological Investigations of the Lithosphere in the Swarm-Earthquake and CO$_2$ Degassing Region Vogtland/NW-Bohemia

Impressum

Wolfram H. Geissler

Seismic and Petrological Investigations of the Lithosphere in the Swarm-Earthquake and CO$_2$ Degassing Region Vogtland/NW-Bohemia

————

Scientific Technical Report STR05/06

... Die Quellen zu der Geschichte der Erde bewahrt sie selber
wie in einem Schriftengewölbe in ihrem Innern auf,
Quellen, die vielleicht in Millionen Urkunden niedergelegt sind
und bei denen es nur darauf ankömmt, daß wir sie lesen lernen
und durch Eifer und Rechthaberei nicht verfälschen. ...
– Adalbert Stifter, Der Nachsommer

Abstract

Western and Central Europe is affected by widespread rifting and associated volcanism in the foreland of the Alpine orogene. There is still an ongoing discussion on the causes of that rifting: passive rifting due to stresses induced by the Alpine collision and the North-Atlantic opening or active rifting due to active mantle up-welling. Teleseismic tomography studies imaged anomalous low seismic velocities beneath the French Massif Central and the Eifel area/Rhenish Massif, Germany, which can be interpreted as small-scale mantle plumes beneath the Tertiary to Quaternary volcanic fields. The existence of similar "mantle fingers" beneath the other volcanic fields in Central Europe was suggested, including the Eger Rift.

The Eger Graben is the approximately 50 km wide and 300 km long ENE-WSW striking central graben structure of the Eger Rift, which experienced several phases of magmatic activity since the Upper Cretaceous-Tertiary boundary. CO_2 emanations, sparse alkaline volcanic activity, neotectonic movements, and an unusual intraplate swarm-earthquake activity in the Vogtland/NW-Bohemia region accompany the recently active rifting process in the western part of the rift.

The present study focuses on the seismic structure and petrological composition of the lower crust and uppermost mantle beneath the presently active swarm-earthquake region and CO_2 degassing field Vogtland/NW-Bohemia.

Seismic data of several temporary and permanent seismic stations in the region provided the base of a receiver function study. Using this method, local depth variations of the Moho discontinuity could be detected. Moho depths range from 27 km beneath the Cheb Basin to 38 km beneath the central Bohemian Massif. A local Moho updoming from about 31 to 27 km was detected beneath the area with the CO_2 emanation centres and the Quaternary volcanoes at the surface, and the main swarm-earthquake activity in the upper crust. The lateral dimension of the effected area is approximately 40 km wide. Locally weak conversions at the Moho and increased reflectivity in the lower crust may indicate a magmatic overprinting of the crust-mantle boundary.

The results of this study also include the first average crustal v_p/v_s ratios on a local scale in the area under investigation. The v_p/v_s ratios range from 1.63 to 1.89 with a mean value of 1.73.

Furthermore, using teleseismic receiver functions, a local positive "6 s phase" was detected underneath the area of CO_2 emanations and Quaternary volcanism. This phase might stem from a converter at about 50 to 60 km depth. Possibly, this converter coincides with an upper mantle reflector observed previously by reflection seismic studies.

Abstract

The receiver function study also shows an apparent deepening of the 410 km discontinuity beneath the area under study. Probably, this apparent deepening is the result of lower seismic velocities in the upper mantle in comparison to the IASP91 reference model. However, a real deepening of the '410' cannot be ruled out completely at the present stage of investigation.

Additionally, (ultra-) mafic nodules (xenoliths, megacrysts), sampled from a tephra deposit near the Quaternary scoria cone Železna Hůrka, were investigated as rocks of the lower crust/uppermost mantle composition in this area. Most of the analysed xenoliths are wehrlitic samples, clinopyroxenites, or hornblendites and show cumulus textures. They probably represent cumulates of the host melt or fragments of small dikes/sills of crystallized alkaline melts, which intruded into the uppermost mantle and lower crust before the host melt rose to the surface. Spinel lherzolite xenoliths, the typical upper mantle rocks beneath Central Europe, could not be found in the Quaternary volcanics. Megacrysts of olivine, clinopyroxene, amphibole and phlogopite were also sampled and analysed in this study. The pressure (depth) of origin was estimated for several xenoliths using different available geothermobarometers; most estimates are in the range 8 to 12 kbar (29 to 41 km). Depth estimates from clinopyroxene and amphibole megacrysts are more or less in the same range (7 to 11 kbar; 25 to 38 km). Assuming, that at least some of the megacrysts might be deep-seated phenocrysts, these estimates provide constraints on the depth level of magmatic reservoirs in the study area. Since CO_2-dominated degassing is presently going on and previously isotope (He, C) geochemical investigations on these gases showed upper mantle signatures, there might still exist active melts at this depth level.

Up to now, only two Quaternary volcanic vents are known in the study area. Maybe the alkaline magmatic activity is mostly concentrated in the uppermost mantle and lower crust and causes there metasomatism, resulting in an upper mantle composition dominated by olivine and clinopyroxene (± amphibole, ± phlogopite). A comparison of calculated seismic velocities shows that rocks similar to the analysed xenoliths have lower seismic velocities than normal upper mantle rocks (spinel lherzolites). Therefore, the seismic discontinuity in about 50 to 60 km depth could represent the base of a local metasomatic mantle containing a few percent of partial melts.

The seismic and petrological results are discussed together with the results of previous regional seismic, seismological, and geochemical and isotope investigations on CO_2-dominated gas emanations. All available information is finally compiled into a conceptional model of the lithosphere in the swarm-earthquake and CO_2 degassing region Vogtland/NW-Bohemia. An interconnection between the different geodynamic processes (neotectonic movements, swarm-earthquakes, CO_2 degassing) observed in the area under study by presently active deep-seated magmatic activity ("magmatic underplating") is proposed.

Zusammenfassung

West- und Mitteleuropa sind gekennzeichnet durch weitverbreitete Rift-Prozesse und damit verbundenen Vulkanismus im Vorland des Alpen-Orogens. Als Ursachen werden lokale passive Extension im Spannungsfeld der Alpinen Kompressionstektonik und der Nordatlantiköffnung sowie aktive Weitungsprozesse in Beziehung zu Mantelaufwölbungsprozessen diskutiert. Anomal niedrige seismische Geschwindigkeiten wurden durch teleseismische Tomographie-Studien unter dem Französischen Zentralmassiv und unter der Eifel (Rheinisches Massiv, Deutschland) abgebildet. Diese negativen Geschwindigkeitsanomalien können als kleinskalige Aufstrombereiche von Mantelmaterial (Mantel Plumes) unter den tertiären und quartären Vulkanfeldern interpretiert werden. Die Existenz ähnlicher „Mantel-Finger" wurde auch für die anderen Vulkanfelder in Mitteleuropa, einschließlich des Eger-Rifts, postuliert.

Der Eger-Graben ist die etwa 50 km breite und 300 km lange ENE-WSW streichende zentrale Grabenstruktur des Eger-Rifts. Das Gebiet ist gekennzeichnet durch eine mehrphasige magmatische Aktivität seit der Grenze Oberkreide/Tertiär. Der quartäre bis rezente Rift-Prozess ist verbunden mit CO_2-Entgasungen, spärlicher vulkanischer Aktivität, neotektonischen Bewegungen sowie einer ungewöhnlichen Intraplatten-Schwarmbebenaktivität in der Region Vogtland/NW-Böhmen.

Die vorliegende Arbeit beschäftigt sich mit der Analyse der seismischen Struktur und der petrologischen Zusammensetzung der unteren Erdkruste und des obersten Mantels unter der derzeit aktiven Schwarmbebenregion und dem CO_2-Entgasungsfeld Vogtland/NW-Böhmen.

Seismische Daten von verschiedenen temporären und permanent installierten Erdbebenstationen im weiteren Untersuchungsgebiet sind die Grundlage für eine Studie mittels P-zu-S konvertierter seismischer Wellen (*receiver functions*). Mit dieser Methode konnten lokale Tiefenvariationen der Moho-Diskontinuität beobachtet werden. Die Tiefenlage der Moho reicht von 27 km unter dem Cheb Becken bis zu 38 km unter dem zentralen Böhmischen Massiv. Eine lokale Aufwölbung der Moho von einigen Kilometern (von 31 auf 27 km) deckt sich mit der Lage der CO_2-Entgasungszentren sowie der Position der quartären Vulkane an der Erdoberfläche und überlappt mit der Epizentralverteilung der Haupt-Schwarmbebenaktivität in der oberen Kruste. Der Durchmesser der Moho-Aufwölbung beträgt ungefähr 40 km. Lokal beobachtete schwache Moho-Konversionen und eine erhöhte Reflektivität der Unterkruste deuten möglicherweise auf eine magmatische Überprägung der Kruste-Mantelgrenze hin.

Die Ergebnisse dieser Arbeit schließen außerdem die ersten mittleren krustalen v_p/v_s Verhältnisse im lokalen Maßstab für das Untersuchungsgebiet ein. Die beobachteten Werte liegen zwischen 1,63 und 1,89, der Mittelwert beträgt 1,73.

Zusammenfassung

Unter dem Gebiet mit CO_2-Entgasungen und quartärem Vulkanismus wurden weiterhin lokal positive konvertierte Phasen mit einer Verzögerungszeit von 6 Sekunden *("6 s phase")* detektiert. Sie können wahrscheinlich einem seismischen Konverter in 50 bis 60 km Tiefe zugeordnet werden. Möglicherweise entspricht dieser Konverter einem Reflektor im oberen Erdmantel, der bereits in reflexionsseismischen Messungen beobachtet wurde.

Die *receiver function*-Studie zeigt außerdem ein scheinbares Abtauchen der 410-km-Diskontinuität unter dem Untersuchsuchungsgebiet. Wahrscheinlich wird dieses scheinbare Abtauchen durch verringerte seismischer Geschwindigkeiten im oberen Erdmantel im Vergleich zum IASP91 Referenzmodell verursacht. Zum derzeitigen Untersuchungsstand kann jedoch auch ein reales Abtauchen der „410" nicht gänzlich ausgeschlossen werden.

Als zweiter Schwerpunkt dieser Arbeit wurden (ultra-) mafische Knollen (Xenolithe, Megakristalle) als Gesteine der unteren Erdkruste und des oberen Erdmantels in der Region untersucht, die einem Tephra-Vorkommen in der Nähe des quartären Schlackenkegels Železna Hůrka (Eisenbühl) entstammen. Die meisten der analysierten Xenolithe sind Wehrlite, Klinopyroxenite oder Hornblendite und zeigen Kumulus-Texturen. Sie repräsentieren wahrscheinlich Kumulate der Wirtsschmelze oder Bruchstücke von kleinen Gängen kristallisierter alkaliner Schmelzen, die in den obersten Mantel und die Unterkruste intrudierten, bevor die Wirtsschmelze zur Erdoberfläche aufstieg. Spinell-Lherzolith-Xenolithe, die typischen Gesteine des oberen Erdmantels unter Mitteleuropa, konnten in den quartären Vulkaniten bisher nicht gefunden werden. Megakristalle (Olivin, Klinopyroxen, Amphibol, Phlogopit) wurden für die Studie ebenfalls beprobt und untersucht. Die Herkunftstiefen (Drucke) wurden für einige Xenolithe anhand unterschiedlicher verfügbarer Geothermobarometer abgeschätzt. Die erhaltenen Druckwerte liegen in der Mehrzahl zwischen 8 und 12 kbar, was einer Herkunftstiefe von etwa 29 bis 41 km entspricht. Die Schätzungen für die Klinopyroxen- und Amphibol-Megakristalle liegen im selben Bereich (7 bis 11 kbar, 25 bis 38 km). Unter der Annahme, dass zumindest einige der Megakristalle Hochdruck-Phänokristalle sind, bieten diese Abschätzungen Hinweise auf den Tiefenbereich magmatischer Reservoire im Untersuchungsgebiet. Isotopen-geochemische Untersuchungen (He, C) an den rezent austretenden CO_2-reichen Gasen ergaben deutliche Signaturen des oberen Erdmantels. Wahrscheinlich existieren derzeit entgasende Schmelzen in dem durch die p-T Abschätzungen abgegrenzten Tiefenbereich.

Bis jetzt sind nur zwei quartäre Eruptionszentren im Untersuchungsgebiet bekannt. Eventuell ist die derzeitige alkaline magmatische Aktivität im obersten Mantel und in der Unterkruste konzentriert. Diese führt dort möglicherweise zu metasomatischen Prozessen, die in einer Zusammensetzung des oberen Erdmantels resultieren, die durch Olivin und Klinopyroxen dominiert ist (± Amphibol, ± Phlogopit). Ein Vergleich von berechneten seismischen Geschwindigkeiten zeigt, dass Gesteine, die

ähnlich zu den analysierten Xenolithen sind, geringere seismische Geschwindigkeiten besitzen als die typischen Gesteine des oberen Mantels (Spinell-Lherzolithe). Die beobachtete seismische Diskontinuität in 50 bis 60 km Tiefe könnte somit die Basis eines lokal metasomatisch überprägten Mantels sein, der außerdem wenige Prozent partieller Schmelzen enthält.

Die seismischen und petrologischen Ergebnisse werden zusammen mit den Ergebnissen vorhergehender regionaler seismischer, seismologischer sowie gas-geochemischer und Isotopen-Studien an den CO_2-Entgasungen diskutiert. Die verfügbaren Informationen werden schließlich in ein Konzeptionsmodell der Lithosphäre unter dem Schwarmbeben- und CO_2-Entgasungsgebiet Vogtland/ NW-Böhmen integriert. Eine Verbindung zwischen den verschiedenen im Untersuchungsgebiet beobachteten geodynamischen Prozessen (neotektonische Bewegungen, Schwarmbeben, CO_2-Entgasungen) durch rezente verdeckte tiefe magmatische Aktivitäten („*magmatic underplating*") wird vorgeschlagen.

Contents

Contents

List of figures and plates

List of tables

List of abbreviations and symbols

SCLM	SubContinental Lithospheric Mantle
ECRS	European Cainozoic Rift System
EMPA	Electron Microprobe Analysis
GFZ	GeoForschungsZentrum
GRSN	German Regional Seismic Network
H	crustal thickness
ICP-MS	Inductively Coupled Plasma Mass-Spectrometry
IG CAS	Institute of Geophysics, Czech Academy of Sciences
IPE Brno	Institute of Physics of the Earth, Masaryk University Brno
KH	Komorní Hůrka
KTB	Kontinentale Tief-Bohrung
KRASNET	KRAslice seismic NETwork
LVZ	Low Velocity Zone
M_L	Local Magnitude
ON	Olivine Nephelinite
p	pressure
REE	Rare Earth Elements
SZGRF	Seismologisches Zentralobservatorium Gräfenberg
T	Temperature
WEBNET	WEst-Bohemian seismic NETwork
XRF	X-Ray Fluorescence spectrometry
ZH	Železna Hůrka

Symbols for rock-forming minerals used [mainly based on *Kretz,* 1983]:

am	amphibole (undifferentiated)	pt	peridotite
fsp	feldspar (undifferentiated)	(ol-)X	(olivine) megacryst
gl	glass	c	core (composition)
gm	groundmass	r	rim (composition)
m	mica (undifferentiated)	s	sector (composition)
o	ore (undifferentiated)	I	intergrowth
sulph	sulphide		

ac	acmite (aegirine)	kfs	K feldspar
ab	albite	mag	magnetite
an	anorthite	ms	muscovite
ap	apatite	ol	olivine
bt	biotite	or	orthoclase
cpx	Ca clinopyroxene	opx	orthopyroxene
chl	chlorite	prg	pargasite
chr	chromite	phl	phlogopite
crd	cordierite	pl	plagioclase
en	enstatite (ortho)	qtz	quartz
fa	fayalite	rt	rutile
fs	ferrosilite (ortho)	sp, spl	spinel
fo	forsterite	st	staurolite
grt	garnet	ttn	titanite
hbl	hornblende	wo	wollastonite
ilm	ilmenite	zrn	zircon
jd	jadeite		

A   Introduction and scope of this study

In this chapter, the general geological and geophysical settings of the area under study are introduced, including results from previous studies on the swarm-earthquake activity, volcano-tectonic evolution, and gasgeochemical and -isotope studies on CO_2-rich emanations. Furthermore, results from previous seismic and xenoliths studies in the region are presented.

A.1   The European Cainozoic Rift System and associated intraplate volcanic fields

The study area – the western part of the Eger Rift (Figure A.1) – belongs to the European Cainozoic Rift System (ECRS) [*Ziegler,* 1992; *Prodehl et al.,* 1995]. This system of graben structures and intraplate volcanic fields spreads over a distance of some 1000 km, including the French Massif Central, the Upper Rhine Graben, the Eifel, the North Hessian Depression, the Vogelsberg, the Eger Rift, the Elbe Zone, and the Pannonian Basin. Graben structures evolved on top of uplifted basement blocks (Variscan massifs); Tertiary and Quaternary volcanism is mainly concentrated on the flanks of these graben structures along boundary faults or on the adjacent uplifted blocks. Dominantly (ultra-) alkaline, but also more evolved, magmas were erupted. A detailed overview about the Cainozoic volcanism can be found in *Wimmenauer* [1974] and *Wilson and Downes* [1992]. The most recent expressions of magmatic activities within the European Cainozoic Rift System are the CO_2 degassing fields. The isotope (He, C, and N) composition of CO_2-rich gas emanations of mineral springs and mofettes from the French Massif Central [*Matthews et al.,* 1987], the East and West Eifel volcanic fields/Germany [*Griesshaber et al.,* 1992; *May,* 2002] and the western Eger Rift/Czech-German border region [*O´Nions et al.,* 1989; *Weinlich et al.,* 1999, 2003] gives evidence for the ascent of gases from fluid reservoirs in the European subcontinental mantle.

There are different models to explain the widespread rifting and associated volcanism in the foreland of the Alpine orogene. Most of them are related to the effects of Alpine collision [*Illies,* 1975; *Lippoldt,* 1982; *Ziegler,* 1992; *Stackebrandt and Franzke,* 1989; *Regenauer-Lieb,* 1999]. However, there also exist ideas of a mantle plume or several small mantle plumes (mantle fingers) as the source of the magmatic activity [*Granet et al.,* 1995; *Goes et al.,* 1999]. Such models mainly base on tomographic evidence. Teleseismic tomography studies have imaged anomalous low seismic velocities under the French Massif Central [*Granet et al.,* 1995] and the Eifel area/Rhenish Massif, Germany [*Ritter et al.,* 2001]. A combination of both end-member models was proposed by *Merle and Michon* [2001], who suggested mantle convection on a regional scale and therefore up-welling beneath the volcanic fields due to a descending lithospheric bulge beneath the Alps. The most recent overview on the evolution of the European Cainozoic Rift System is given by *Dezes et al.* [2004].
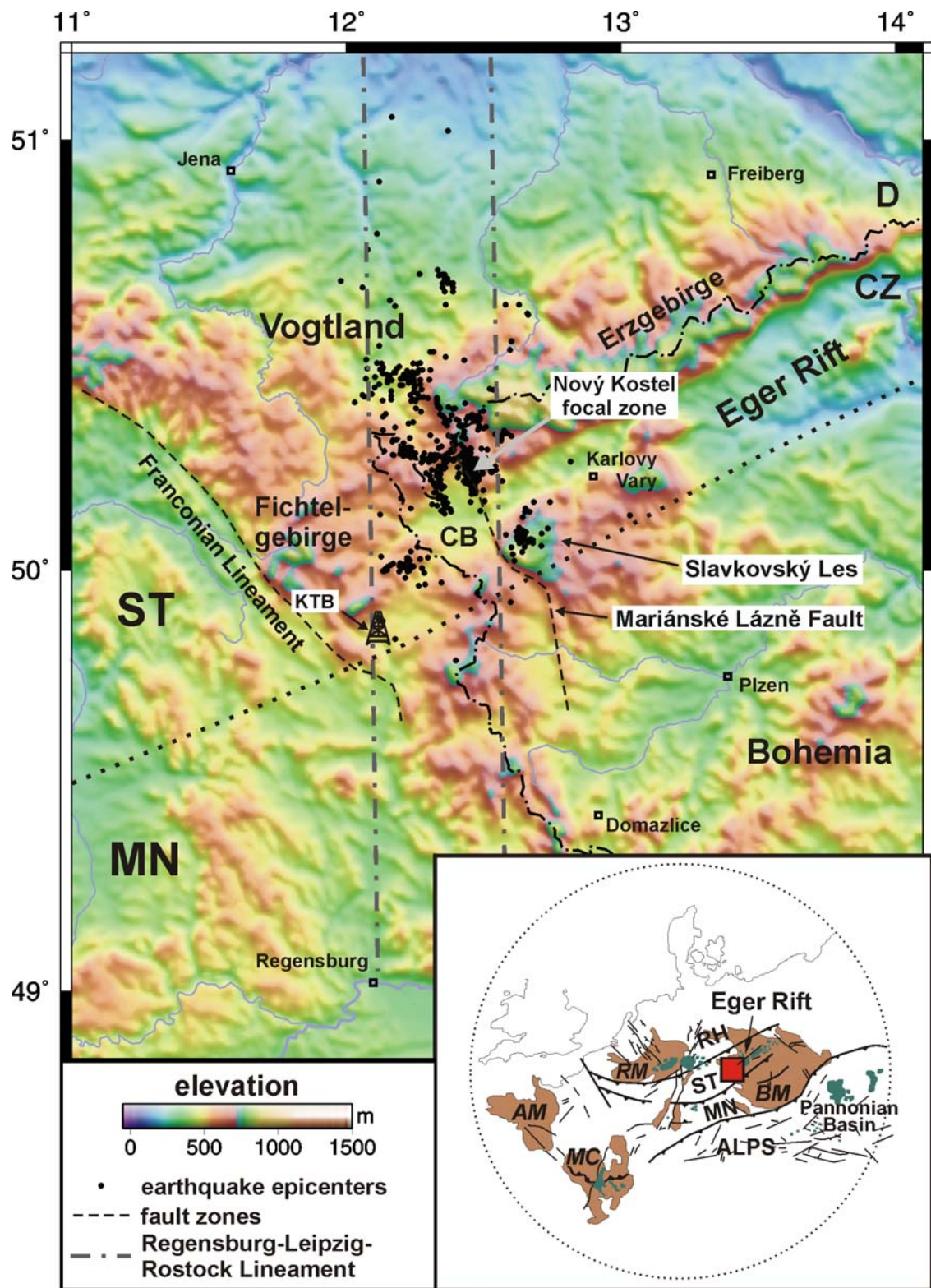
Figure A.1
Topographic map (GTOPO30 from USGS EROS DATA Center) of the northwestern part of the Bohemian Massif with earthquake epicentres 1985-1997 (black dots, according to *Neunhöfer* [2000] and SZGRF Vogtland Bulletin). Main earthquake swarm activity is concentrated in the Nový Kostel focal zone. Inset map: Position of the study area within the western and central European volcanic provinces modified after *Wilson and Downes* [1991] (read square – study area, green – Cainozoic volcanics, brown – basement massifs).
KTB – location of the German Continental Deep Drilling Boreholes (KTB), CB – Cheb Basin, MC – Massif Central, AM – Armorican Massif, RM – Rhenish Massif, BM – Bohemian Massif, MN – Moldanubian zone, RH – Rhenohercynian zone, ST – Saxothuringian zone.

A.2   Geological and geophysical settings of the western Bohemian Massif

The study area – the Vogtland/NW-Bohemia/NE-Bavaria region belongs to the western part of the Bohemian Massif and is situated in the transition zone between two Variscan structural units, the Saxothuringian zone (ST) in the north and the Teplá-Barrandian/Moldanubian zone (MN) in the south (see Figures A.1, A.2). These structural units are composed of magmatic and metamorphic rocks, which are covered by undeformed sediments of Permo-Carboniferous, Jurassic, Cretaceous and Cainozoic age in part. The whole region in the western and northern parts of the Bohemian Massif has been affected by alkaline magmatism/volcanism at least since the Upper Cretaceous.

A.2.1   Pre-Tertiary geology of the study area

The crust and uppermost mantle of the Bohemian Massif were profoundly affected by several geotectonic cycles (rifting, subduction, collision) during the last 2 Ga. Early stages of the evolution of continental crust and mantle in Central Europe from 2.0 Ga to 0.7 Ga are still unconfirmed. Nd crustal residence ages combined with xenocrystal and detrital zircon ages of crustal rocks from the NE margin of the Bohemian Massif suggest mixing of predominantly Paleoproterozoic material with subordinate amounts of juvenile material of Grenvillian age and Neoproterozoic to early Palaeozoic material [*Hegner and Kröner,* 2000]. The Avalonian-Cadominan/Panafrican evolution of terranes accreted in the Variscan belt of Central Europe shows several subduction events and island arc settings (660-540 Ma), obduction, intensive magmatism and crustal extension (540-530 Ma), and rifting/ocean basin formation (490-440 Ma) [*Linnemann et al.,* 2000]. During the Variscan orogeny the crust/lithosphere was affected by subduction, collision, thickening and post-collisional extension (360-280 Ma). Until now no structural evidence for these tectonic processes in Variscan and pre-Variscan times could be observed definitely within the upper mantle beneath Central Europe. There are only indications for divergent dipping paleosubduction zones from seismic anisotropy studies in the western Bohemian Massif [*Babuška and Plomerová*, 2001]. The influence and imprint of Mesozoic (especially Cretaceous) tectono-magmatic events on the present lithospheric structure is still poorly known. Such events are ultramafic magmatism in central Germany (UML-carbonatite complex of Delitzsch) [*Röllig et al.,* 1990; *Seifert et al.,* 2000] and Upper Lusatia [*Renno et al.,* 2003] and crustal stacking along the Franconian Lineament, as it is evident from the KTB area [e.g., *Zulauf and Duyster,* 1997a, b; *Wagner et al.,* 1997; *Tanner et al.,* 1998].

0   20   40 km

Regensburg-Leipzig-Rostock Lineament

■ Neovolcanics   ▨ Mesozoic   ⬚ faults, thrusts
□ Cainozoic   ▧ Paleozoic, Proterozoic
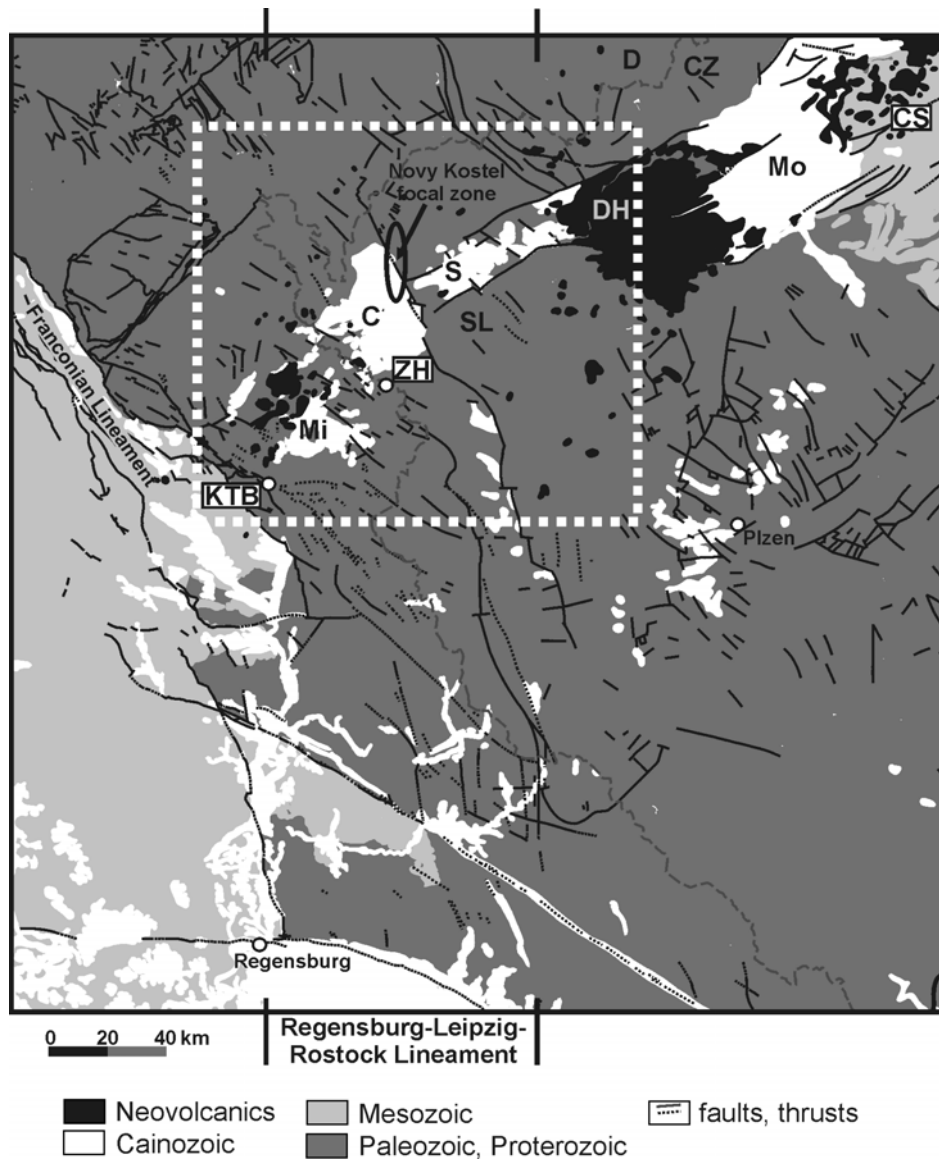
Figure A.2
Distribution of Tertiary-Quaternary volcanic fields and sedimentary basins in the western part of the Bohemian Massif [modified after *Bayerisches Geologisches Landesamt,* 1998]. The WSW-ENE striking line of the sedimentary basins: Mitterteich (Mi), Cheb (C), Sokolov (S), and Most (Mo) basins as well as the volcanic fields Doupovske Hory (DH) and Česke Středohoři (CS) belong to the Eger (Ohře) Rift. KTB = location of the German Continental Deep Drilling Boreholes; ZH – Železná Hůrka volcano, Quaternary (sample location for mantle xenoliths), SL – Slavkovský Les. The main working area (the western Eger Rift) is marked by the box.

A.2.2   Tectono-magmatic evolution of the Eger (Ohře) Rift

As already mentioned above, the Atlantic opening and Alpine orogeny affected Central and Western Europe during Cretaceous to Cainozoic times. Rifting and alkaline volcanism in the foreland of the Alpine orogene in this period were associated with either passive or active mantle up-welling. At the Upper Cretaceous-Tertiary boundary, an approximately 50 km wide and 300 km long ENE-WSW striking continental rift evolved in the area of the Palaeozoic suture originating from the collision of Laurasia (Laurentia-Baltica) and Africa (Gondwana). The Cretaceous to Quaternary tectono-magmatic

evolution of the Eger Rift area comprises several phases [*Malkovský,* 1976; *Ulrych and Pivec,* 1997; *Ulrych et al.,* 1999; *Kämpf et al.,* 1999a; *Špičáková et al.,* 2000; *Renno et al.,* 2003]. Presumably, the magmatic activity began with plume activated dome uplift during the Early Cretaceous. The pre-rift phase was accompanied by mafic to ultramafic dike intrusions from the early Cretaceous to the Palaeocene (126 - 51 Ma). However, it is still uncertain if the Cretaceous magmatic activity is really related to the Eger Graben evolution. The main rifting phase with incipient graben formation and voluminous intraplate alkaline volcanism lasted from about 42 Ma to 9 Ma. A detailed overview of the Cainozoic volcanic activity in the western part of the Bohemian Massif is given by *Ulrych et al.* [2003].

The recent active rifting process during Quaternary with the further formation of the Cheb Basin is accompanied by CO_2 emanations at the surface in NW-Bohemia, southern Vogtland and eastern Fichtelgebirge area, sparse alkaline volcanic activity, neotectonic uplift in the Slavkovský Les area and earthquake swarm activity in the Vogtland/NW-Bohemia region.

A.2.3   Seismicity of the region

The Vogtland/NW-Bohemia region is known as one of the most interesting European earthquake swarm regions with thousands of small and intermediate magnitude swarm-earthquakes ($M_L < 5$). The term "earthquake swarm" ("Erdbebenschwarm") was first introduced in this region more than hundred years ago by *Knett* [1899] and *Credner* [1900] for sequences of earthquakes that cluster in time and space. Primarily, earthquake swarms are a peculiarity of volcanic regions and mid-ocean rifts. Swarms in intraplate regions without active volcanism are unusual. Vogtland/NW-Bohemia represents such a region with an anomalous high swarm activity. The youngest known volcanic activity in the area occurred about 0.3 - 0.5 Ma [*Wagner et al.,* 2002; *Geissler et al.,* 2004b].

Within the last one hundred years stronger swarms ($M_L > 3$ to 4) were recorded at the turn of 19th to the beginning of the 20th century in 1897, 1901, 1903 and 1908 and at the end of the 20th century in 1985/86 and 2000 [*Bormann,* 1989; *Klinge et al.,* 2003; *Fischer and Horálek,* 2003; *Neunhöfer and Meier,* 2004]. Swarms with macro-seismically perceptible shocks also occurred in 1929, 1936 and 1962. After the 1962 swarm, the first local seismic network was installed. Duration of the main swarm activity of one or a few months including several phases of enhanced swarm activity (lasting only a few days) seems to be typical for large swarms. Smaller swarms ($M_L < 3$) with durations of a few days occur more or less regularly every 2 to 4 years. All stronger swarms in the last hundred years occurred at intersections between local faults of the N-S trending Regensburg-Leipzig-Rostock Lineament with ENE-WSW, NW-SE and NNW-SSE trending faults [*Hemmann and Kämpf,* 2002]. Since 1985/86 most swarms are located near Nový Kostel (50.24°N, 12.44°E) following a 14 km long N-S trending line in a depth of about 8 km at the intersection of the N-S trending Nový Kostel-Počátky-Zwota zone

with the NNW-SSE trending Mariánské Lázně fault zone (Figure A.3) [*Švancara et al.,* 2000; *Bankwitz et al.,* 2003a, b; *Fischer and Horálek,* 2003]. The earthquakes of individual swarms are clustered in extremely small volumes of only a few cubic kilometres [*Fischer and Horálek,* 2003; *Neunhöfer and Meier,* 2004]. The N-S trending Regensburg-Leipzig-Rostock Lineament seems to continue further to the south into the Molasse Basin and the Alps [*Lehrberger et al.,* 2003].
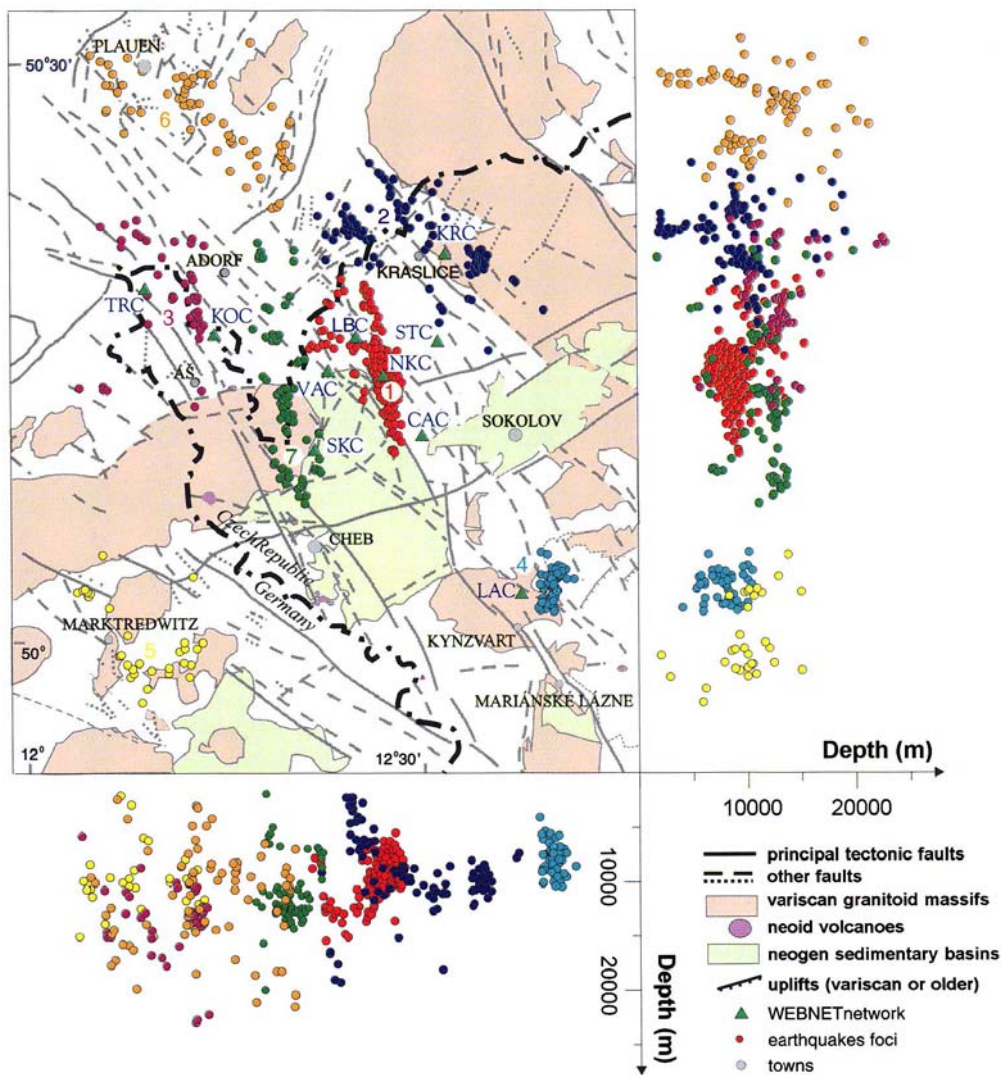
Figure A.3
Spatial distribution of earthquake hypocentres 1991-1999 [from *Horálek et al.,* 2000] based on locations with WEBNET and KRASLICE network stations. Seven focal zones were distinguished by colours. Recently, the main earthquake swarm activity is concentrated in the Nový Kostel focal zone (red).

Focal mechanisms of most of the events with $M_L > 2$ since 1985 show similar patterns of seismic dislocation [*Wirth et al.,* 2000]. Sources with significant non-double-couple components up to 60 % dominated in the second and third phases of the January 1997 swarm in the main focal zone Nový Kostel [*Horálek et al.,* 2000a, 2002]. Similarly, non-double-couple (20 to 40 %) sources were revealed for some events of the 2000 earthquake swarm (focal zone Nový Kostel) by *Plenefisch and Klinge*

6

[2003]. Source mechanisms with significant non-double-couple components indicate tensile earthquakes, which seem to be caused by a high-fluid pressure in the region [*Vavryčuk,* 2001]. *Parotidis et al.* [2003] hypothesized ascending magmatic fluids trigger the earthquakes by causing pore-pressure perturbations, which change the effective stresses resulting in seismic activity. Recent studies show, that also seismic anisotropy in the source region should be considered when discussing non-double-couple components [*Rössler et al.*, 2003].

The most recent earthquake swarm with about 70 events (M_{Lmax}=1.4) was registered on February 22, 2004 near Nový Kostel [*Boušková et al.,* 2004]. It did not occur in the main focal zone. The depth was estimated to about 14 km, i.e. deeper than the presumed 12 km of the brittle-ductile boundary in this area [*Boušková et al.,* 2004].

A.2.4 CO_2 emanations at the Earth's surface

In principle, insights from seismological and geochemical results point to a general connection between fluid flow (predominantly CO_2) and seismic activity in the crust of the studied area [*Kämpf et al.*, 1992; *Kämpf,* 1994; *Weise et al.*, 2001; *Vavryčuk,* 2001; *Bräuer et al.*, 2003; *Parotidis et al.,* 2003]. Recently, a subcontinental mantle related gas flow to the Earth's surface was observed indicating a correlation between the gas flow rate and the earthquake swarm activity for the year 2000 [*Koch and Heinicke,* 2003].

Previously, the composition and flux of gas emanations, and the isotopic ratios of CO_2 and He of 101 mineral springs and dry gas vents (mofettes) in the western Eger Rift were analysed [*Weinlich et al.*, 1999, 2003; *Geissler et al.,* 2004a] The CO_2-dominated portion in the free gas phase (> 99 vol.% CO_2) cluster in an area of approximately 1500 km^2 (Figure A.4). Four geochemically similar, but tectonically separate gas escape centres could be distinguished: Františkovy Lázně / Cheb Basin (I), Mariánské Lázně (II), Konstantinovy Lázně (III), and Karlovy Vary (IV). The gas escape centres I, II, and IV show always a free gas flux of more than 85000 dm^3 h^{-1} [*Weinlich et al.*, 1999]. All gases are CO_2-rich (> 99 vol.% CO_2) and have $\delta^{13}C$ values ranging from -1.8 to -4.0‰. The ^{3}He/^{4}He ratios reach up to 5.9±0.17 Ra in the Cheb Basin (mofette Bublák) as a mean value of 14 samples [*Bräuer et al.,* 2004]. Olivine phenocrysts and xenoliths from the subcontinental lithospheric mantle (SCLM) show a homogeneous helium isotopic ratio (R/Ra) of approximately 6.1 [*Gautheron and Moreira,* 2002]. The helium isotope ratios of the Cheb Basin [*Weinlich et al.*, 1999, 2003; *Bräuer et al.,* 2004] are in the same range as found for xenoliths from the sub-continental mantle worldwide [*Gautheron and Moreira,* 2002]. That makes it plausible, that the CO_2-dominated gas of the gas escape centres at the surface carries a very high portion of pure lithospheric mantle (SCLM) fluid. Helium, CO_2, and other volatiles may be released during melting/crystallization in the lithospheric continental mantle.
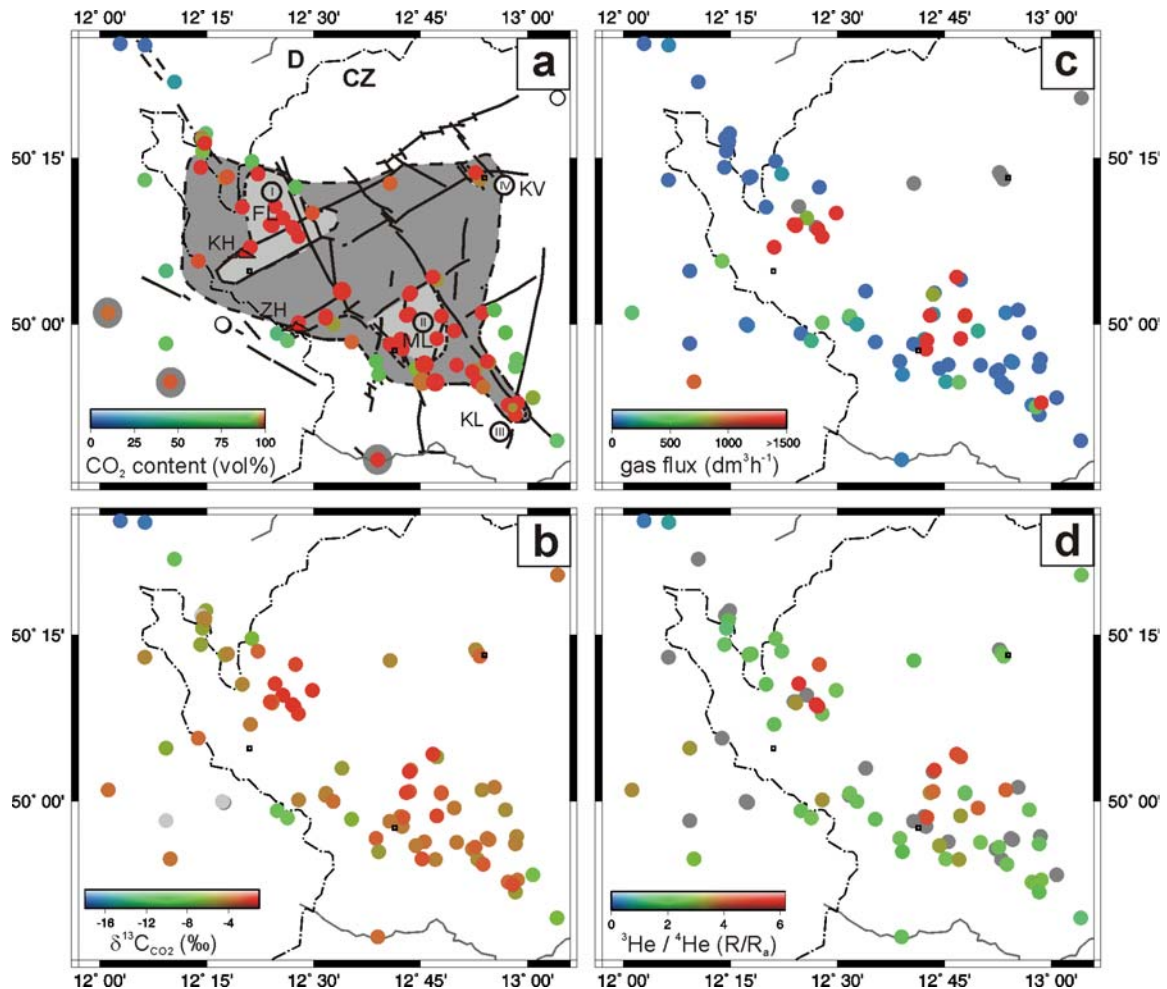
Figure A.4
Results from gasgeochemical and –isotope (C, He) studies of CO_2-dominated emanations in the Vogtland/NW-Bohemia area [data from *Weinlich et al.,* 1999, 2003; *Geissler et al.,* 2004a]. **(a)** CO_2 content of the free gas phase of mineral springs and mofettes: light grey – CO_2 escape centre; dark grey – surrounding of the main escape centres, the CO_2 content of the dark grey coloured area is >99 vol.% [after *Weinlich et al.,* 1999]; **(b)** $\delta^{13}C$ values: the $\delta^{13}C$ values of the CO_2 escape centre and surrounding of the degassing centres ranging from –1.8 to –4.0‰; **(c)** gas flux (free gas): flux within the main escape centres FL and ML is significantly higher than it could be indicated by the colour-scale; **(d)** $^3He/^4He$ (R/Ra) ratios: the helium isotopic ratios of the CO_2 escape centre and the periphery, ranging from R/Ra 5.9 to 0.2.
FL – Františkovy Lázně, ML – Mariánské Lázně, KL – Konstantinovy Lázně, KV – Karlovy Vary, KH – Komorní Hůrka, ZH – Železná Hůrka.

The two most prominent high gas flux CO_2 degassing centres (Františkovy Lázně / Cheb Basin and Mariánské Lázně) cluster in areas of approximately 150 km^2. The gas flux, CO_2 content, $\delta^{13}C$ values, and $^3He/^4He$ ratios decrease with distance from the CO_2 emission centres, whereas the fractions of N_2 and trace gases increase (Figure A.4b-d). *Bräuer et al.* [2003] estimated that the fluid transport velocity in the upper crust ranges between 400m/day near a centre of CO_2 emanation and 50m/day in the periphery. $^3He/^4He$ ratios, $\delta^{13}C$ values, gas composition, gas flux rate and fluid transport velocity give evidence for a deep-seated, presently active magmatic source.

The location of the degassing centres at the surface points to the location of the covered magmatic source. This magmatic degassing at the surface in the Vogtland/NW-Bohemia area was the main motivation to start this local-scale mapping of the Moho discontinuity and the subcrustal mantle.

A.3   The Moho and the upper mantle in previous studies

A.3.1   The Moho structure

In the past the region was studied by several reflection and refraction seismic experiments [e.g., *Giese, 1976*; *DEKORP Research Group,* 1988, 1994; *Bormann et al.,* 1989; *Schmoll et al.,* 1989; *Schulze and Lück,* 1992; *Behr et al.,* 1994; *Tomek et al.,* 1997; *Enderle et al.,* 1998]. Some of these measurements were related to the German Deep Drilling Project "Kontinentale Tiefbohrung" (KTB) [*Emmermann and Lauterjung,* 1997]. The mean P-wave velocity of the crust in the area under investigation ranges between 6.0 and 6.3 km/s with higher values towards the south within the Bohemian Massif [e.g., *Bormann et al.,* 1989].

The Moho discontinuity in the KTB area is not uniformly imaged by reflection seismic studies. It exists only locally as a pronounced reflector [*Tillmanns et al.,* 1996]. An updoming of the Moho discontinuity beneath the boundary region of the Moldanubian and Saxothuringian zones was reported, but the reflection character is diffuse [*DEKORP Research Group,* 1988].
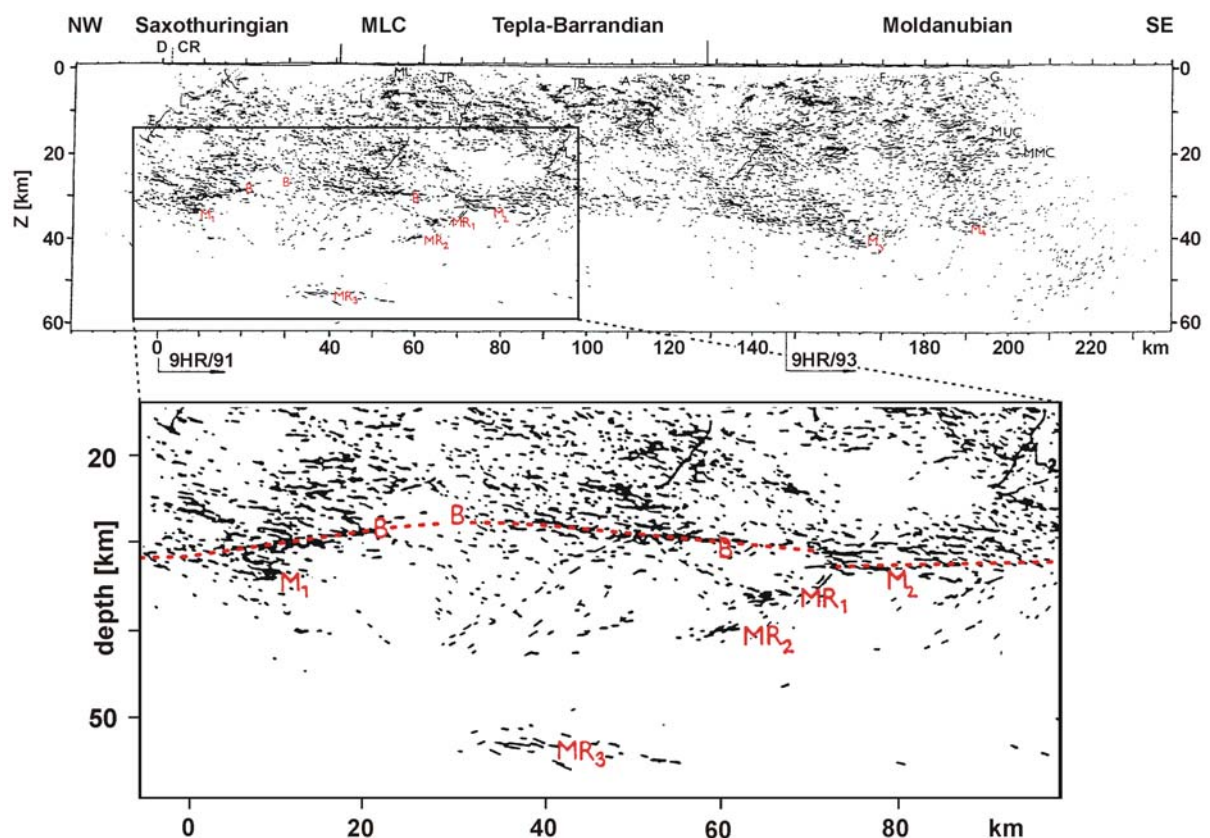
Figure A.5
Results from deep-seismic reflection profile 9HR, running from the Czech-German border near Klingenthal south-eastwards [*Tomek et al.,* 1997]. See Figure B.2 for location of the profile. The profile crosses the study area between the border and the Tepla-Barrandian Unit. M_{1-4} are interpreted as Moho reflections; B possibly stem from basaltic intrusions; MR_{1-3} denote upper mantle reflections. A Moho antiform beneath the Saxothuringian zone is clearly visible, exactly where the Eger Graben is located at the surface (Sokolov Basin).

The crustal thickness along the profile DSS-VI is about 30 km where it crosses the Eger Rift east of Karlovy Vary [*Mayerov*á *et al.,* 1994]. A crustal thickness of 28 km in the western Erzgebirge region was published by *Bormann et al.* [1989]. The crust thickens southwards to about 37 km in the Central Moldanubian [*Mayerov*á *et al.,* 1994]. No clear Moho reflections were recorded beneath the western Eger Rift by the reflection seismic profile 9HR, which runs from near station KLIN to BOH2 (see Figure B.2) and further to the southeast [*Tomek et al.,* 1997; Figure A.5]. The interpolation of the inclined Moho reflection bands in the north and south results in an approximate Moho depth of 29 km (9.2-9.5 seconds two-way travel-time (TWT), v_p = 6.3 km/s). The Moho depth north of the Eger Rift ranges from 30 to 32 km [*Enderle et al.,* 1998].

Based on the existing seismic data many regional contour maps of Moho depth were compiled [e.g.; *Bormann et al.,* 1989; *Mayerov*á *et al.,* 1994; *Prodehl et al.,* 1992, 1995; *Giese,* 1995; *Dezes and Ziegler,* 2002; see Figure A.6]. The problem of almost all seismic profiles in the past is, that they end at the border between countries, and therefore, maps of Moho depth do not show the complete Moho topography of the area under investigation.
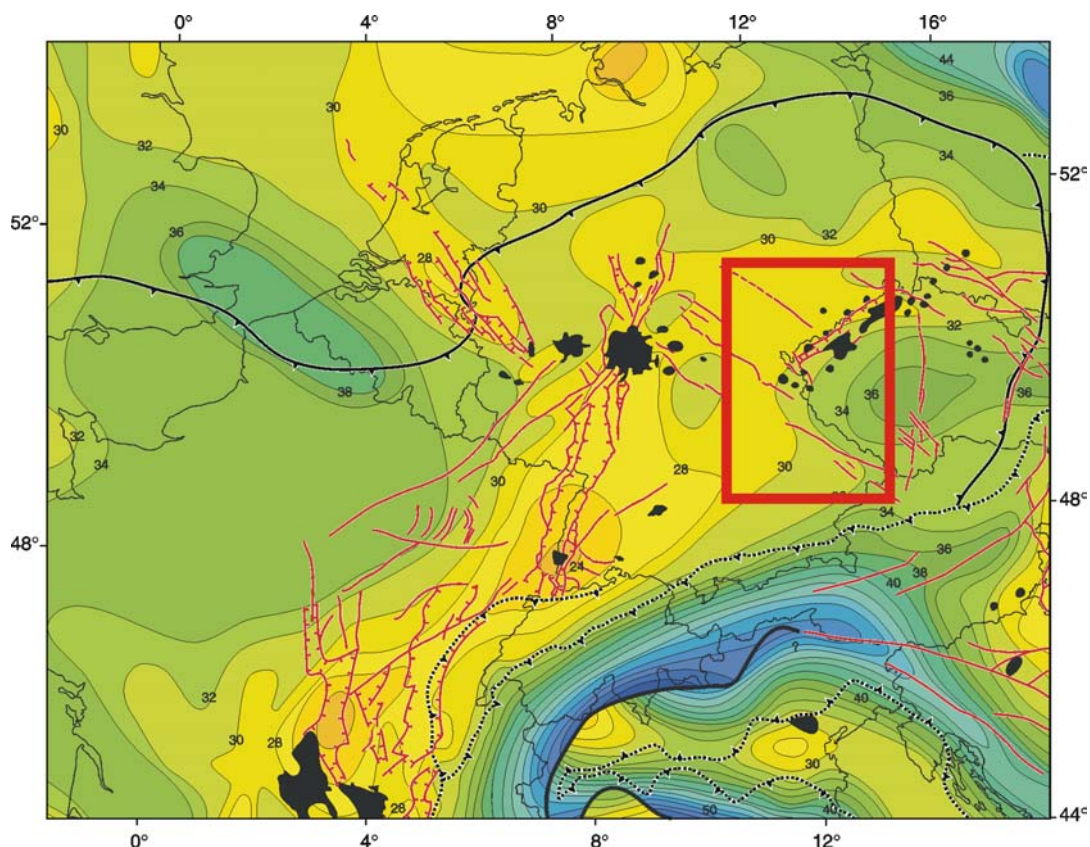
Figure A.6
Depth of the Moho discontinuity (km) in Central Europe from *Dezes et al.* [2004] with the position of the study area (red square). Also shown are the positions of Cainozoic volcanic centres (black filled areas), major graben structures and fault zones (red lines), as well as the position of the Variscan Deformation Front (solid black line) and Alpine thrusts (dotted black lines). The Moho depth beneath the study area ranges from about 28 to more than 36 km, according to *Dezes et al.* [2004].

A.3.2   Seismic constraints on the upper mantle structure

Global seismic tomography imaged a low velocity structure between 660 and 2000 kilometres depth beneath Central and Western Europe [*Goes et al.,* 1999]. Mantle fingers with low seismic velocities were found in the uppermost 300 km beneath the French Massif Central and the Eifel/Rhenish Massif by *Granet et al.* [1995] and *Ritter et al.* [2001], respectively. There are also indications for reduced seismic velocities in the upper mantle beneath the western Eger Rift region, mainly from studies of P wave residuals [*Rajkes and Bonjer*, 1976; *Faber et al.,* 1986; *Plomerová and Babuška,* 1988; *Plomerová et al.,* 1998]. *Passier and Snieder* [1996] obtained a three-dimensional shear wave velocity distribution beneath central and southern Germany. Prominent features of the model are low velocities in the uppermost mantle between 80 and 120 km along the Eger Rift, and between 80 and 200 km beneath the western Eger Rift and the Eifel. *Passier and Snieder* [1996] suggest the creation of magma in the asthenosphere or at the base of the lithosphere beneath these regions. However, a coupling between the lower and upper mantle beneath central and Western Europe has remained widely speculative. Coupling between the upper mantle fingers and the crust is also not well understood. Resolution differences between the different seismic methods used so far cause a structural gap in this subcrustal depth range.

A.3.3   Results of thermobarometric studies on xenoliths from adjacent volcanic fields

As already mentioned above, the probable source region of the (ultra-) mafic magmas (nephelinitic-melilititic) is the boundary between the asthenosphere and the basal lithosphere (the uppermost mantle). If the magmas erupt directly from those depths, they often contain inclusions (cognate and xenolithic), which give important information on the composition of the uppermost mantle and lower crust, as well as on geodynamic processes in the lithosphere (metasomatic-magmatic overprinting, deformation, partial melting). The Tertiary volcanic fields adjacent to the area under study were already investigated in terms of the origin of their spinel peridotite inclusions (Table A.I). First geothermobarometric results from NE-Bavaria (western prolongation of the Eger Rift) were published by *Huckenholz and Noussinanos* [1977] and later by *Huckenholz and Kunzmann* [1993]. Spinel peridotites and crustal xenoliths within the volcanic rocks of the Rhön were studied by *Franz et al.* [1997], *Franz and Seifert* [1998], and *Witt-Eickschen and Kramm* [1997]. Mantle and lower crustal xenoliths from the Elbe fault zone and Upper Lusatia (eastern Eger Rift area) were investigated, e.g., by *Kramer* [1988], *Seifert and Kramer* [2000], *Vokurka and Povondra* [1983], *Medaris et al.* [1997, 1999], and *Ulrych et al.* [2000]. Mean temperatures of equilibration of spinel lherzolites, harzburgites, and wehrlites range from 840°C to 1270°C; equilibration pressures between 10 and 27 kbar (30-90 km depth) were obtained by the different authors.

Table A.I Results of geothermobarometric studies on upper mantle xenoliths from volcanic fields adjacent to the western Eger Graben area (Rhön, NE Bavaria, Elbe Zone – eastern Eger Rift area).

Locality	xenolith type	T [°C]	p [kbar]	reference
NE-Bavaria	sp-lherzolites groundmass	1139±15 ~1000	26±2	*Huckenholz and Noussinanos* [1977]
	sp-lherzolites	920-1075		*Huckenholz and Kunzmann* [1993]
Rhön	sp-lherzolites/ wehrlites	840-1050	11-24	*Franz et al.* [1997]
	sp-lherzolites/ harzburgites	1190-1270	19-26	
	sp-lherzolites	920-950 840-850	10-13 26-27	*Witt-Eickschen and Kramm* [1997]
Kozákov	sp-lherzolites sp-lherzolites	1243±33 975-1090	17.7±2.4 12.0-18.6	*Vokurka and Povondra* [1983] *Medaris et al.* [1997, 1999]
Elbe Zone	sp-lherzolites harzburgites	1110 1040		*Kramer and Seifert* [2000]
Eastern Erzgebirge	sp-lherzolites harzburgites	1020 955		*Kramer and Seifert* [2000]
Lusatia	sp-lherzolites harzburgites	1000 860		*Kramer and Seifert* [2000]

The former presence of garnet within some spinel lherzolite samples was inferred from LREE/HREE ratios, occurring pyroxene-spinel clusters, and isotopic ratios (^{143}Nd/^{144}Nd) of clinopyroxenes [*Witt-Eickschen and Kramm,* 1997]. According to *Witt-Eickschen and Kramm* [1997], garnet-bearing peridotite entered the spinel stability field as a consequence of mantle diapirism. The age of metasomatism and enrichment of former depleted upper mantle is discussed as pre-Cainozoic, probably Hercynian in age. K-Ar model ages of xenoliths from Saxony, ranging between 89 and 254 Ma, are possible indications for an upper mantle where Variscan and older mantle melts were derived from [*Kramer*, 1988].

A.4 Scope of this study

The results of teleseismic tomography and fluid mapping at the surface (gas composition, gas flow, isotopes) in continental rift environments (e.g., European Cainozoic Rift System) are not completely compatible. Teleseismic tomography studies are commonly focused to >100 km depths, whereas the data of magma/gas researches are mainly directed to subcrustal and crustal depths (<100 km). The results of the fluid mapping from the western Eger Rift/Czech-German border region [*O´Nions et al.,* 1989; *Weinlich et al.,* 1999, 2003] have to be combined with geophysical and petrological indications for the lithospheric structure in the same area to locate the source region of the gases and to understand the deep covered processes, which lead to the observed fluid activity. This was the motivation to start a local-scale mapping of the Moho discontinuity and the subcrustal mantle in the Czech/German border area of the western Bohemian Massif using seismic and petrological methods.

This work consists of two main parts including results from two different geoscientific methods. At first, I present results from a passive seismic study (Ps receiver functions). At second, I present petrological data and their interpretation from a xenolith study. Finally, I try to integrate the results from both methods into a conceptional model that is able to explain the new seismic and petrological data together with results from previous seismic, seismological, and gasgeochemical investigations. The combination of xenolith investigations and geophysics is a useful tool to study the crust-mantle transition, as it is already mentioned by *O'Reilly and Griffin* [1985]: "The integration of petrological and geophysical data allows interpretation of stratigraphy of the lower crust – upper mantle, of the nature of the Moho and of the thermal evolution of the upper lithosphere for the time range represented by the host volcanic rocks".

I discuss the seismic structure and possible petrological composition of the crust-mantle boundary and the uppermost mantle beneath the western Eger (Ohře) Rift in relation to the composition, isotope (C, He) geochemistry and gas flow of active mantle fluids (CO_2-dominated emanations at the surface), magmatic underplating of the continental crust and intraplate seismicity (earthquake swarms in the upper crust). Direct compilation of seismic evidence (e.g., Moho depth map) with composition, gas flow and isotope (He, C) values of fluids are rare in the literature [*Marty et al.,* 1992].

B   Seismic investigations (receiver functions)

The Moho depth and morphology is one of the most important features to characterize the overall structure of the lithosphere, i.e. it is a key for the reconstruction of the tectonic evolution of the region. The depth variations of the discontinuities bounding the mantle transition zone at about 410 km and 660 km depths ('410' and '660') are also important to characterize the (physical/chemical) properties of the upper mantle and the mantle transition zone.

The receiver function method is an excellent tool for detecting seismic discontinuities (e.g., Moho) within the lithosphere and the deeper upper mantle analysing Ps conversions [*Vinnik,* 1977; *Langston,* 1979; *Zandt et al.,* 1995]. The fundamentals of the method are described, e.g., by *Kind and Vinnik* [1988] and *Kind et al.* [1995]. The method allows the evaluation of crustal and mantle structures at regional scales (plumes, subduction zones, and continental plate boundaries). Case studies demonstrate the high scientific potential of the receiver function method: Hawaiian and other oceanic mantle plumes [*Li et al.,* 2000a, 2003a], Japan and Hellenic subduction zones [*Li et al.,* 2000b, 2003b], Central Andes [*Yuan et al.,* 2000, 2002], detached Indian lithospheric mantle beneath Tibet [*Kosarev et al.,* 1999; *Kind et al.,* 2002], and the structure of the continental plate boundary between the Baltic Shield and the German-Polish Basin in Europe [*Gossler et al.,* 1999; *Alinaghi et al.,* 2003]. P-SV conversions also provide evidence for a magma chamber beneath the Campi Flegrei Caldera near Naples, Italy [*Ferrucci et al.,* 1992].

B.1   Observational technique (receiver function method)

The basis of the receiver function analysis is three-component recording of teleseismic events. P-to-S conversions at seismic discontinuities are caused by incident P-waves being partly converted to S-waves. These phases travel their last leg with shear wave velocity and arrive in the coda of the P-wave on the radial component, consequently. Amplitudes, arrival times, and polarity of the Ps-phases are mainly sensitive to the shear wave velocity distribution beneath the recording site. These converted phases can be extracted from the P-coda applying several processing steps, including rotation into the ray co-ordinate system of the P-, SV- and SH components, restitution of broadband ground displacement, deconvolution in time domain to remove the source time function and travel path effects [e.g., *Kind et al.,* 1995], distance move-out (time) corrections for a reference epicentral distance of 67° [*Yuan et al.,* 1997], and stacking. The processed receiver functions provide images of the crust and upper mantle similar to steep angle reflection images of the crust. The seismic wave periods used (one to several seconds; strongly depending on the instruments used and noise conditions) are longer than in controlled source seismic measurements, because teleseismic earthquakes are utilized as sources.

Also, multiple reflections and conversions between the base of the crust and the surface of the Earth occur and must be considered (Figure B.1). For the calculations of move-out corrections and the Moho piercing point locations, the IASP91 seismic velocity model [*Kennett*, 1991; *Kennett and Engdahl*, 1991] was used.

The depth of the Moho and the average crustal v_p/v_s ratio were computed using the method of *Zhu and Kanamori* [2000], which considers besides the direct conversion from the Moho, also its multiples. *Zandt et al.* [1995] and *Zandt and Ammon* [1995] used a similar approach. A grid search for the maximum-stacked amplitude in the Moho depth (H) versus v_p/v_s domain was carried out in the interval of 20 to 60 km depth and 1.5 to 2.0 for the v_p/v_s ratio. Because the multiple phases have nearly identical curves in the H-v_p/v_s domain and sample a broader area, primary phases and the two multiple conversions were weighted before stacking with the values 0.5, 0.25 and 0.25, respectively, according to the suggestions of *Zhu and Kanamori* [2000].

To get an idea of the response of crustal structure in the investigated area, synthetic receiver functions were calculated for published seismic velocity models from the western and northern Bohemian Massif (see Figure B.10, below) using the approach of *Kind et al.* [1995]. They assumed that the Earth's crust could be modelled as a stack of horizontal homogenous layers over a homogeneous half-space. The incoming P-wave is considered to be a plane wave with a specific apparent velocity. *Kind et al.* [1995] showed that there are only small differences in the results using plane waves or reflectivity theoretical seismograms.

B.2   Data

In this study, teleseismic data from broadband and short-period seismological stations of several temporary networks, operated by the Seismologisches Zentralobservatorium Gräfenberg (SZGRF), the GeoForschungsZentrum Potsdam (GFZ), the Dublin Institute for Advanced Studies (DIAS), and the Universities of Munich, Potsdam and Stuttgart, and permanent networks of SZGRF, GRSN (German Regional Seismic Network), and the Institute of Geophysics, Praha of the Czech Academy of Sciences (IG CAS), were analysed (Figure B.2). Furthermore, the data from two permanent short-period seismic networks in NW-Bohemia (Figure B.2b), the WEBNET of IG CAS and the KRASNET of the Institute of Physics of the Earth, Brno (IPE Brno), were studied. More details are given in Tables B.I and B.II. The stations equipped with MARK (1s) seismometers (Table B.I) were restituted up to 12 seconds and are further referred as broadband stations. Almost all stations in the central study area (northeast of the Franconian Lineament) are grounded on crystalline rocks.
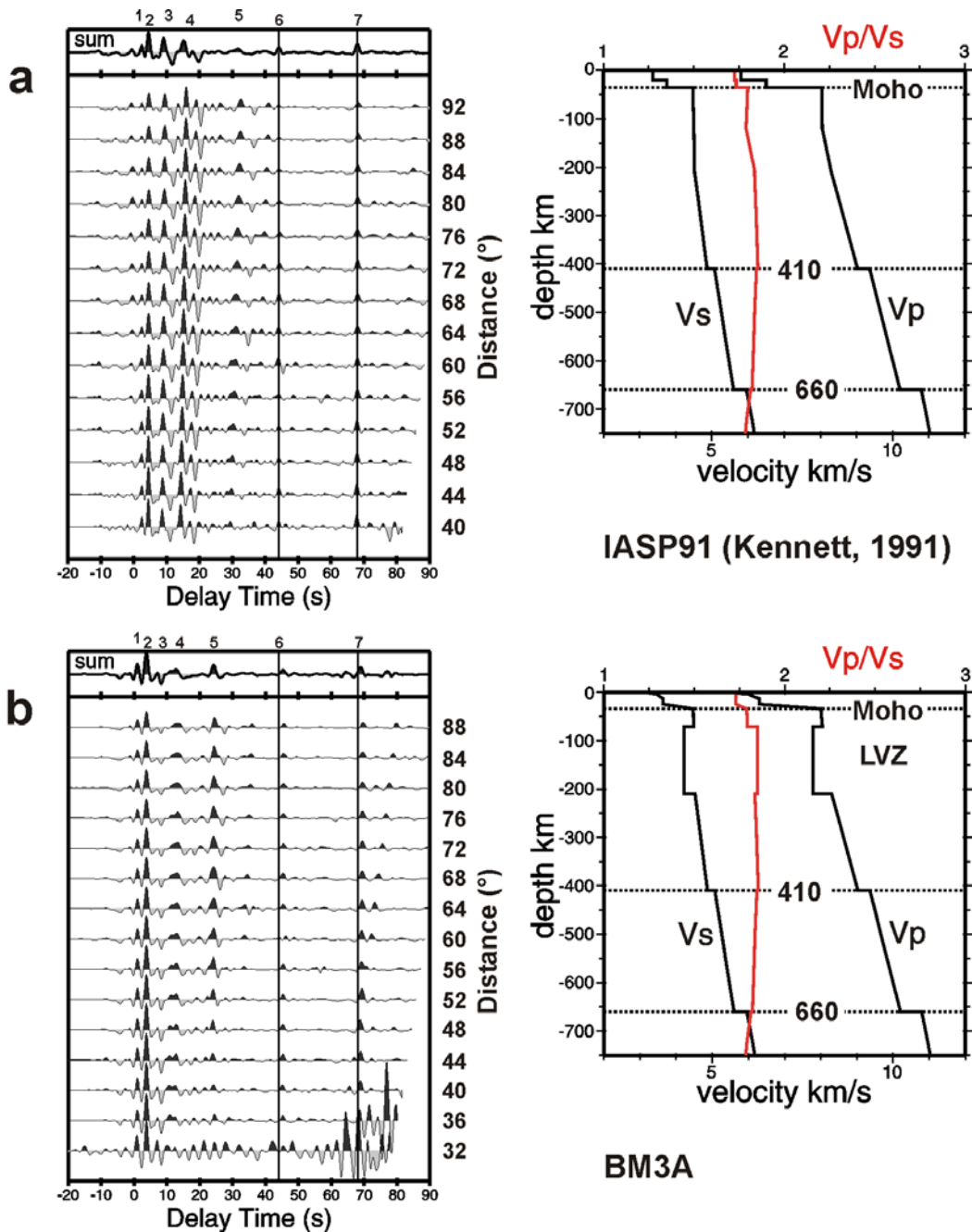
Figure B.1
Synthetic receiver functions from reflectivity theoretical seismograms [reflectivity method of *Kind*, 1985] calculated for **(a)** the IASP91 velocity model [*Kennett and Engdahl,* 1991] and **(b)** a hypothetic regional velocity model incorporating an asthenospheric low-velocity zone (LVZ; 71 to 210 km depth), which is missing in the IASP91 reference model. The source was presumed near the surface. The seismic velocity structure is the same at the source and receiver sides. Synthetic seismograms were processed like the natural data. Move-out corrected receiver functions are shown for different epicentral distances.

Converted (primary and multiple) phases are clearly visible within the first 20 seconds delay time, which stem from the Moho (2, 4) and crustal discontinuities (1, 3 for IASP91). Phases (5) around 30 seconds delay time for the IASP91 model **(a)** might represent further multiple phases from the crust, whereas the phase (5) visible in **(b)** stem from the sharp base of the hypothetical upper mantle low-velocity layer. The conversion from the upper boundary of the low-velocity layer is visible as a minimum at 8 seconds delay time (3). But in natural data it might be difficult to detect it due to interferences with the Moho conversion and crustal multiples.

Vertical solid lines at about 44.1 and 68.1 seconds delay time mark the delay times of converted phases from the discontinuities of the mantle transition zone ('410' and '660'), according to the IASP91 velocity model. As expected, the modelled conversions (6, 7) in **(a)** fit the theoretical delay time, whereas converted phases in model **(b)** arrive later than predicted by the IASP91 reference model (45.4 and 68.9 seconds delay time).

17
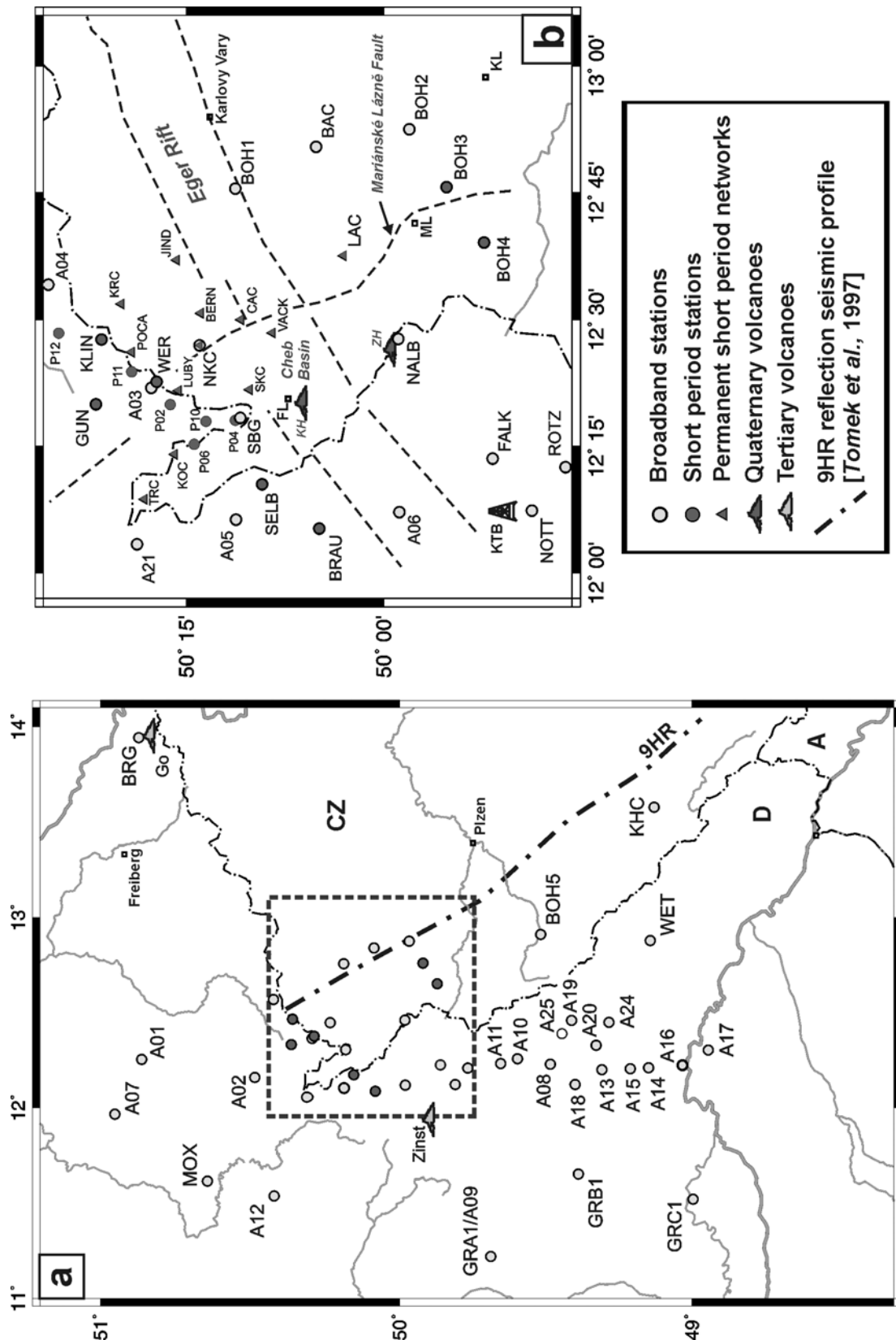
Figure B.2
(a) Distribution of the seismological stations in the western Bohemian Massif, from which data are used in this study. Also shown are the xenolith sample sites Gottleuba (Go) and Zinst. **(b)** Enlarged map of the Vogtland/NW-Bohemia region with the locations of all short period and broadband stations, the 9HR reflection seismic profile [*Tomek et al.*, 1997], main faults (hatched lines), and the Quaternary scoria cones.
KTB – location of the German Continental Deep Drilling Boreholes (KTB), FL – Františkovy Lázně, ML – Mariánské Lázně, KL – Konstantinovy Lázně, KV – Karlovy Vary, KH – Komorní Hůrka, ZH – Železná Hůrka.

Seismic events within an epicentral distance range from 30° to 97° and magnitudes > 5.5 were analysed. Only events with a good signal-to-noise-ratio of the P-onset and without disturbances within 100 seconds after the P-onset were selected. The theoretical back-azimuth angle was used for rotation, whereas the incidence angle was generally computed from the waveforms of the radial and vertical components.

B.3   Results

B.3.1   Observed receiver functions (single and sum traces)

Good observations of the Moho conversions and the crustal multiples were made at about 50 stations in the region under study (Figures B.3, B.4). Most stations of the KRASNET and WEBNET networks (Figure B.5) yielded also good Moho conversions, in spite of their short period seismometers and the short recording windows (triggered operation mode). Finally, also the short-period stations of the temporary deployment during the earthquake swarm 2000 yielded acceptable receiver functions, but the number of analysed events is strongly limited (Figure B.5).

At some stations, positive Ps-phases originating in the upper crust within 2 seconds after the P-onset were observed. Most of the crustal arrivals are related to strong velocity gradients, which exist in the uppermost crystalline crust [*Malek et al.*, 2001; *Hemmann et al.*, 2003] or a sedimentary cover (e.g., stations GRA1, GRB1, GRC1, FUR). Receiver function modelling of published velocity models confirms these effects of the uppermost kilometres (see Figure B.10). Later Ps conversions within 3 seconds delay time might be caused by deeper structures like the "Erbendorf body" (*DEKORP Research Group*, 1988; *Schmoll et al.,* 1989) beneath the station NOTT. Deeper crustal arrivals were also observed at the short-period stations SKC, CAC and LAC (Figure B.5).

At almost all stations strong conversions with positive polarity (indicating velocity increase downwards) with delay times of about 3.6 seconds after the P-wave can be seen in single traces (Figure B.3) as well as in the stacked traces (Figures B.4 and B.5). These conversions can be attributed to the Moho discontinuity. Moho multiples are visible in Figures B.3 and B.4 near 13 seconds (positive, PpPs) and 16 seconds (negative, PpSs+PsPs). These multiples are weaker or do not exist in Figure B.5 because only short-period stations are displayed there. Multiples loose higher frequencies when travelling two times more through the attenuating and scattering crust. At station NKC, a distortion of the Moho multiples is visible in traces from southeastern to western azimuths, whereas only a slight anomaly exists in the direct Moho conversions. This might be an indication for an anomaly at the crust-mantle boundary 10 to 20 km away from the station.
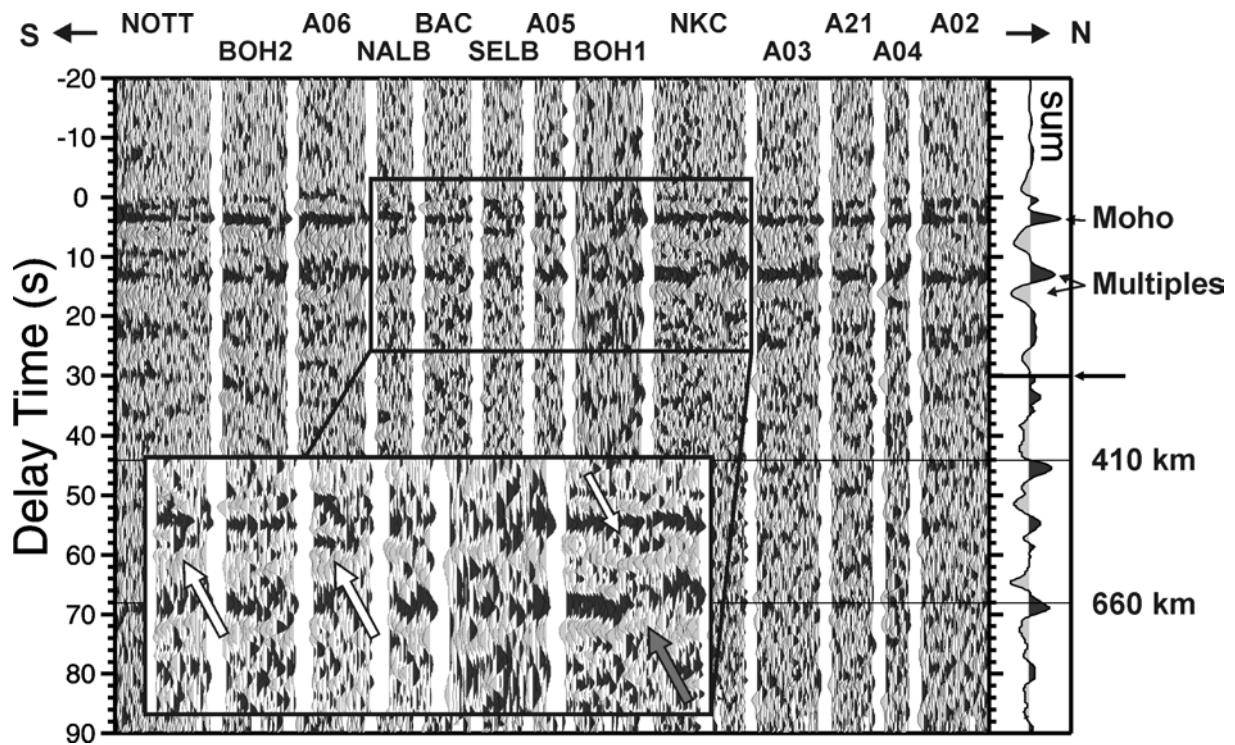
Figure B.3
Individual receiver functions for some stations within the region shown in Figure B.2b. Traces were high-pass filtered with 12 seconds corner period and move-out corrected. A delay time of 0 second is equivalent to the P-wave arrival time. Traces were clock-wise sorted after back-azimuth for each station (from left to right).
The average delay time for P-to-S converted waves from the Moho discontinuity is about 3.6 seconds. Multiple phases from the Moho arrive with about 13 and 16 seconds delay time. At station NKC, a distortion of the Moho multiples is visible in traces from southeastern to western azimuths (to the right of the dark grey arrow), whereas there are only slight variations in the direct Moho conversions. Additional phases with 6 seconds delay time are visible at the stations SELB, NALB and NKC (light arrows). The conversions from the upper mantle discontinuities at 410 km and 660 km depth can be seen in the stack trace. The amplitudes are four times enlarged in the delay time window from 30 to 90 seconds (arrow: change in scale). Both Ps phases arrive later as predicted by the IASP91 velocity model [straight lines; *Kennett and Engdahl*, 1991], possibly indicating lower seismic velocities above the 410 km discontinuity than in the IASP91 velocity model.

Additionally, conversions are observed at about 6 to 9 seconds delay time at some stations. Especially interesting is a phase near 6 seconds delay time beneath the region of earthquake swarms, which is detectable beneath several stations in this area (stations SELB, NALB, and NKC in Figure B.3). Stacking the single traces with move-out corrections for primary and multiple phases implies that the observed "6 s phase" might be a primary one, however the move-out differences are very small and are within the resolution limits.

Signals from 410 and 660 km discontinuities are delayed by up to 2 seconds compared to theoretical delay times calculated from the IASP91 reference model (sum trace in Figure B.3). This could be an indication for reduced seismic velocities in the upper mantle (above 410 km) relative to the reference earth model. Further results and discussion dealing with the mantle transition zone discontinuities follow below in section B.3.4.
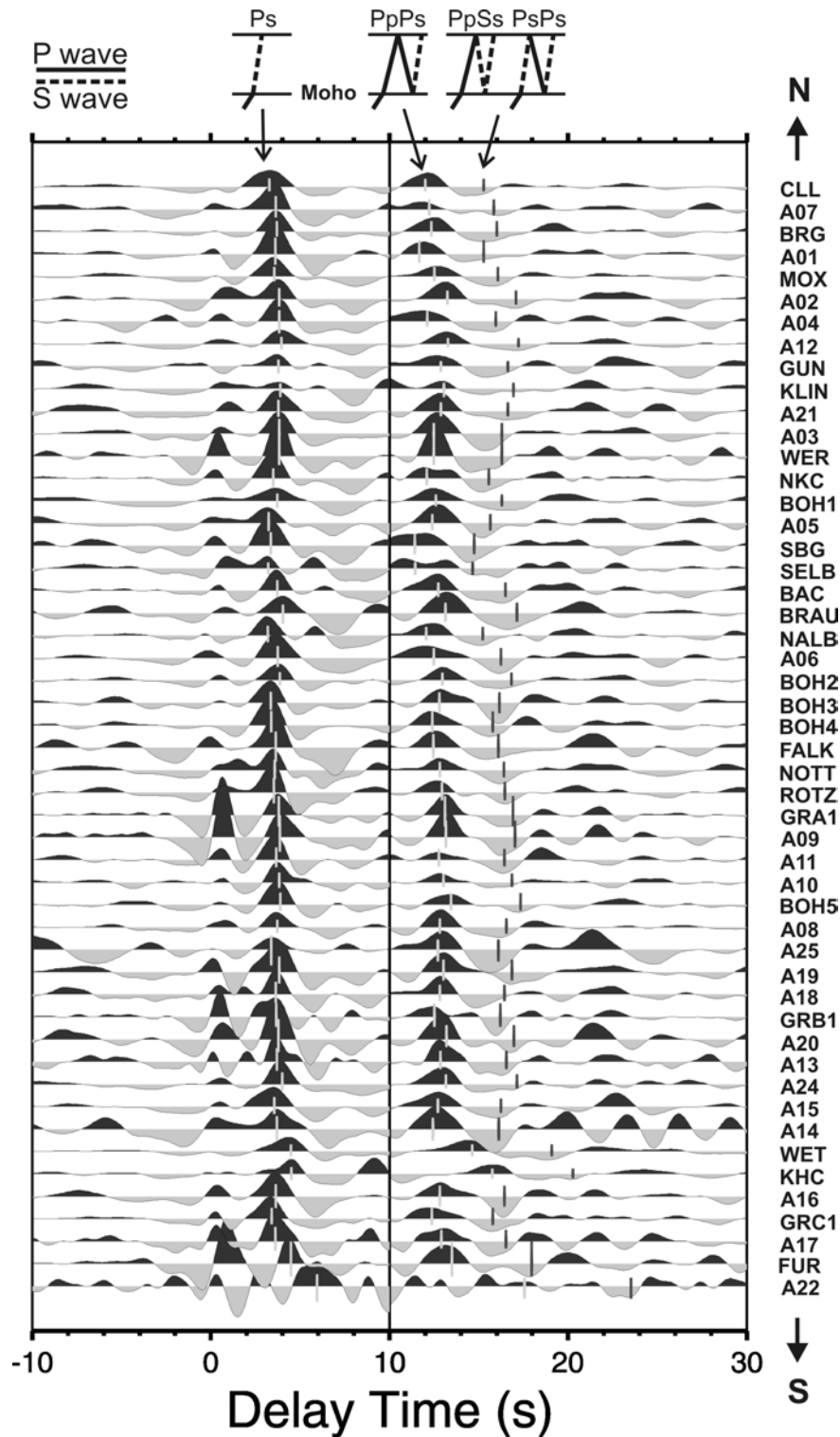
Figure B.4

Stacked receiver functions from broadband stations, aligned from the north (top) to the south (bottom). Traces were high-pass filtered with 12 seconds corner period and move-out corrected for primary Ps (-10 to 10 seconds delay time) and multiple PpPs (10 to 30 seconds delay time) conversions before stacking. The average delay time for P-to-S converted waves from the Moho discontinuity is about 3.6 seconds. Multiple phases (PpPs and PpSs+PsPs) from the Moho arrive with about 13 and 16 seconds delay time. Re-calculated delay times of the direct Ps-converted phase and its multiples from the Moho are marked, using the Moho depths and v_p/v_s ratios from Table B.1 and an average crustal P-wave velocity of 6.3 km/s.

Stations CLL, FUR, and A22 are situated outside the area shown in Figure B.2a. The deepening of the Moho towards the Alps can be seen at station A22 (near Innsbruck, Austria).

21

Table B.I. Seismological station parameters (including station code, latitude, longitude, elevation, operating institutions, recording time, and seismometer type) for broadband instruments, crustal thickness (H_c), crustal v_p/v_s ratio, Ps delay times (t_{ps}) for the Moho, '410' and '660' discontinuities, and number of stacked traces (n). The data were band-pass filtered using different corner periods for the analyses of the Moho (temporary stations: 1 to 12 seconds; permanent stations: 1 to 20 seconds) and '410'/'660' (temporary stations: 5 to 20 seconds; permanent stations 5 to 50 seconds) discontinuities, respectively. Different numbers n belong to the analyses for the Moho and the mantle transition zone discontinuities, respectively.

Station	Lat [°E]	Lon [°N]	Elev. [m]	Institution	Data	Seismometer	H_c [km]	v_p/v_s	t_{ps}[s] Moho	t_{ps}[s] 410	t_{ps}[s] 660	n
CLL	13.003	51.308	230	GRSN	1993 - 1997	STS-2	29.5±2.0	1.67±0.11	3.3	43.3	67.7	180/230
BRG	13.943	50.873	296	GRSN	1993 - 1997	STS-2	29.3±1.8	1.76±0.08	3.6	44.8	68.4	177/210
MOX	11.656	50.645	455	GRSN	1992 - 1997	STS-2	30.3±1.8	1.71±0.07	3.5	44.0	68.0	193/228
TNS	8.449	50.224	815	GRSN	1991 - 1997	STS-2	24.5±2.0	1.74±0.11	2.8	45.6	69.5	236/272
WET	12.878	49.144	613	GRSN	1991 - 1997	STS-2	34.3±1.8	1.79±0.09	4.4	45.3	68.6	249/298
STU	9.190	48.770	360	Stuttgart/GEOFON	1996 - 2003	STS-2	24.8±2.3	1.73±0.11	2.9	44.6	67.8	54/354
BFO	8.330	48.331	589	GRSN	1991 - 1997	STS-2	27.0±1.5	1.67±0.10	2.9	44.0	68.1	219/277
FUR	11.277	48.164	565	GRSN	1991 - 1997	STS-2	30.5±1.5	1.89±0.06	4.3	44.3	68.1	236/282
GRA1	11.222	49.692	500	SZGRF	1980 - 1997	STS-1	31.5±0.5	1.73±0.05	3.7	45.7	68.7	397/694
GRB1	11.652	49.391	494	SZGRF	1980 - 1997	STS-1	29.8±1.3	1.75±0.06	3.6	44.5	68.3	349/622
GRC1	11.521	48.996	512	SZGRF	1980 - 1997	STS-1	30.3±1.8	1.68±0.07	3.3	43.9	68.8	325/587
NKC	12.361	50.233	564	IG CAS	2000 - 2003	STS-2	28.8±1.8	1.73±0.07	3.4	47.7	69.3	89
DPC	16.322	50.350	784	IG CAS	2000 - 2003	STS-2	27.8±1.3	1.80±0.08	3.7	44.5	69.1	144
PRU	14.542	49.988	302	IG CAS	2000 - 2003	CMG-3T	33.0±1.0	1.67±0.05	3.6	45.4	70.6	107
KHC	13.578	49.131	700	IG CAS	2000 - 2003	STS-2	38.3±1.8	1.71±0.05	4.5	44.8	68.7	156
BOH1*	12.757	50.188	420	GFZ/SZGRF	1997 - 2001	40T/ MARK/ TSJ	30.0±1.5	1.75±0.10	3.6	45.8	68.5	30/13
BOH2*	12.874	49.967	660	GFZ/SZGRF	1997 - 1998	GURALP-40T	30.8±1.8	1.76±0.09	3.8	45.3	68.6	36
BOH3	12.760	49.920	610	GFZ/SZGRF	1997 - 1998	MARK-L-4-3D	32.0±1.5	1.63±0.07	3.3	45.9	69.1	15
BOH4	12.651	49.872	605	GFZ/SZGRF	1997 - 1998	MARK-L-4-3D	30.5±1.5	1.67±0.07	3.3	45.2	69.6	21
BOH5*	12.000	49.520	380?	GFZ/SZGRF	1997 - 1998	GURALP-40T	32.3±1.8	1.73±0.07	3.8	45.4	69.0	30
NOTT	12.910	49.811	490	KTB/Munich	1995	STS-2	31.3±1.3	1.69±0.05	3.5	46.3	69.2	42/44
FALK	12.225	49.861	465	KTB/Munich	1995	STS-2	29.8±1.8	1.74±0.07	3.6	45.8	68.1	12
ROTZ	12.208	49.768	430	KTB/Munich	1995	STS-2	31.8±1.3	1.67±0.05	3.5	46.0	70.0	18/16
A01	12.255	50.863	270	GFZ/SZGRF	1995 - 1996	GURALP-3T	27.3±1.8	1.80±0.08	3.5	48.0	68.8	26
A02	12.159	50.487	414	GFZ/SZGRF	1995 - 1996	GURALP-3T	31.8±1.3	1.72±0.08	3.8	45.5	67.1	30
A03	12.364	50.294	670?	GFZ/SZGRF	1995 - 1996	GURALP-3T	29.3±1.3	1.79±0.07	3.8	44.7	49.6	28/27
A04	12.568	50.424	915?	GFZ/SZGRF	1995 - 1996	STS-2	28.0±1.5	1.81±0.11	3.8	44.7	67.1	9

* GURALP-40T seismometers were provided by the Dublin Institute for Advanced Studies (DIAS).

Table **B.I.** (continued).

Station	Lat [°E]	Lon [°N]	Elev. [m]	Institution	Data	Seismometer	H_c [km]	v_p/v_s	t_{ps}[s] Moho	t_{ps}[s] 410	t_{ps}[s] 660	n
A05	12.104	50.187	670	GFZ/SZGRF	1995 - 1996	3T/MARK	29.5±1.5	1.68±0.08	3.4	(50.4)	(66.9)	22
A06	12.119	49.980	635	GFZ/SZGRF	1995 - 1996	GÜRALP-3T	29.5±2.0	1.77±0.09	3.6	45.5	71.0	30
A07	11.967	50.952	469	GFZ/SZGRF	1995 - 1996	GÜRALP-3T	29.0±2.0	1.76±0.08	3.5	44.9	68.4	20
A08	12.229	49.487	499	GFZ/SZGRF	1995 - 1996	GÜRALP-3T	30.8±1.3	1.73±0.07	3.7	45.4	68.5	19
A09	11.222	49.692	597	GFZ/SZGRF	1995 - 1996	STS-2	31.5±1.0	1.74±0.06	3.9	46.0	67.5	15
A10	12.258	49.599	665	GFZ/SZGRF	1995 - 1996	GÜRALP-3T	31.0±1.0	1.75±0.05	3.7	46.3	66.4	17
A11	12.233	49.656		GFZ/SZGRF	1995 - 1996	STS-2	30.8±1.8	1.72±0.06	3.6	46.1	68.8	29
A12	11.538	50.422	448	GFZ/SZGRF	1995 - 1996	STS-2	31.5±1.5	1.76±0.08	3.9	45.3	69.1	28
A13	12.200	49.311	512	GFZ/SZGRF	1995 - 1996	STS-2	31.0±1.0	1.72±0.05	3.6	46.5	68.1	10
A14	12.211	49.150	428	GFZ/SZGRF	1995 - 1996	STS-2	29.3±1.8	1.76±0.08	3.7	(47.8)	(68.9)	2
A15	12.205	49.213		GFZ/SZGRF	1995 - 1996	STS-2	31.0±1.5	1.69±0.08	3.5	44.5	68.1	28
A16	12.224	49.033	212	GFZ/SZGRF	1995 - 1996	STS-2	31.0±1.5	1.71±0.08	3.6	45.1	69.4	22
A17	12.303	48.944	360	GFZ/SZGRF	1995 - 1996	STS-2	31.5±1.5	1.69±0.06	3.5	44.5	67.4	19
A18	12.122	49.402		GFZ/SZGRF	1995 - 1996	STS-2	31.0±1.0	1.71±0.06	3.6	45.2	69.8	16
A19*	12.459	49.414	475	GFZ/SZGRF	1995 - 1996	GÜRALP-40T	31.0±1.5	1.75±0.07	3.8	44.2	69.3	17
A20	12.328	49.330		GFZ/SZGRF	1995 - 1996	STS-2	31.8±1.3	1.72±0.06	3.7	46.7	66.9	9
A21	12.056	50.312		GFZ/SZGRF	1995 - 1996	GÜRALP-3T	30.8±1.3	1.74±0.07	3.7	48.5	68.5/72.4	19
A22	11.300	47.150	555	GFZ/SZGRF	1995 - 1996	STS-2	39.3±2.8	1.92±0.11	6.0	(47.7)	(67.9/72.0)	7
A24	12.449	49.286	555	GFZ/SZGRF	1995 - 1996	GÜRALP-3T	31.0±1.5	1.78±0.08	3.9	47.5	69.0	13
A25*	12.389	49.447	780	GFZ/SZGRF	1995 - 1996	GÜRALP-40T	31.5±2.0	1.65±0.10	3.4	-	-	3
WER	12.376	50.287	708	GFZ/SZGRF	1999 - 2000	MARK-L-4-3D	29.3±1.3	1.79±0.08	3.7	(49.5)	(69.2)	10
GUN	12.332	50.364	640	GFZ/SZGRF	1999 - 2000	MARK/TSJ-10	30.8±1.8	1.74±0.07	3.7	(49.1)	(68.2)	14/7
KLIN	12.462	50.358	580	GFZ/SZGRF	1999 - 2001	MARK-L-4-3D	31.0±1.0	1.76±0.06	3.8	-	-	21
SELB	12.179	50.154	660	GFZ/SZGRF	1999 - 2001	MARK/ TSJ-10	27.8±1.3	1.70±0.06	3.1	45.5	67.7	18/14
NALB	12.461	49.981	530	GFZ/SZGRF	2000 - 2001	MARK/STS2/TSJ	30.0±1.5	1.64±0.06	3.1	47.4	69.3	16/17
BAC	12.840	50.086	595	GFZ/SZGRF	2000 - 2001	TSJ-10	30.5±1.0	1.74±0.06	3.7	45.9	69.6	21
SBG	12.305	50.182	600?	GFZ/SZGRF	1998 - 2001	TSJ-10	27.3±2.3	1.74±0.11	3.2	(45.8)	(67.4)	5
BRAU	12.087	50.082		GFZ/SZGRF	1998 - 1999	MARK-L-4-3D	30.8±1.8	1.79±0.11	4.0	-	-	7
						Average:	30.5±1.5	1.73±0.08	3.6			

* GÜRALP-40T seismometers were provided by the Dublin Institute for Advanced Studies (DIAS).

23

Table B.II. Same as in Table B.I for short-period networks (except of Ps delay times for the '410' and '660'). v_p/v_s ratios were taken from nearby broadband stations to calculate crustal thickness from Moho Ps dealy time (t_{Ps}).

Station	Lat [°E]	Lon [°N]	Elev. [m]	Institution	Data	Seismometer	H_c [km]	v_p/v_s	t_{ps}[s]	n
POCA	12.435	50.319	800	IPE Brno	1997 - 1998	WDS	30.7	1.77	3.9	29
LUBY	12.359	50.260	625	IPE Brno	1997 - 1998	WDS	28.0	1.78	3.6	31
JIND	12.617	50.262	722	IPE Brno	1997 - 1998	WDS	28.3	1.75	3.5	15
BERN	12.512	50.232	635	IPE Brno	1997 - 1998	WDS	29.9	1.73	3.6	20
TRC	12.151	50.310	566	IG CAS	1997 - 1998	SM-3?	31.1	1.74	3.8	40
KOC	12.234	50.265	575	IG CAS	1997 - 1998	SM-3	31.9	1.74	3.9	50
KRC	12.530	50.332	760	IG CAS	1997 - 1998	SM-3	27.1	1.76	3.4	53
NKC	12.448	50.233	564	IG CAS	1997 - 1998		29.0	1.73	3.5	54
CAC	12.499	50.181	578	IG CAS	1997 - 1998	SM-3?	29.5	1.74	3.6	11
SKC	12.361	50.170	455	IG CAS	1997 - 1998	LE-3D	28.6	1.74	3.5	16
LAC	12.514	49.967	838	IG CAS	1997 - 1998	SM-3	28.6	1.74	3.5	44
P02	12.396	50.319		Uni Potsdam/GFZ	2000	LEN5s/MARK	28.8	1.78	3.7	3
P04	12.300	50.188		Uni Potsdam/GFZ	2000	LEN5s/MARK	27.0	1.74	3.3	6
P06	12.253	50.240		Uni Potsdam/GFZ	2000	LEN5s/MARK	23.7	1.74	2.9	9
P10	12.298	50.225		Uni Potsdam/GFZ	2000	LEN5s/MARK	25.4	1.74	3.1	3
P11	12.331	50.270		Uni Potsdam/GFZ	2000	LEN5s/MARK	28.6	1.74	3.5	7
P12	12.472	50.411	825?	Uni Potsdam/GFZ	2000	LEN5s/MARK	31.1	1.74	3.8	8
						Average:	28.7	1.75	3.5	
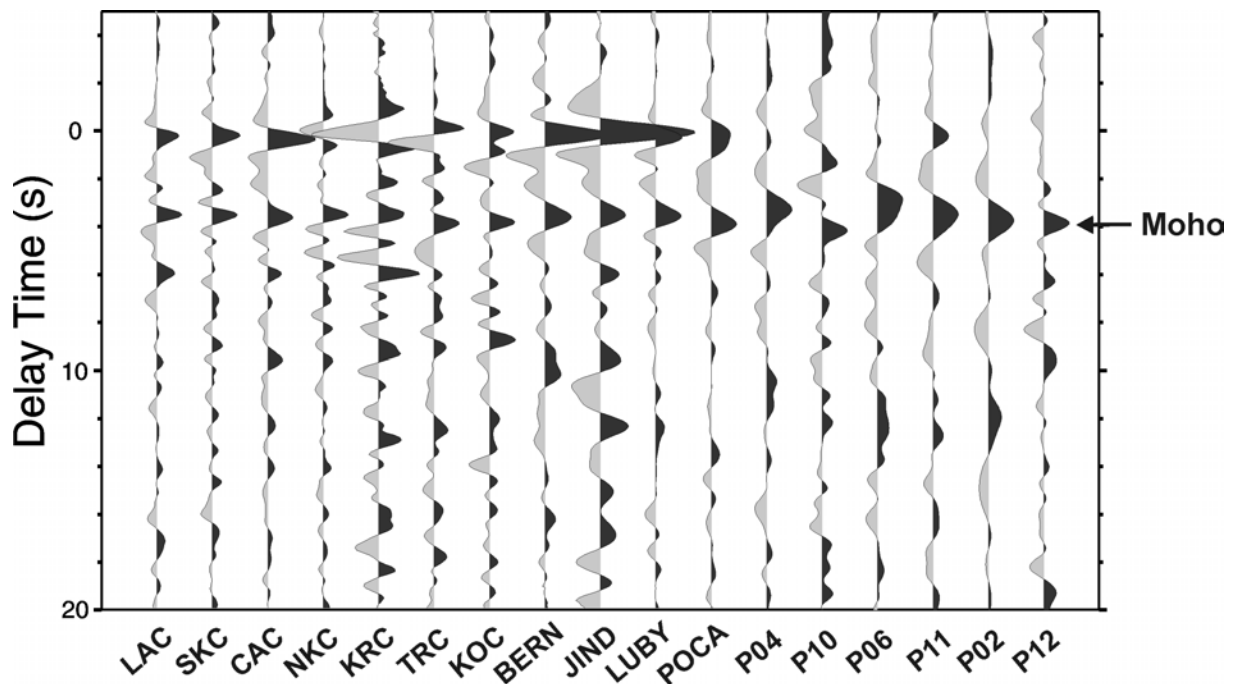
Figure B.5
Stacked receiver functions from short-period stations. Integration was applied instead of the usual restitution of ground displacement before the traces were high-pass filtered with 5 seconds corner period. Conversions at the Moho are observed, whereas short period instruments did not allow the identification of multiple phases.

There are also positive phases visible in the sum traces at individual stations at about 20 seconds delay time, but they are not very coherent from station to station. These phases might be a hint for a discontinuity near 220 km depth as proposed in the PREM-model [*Dziewonski and Anderson,* 1981]. Generally, Ps conversions from the 220 km discontinuity interfere with crustal multiples, and they are therefore difficult to detect using Ps receiver functions [see *Kind and Vinnik,* 1988].

B.3.2   Moho depth

To compute the Moho depth (crustal thickness) and v_p/v_s ratios, the data were stacked using a method introduced by *Zhu and Kanamori* [2000] (Table B.I and Figure B.6). In Figure B.7a-c the observed Moho Ps delay times, Moho depths, and v_p/v_s ratios from all broadband stations and stations with MARK-L-4-3D seismometers in the region were mapped. The corresponding values are given in Table B.I. To a first approximation, the map of Ps delay times (Figure B.7a) can be regarded as an initial Moho map assuming a constant v_p/v_s ratio of 1.73 for all stations and multiplying the recorded delay times by an empirical value of 8.4 km/s. Obviously most of the region has delay times of about 3.7 seconds (green dots, about 31 km depth). In the Vogtland/NW-Bohemia region and the area near the station GRC1, the converted phases from the Moho arrive 3.0 to 3.3 seconds after the P-wave (reddish dots, 25 to 28 km depth). Later arrivals (4.3 to 4.5 seconds delay time, blue dots, 36 to 38 km depth) are observed at the stations WET and KHC in the southeast of the area under study.
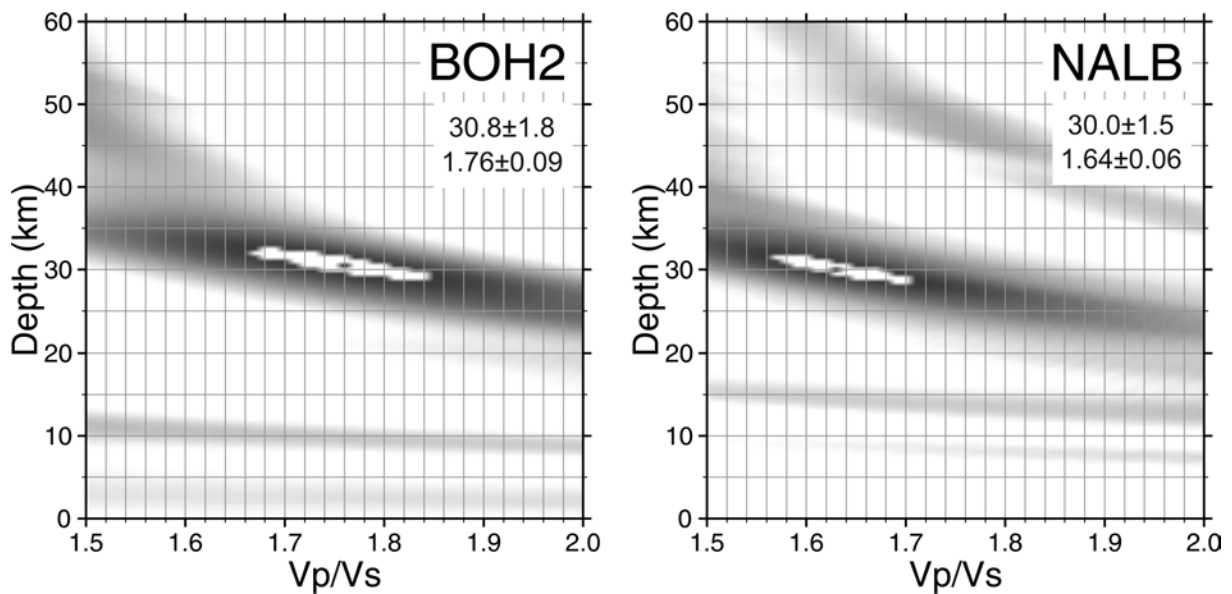
Figure B.6
Inversion results of Moho depth versus v_p/v_s ratio for the stations BOH2 and NALB. The maximum stacked amplitudes were found by grid search within the intervals of 20 to 60 km for the Moho depth and 1.50 to 2.00 for the v_p/v_s ratio. An average crustal P-wave velocity of 6.3 km/s was assumed. The surrounding white area marks the region of 95 % of the maximum stacked amplitude. The half-width of the 95 %-region gives an estimate of the uncertainty of the method.

Figure B.7 (next page)
(a) Map of Moho conversion times (Ps delay times, Table B.I) for the broadband stations. The mean value for all stacked traces at a specific station is projected onto the piercing points of rays at Moho level (30 km depth). This shows the back-azimuth coverage at each station. As can be expected, the permanent observatories have better back-azimuth coverage than temporary stations with only a few months of registration time. **(b)** Map of Moho depths and **(c)** map of v_p/v_s ratios compiled on the basis of the results of the inversion method proposed by *Zhu and Kanamori* [2000] (see Table B.I; assuming an average crustal P-wave velocity of 6.3 km/s).
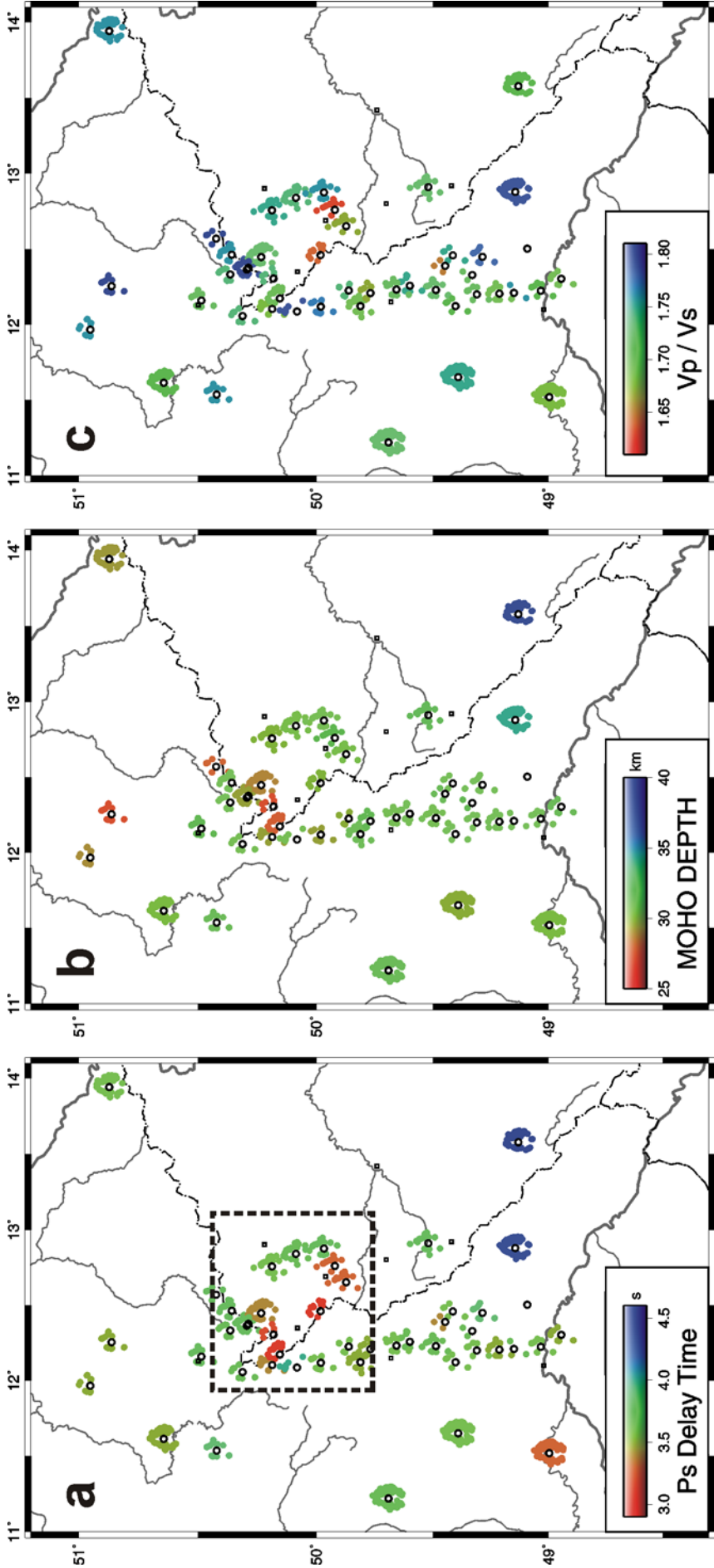
The results from the receiver function analysis after *Zhu and Kanamori* [2000] were compiled into a map of Moho depths (crustal thicknesses) for the region NW-Bohemia/NE-Bavaria/Vogtland (Figure B.7b). This map is not corrected for the station elevation. In general, the Moho depth increases from NW (31 km) to SE (38 km). Beneath the Cheb Basin the Moho seems to dome up to at least 27 to 28 km. However, this anomaly does not reach as far south as the Ps delay time anomaly in Figure B.7a. Moho depths of about 27 to 28 km were also obtained further north (station A01). The area around GRC1 shows no Moho depth anomaly as in the Ps delay times. This is due to a decreased v_p/v_s ratio (see Figure B.7c). Stations WET and KHC in the SE show the deepest Moho (34 and 38 km). Generally, the observed Moho depths are in good agreement with values obtained by several regional refraction and reflection seismic studies.

B.3.3   Crustal v_p/v_s ratios

A map of the v_p/v_s ratios (Figure B.7c) was compiled from the inversion results listed in Table B.I. The average value in the region is 1.73. Higher v_p/v_s ratios (1.76-1.81) are measured beneath the western Erzgebirge Mountains (stations A03, A04, WER). Decreased values (1.63-1.69) are obtained beneath the German-Czech border region east of the KTB (stations NALB, BOH3, BOH4), the southern KTB-area (stations NOTT, ROTZ), and north and west of Regensburg (stations A15, GRC1). Very high values of 1.89 were measured beneath the Molasse Basin and the northern Alps (stations FUR and A22, not on the map). The discrepancy between different Moho depths and nearly identical Moho Ps delay times at the two CO_2 emanation centres, FL (Františkovy Lázně / Cheb Basin; stations SELB, SBG) and ML (Mariánské Lázně; stations BOH3, BOH4), is associated with the observation of lower v_p/v_s ratios in the more southern area. Similar observations were also made in other areas worldwide [e.g., *Yuan et al.,* 2002].

There exist several possibilities to explain such relatively low values, which seem to be very low compared to laboratory measurements of typical crystalline crustal rocks. *Christensen* [1996] estimated an average v_p/v_s ratio for the continental crust of about 1.76 from laboratory measurements of typical crustal rocks. Values < 1.65 were only measured for rocks with high quartz content. Another possibility to explain low values is the presence of fluids under normal pore pressure within pores of low aspect ratio [*Lüschen et al.,* 1993]. Recently published seismic velocity models for the upper crust of NW-Bohemia [e.g., *Janský et al.,* 2000; *Málek et al.,* 2000] also show relatively low v_p/v_s ratios. Possibly, the low v_p/v_s ratios observed for the upper crust are valid for the whole crust in distinct parts of the regions. Maybe quartz-rich rocks or the presence of fluids dominate these parts.

Generally, a sedimentary cover containing layers with very low shear wave velocities could influence the distribution of v_p/v_s ratios, but almost all stations in this study are grounded on crystalline rocks.

Some stations in the southwestern study area (GRA1, GRB1, GRC1, A13, and A17) are installed on sedimentary rocks, up to approximately 1200 m thick [see *Krüger and Weber,* 1992]. However, this thin sedimentary cover should not have a huge influence on the average crustal v_p/v_s ratio. High v_p/v_s ratios at the southernmost stations FUR and A22 might be influenced by thick sedimentary successions [see *Bachmann et al.,* 1987].

The observed anomaly in v_p/v_s ratios could also be caused by structural effects like topography at the Moho, which is observed beneath the western Eger Rift. *Zandt et al.* [1995] obtained v_p/v_s ratios of 1.62 to 1.64 for the westernmost Basin and Range Province, North America. They discussed the very low values in that region as being possibly caused by the breakdown of the assumption that the crust is laterally homogeneous. A lateral change in crustal thickness of 5 km together with an unchanged Moho conversion time would lead to a v_p/v_s change of 3.5 % (1.67 instead of 1.73) according to *Zandt et al.* [1995]. Direct conversions and multiples sample different paths within the crust. Therefore, lateral variations also might influence the results. The direct Moho conversions sample the Moho about 5 to 10 km away from the station, whereas the crustal multiples sample the Moho over a distance of 5 to 30 km from the station.

B.3.4   Discontinuities of the mantle transition zone

The seismic discontinuities bounding the mantle transition zone in depths of approximately 410 km and 660 km are interpreted as dominantly caused by the isochemical phase transformation of olivine into spinel structure and its final breakdown to perovskite and magnesiowüstite [e.g., *Helffrich and Wood,* 2000; *Lebedev et al.,* 2002] at pressures of approximately 14 GPa and 24 GPa, respectively. Both transformations are temperature dependent, but have opposing Clapeyron slopes [e.g., *Katsura et al.,* 2004; *Fei et al.,* 2004]. This means, if the temperature is higher than normal (e.g., in a plume environment), the '410' should be deeper (higher pressures) and the '660' shallower (lower pressures). Topography of the upper mantle seismic discontinuities seems to be largely uncorrelated at a global scale, and '660' topography is significantly larger in peak-to-peak amplitude according to *Shearer* [2000]. Studies of triplications, of reflected and converted phases are widely used methods to investigate the seismic discontinuities of the mantle transition zone; very common are Ps receiver function studies [e.g., *Kind and Vinnik,* 1988; *Stammler et al.,* 1992; *Petersen et al.,* 1993; *Chevrot et al.,* 1999; *Li et al.,* 2000a, 2003a; *Shearer,* 1991, 2000].

One common approach to study the depth of the upper mantle discontinuities with receiver functions is stacking of the move-out corrected single traces for each station separately, especially for widely spaced stations and short registration periods. As already discussed above, strong converted phases

within 20 seconds delay time are caused by a sedimentary cover (especially beneath the Gräfenberg Array) or velocity gradients in the uppermost crystalline crust, the Moho discontinuity and its multiple phases. About four times weaker (in amplitude) converted phases are visible at 44 to 46 seconds and 67 to 69 seconds delay times (Figure B.8). These phases should be related to the upper mantle discontinuities, as it could be shown in Figure B.1 calculating synthetic receiver functions for relatively simple velocity models. The observed delay times of converted phases from the discontinuities of the mantle transition zone at single stations are listed in Table B.I.
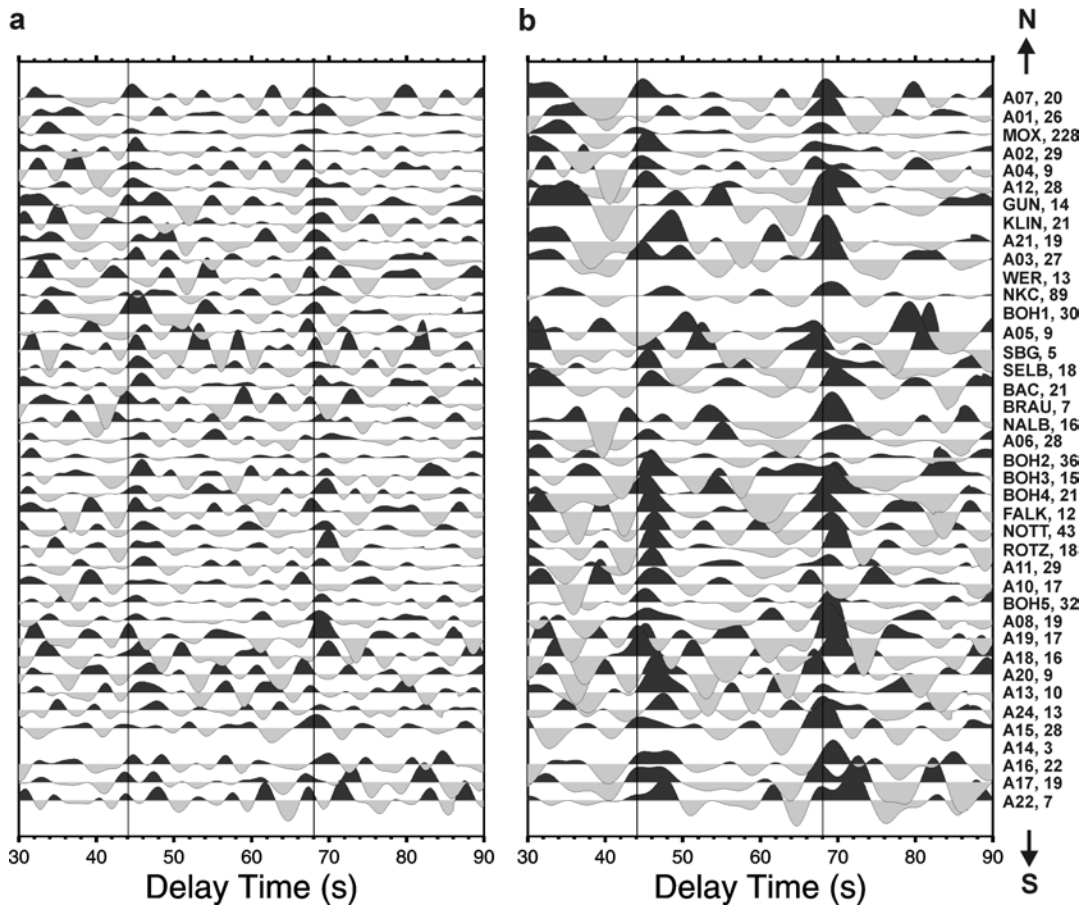
Figure B.8
Stacked move-out corrected (for 67° epicentral distance) traces of the single station analysis of permanent and temporary stations in the western Bohemian Massif. Different band-pass filters were applied **(a)** with corner periods of 3 and 20 seconds, **(b)** with corner periods of 5 and 20 seconds. Theoretical delay times of the '410' and '660' conversions predicted by the IASP91 velocity model [*Kennett*, 1991] are marked by vertical solid lines. An apparent deepening (late arrivals) of the '410' is evident for several stations (see also Table B.I).

Delayed arrival times of the '410' and '660' of up to 2 seconds were observed at many stations in the western Bohemian Massif. The differential travel times for converted phases from the transition zone ($dt_{660-410}$) are generally about 24 ± 0.5 seconds (see Table B.I; Figure B.8). At some stations, a lower $dt_{660-410}$ might indicate a real thinning of the transition zone [see *Li et al.,* 2003a], assuming no seismic velocity variations within the transition zone. No indications (coherent phases) for a seismic discontinuity at 520 km depth are observed in this study.
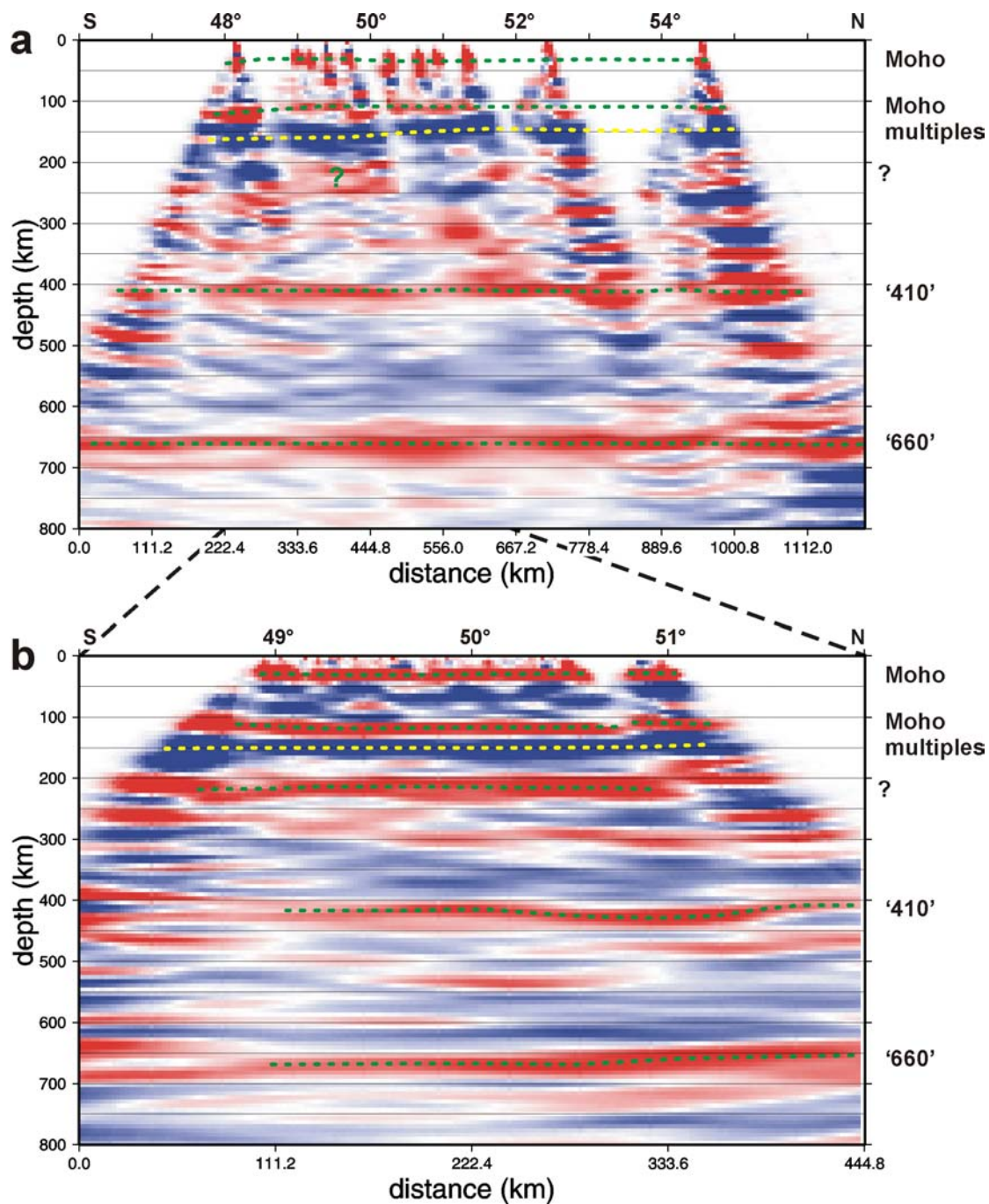
Figure B.9
Migrated sections along 12°E and 12°30'E with data from permanent **(a)** and temporary **(b)** stations in the study area, respectively. For the migrated profile along 12°E teleseismic data from permanent stations FUR, KHC, WET, GRA1, GRB1, GRC1, PRU, NKC, MOX, BRG, CLL, CLZ, BRNL, RUE, and RGN were used and processed in the same way as the data from the temporary stations. Data were provided by the data centres in Erlangen (GRF, GRSN), Potsdam (GEOFON) and Praha (IG CAS). IASP91 seismic velocity model [*Kennett*, 1991] was used for migration.

The apparent deepening of the '410' between 50.5 and 51°N **(b)** is most probably caused by velocity variations in the upper mantle. Delayed '410' conversions are observed at stations further to the south, as it is obvious from Figure B.8. Since most events come from northeastern back-azimuths, the delay is projected towards the north along a N-S profile. However, also a real deepening 'of the 410' cannot be excluded at the present stage of investigation.

A strong phase at about 210 km might be an indication for a seismic discontinuity (like the '220' in PREM; *Dziewonski and Anderson* [1981]) or can be a further multiple phase from the Moho. The later interpretation would imply a generally very strong velocity contrast at the Moho and only small damping of teleseismic waves within the crust.

Figure B.9 shows a north-south migrated section projected along a profile at 12°30'E using data from the temporary networks in the western Bohemian Massif (b) in comparison to a migrated section along 12°E using data from permanent stations in Germany and the Czech Republic (a). For the migration, again the IASP91 velocity model was used. The overall structure is similar for both data sets, including a strong phase in about 200-250 km depth beneath the temporary stations in the western Bohemian Massif, and the discontinuities of the transition zone. North (-east) of the Vogtland/NW-Bohemia area a small-scale deepening of the '410' by about 20 km is indicated.

In my opinion, this apparent deepening is an effect of the upper mantle velocity structure [see also *Kind and Vinnik,* 1988], which is consistent with receiver function modelling (Figure B.1). This is also indicated by the variations in delay times of the '410' recorded at different single stations close to each other (Figure B.8, Table B.I). However, a further detailed analysis (including mapping) of the '410' and '660' discontinuity conversions in the area is necessary. As in the single station analysis, no (coherent) conversions from a seismic discontinuity at 520 km depth could be observed.

B.3.5   Synthetic receiver functions for published crustal seismic velocity models

Synthetic receiver functions calculated for published regional seismic velocity models, using the plane wave approximation, are shown in Figure B.10. The different models resulted from refraction (Figure B.10a-c, e-f) and reflection seismic studies (Figure B.10g-i) as well as from analysis of surface waves (Figure 10d). There are simple models without strong velocity contrast/gradients in the crust, models with a high-velocity lower crustal layer, and with high- or low-velocity layers in the upper to middle crust. For comparison of the synthetic with the observed receiver functions sum traces with (trace V2, bottom) and without the "6 s phase" (trace V1, middle), and receiver functions from a nearby station (top) are shown. It is evident from Figures B.10 and B.4 that relative smooth crustal velocity models can explain most of the observed data whereas complex P-wave models (mainly from reflection seismic studies) with more than one high- or low- velocity layer in the crust do not explain the observed data.

Figure B.10 (next page)
Synthetic receiver functions (solid line) from published regional seismic velocity models. For comparison, observed receiver functions (dashed lines) are shown: the sum traces with (trace V2, bottom) and without the "6 s phase" (trace V1, middle) and sum traces from nearby stations (top). The plane wave approximation [*Kind et al.,* 1995] was used for the calculation. The sum traces of the corresponding L components were used as input P-signal. Scale shown corresponds to 10 % of the amplitude of the primary P-signal. Most of the models can explain at least the primary and multiple Moho phases in the observed receiver functions.

Gräfenberg - *Aichele* [1976]

MOKH - *Plešinger et al.* [1994]

MVE90 CMP1 - *Behr et al.* [1994]

GRANU95 shotpoint F - *Enderle et al.* [1998]

W-Bohemian Massif - *Strößenreuther* [1982]

MVE90 CMP2 - *Behr et al.* [1994]

Vogtland - *Köhler et al.* [1989]

Vogtland - *Schulze and Lück* [1992]

KTB MN - *Schmoll et al.* [1989]
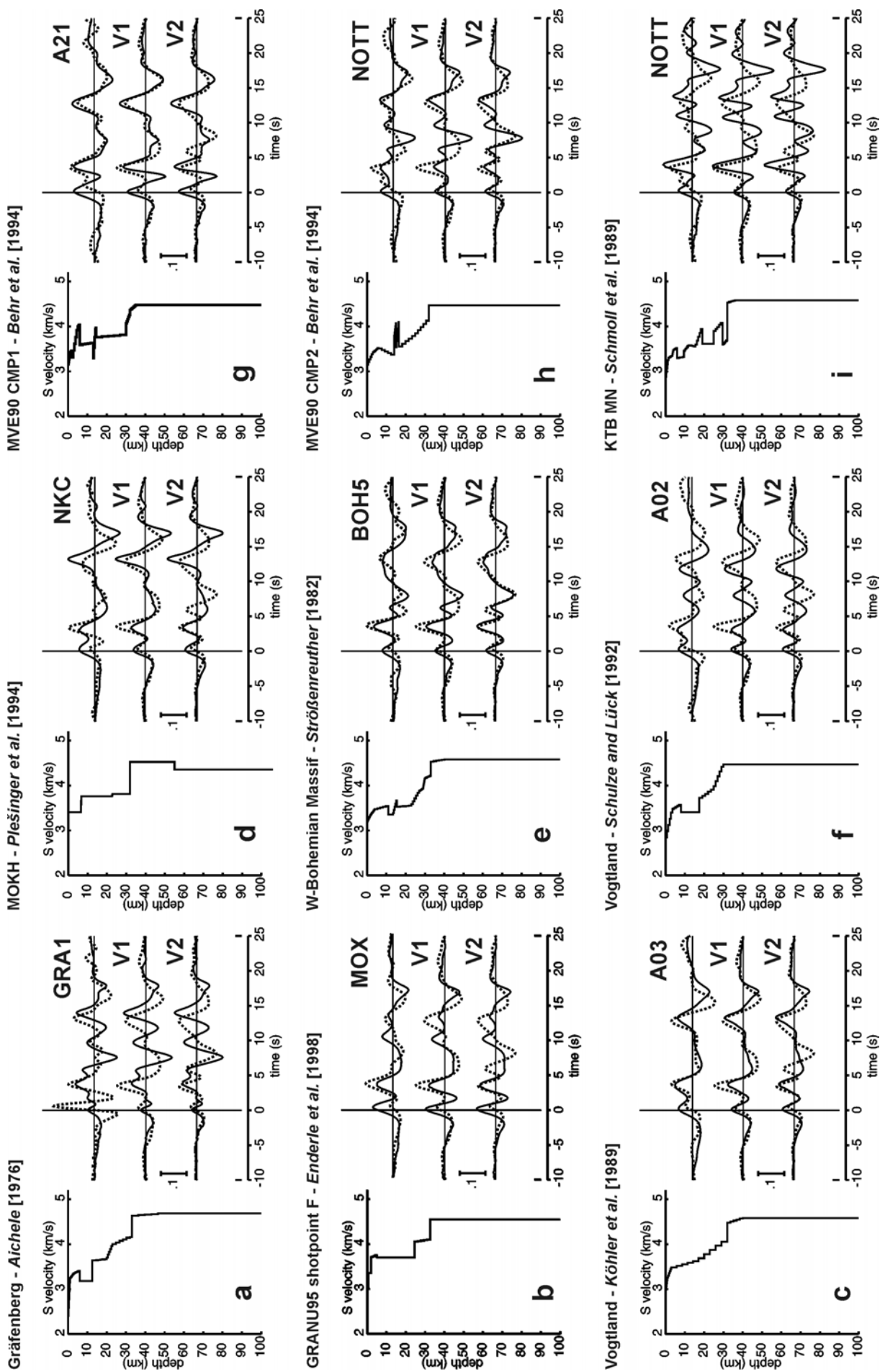
B.3.6   Uncertainties and resolution of the method

Variations depending on recording time and back-azimuth coverage

The vast amount of seismic data from the permanent stations GRA1 (1980-1997) and MOX (1993-1997) was studied in more detail to estimate the uncertainties of the results due to short recording periods at temporary stations. The Moho depth, v_p/v_s ratio, and Moho Ps delay time were analysed for different time spans (from 2 months up to 18 years) and for different back-azimuths, respectively (Figure B.11; Table B.III). From Figure B.11 it is obvious that several tens of traces are needed to obtain a stable result. Typically, this requires at least one year of recording time. The inverted Moho depths and v_p/v_s ratios can vary for short time spans (only few events) by up to 2 km and 0.05, respectively. The crustal thickness and v_p/v_s ratio may depend on the back-azimuth of teleseismic events, and therefore, also on the back-azimuth distribution of seismic events at the stations. The values obtained vary by up to 2 km for crustal thickness and 0.07 for v_p/v_s ratio at the two stations GRA1 and MOX for different back-azimuths. These variations might be caused by real Moho topography around the stations, and therefore they are not considered as an error of the method. Because there is no perfect back-azimuth coverage for most of the temporary stations, the data were stacked over all back-azimuths. This way, an average crustal thickness beneath each station was obtained.

Uncertainty of the grid search method and Ps delay time measurements

One can estimate an error of the grid search if one assumes that all stacks in the crustal thickness-v_p/v_s ratio domain within the 95 % contour of the maximal stacked amplitude are possible solutions (white areas in Figure B.6). This procedure results in estimated errors for the average values of v_p/v_s ratios and crustal thicknesses of ±0.08 and ±1.5 km, respectively (Table B.I). A systematic error also could exist due to the assumed average crustal P-wave velocity of 6.3 km/s. Lateral variations of the average P-wave velocity within rifts and at terrane boundaries might exist. If one assumes a higher P-wave velocity of about 6.5 km/s, as it might be the case for the central Bohemian Massif, then the Moho depth increases by about 2 km. If one assumes 6.0 km/s, the values decrease by about 2 km. In this analysis, v_p/v_s ratios vary by about 0.03, but show no direct dependence on P-wave velocity. Up to now, there is no information available on small-scale average seismic velocity variations in the region. That's why a constant value was used. Also, I do not think that the average crustal P-wave velocity varies over short distances by more than 0.2 km/s. Therefore, the observed variations in Moho depth do probably not depend significantly on crustal P-wave velocity in the region under study. However, a linear trend to underestimated Moho depths might exist towards the central Bohemian Massif.
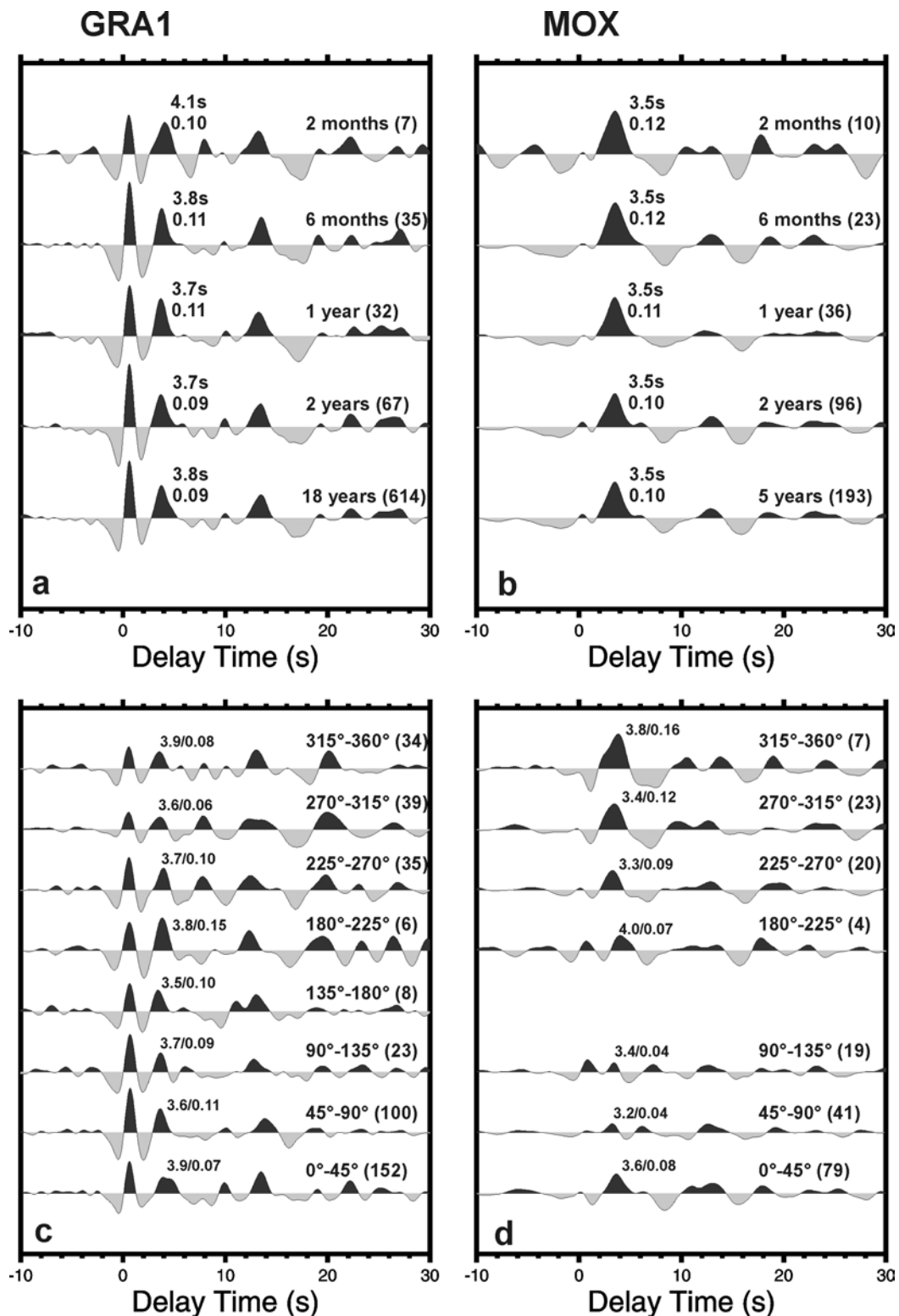
Figure B.11
Stacked receiver functions from stations GRA1 and MOX from different time spans **(a, b)** and back-azimuths **(c, d)**. The numbers to the right of the time spans or back-azimuth windows indicate the number of stacked traces. Traces were high-pass filtered with 20 seconds corner period and move-out corrected before stacking. The numbers at the converted phase from the Moho represent the observed delay times and the relative amplitude ratios SV/P (amplitude of the converted phase on the SV/Q component after deconvolution with the P wave signal on the L component). Only small variations of the waveform were observed for the different time spans except for that of only 2 months, both at GRA1 and MOX **(a, b)**. Note that there are only small variations of the Moho conversion at station GRA1 with back-azimuth **(c)**, whereas there are strong variations at station MOX **(d)**. It seems that a complex Moho structure (branching) exists northeast of MOX.

The delay times of the direct Ps-converted phase and its multiples from the Moho were re-calculated using the Moho depths and v_p/v_s ratios from Table B.I, and an average crustal P-wave velocity of 6.3 km/s. The obtained values show a good agreement with the observed data (Figure B.4). This indicates that the method works well, at least at stations with a more or less simple velocity structure and clear primary and multiple Moho conversions.

Analysing 18 years of data from station GRA1 (1980-1997) for each year separately, variations in the Moho Ps delay times of 0.1 to 0.2 seconds could be observed (see Figure B.12, Table B.III). Therefore, the uncertainty of Moho Ps delay time measurements for temporary stations, which were operated for one year, might also be in the range 0.1 to 0.2 seconds. Delay times t_{p410s} and t_{p660s} observed in station stacks of GRA1 for different years of observation vary by about 0.5 to 1.0 seconds, showing no dependency on the filter used. Therefore, it can be assumed that the uncertainty for delay time measurements of conversions from the mantle transition zone ('410' and '660') are in the range of 0.5 to 1.0 seconds also for the temporary stations.
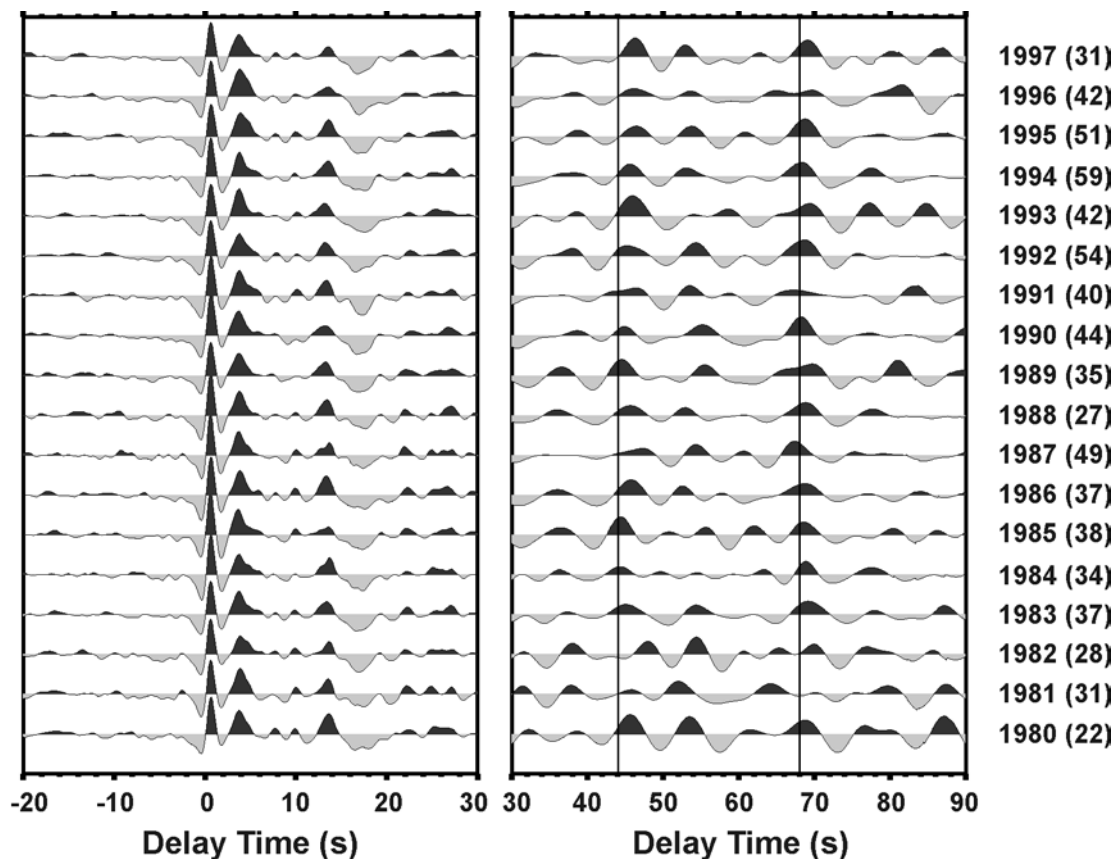
Figure B.12
Stacked receiver functions from stations GRA1 for every year between 1980 and 1997. The numbers to the right of the year indicate the number of stacked traces. Data were high-pass filtered with 50 seconds corner period in the time range -20 to 30 seconds delay time and band-pass filtered (corner periods 5 to 50 seconds) from 30 to 90 seconds delay time, respectively (see also Table B.III).

Summarizing, the maximum uncertainty for the observation of variations in the average crustal thickness ΔH is ±1.5 to ±2 km, and for v_p/v_s ratio ±0.08. The uncertainty of Moho Ps delay time measurements is in the range 0.1 to 0.2 seconds, which results also in about ±1.5 km for crustal thickness variations. The uncertainty of Ps delay time measurements for the '410' and '660' in single station stacks is about 0.5 to 1.0 seconds.

Table B.III. Variations of Ps delay times (Moho, '410', '660'), crustal thickness H, and average crustal v_p/v_s ratio at station GRA1 for the years 1980-1997. Data from each year were analysed separately in comparison to the whole data set.

Year	HP 20s v_p/v_s	HP 20s H (km)	HP 20s t_{PMs} (s)	HP 50s t_{PMs} (s)	relative amplitude	BP 3s-20s t_{P410s} [s]	BP 3s-20s t_{P660s} [s]	BP 3s-20s $dt_{660-410}$ [s]	BP 5s-20s t_{P410s} [s]	BP 5s-20s t_{P660s} [s]	BP 5s-20s $dt_{660-410}$ [s]	n
1980	1.71	32.0	3.7	3.7	0.10	45.2	68.8	23.6	45.7	68.7	23.0	22
1981	1.76	31.0	3.9	3.9	0.11	45.5	69.1	23.6	45.8	(67.2)	21.4	31
1982	1.74	31.5	3.8	3.9	0.08	48.5	69.7	21.2	48.0	69.9	21.9	28
1983	1.73	31.5	3.7	3.7	0.10	45.0	69.0	24.0	45.1	69.1	24.0	37
1984	1.72	32.0	3.7	3.7	0.09	45.0	69.0	24.0	44.3	68.8	24.5	34
1985	1.68	32.5	3.6	3.6	0.11	44.7	(68.9)	24.2	44.4	68.5	24.1	38
1986	1.74	31.5	3.8	3.8	0.10	45.1	68.8	23.7	45.8	68.7	22.9	37
1987	1.71	32.0	3.7	3.7	0.10	45.7	67.2	21.6	47.3	67.4	20.1	49
1988	1.75	31.5	3.8	3.8	0.10	46.0	69.2	23.2	45.7	68.8	23.1	27
1989	1.73	31.5	3.7	3.7	0.09	44.7	68.2	23.5	44.5	69.7	25.2	35
1990	1.71	31.5	3.7	3.7	0.10	45.0	68.3	23.3	44.9	68.2	23.3	44
1991	1.73	31.5	3.8	3.8	0.11	47.2	68.4	21.2	46.4	67.3	20.9	40
1992	1.73	31.5	3.8	3.8	0.09	44.2	69.4	25.2	45.1	68.7	23.6	54
1993	1.74	31.0	3.7	3.7	0.11	45.6	68.8	23.2	46.0	69.3	23.3	42
1994	1.74	31.5	3.8	3.8	0.10	45.4	69.1	23.7	45.6	68.3	22.7	59
1995	1.74	31.5	3.9	3.9	0.10	45.1	69.2	24.1	46.5	68.7	22.2	51
1996	1.75	31.5	3.8	3.8	0.12	45.6	69.3	23.7	46.1	69.6	23.5	42
1997	1.72	31.5	3.7	3.8	0.09	46.4	69.4	23.0	46.3	69.1	22.8	31
Mean	**1.73**	**31.6**	**3.8**	**3.8**	**0.10**	**45.5**	**68.9**	**23.3**	**45.8**	**68.7**	**22.9**	**39**
σ	0.02	0.4	0.1	0.1	0.01	1.0	0.6	1.0	0.9	0.8	1.2	
1980-1997	1.73	31.5	3.7	3.8	0.10	45.0	68.9	23.9	45.7	68.7	23.0	701

Another problem is the use of short period data without clear crustal multiples, especially at the WEBNET and KRASNET stations (Figure B.5). For the stations from these networks, crustal thicknesses were calculated from the observed Moho Ps delay times using v_p/v_s ratios from adjacent broadband stations. Unfortunately, the stations from the short-period networks were operated in a triggered mode, and the length of the time windows used for deconvolution is sometimes very small (only about 20 seconds). At station NKC, data from a broadband and a short-period seismometer were analysed, but from different time intervals (Tables B.I and B.II; Figures B.4 and B.5). At another site (nearby stations A03 and WER; Figure B.4, Table B.I) two different seismometers were operated at different times. For both locations, similar results could be obtained using different instruments.

B.4   Geophysical indications for Moho updoming and the origin of the "6 s phase"

B.4.1   Local Moho updoming beneath the western Eger Rift

In this section, the discussion of Moho depth variations is focused on the area of swarm-earthquakes, active mantle degassing, and Quaternary volcanism in the Vogtland/NW-Bohemia region. The local Moho depth distribution is plotted in Figure B.13, including the results from the short period stations that are not plotted in Figure B.7. Moho depths at short period stations are computed using v_p/v_s ratios of neighbouring broadband stations. Crustal thickness beneath the western Eger Rift is only about 27 km, whereas it is about 31 km in the surroundings. It is clear from the discussion of uncertainties above, that the observed updoming beneath the western Eger Rift is near the observation limit at a single station. Because different independent stations show an updoming in this area, in the Ps delay times (up to 0.8-1.0 seconds) as well as in the inverted Moho depths (about 4 km), I think that the observation is real. It is unlikely that errors in one region point always in the same direction, they should scatter.

Moho updoming seems to be restricted to the crossing of the Eger Rift and the Regensburg-Leipzig-Rostock Lineament (Cheb Basin; Figures A.1, B.13), however, there is no control (data) on the situation further to the northeast. To the southwest, no decreased Moho depths can be observed beneath the continuation of the Eger Rift. The area, where an updoming of the Moho is observed, has an NNW-SSE extension of approximately 40 km. The top of this Moho antiform is located beneath the gas escape centre Františkovy Lázně/Cheb Basin (section A.2.4; Figures A.4, B.13).

Moho updoming beneath continental rifts is nothing unusual, and it is observed beneath the southern Upper Rhine Graben [*Prodehl et al.,* 1995], the French Massif Central [*Zeyen et al.,* 1997], the Rio Grande Rift [*Baldridge et al.,* 1995], and the Kenya Rift [*Braile et al.,* 1994]. It seems to be a common structural feature of graben systems. However, there seems to exist also strong variations in Moho

depths along the axial grabens, as in the case of the Kenya Rift [*Mechie et al.,* 1994a]. One important feature in the western part of the Eger Rift is the local scale overlapping of Moho updoming with upper mantle derived gas exhalations and Quaternary volcanism (Figure B.13).
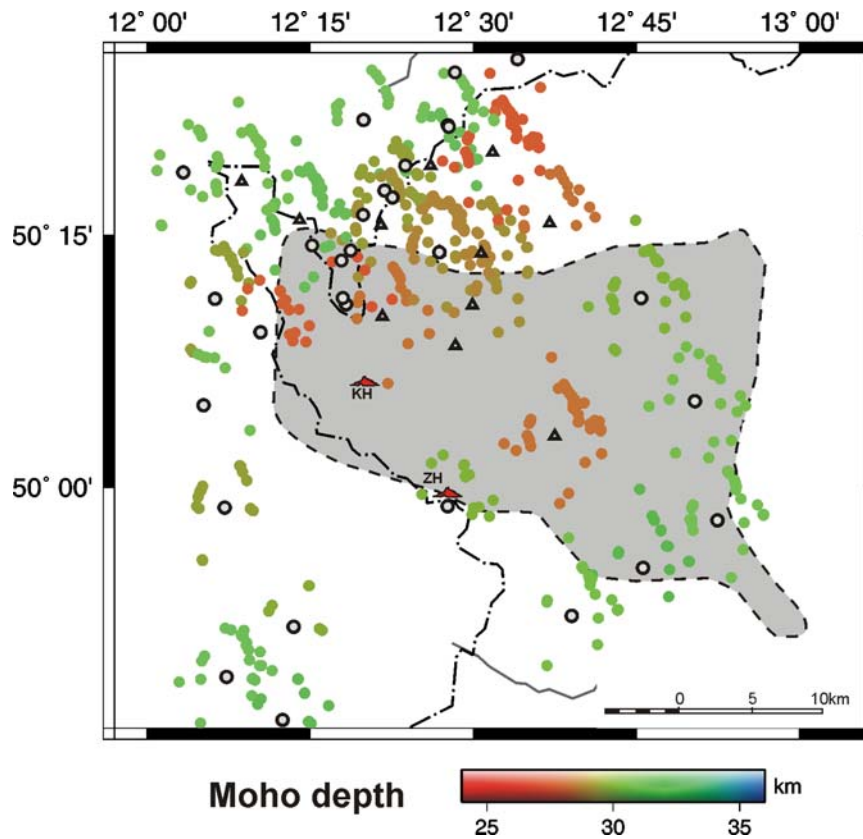
Figure B.13
Comparison of the Moho depths and the results of gas geochemical investigations (see Figure A.4). This map also contains the calculated Moho depths for the short period stations (see Table B.II).
Grey: CO_2 emanation area; KH – Komorní Hůrka, ZH – Železná Hůrka.

At the broadband station BOH1 within the Eger Rift, no clear Moho Ps conversions (Figure B.3) could be observed, mainly in the NE-back-azimuths (0-45°, Figure B.13). This points to a broad gradient zone, strong lateral heterogeneity at Moho level, or an inclination of the crust-mantle boundary in this area. Similar observations were also made at other stations (BOH2, SELB, NALB, KLIN, and GUN) associated with the find of a converted phase at about 6 seconds delay time, possibly stemming from beneath the Moho. In the case of BOH1 the area with the "diffuse" Moho character correlates well with the reflection free part in the 9HR seismic profile [*Tomek et al.,* 1997]. The reflection free parts might be caused by „bad" shots and industrial noise in the Sokolov Basin, a lignite mining area [*Tomek,* personal communication]. *Behr et al.* [1994] also found indications for a disturbed Moho with variations of 2 to 3 km beneath the Western Eger Rift. Offline observations of shots along the MVE'90 seismic profile indicate that the Moho is shallower beneath the Cheb Basin than further to the northeast beneath the Sokolov Basin [Figure 2.16 in *Behr et al.,* 1994].

Wilson et al. [2003] observed similar diffuse Moho conversions at stations above the Coso geothermal area, California. In their case, the converted phases seem to be strongly influenced by a magmatic system within the upper crust. No strong geothermal anomaly or magmatic system seems to exist in the upper crust beneath the Vogtland/NW-Bohemia area, with the exception of the Karlovy Vary Spa area. Hot springs in this area are attributed to a highly radiogenic Variscan granite complex (Karlovy Vary pluton) [see *Förster and Förster,* 2000]. Therefore, I conclude that the diffuse and weak Moho conversions really show effects at the crust-mantle boundary beneath the region.

B.4.2   The origin of the "6 s phase" – conversions from subcrustal depths or multiples from an intracrustal layer?

Clear converted phases with delay times of about 6 seconds are observed at stations SELB, NALB and NKC (Figure B.3, light arrows). Indications for such a phase were also found near stations BAC, BOH2, LAC, KLIN and GUN. The study area was divided into several boxes, and a common conversion point method was applied to search for the spatial distribution of the "6 s phase" (Figure B.14). The size and distribution of the boxes was chosen after several tests, including stacking within back-azimuth windows at single stations.

Receiver function modelling

To check the origin of the "6 s phase", synthetic receiver functions were calculated (Figure B.15) using the plane wave approximation [*Kind et al.,* 1995]. At first, a model with a more or less simple crustal structure is modelled, which can explain the data without the "6 s phase" (Figure B.15a). Subsequently, single low- or high seismic velocity layers were added into the crust and uppermost mantle. The response of each model is compared to the observed receiver functions, the sum of all traces without a "6 s phase" (trace V1, top) and with a "6 s phase" (trace V2, bottom).

Indications for low velocity channels in the middle crust as modelled in Figure B.15b were observed by several active seismic measurements [e.g., *Knothe*, 1972; *Strößenreuther*, 1982; *Holbrook et al.,* 1988; *Behr et al.,* 1994]. This relative simple model shows the best fit with the observed data up to 25 seconds delay time. Further tests showed that a low velocity channel (about 2 km thick, depth 11-13 km) within the crust cause multiples at about 6 seconds delay time. The velocity reduction could be due to lithological contrasts (e.g., quartzite) or due to the presence of fluids. Assuming a constant v_p/v_s ratio for the whole crust, velocities are reduced both by 8 % (5.7 instead of 6.2 km/s for v_p). In a fluid-rich layer the v_p/v_s ratio might be increased. *Faul et al.* [1994] published values for the velocity reduction per 1 % melt or fluid distributed in thin, elongated inclusions or within triple junction

tubules (1 to 1.8 % for v_p, 2.3 to 3.3 % for v_s). If I assume that these values obtained for basic to ultrabasic melt inclusions at upper mantle conditions are also more or less valid for a mid-crustal regime, the observed data could be modelled as an intracrustal layer filled with 3 to 5 % fluids. In this case, the v_p/v_s ratio is about 1.87 (velocity reduction: 5 % for P-waves, 11.5 % for S-waves). The lateral extension of such low-velocity zones should be at least 5 km, because only in this case multiple phases would be observed.

High velocity layers within the crust (Figure B.15c) might represent geologic bodies comparable to the "Erbendorf body", which is postulated beneath the KTB [*DEKORP*, 1988; *Emmermann and Lauterjung*, 1997]. The fit between synthetic and observed receiver functions in the first 6 seconds is not as good as for the other models, indicating that it might not be the most realistic model.

Model d (Figure B.15d) shows a hypothetic single thick magma reservoir in a "normal" upper mantle, assuming about 5 to 7 % magma dispersed in a more than 5 km thick layer within the lithosphere. Velocities are reduced by about 9 % (P-waves) and 16.5 % (S-waves; v_p/v_s equals 1.95), respectively, according to the maximum values published by *Faul et al.* [1994]. Model d does not fit the observed data at delay times greater than 14 seconds. If this low velocity anomaly would be a widespread phenomenon (channel) and no anelastic damping or scattering exist (as it is assumed by the modelling) one would expect to observe the strong multiple phases from this layer in the real data. However, if the anomaly is only a local phenomenon with a lateral extension of less than 25 to 30 km, or there exist strong damping and scattering, no multiple phases would be observed.

Model e (Figure B.15e) shows a (relative) high-velocity layer between upper mantle with reduced P- (S-) wave velocities compared to the IASP91 reference model (7.6 km/s above and 7.8 km/s below instead of 8.2 km/s). The discontinuities in the upper mantle can also be modelled as sharp boundaries. A sharp discontinuity in about 50 km depth produces a strong multiple phase at 20 seconds delay time in the synthetic traces, whereas a gradient zone at that depth range produces only a weak multiple, which might be not observable in the real data due to damping and scattering. These models might represent some eclogitic bodies within a "normal" uppermost mantle or a layer of "normal" mantle in-between "fluidised" mantle. Reduced seismic velocities in the upper mantle and an uplift of the asthenosphere were reported from surface wave studies [*Plešinger et al.,* 1994; *Passier and Snieder*, 1996] and studies of P-residuals [*Plomerová et al., 1988; Plomerová and Babuška,* 1998].

In all models discussed above (Figure B.15), it is necessary to introduce a broad gradient zone in the lower crust and at the Moho instead of a sharp velocity contrast to fit the amplitudes of the observed Moho conversions. Because the modelled sum trace is the result of stacking data from stations with different Moho depths, the contrast and therefore the amplitudes of conversions are damped. However, observations of very weak (in amplitude) conversion at several single stations (e.g., BOH1, SELB; Figure B.3) in the CO_2 degassing area might indicate the local presence of a gradient zone rather than a sharp (1st order) seismic discontinuity.
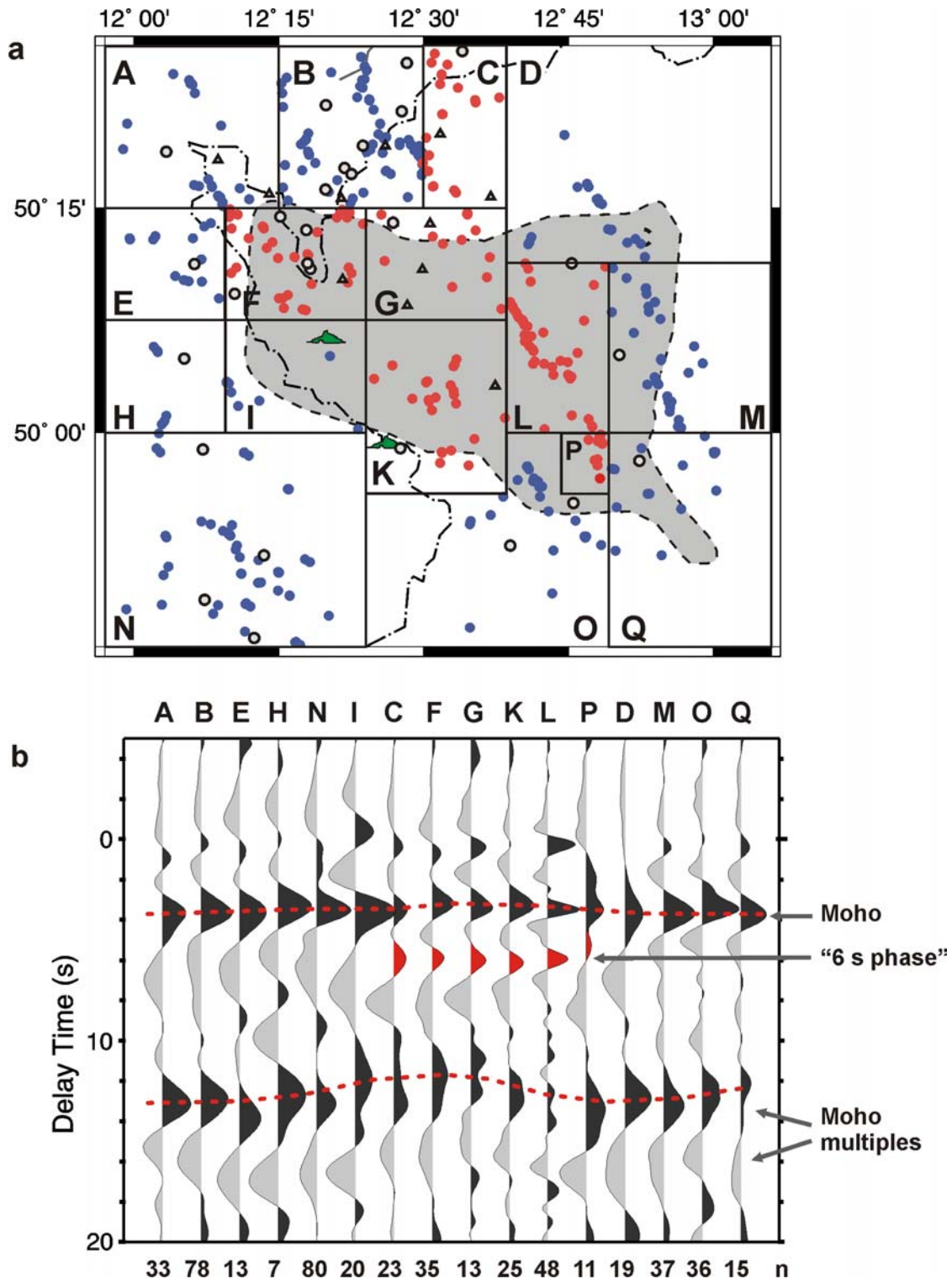
Figure B.14
(a) Distribution of piercing points at 50 km depth. Receiver functions with common conversion points were stacked in each box A-Q **(b)**. Blue dots mark boxes without a "6 s phase". Red dots mark boxes with the "6 s phase". Latter ones correlate with the distribution of mantle-dominated CO_2 emanation vents at the surface (grey shading, see also Figure A.4). Green triangles: locations of the two Quaternary scoria cones.
For the mapping of the "6 s phase" data from short period stations, which are mostly located in the main epicentral area, are included. Therefore, the signals from the Moho and the "6 s phase" contain higher frequencies than the traces in the surrounding area. The radius of the first Fresnel zone at 50 km depth, which can be used as an approximation for lateral resolution, is about 20 km. Note that the Quaternary volcanoes are located at the western edge of the red "6 s region". The Moho updoming beneath the central study area is obvious from the stack traces in **(b)**, especially looking at the first Moho multiples.

41
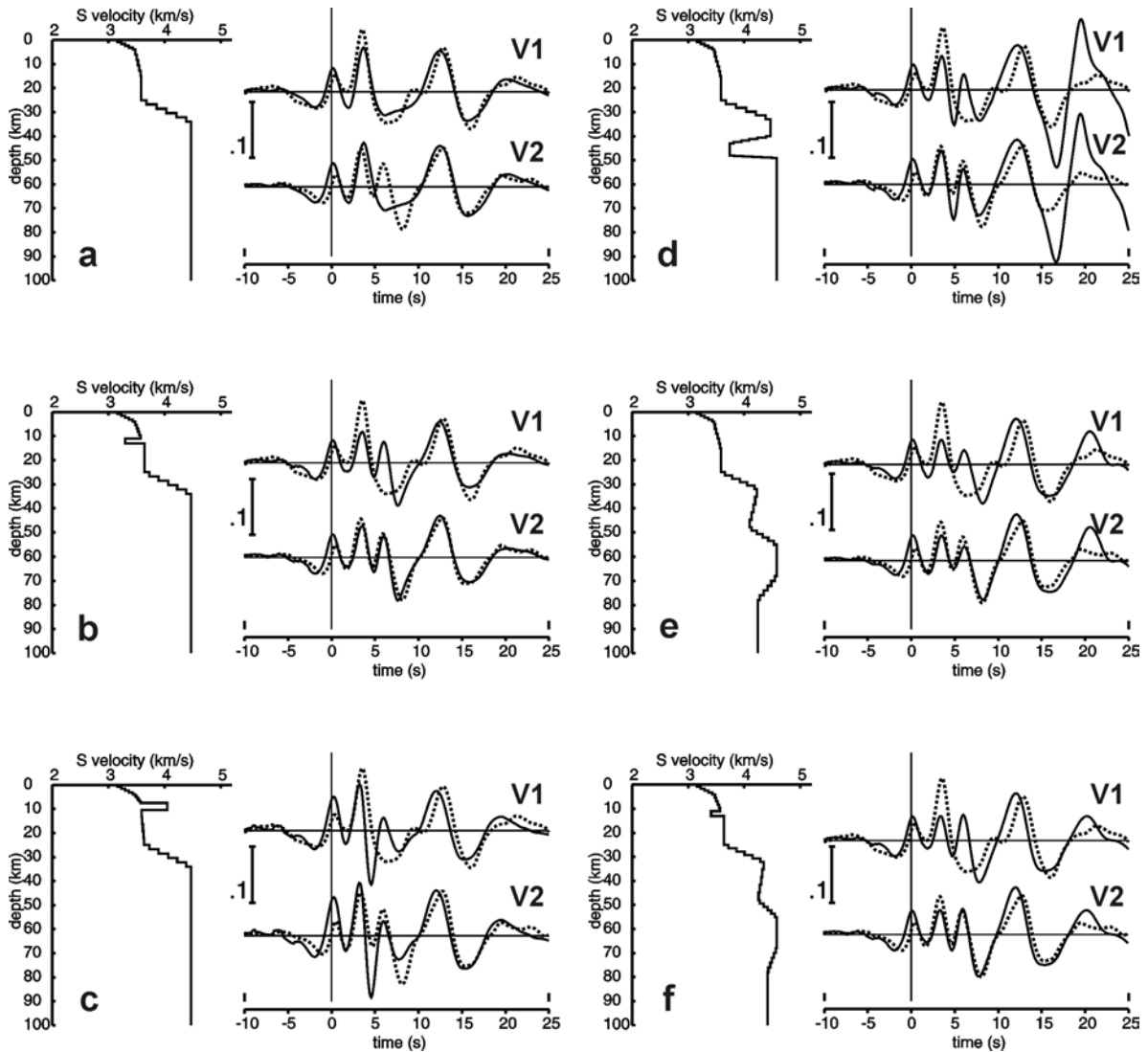
Figure B.15

Forward modelling of observed receiver function waveforms for a number of relative simple models (model response shown by solid lines). V1 – stack of all traces without the "6 s phase" in Figure 8, V2 – stack of all traces with the "6 s phase" (data shown by dashed lines). Plane wave approximation [*Kind et al.,* 1995] was used. The input P-signal is the sum of the corresponding L traces. The scale gives the portion of primary deconvolved P signal, that means Moho Ps conversions are about 10 % in amplitude of the incoming P-wave.

Model **a** shows a simple crustal structure with a gradient zone at Moho depths. This simple model cannot explain the observed phase at 6 seconds delay time. Model **b** shows the effect of a low velocity layer in the upper-middle crust between 11 and 13 km. This depth range corresponds to the base of the seismogenic zone in the area. The model is similar to that of *Strößenreuther* [1982] from the Bavarian forest. Model **c** simulates a high-velocity layer in the upper crust (7.5 to 10.5 km depth). High velocities might be indicative for equivalents of the postulated "Erbendorf body" further to the west [*DEKORP,* 1988; *Emmermann and Lauterjung,* 1997]. Model **d** represents a hypothetic thick magmatic layer in the upper mantle with about 5 to 7 % melt content and a velocity reduction of up to 9 % for v_p and 16.5 % for v_s, according to *Faul et al.* [1994]. Model **e** simulates a high velocity layer in the upper mantle. "High velocity" is relative: the layer could represent a real high velocity layer in a "normal" upper mantle or a layer of "normal" mantle in-between mantle with reduced seismic velocities. Results from surface wave studies [*Plešinger et al.,* 1994; *Passier and Snieder,* 1996] argue for the latter case. Model **f** represents a combination of models b and e with reduced amplitudes (50 %) of each velocity anomaly.

C Petrological studies on xenoliths

In addition to the seismological investigations, xenoliths from a Quaternary tephra deposit were sampled to study the presumed source region of the CO_2-dominated gas petrologically. After the description of the sample site, an introduction into the used chemical analytical methods and into the geothermobarometry follows. Then the samples are described. Finally, the obtained petrological and mineral-chemical results are presented and discussed. Pressure-temperature (p-T) conditions of equilibration or crystallization are estimated from mineral-chemistry.

C.1 Sample site

Several (ultra-) mafic xenoliths/nodules as well as crustal xenoliths were sampled from a temporary outcrop in a tephra deposit in Mýtina (50.005°N, 12.444°E), approximately 1.5 km north of the Quaternary scoria cone Železná Hůrka (49.992°N, 12.444°E; Figures C.1, C.2) [*Kämpf et al.,* 1998; *Geissler et al.,* 2004b]. First detailed works on the tephra deposit as well as the ultramafic nodules and megacrysts were done by *Reuss* [1852] and *Proft* [1894].

The temporary outcrop was documented lithostratigraphically (Figure C.3), and samples were geochemically analysed using XRF and ICP-MS. Samples of wall rock (large blocks within the lower unit UF) and nephelinitic bombs were analysed for comparison. The excavated profile (approximately 4 m thick) consists of clayey material (weathered bedrock) at the base, tuff (lower unit with three sequences: UFa, UFb, UFc) and overlying tephra (upper unit, three sequences: OFa, OFb, OFc). The tuff is well stratified showing an average layer thickness of 1 to 3 cm. The middle part of the lower unit (UFb) contains a lot of wall rock fragments with a maximum dimension of 60 x 40 x 40 cm.

The petrochemical data (see Appendix C.i) were used to estimate the juvenile (magmatic) or wall rock content of the different tephra layers.

$$(C.1) \qquad magmatic\ component\ [\%] = \frac{X_{sample} - X_{wall\ rock}}{X_{nephelinite} - X_{wall\ rock}}$$

For this estimation contents of TiO_2, MgO, CaO, P_2O_5, Sr, Cr, Nb, and V were used (Figure C.3). Similar results can be obtained using other trace elements and REEs. Obviously, the magmatic components in UF rise from about 15% to 30 % topwards, whereas it is about 60% in OF. The reciprocal content of wall rock in UF ranges from about 85% to 70%, similar to values known from the West Eifel maar deposits (about 80%, according to *Zimanowski* [1986]).
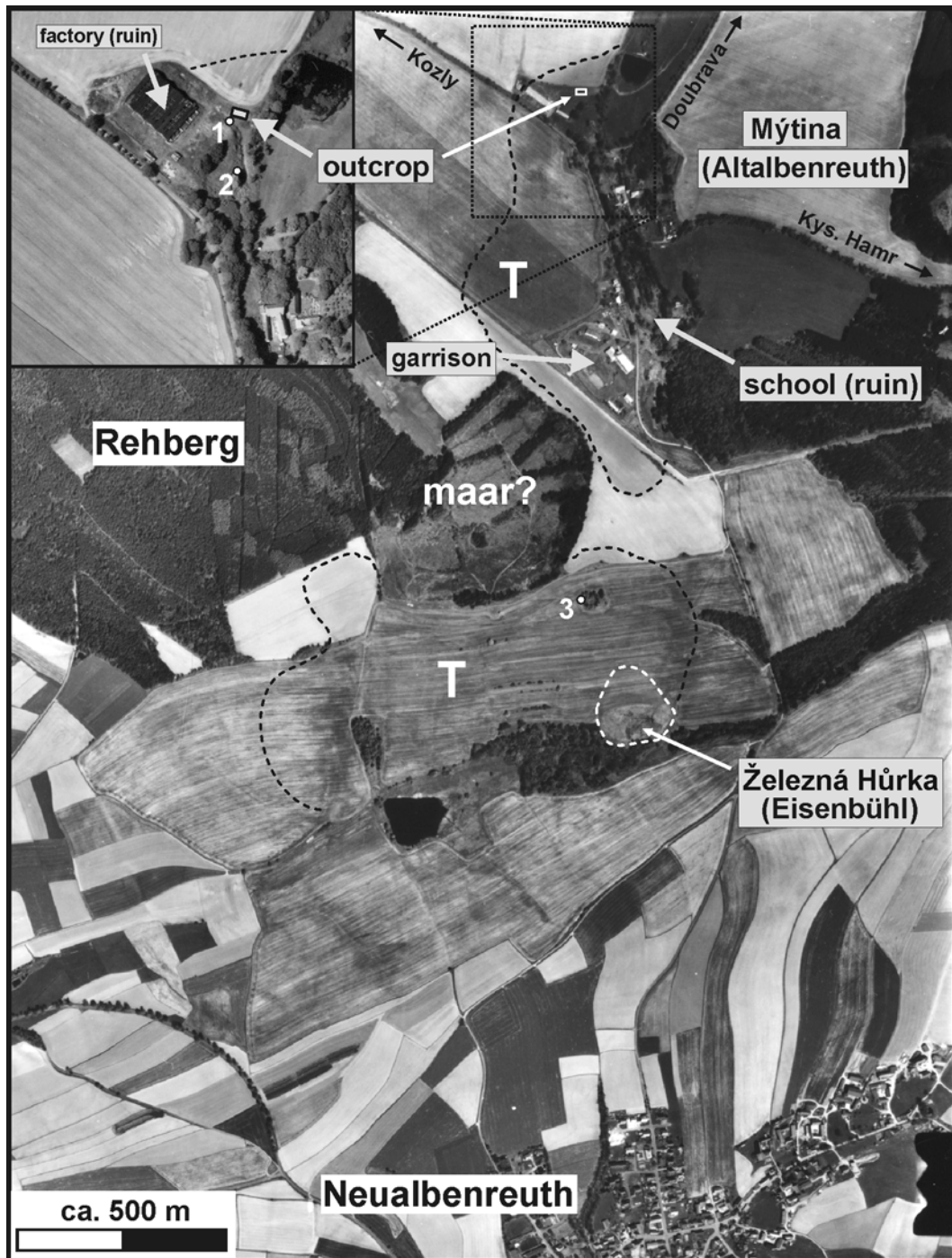
Figure C.1
Location of the temporary exploratory excavation "Mýtina", the approximate positions of previous temporary outcrops are marked (1 – sampling by *Kämpf* 1996; 2 – sampling by *Schwarzkopf* 1997), supposed tephra deposits (T) in the surrounding of the Železná Hůrka (3 – outcrops of tephra in a former quarry). The assumed boundaries of the tephra deposits are supported by the interpretation of field studies and aerial photographs (*Bayerisches Landesvermessungsamt* 1993 and 2001, nr. 93101/0 014 and 101007/0 316). From *Geissler et al.* [2004b].

The age of the tephra deposit was determined by *Wagner et al.* [2002] to about 300 ky using fission track and alpha-recoil track measurements on apatites and phlogopite [*Geissler et al.,* 2004b]. The Železná Hůrka scoria cone (lower unit) is approximately 500 ky old according to *Wagner et al.* [2002], however the uncertainties of the dating methods used are very high.
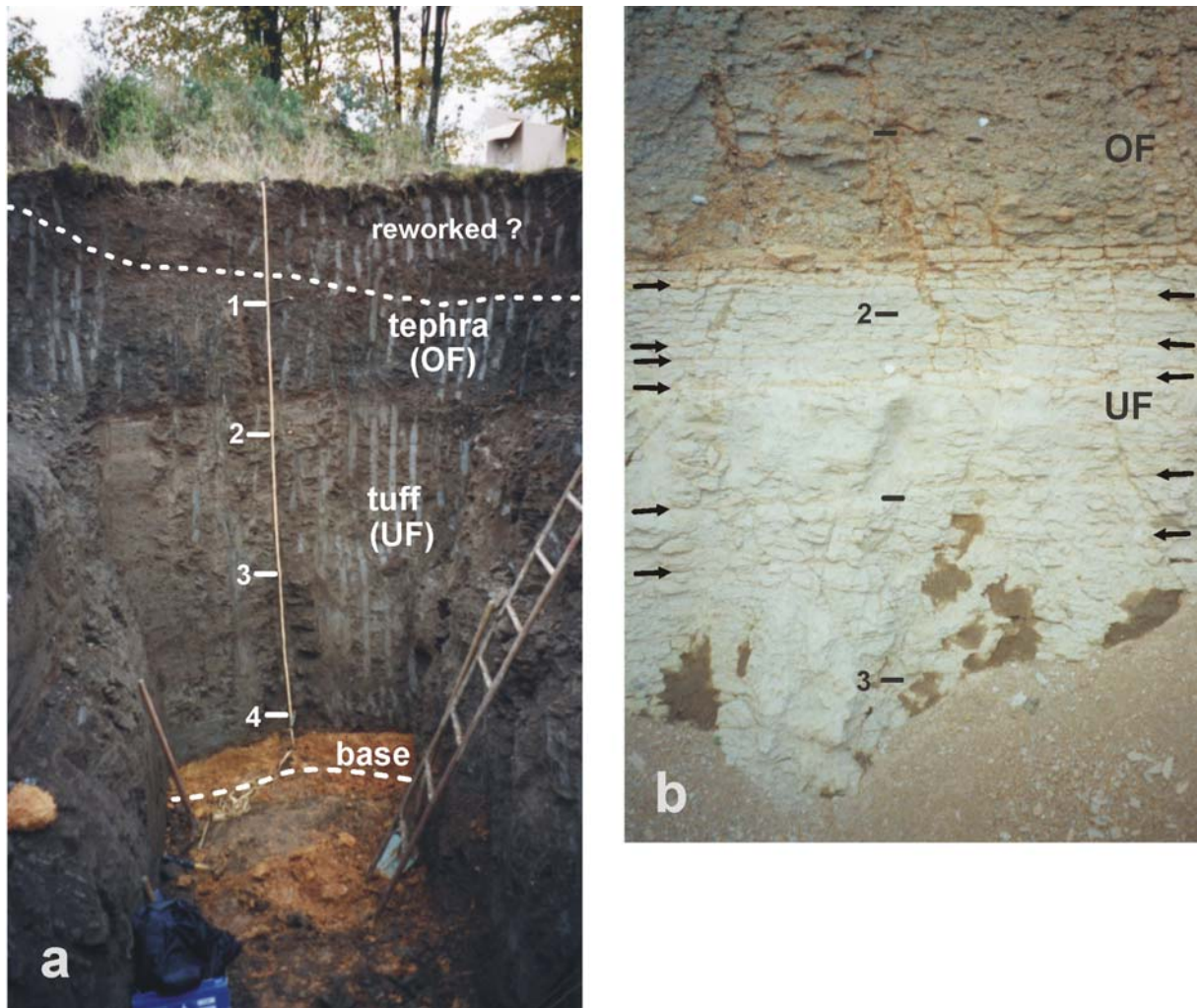
Figure C.2
The tephra-tuff deposit north of Mýtina, (temporary exploratory excavation); location in Figure C.1 (photographs by W.H. Geissler). **(a)** Total view (October 2002, fresh), **(b)** Total view (June 2003, weathered); note the high number of thin layers within the Lower Unit (arrows). From *Geissler et al.* [2004b].

C.2   Analytical methods and basics of geothermobarometry

Samples from nephelinitic host rock, ultramafic nodules/xenoliths, and crustal xenoliths were analysed for their chemical and mineralogical composition by microscopy and several chemical procedures, including X-ray fluorescence (XRF), inductively coupled plasma mass-spectrometry (ICP-MS), and mineral-chemical analyses by electron-microprobe analysis (EMPA). Whole-rock chemistry, both major and trace elements including rare earth elements (REE), were analysed in the laboratories of the GeoForschungsZentrum Potsdam. Results from mineral-chemical investigations can be used for geothermobarometric calculations, which are mainly based on empirically and experimentally calibrated formulas.
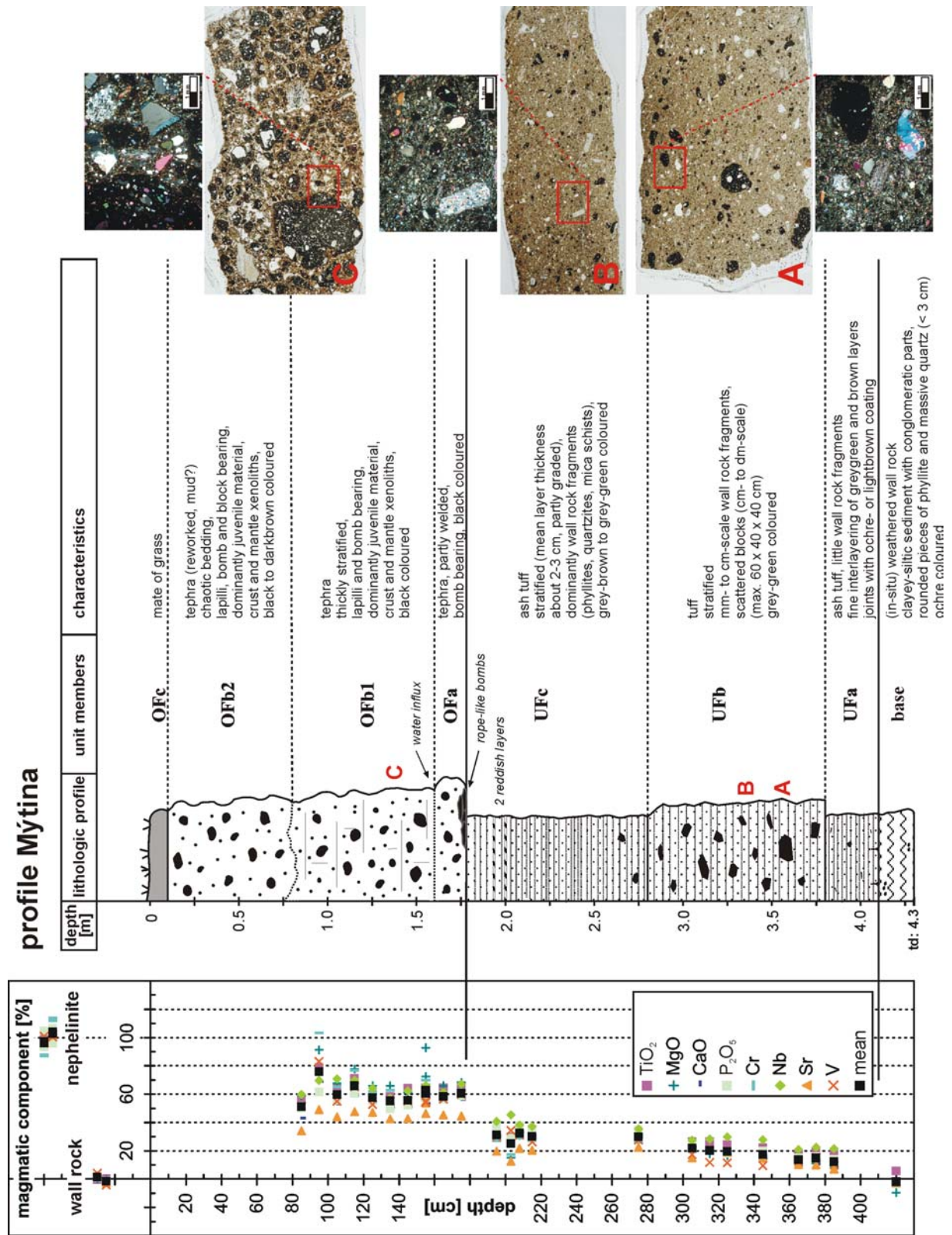
Figure C.3
Lithostratigraphy of the tephra-tuff-deposit within the excavation Mýtina (central part; from *Geissler et al.* [2004b]) together with photographs of thin-sections (right; made by E. Gantz, B. Stöcker, and W.H. Geissler). Thin-sections are about 4 cm long. Also shown is a "geochemistry" log (left) to demonstrate the content of juvenile magmatic material within the tephra-tuff layers (for data see Appendix C.i). UF - lower unit (tuff), OF - upper unit (tephra). The juvenile clasts of UF are vesicle free/poor. The country rock clasts of UF range in size from fine ash to 60 x 40 x 40 cm.

Sample preparation for whole-rock chemical analyses (ICP-MS, XRF) includes crushing to a grain size <62 μm and homogenisation. Thin-sections for microscopy and electron-microprobe analyses were made by the preparation laboratory of the GFZ Potsdam. The sections have commonly a thickness of 25 μm.

C.2.1   Geochemical (XRF, ICP-MS) and mineral-chemical (EMPA) investigations

In this chapter the basics of the analytical methods for rock and mineral chemistry will be introduced. A more detailed description of the theories, instruments, and analytical procedures can be found, e.g., in *Zussmann* [1977], *Gray* [1988], *Klein and Hurlbut* [1993], and *Dulski* [2001].

C.2.1.1   X-ray fluorescence spectrometry (XRF)

The sample, grounded to a fine powder, is compressed into a circular pellet or fused into a glass disc. This pellet/disc is shortly irradiated with primary X-rays. X-rays are absorbed by the sample according to Beer's law. The absorbed X-ray energy cause generation of a secondary X-ray emission spectrum, which is characteristic for each element in the sample. During absorption of the primary X-rays electrons in the inner shell are displaced. Vacancies will most probably be filled by electrons from the next outer shell creating a new vacancy. "Electron jumps" cause emission of energy in the form of the characteristic secondary X-radiation. The emission phenomenon is called X-ray fluorescence. Each element has characteristic spectral lines. The secondary X-ray spectrum (consisting of a low-intensity continuous background and element peaks) is resolved into spectral lines by an X-ray spectrometer, consisting of a diffracting crystal and an X-ray detector (X-ray counting device: scintillation counter or flow proportional counter).

C.2.1.2   Inductively coupled plasma mass-spectrometry (ICP-MS)

ICP-MS is a multi-element analytical method, which allows the quantification of concentrations of many trace elements, including the rare earth elements (REE) within rocks, minerals and natural waters [*Dulski*, 2001]. The method is described by *Gray* [1988] in more detail.

Inductively coupled plasma is produced, if energy is transmitted via an induction coil to a gas. The soluted sample is transformed into a gas-supported aerosol using a pneumatolytic nebulizer and is subsequently introduced into the plasma. The reproducible extraction of ions from the plasma to the

mass-spectrometer is complicated, because both have totally different temperature and pressure conditions (1 atm, 7000K and $\leq 10^{-5}$ mbar, 300K, respectively). The ions are collected by a conic collector and separated by mass using a quadrupol mass filter. The counting of ions is done in an electron multiplicator in the impulse counting mode.

C.2.1.3   Electron microprobe analysis (EMPA)

The methodology of electron microprobe analysis is similar to the XRF method. Only the primary X-radiation is replaced by a sharply focused electron beam, which allows the qualitative and quantitative analysis of a minute volume of material (10-20 μm^3 or 10^{-11}g minimum for silicate materials). The heart of the electron microprobe is an X-ray spectrometer. X-rays within the sample volume are excited by an electron beam, which is sharply focused by electromagnetic lenses down to a diameter of 2 to 10 (20) μm. A heated tungsten filament serves as the source of the free electrons (energy source). The electron beam has enough energy to displace inner-shell electrons of the constituent atoms of the sample. Outer shell electrons fill inner-shell vacancies and loose their energy, which is emitted as characteristic X-rays. The characteristic X-ray spectrum of the elements within a crystal or glass is recorded wavelength dispersive by a crystal spectrometer or energy dispersive by a semiconductor spectrometer. The duration of point measurements range between 2 and 7 min depending on the number of analysed elements and required accuracy (counting times).

Using the electron microprobe two-dimensional element scans or line scans are possible to study the zoning of elements within minerals (e.g., Al or Ti in clinopyroxene). The focused electron beam causes heating of the sample analysis area. Therefore, the beam diameter should be greater analysing samples with a higher content of H_2O, F, and alkalis (e.g., feldspars, mica and glass analyses).

C.2.2   Geothermobarometry of xenoliths

To combine petrologic and seismic data, it is necessary to estimate the depth of origin of the xenoliths. In the past, strong efforts were made to calibrate geothermobarometer, empirically and experimentally, for mineral assemblages equilibrated under pressures typical for the lower crust (garnet-bearing metamorphic rocks) and upper mantle (spinel and garnet lherzolites [see *Pearson et al.,* 2004]). Unfortunately, the Mýtina (ultra-) mafic xenolith suite provides no possibility to use these standard upper mantle geothermobarometers, which are calibrated for orthopyroxene- and garnet-bearing upper mantle rocks. Calibrations for other assemblages are rare, however, *Ernst and Liu* [1998] and *Huckenholz et al.* [1992] proposed geothermobarometers for amphibole-bearing xenoliths. *Nimis and*

Ulmer [1998] and *Nimis* [1999] published barometric formulations for clinopyroxenes. Temperature of equilibration can be estimated using the Mg^{2+} - Fe^{2+} partitioning between coexisting olivine and spinel. Geothermobarometers used in this study are outlined below.

C.2.2.1   Amphibole thermobarometry

Ti-rich amphiboles, found as phenocrysts and xenocrysts in many alkali basaltic rocks, are a near-liquidus phases, stable up to ca. 31 kbar and 1100°C [*Schulze*, 1987]. Several studies showed that the chemistry of amphiboles is sensitive to pressure, temperature, oxygen and water fugacities [e.g., *Helz*, 1982; *Spear*, 1981; *Wones and Gilbert*, 1981]. There exist a lot of empirical and experimentally calibrated thermo/barometers for mostly amphibole-bearing quartz-rich intrusions [e.g., *Otten*, 1984; *Hammarstrom and Zen*, 1986; *Hollister et al.*, 1987; *Johnson and Rutherford*, 1989; *Schmidt*, 1992]. They are calibrated for a mineral assemblage of hornblende, melt, fluid, biotite, quartz, sanidine, plagioclase, sphene, magnetite or ilmenite.

Ernst and Liu [1998] compiled a p-T scheme based on the Al_2O_3 and TiO_2 contents in amphiboles. This scheme can be used for metabasaltic assemblages containing coexisting Al-rich (e.g., plagioclase, epidote, garnet) and Ti-rich phases (e.g., ilmenite, titanite, rutile), and closely approached chemical equilibrium under crustal or uppermost mantle conditions. It should be also applicable, with caution, to inhomogeneous specimens. Al increases with both p and T, but also compositional variations (high proportions of melt) seem to influence partitioning of Al_2O_3 in Ca-amphibole. TiO_2 content correlates positively with temperature and can be used as a geothermometer above 500°C, where solubility of Ti in calcic amphiboles becomes substantial. According to *Ernst and Liu* [1998], the Al- and Ti-contents of amphibole can give an estimate for the solidification depth of an intrusion, or the equilibrium pressure of a magma chamber before eruption. This thermobarometer should be especially applicable at crustal/lithospheric pressures (up to ~1.2 GPa).

Huckenholz et al. [1992] studied the exchange reactions of Ca, Ti and Na between coexisting calcic amphiboles (potassian and titanian pargasites) and clinopyroxenes (diopside), which crystallized from a melt with magnesio-hastingsite composition. Their results provide pressure constraints for calcic amphiboles (potassian and titanian pargasites) coexisting with clinopyroxenes. *Huckenholz et al.* [1992] proposed that the Na/Ca exchange between both minerals could be used for pressure estimates in alkali basalt systems (4-45 kbar).

(C.2) $$P\,[kbar] \pm 2\,kbar = 48.04 - 23.94 \ln \frac{(Na/Ca)_{amph}}{(Na/Ca)_{cpx}}$$

Pressure estimates of natural amphibole-clinopyroxene pairs can be made, when alkali basalts close to nepheline basanite, olivine nephelinite, or pargasite composition is available with Na/Ca ratios of 0.25 to 0.60, and they bear both amphibole and clinopyroxene. The barometer is not applicable for peridotite systems and alkali basalts + H_2O-excess systems (then $K_D > 6$).

C.2.2.2   Olivine-spinel thermometry (spinel barometry)

Mg^{2+} - Fe^{2+} partitioning between coexisting spinel and olivine (formula C.3) was first suggested as potential geothermometer by *Irvine* [1965]:

$$(C.3) \qquad 1/2\, Fe_2SiO_4 + Mg(Cr_\alpha Al_\beta Fe_\gamma^{3+})_2 O_4 = 1/2\, Mg_2SiO_4 + Fe(Cr_\alpha Al_\beta Fe_\gamma^{3+})_2 O_4$$
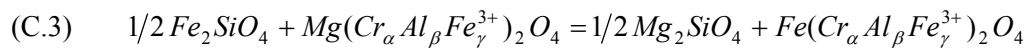
where α, β, and γ are the atomic fractions of the respective trivalent cations. This exchange is temperature-sensitive, especially for Cr-rich spinels. The first calibration was made by *Jackson* [1969] from available thermo-chemical data. *Roeder et al.* [1979] re-evaluated this formulation of the *Irvine* olivine-spinel geothermometer using a different free energy value of $FeCr_2O_4$. Their equation to estimate the temperature of equilibration is:

$$(C.4) \qquad T\,[K] = \frac{3480\alpha + 1018\beta - 1720\gamma + 2400}{2.23\alpha + 2.56\beta - 3.08\gamma - 1.47 + 1.987\ln K_D}$$

where $\alpha = \dfrac{Cr}{Cr + Al + Fe^{3+}}$, $\beta = \dfrac{Al}{Cr + Al + Fe^{3+}}$, $\gamma = \dfrac{Fe^{3+}}{Cr + Al + Fe^{3+}}$, and

$$(C.5) \qquad K_D = \frac{(X_{Mg} / X_{Fe^{2+}})_{olivine}}{(X_{Mg} / X_{Fe^{2+}})_{spinel}}$$

is the equilibrium constant for the Mg^{2+}/Fe^{2+} exchange between coexisting olivine and spinel. *Fabries* [1979] pointed out that there are problems with end-member spinels, especially spinels with low Cr/(Cr+Al) ratios as common in lherzolitic rocks. In this case the calculated temperatures could be too high. His formulation of the olivine-spinel thermometer is given below:

$$(C.6) \qquad T\,[K] = \frac{4250\, Y_{Cr}^{sp} + 1343}{\ln K_D^0 + 1.825\, Y_{Cr}^{sp} + 0.571}$$

$$\ln K_D^0 = \ln K_D - 4.0\, Y_{Fe^{3+}}^{sp} \qquad \text{[according to } Irvine, 1965]$$

$$\ln K_D^0 = \ln K_D - 2.0\, Y_{Fe^{3+}}^{sp} \qquad \text{(T = 1200°C, } Roeder\ et\ al.\ [1979])$$

According to *Fabries* [1979], the uncertainty due to analytical errors in the determination of Mg and Fe^{2+} in spinel and olivine, and Cr, Al, and Fe^{3+} in spinel is about ±50 K [see also *Jackson,* 1969]. These first versions of olivine-spinel thermometer did not take into account the influence of oxygen fugacity f_{O2} [*O'Neill,* 1981]. *Ballhaus et al.* [1991] calibrated a oxygen geobarometer and provided a corrected and simplified version of the olivine-spinel thermometer from *O'Neill and Wall* [1987]:

(C.7)

$$T[K] = \frac{(6530 + 280p + 7000 + 108p)(1 - 2X_{Fe}^{ol}) - 1960(X_{Mg}^{sp} - X_{Fe^{2+}}^{sp}) + 16150X_{Cr}^{sp} + 25150(X_{Fe^{3+}}^{sp} + X_{Ti}^{sp})}{R \ln K_D \{Mg / Fe^{2+}\}_{ol/sp} + 4.705}$$

X_{Ti}^{sp} is the number of Ti cations in spinel to 4 oxygens, $K_D \{Mg / Fe^{2+}\}_{ol/sp} = \dfrac{(X_{Mg} / X_{Fe^{2+}})_{olivine}}{(X_{Mg} / X_{Fe^{2+}})_{spinel}}$,

X_{Cr}^{sp} and $X_{Fe^{3+}}^{sp}$ are the $\dfrac{Cr^{3+}}{\Sigma R^{3+}}$ and $\dfrac{Fe^{3+}}{\Sigma R^{3+}}$ ratios in spinel, respectively. *R* is the molar constant *R* = 8.3143 J·mol⁻¹K⁻¹. *p* is in GPa.

The formulation of *O'Neill and Wall* [1987] is:

(C.8)

$$T[K] = \frac{6530 + 28p + (5000 + 10.8p)(X_{Mg}^{ol} - 2X_{Fe}^{ol}) - 1960(1 + X_{Ti}^{sp})(X_{Mg}^{sp} - X_{Fe^{2+}}^{sp}) + 18620X_{Cr}^{sp} + 25150(X_{Fe^{3+}}^{sp} + X_{Ti}^{sp})}{R \ln K_D \{Mg / Fe^{2+}\}_{ol/sp} + 4.705}$$

The pressure dependence of the olivine-spinel thermometer resulted from the work of *O'Neill* [1981]. *O'Neill* [1981] found that the Cr-content of spinels influences the depth (pressure) of the transition between spinel and garnet lherzolite and can be used as a maximum pressure (depth) indicator:

(C.9) $p = p^0 + 27.9 (X_{Cr}^{sp} + X_{Fe^{3+}}^{sp})$

whereas p^0 is approximately 17.6-19.8 kbar at 1100°C, and X_{Cr}^{sp} and $X_{Fe^{3+}}^{sp}$ are the mole fractions of chromium and ferric iron in spinel.

Medaris et al. [1999] used the olivine-spinel thermometer as a barometer. They fitted temperature data derived with the formulation of *Ballhaus et al.* [1991] to a model geotherm (underplating scenario with subsequent cooling) to get depth estimates for spinel peridotite nodules from the Kozákov volcano (Elbe Zone, CZ).

There are several limitations of the olivine-spinel geothermometry, which have to be kept in mind. The equilibrium exchange of Mg^{2+} and Fe^{2+} between spinel and olivine is one of the fastest exchange reactions. It is still effectively during cooling down to relatively low temperature (subsolidus), while other exchange reactions in peridotites (e.g., pyroxene exchange reactions) are blocked at higher temperatures (*Fabries,* 1979). The decision if olivine and spinel are coexistent equilibrium phases and the estimation of Fe^{3+} contents from electron microprobe data via stoichiometric derivation are further problems.

C.2.2.3   Pyroxene thermometry

Furthermore, the chemical composition of coexisting clinopyroxene and orthopyroxene can be used as a geothermometer. On the basis of experiments and ability tests *Brey and Koehler* [1990] formulated new versions of the two-pyroxene thermometer:

(C.10) $$T_{BKN}\,[K] = \frac{23664 + (24.9 + 126.3\,X_{Fe}^{cpx})\,p}{13.38 + (\ln K_D^*)^2 + 11.59\,X_{Fe}^{opx}}$$

with $K_D^* = \dfrac{(1 - Ca^*)^{cpx}}{(1 - Ca^*)^{opx}}$, $Ca^* = \dfrac{Ca^{M2}}{1 - Na^{M2}}$ and $X_{Fe}^{opx,\,cpx} = \dfrac{Fe}{Fe + Mg}$.

The Ca content of orthopyroxene alone can be used as a geothermometer:

(C.11) $$T_{Ca-in-opx}\,[K] = \frac{6425 + 26.4\,p}{-\ln Ca^{opx} + 1.843}$$

The partitioning of Na between orthopyroxene and clinopyroxene is also temperature sensitive (thermometer calibrated from natural rock data):

(C.12) $$T_{Na}^{cpx/opx}\,[K] = \frac{35000 + 61.5\,p}{(\ln D_{Na})^2 + 19.8}$$

p is in kbar, $D_{Na} = \dfrac{Na^{opx}}{Na^{cpx}}$.

An older version of the pyroxene thermometer was suggested by *Wells* [1977], however *Lindsley* [1983] pointed out, that it should not be used any longer. *Brey and Koehler* [1990] pointed out that *Well*'s formulation reproduces the experimental results at 900°C, but increasingly underestimates them at higher temperatures.

C.2.2.4   Phlogopite-liquid (glass) thermobarometry

Righter and Carmichael [1996] published results from experiments on olivine and augite minette powders at 1 bar to 2 kbar (water-saturated) and 900 to 1300°C. The oxygen fugacity was controlled between the nickel-nickel oxide (NNO) and hematite-magnetite (HM) oxygen buffers. *Righter and Carmichael* [1996] showed that the partitioning of TiO_2 between biotite and liquid is temperature dependent (uncertainty of ±50 K), whereas the BaO partitioning is pressure and temperature dependent (uncertainty of ±4 kbar).

$$(C.13) \quad \ln D_{TiO_2}^{phl/liq} = \frac{a}{T} + b$$

with the TiO_2 partition coefficient $D_{TiO_2}^{phl/liq} = \frac{TiO_2^{phl}[wt\%]}{TiO_2^{glass}[wt\%]}$

and *a*, *b* as regression coefficients ($a = 17600$, $b = -12.1$). *T* is in Kelvin.

$$(C.14) \quad p = \frac{T}{c}(\ln D_{BaO} - a - \frac{b}{T} - d \ln a_{H_2O})$$

with the BaO partitioning coefficient $D_{BaO}^{phl/liq} = \frac{BaO^{phl}[wt\%]}{BaO^{glass}[wt\%]}$,

and the regression coefficients $a = -2.167$, $b = 4553$, $c = -130.7$, and $d = -0.388$. *T* is in Kelvin; *p* is in kbar. Where phlogopite is close to liquidus a_{H2O} can be set to 1 (phlogopite/biotite as phenocrysts together with either olivine or augite). Reducing a_{H2O} to 0.8 the calculated pressure increases by 10% [*Righter and Carmichael,* 1996].

C.2.2.5   Olivine-clinopyroxene barometry

Köhler and Brey [1990] established a geobarometer, which is based on the calcium exchange between olivine $(\frac{Mg}{Mg + Fe})^{ol} \approx 0.9$ coexisting with clinopyroxene in natural lherzolitic compositions:

$$(C.15) \quad p[kbar] = \frac{-T \ln D_{Ca} - 11982 + 3.61\,T}{56.2}, \qquad T \geq (1275.25 + 2.827\,p)\ [K]$$

$$(C.16) \quad p[kbar] = \frac{-T \ln D_{Ca} - 5792 - 1.25\,T}{42.5}, \qquad T \leq (1275.25 + 2.827\,p)\ [K]$$

where $D_{Ca} = \dfrac{Ca^{ol}}{Ca^{cpx}}$, and Ca^{ol}, Ca^{cpx} are the atomic proportions of Ca in the structural formulae of olivine and clinopyroxene based on 4 and 6 oxygens, respectively. According to *Köhler and Brey* [1990] the uncertainties are in the range of ±1.7 kbar (1σ).

O'Reilly et al. [1997] described the limitations of the above geobarometer. The Ca and Ti contents in olivines in spinel peridotites are well correlated with one another and with temperature, whereas the Ca content is poorly correlated with pressure. A strong temperature dependence of the Ca-in-olivine barometer exists. A temperature uncertainty of ±50 K results in a pressure uncertainty of ±8 kbar. Therefore, pressure estimates span the entire width of the spinel-lherzolite field at 900-1200°C.

C.2.2.6   Clinopyroxene barometry

Nimis and Ulmer [1998] performed crystal structure modelling of Ca-rich clinopyroxene coexisting with basic and ultrabasic melts and calibrated a geobarometer that is based on the structural parameters unit-cell volume (V_{cell}) and M1-site volume (V_{M1}). It should be applicable to anhydrous and hydrous melt compositions (quartz-normative basalts to nephelinite, excluding melts coexisting with garnet or melilite), pressure conditions pertinent to the crust and upper mantle (0 to 24 kbar), as well as a variety of f_{O2} conditions. At a given melt composition, V_{cell} and V_{M1} decrease linearly as pressure increases. The expanded version of the geobarometer (valid for an/hydrous compositions) is very temperature sensitive (underestimating *T* by 20 K cause 1 kbar increase of calculated *p*).

The best way is using of X-ray diffraction data as input for the calculations, however another approach is the calculation from mineral chemical analyses (atomic fractions from microprobe data, via chemistry-structure coefficients; for details see *Nimis* [1995] and *Nimis and Ulmer* [1998]). For pressure calculations the Excel-Worksheet provided by *Nimis* [1999] was used.

According to *Nimis and Ulmer* [1998], most useful results can be obtained for cumulitic products (pyroxenitic xenoliths, megacrysts), but the geobarometer should also be applicable to mantle equilibrium partial-melting residua. Clinopyroxenes that re-equilibrated after magmatic crystallization or melting during subsolidus processes are unsuitable for geobarometric purposes, unless their primary composition can be recovered. *Nimis* [1999] discussed the uncertainties of the clinopyroxene barometry. The errors for the expanded version of the barometer are about 3.1 kbar; low-pressure data (≤15 kbar) are better reproduced (standard deviation σ = 2.6 kbar) than high-pressure data (>18 kbar; σ = 6.1 kbar). The standard deviation is about 1.75 kbar for anhydrous basic or ultrabasic systems. In comparison to the uncertainties of the barometric formulation, the uncertainties in chemical analyses (e.g., by electron microprobe) cause negligible errors.

C.3   Sample description

C.3.1   Mantle xenoliths (ultramafic nodules)

Mantle xenoliths can generally be divided into two groups according to *Lloyd and Bailey* [1975], *Frey and Prinz* [1978], and *Lloyd* [1981, 1987]:

Group I: spinel lherzolites, spinel harzburgites, wehrlites, dunites (composed of olivine, ortho- and clinopyroxene and minor amounts of amphibole and dark mica).

Group II: pyroxenites (mainly clinopyroxene, minor amounts of orthopyroxene and olivine) containing significant amounts of hydrous minerals (titaniferous phlogopite, amphibole) and titanite, (perovskite), titanomagnetite (ilmenite?), apatite, rarely calcite and feldspar.

The (ultra-) mafic xenolith-suite (nodules; further mostly referred as mantle xenoliths) sampled from the Mýtina tephra deposit includes wehrlites, clinopyroxenites, hornblendites (Table C.I; for nomenclature see Figure C.4), chromite-bearing olivine-clinopyroxene aggregates, and megacrysts of olivine, clinopyroxene, amphibole and phlogopite (Plate 1). The xenoliths and megacrysts are commonly coated by the host rock and form cored bombs.

The volcanic host rock (dark grey, vesicular scoria and bombs) can be classified as olivine mela-nephelinite [*Le Bas,* 1987; *Le Bas et al.,* 1992; *Le Maitre,* 1989]. The only partly re-crystallized glassy groundmass contains olivine and strongly zoned titanian diopside phenocrysts, euhedral in form and commonly up to 1 mm maximal size. No feldspathic minerals (plagioclase, alkali-feldspar, nepheline) can be observed by optical microscopy. Additionally to the phenocrysts olivine and clinopyroxene xenocrysts with fragmented or irregular edges in contact to the host rock also occur.

Most of the xenoliths show cumulus textures (Plates 2, 3). No (shear) deformation textures could be observed in the Mýtina samples, but some samples exhibit high porosity (only partly filled with glass).

Wehrlites (MXZH1, -2, -3, -4, -67; Plates 1, 2)
Several wehrlitic samples were identified. The main components are green clinopyroxene and olivine; minor constituents are brown mica (phlogopite) and glass. All samples show a cumulus texture and contain some percent open pore space (in some thin-sections filled with coloured glue) [see *Kämpf et al.*, 1999b]. Euhedral to anhedral crystals occur together in one sample. Grain size is variable in different samples (from less then 1 mm up to more than 1 cm). Boundaries of some nodules imply that the samples have a xenolithic origin rather than being cumulates from the host magma. Spongy zones (sieve texture) can be observed in some clinopyroxenes, especially near the rim.
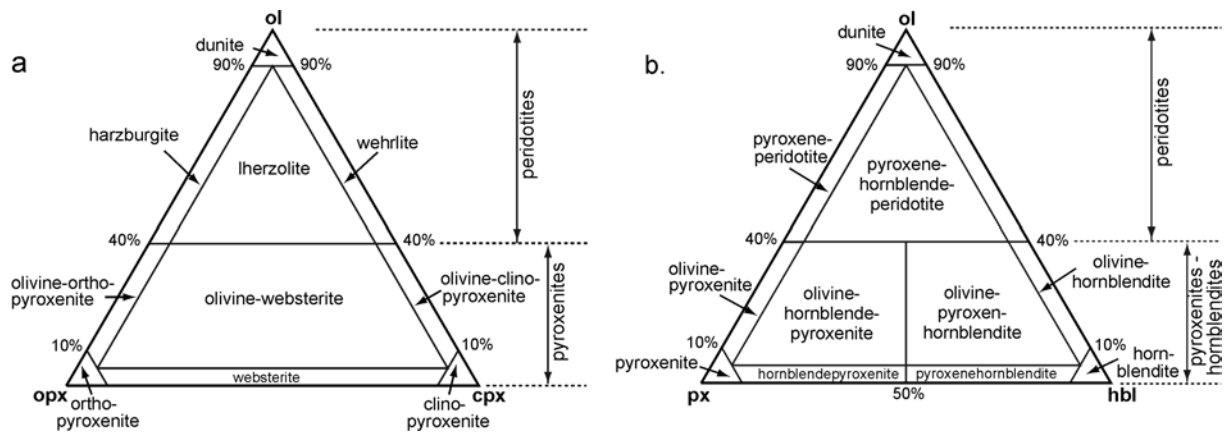
Figure C.4
IUGS classification of ultramafic plutonic rocks [after *Le Maitre,* 1989].
No modal composition was determined, however most of the analysed xenoliths are olivine-clinopyroxene-bearing samples and would plot in the wehrlite and olivine-clinopyroxenite fields (no orthopyroxene) **(a)**. Amphibole and clinopyroxene rich samples (no or minor amounts of olivine) plot in the hornblende- (hbl-) pyroxenite and pyroxene- (cpx-) hornblendite fields **(b)**. Sample MXZH66 can be classified as (pyroxene-) hornblende- (hbl-) peridotite; sample MXZH68 is a hornblendite (almost 100% amphibole). The olivine-orthopyroxene-clinopyroxene-bearing samples from Gottleuba (Go01-1) and Zinst (Zinst-1) would plot in the harzburgite and lherzolite fields, respectively.

Hornblende-peridotite (MXZH66; Plates 1, 3)

Sample MXZH66 contains olivine, clinopyroxene, amphibole and spinel as main phases and shows an equigranular, cumulus texture. This sample is classified as hornblende-peridotite to distinguish it from the typical wehrlites containing olivine, clinopyroxene and phlogopite (± glass). Amphibole and spinel are partly euhedral, whereas olivine and clinopyroxene are anhedral. The average grain size is up to 5 mm. Only one sample was found up to now.

Olivine-clinopyroxene-spinel cumulates (MXZH8, -18, -61, -64; Plate 2)

Additionally to the wehrlitic samples, olivine-clinopyroxene-spinel aggregates were investigated. Commonly there are smaller than the wehrlitic samples and show no regular boundaries, indicating crystallization from the melt (at least for some of the constituents). They also contain dark-brown Cr-rich spinel. Clinopyroxenes have a less spongy appearance than that in the wehrlites. They show titanian diopsidic rims towards the melt (nephelinite).

Clinopyroxenites (MXZH5, -11, -33; Plate 3)

There are several samples containing clinopyroxene as the main constituent. Further minerals are amphibole (up to 50%), ilmenite (± titano-magnetite), apatite (MXZH5), and titanite (MXZH11). They are equigranular and show cumulus textures; the average grain size is several mm, but may reach up to 1 cm. There seem to exist two generations of amphibole in sample MXZH33.

Hornblendites (MXZH12, -13, -68; Plate 3)

Hornblendites are mainly composed of pitch-black amphibole (brown in thin-sections; euhedral to anhedral crystals). Minor phases are clinopyroxene, ilmenite (± titano-magnetite), phlogopite, and sulphide inclusions. Normal grain size is some mm. In samples MXZH12 and MXZH13 up to cm-size amphibole crystals overgrow small clinopyroxene crystals. Glass, phlogopite, skeletal olivine, titano-magnetite, and clinopyroxene phenocrysts occur in vugs in both samples.

Spinel lherzolites/harzburgites (Zinst-1, Go01-1; Plate 2)

Spinel lherzolites are the typical upper mantle xenoliths in the mafic Cainozoic volcanics of Central Europe [e.g., *Menzies and Bodinier,* 1993]. Up to now, such rock fragments could not be found within the Quaternary volcanics in the area under study. For comparison, two spinel peridotite xenoliths from the Mariengründel, about 1km south-southeast of Bad Gottleuba, Saxony (50.842°N, 13.952°E; Elbe Zone; late Miocene?), and from the Wunschenberg quarry near Zinst, NE-Bavaria (49.90°N, 11.94°E; Franconian Lineament; K-Ar whole rock age 28.8±1.8 Ma, according to *Todt and Lippolt* [1975]), are investigated. The average grain size in both samples is up to 5 mm. Most crystals have anhedral grain boundaries. Sample Zinst-1 contains several volume percent clinopyroxene, whereas Go01-1 has only a small amount of clinopyroxene.

Table C.I. Mineral parageneses of studied samples. (Mineral abbreviation according to *Kretz,* 1983; am - amphibole, fsp - feldspar, gl - glass, sp - spinel, sulph - sulphide).

sample	paragenese														rock type
	ol fo%	cpx	opx	fsp	am	phl	sp	ilm	mag	ap	ttn	rt	gl	sulph	
Železná Hůrka															
EB1	82..85			x											ol-megacryst
EB5-ol9	89..85						x								ol-phenocryst
Mýtina															
XKZH1		x	x	x	x	x			(x)			x			norite
XKZH2			x						x						?
XKZH3		x		x						x					? (+zrn)
MXZH66	82	x			x		x		(x)						hbl-peridotite
MXZH5		x			x			x		x					hbl-clinopyroxenite
MXZH11		x			x				x		x				hbl-clinopyroxenite
MXZH33		x			x	(x)		x	x						hbl-clinopyroxenite
MXZH12	(x)	x			x	x		x	x						cpx-hornblendite
MXZH13		x			x	?		x	x						cpx-hornblendite
MXZH68					x				(x)					x	hornblendite
MXZH1,3	88	x			x										wehrlite
MXZH2	88	x													wehrlite
MXZH4	88	x													wehrlite
MXZH8	88	x											x		ol-cpx-cumulate
MXZH18	88	x				?	x						x		ol-cpx-cumulate
MXZH64	86..88	x					x								ol-cpx-cumulate
MXZH61	83..87	x					x						x		ol-cpx-cumulate
MXZH17 (gm)	88						x								ol-phenocryst
MXZH24	82..87	(x)			x								x		ol-megacryst
MXZH69	86	x			x	x							x		ol-megacryst
sp-lherzolites															
Zinst-1	90	x	x				x								sp-lherzolite
Go01-1	90	x	x	?			x								sp-lherzolite (harzburgite)

C.3.2   Megacrysts

The Železná Hůrka and the tephra deposit in Mýtina have been known at least since the 19th century for the occurrence of megacrysts (large single crystals), several cm in size [*Reuss*, 1852; *Proft*, 1894]. A number of samples from both localities, including olivine, clinopyroxene, amphibole and phlogopite crystals, were investigated (Plates 1, 3).

Olivine (MXZH7, -19, -24, -69; EB1)

Some olivine megacrysts occur as euhedral crystals, partly showing skeletal growth. Other samples have irregular grain boundaries. Rounded samples are a third group, indicating disequilibrium with the host melt (e.g., MXZH19). Composite megacryst samples consist of three ore more large olivine crystals (e.g., MXZH69). Most of the olivine megacrysts are porous. Pore boundaries are crystal faces only in a few samples. The vugs are partly filled with glass and groundmass crystals (mostly clinopyroxene); bigger exemplars are empty showing only a thin coating of the pore walls by glass and micro-phenocrysts. One olivine megacryst from Železná Hůrka (EB-1) contains an amphibole inclusion [see *Kämpf et al.,* 1993].

Clinopyroxene (MXZH9, -14, -17, -62; EB2, -6, -7)

Two types of clinopyroxene megacrysts occur, black and green in colour, the latter ones mostly in olivine-clinopyroxene-spinel aggregates. Almost all samples are zoned/rimmed. One sample from the Železná Hůrka shows sector zoning (EB2). Some samples have a spongy appearance, which stems from small melt pockets. Also composite samples (spongy + not spongy crystals) occur (MXZH62). Clinopyroxene megacrysts show all kinds of grain boundaries (subhedral to anhedral, broken, rounded).

Amphibole (MXZH10, -15, -32, -35, -39, -42, -1a, -9)

Amphibole megacrysts look pitch-black in hand specimen and dark-brown in thin-sections. Almost all samples are rounded, indicating disequilibrium with the host melt, at least under conditions during the ascent within the magma column. Only a few samples show well developed crystal faces in hand specimen. But most samples show perfect cleavage under the microscope. Some of the amphibole megacrysts are also porous, containing vugs, partly filled with glass.

Phlogopite (MXZH21, -22, -74)

Thin black mica flakes are very common in the tephra and as inclusions in volcanic bombs. Their length is up to 7 cm. Flake boundaries are rounded. One sample with dimensions of 35x35x35 mm was found (MXZH74).
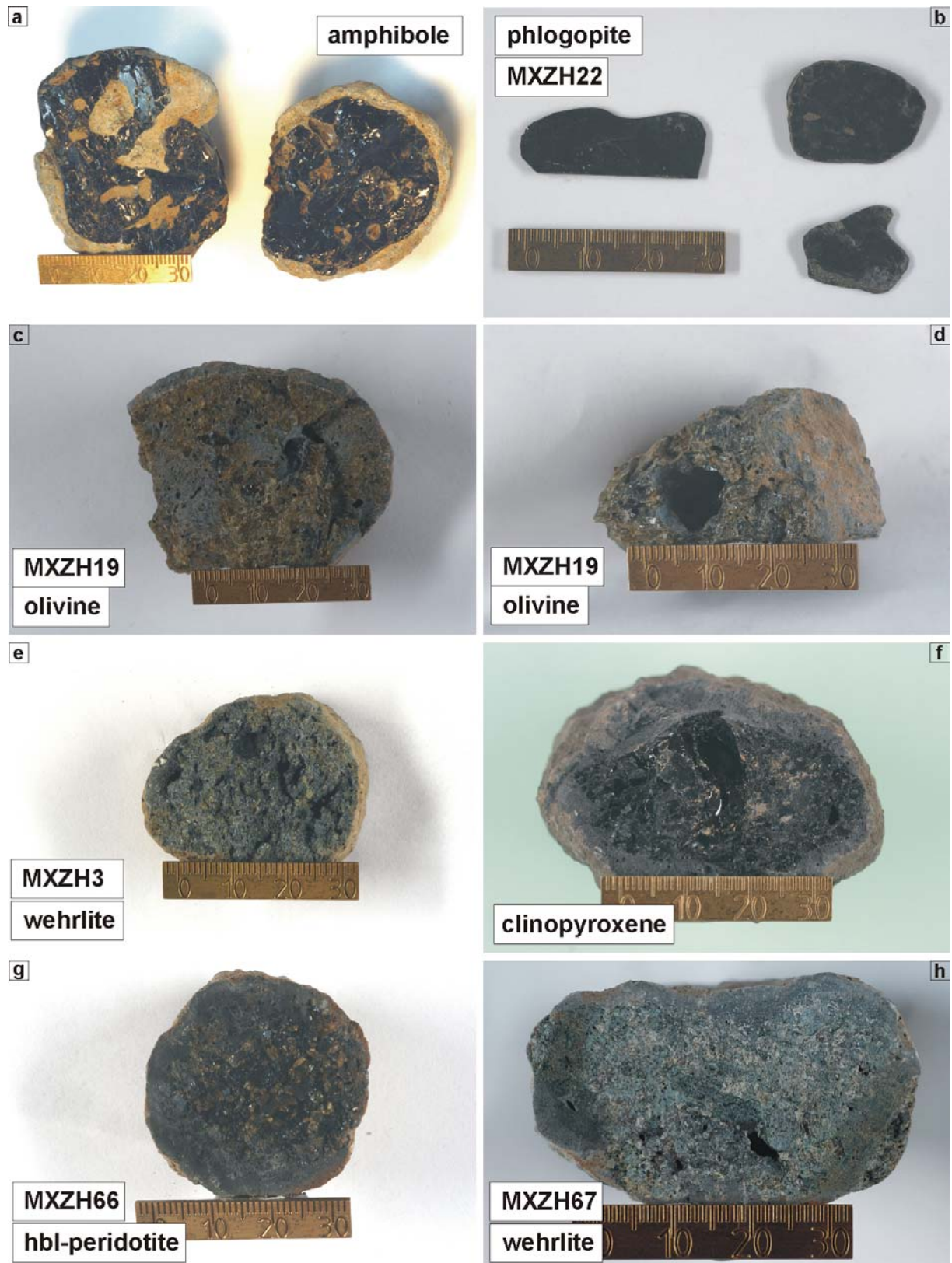
Plate 1
Photographs of typical hand specimen of (ultra-) mafic nodules from the Mýtina tephra. **(a)** Amphibole megacrysts are commonly rounded and have vugs filled with nephelinitic glass; **(b)** phlogopite megacrysts can normally be found as flakes; **(c)** and **(d)** olivine megacryst MXZH19 showing atypically large vugs, which are only partly filled with nephelinitic glass; **(e)** porous wehrlitic xenolith MXZH3, consisting mainly of olivine and clinopyroxene and minor phlogopite; **(f)** black coloured clinopyroxene megacryst showing typical conchoidal fracture; **(g)** amphibole-bearing peridotite (olivine, clinopyroxene, amphibole, spinel); **(h)** porous wehrlitic xenoliths MXZH67 consisting only of olivine and clinopyroxene. (Photographs by E. Gantz, GFZ Potsdam)
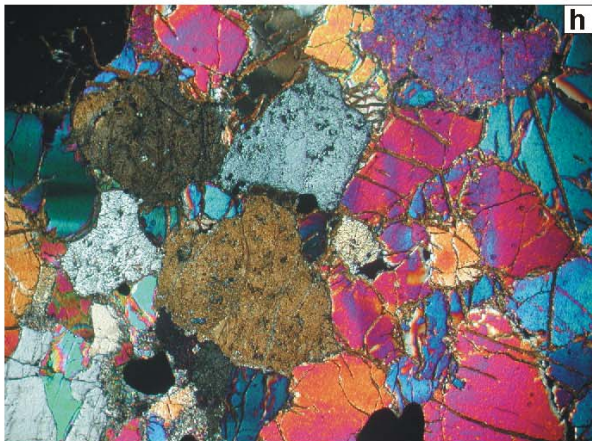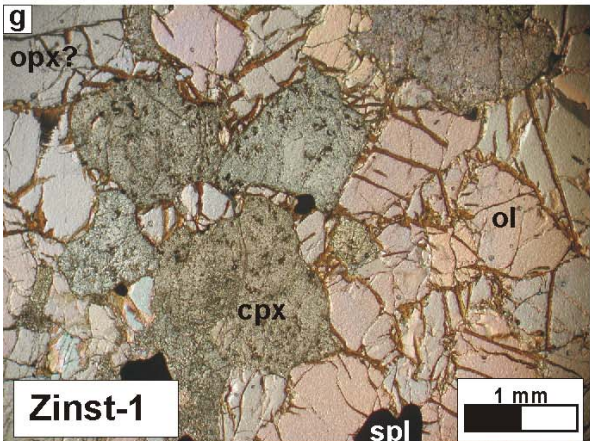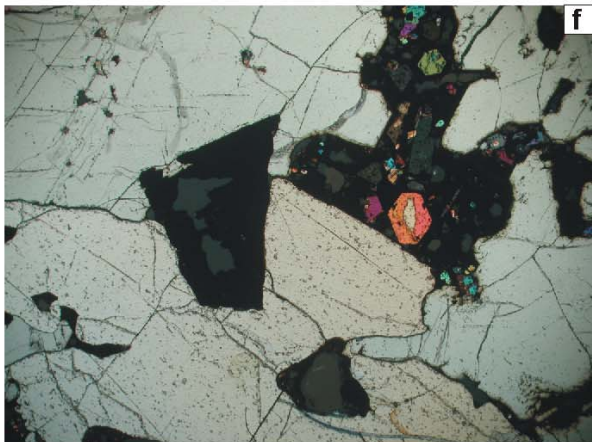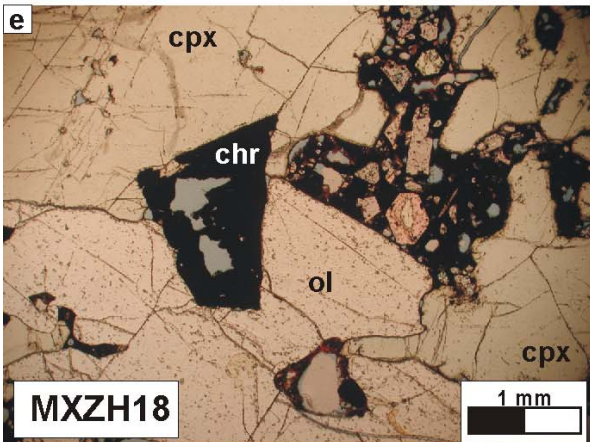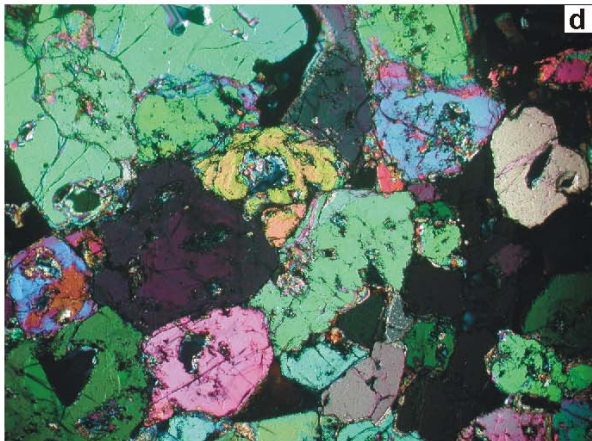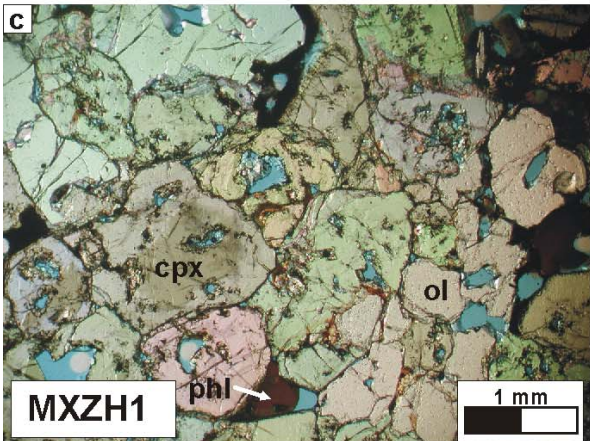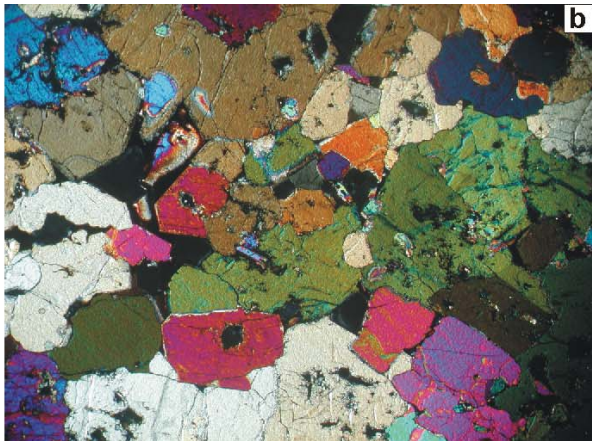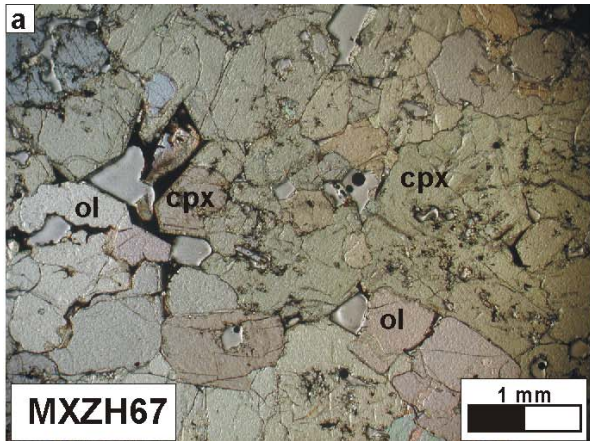
Plate 2
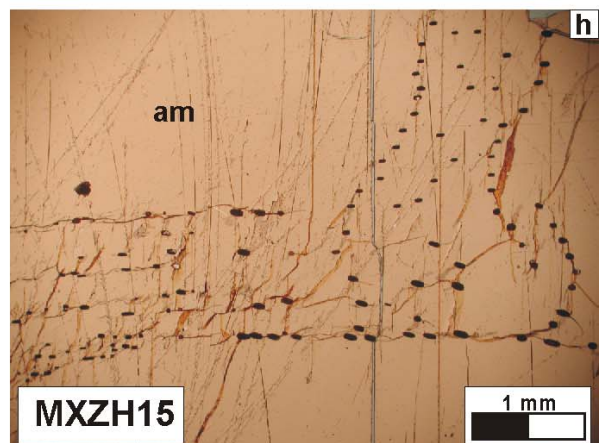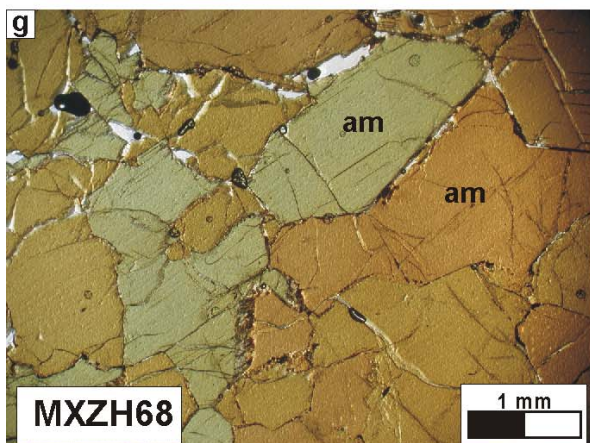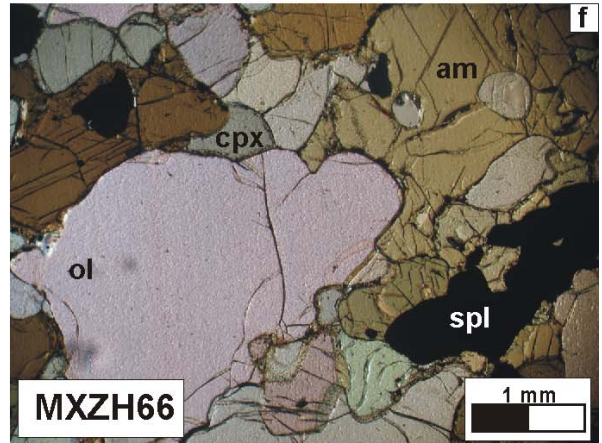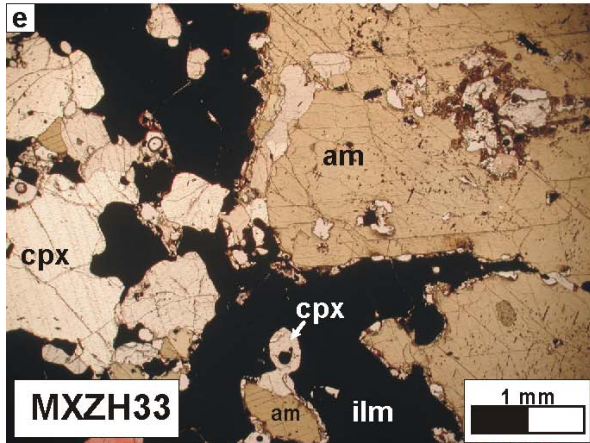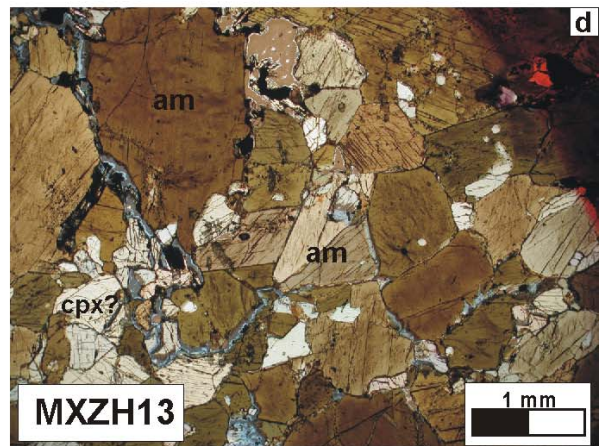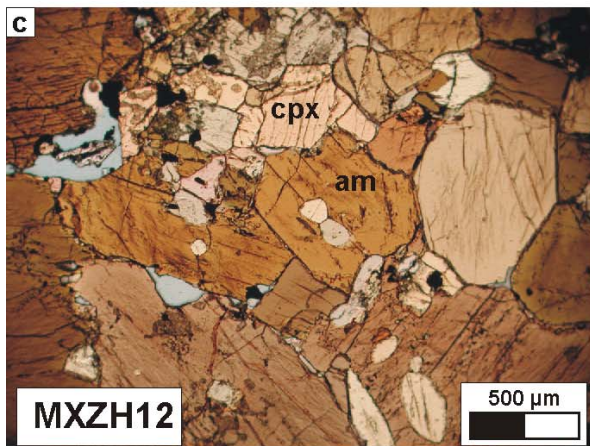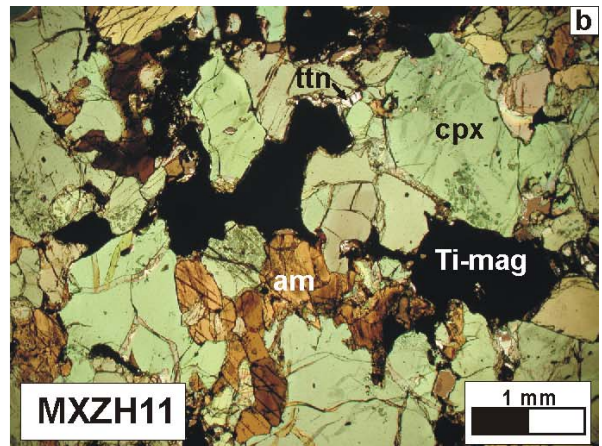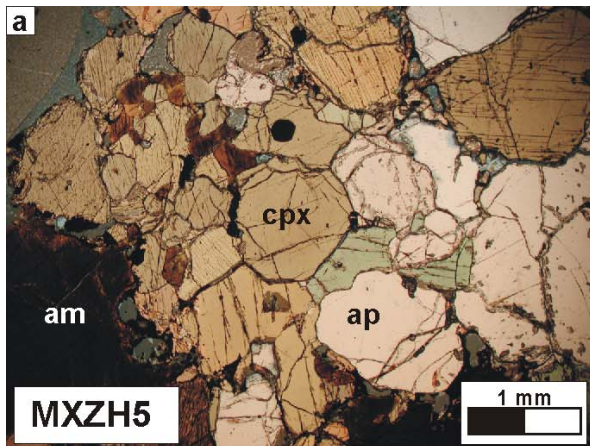
Plate 3

Plate 2
Photographs of thin-sections (left: single, and right: crossed nicols) of typical wehrlitic xenoliths or olivine-clinopyroxene cumulates from the Mýtina tephra **(a)** to **(f);** and a spinel lherzolite xenolith from the Wunschenberg (Zinst, NE-Bavaria).
Samples MXZH67 **(a+b)** and MXZH1 **(c+d)** consist of olivine and clinopyroxene up to several millimetre in grain size. Both samples are porous. MXZH1 further contains phlogopite; and some clinopyroxene grains show zoning (mainly in Ti and Cr, from microprobe measurements). This is probably an indication for an overprinting of sample MXZH1 by heating or metasomatic reactions. MXZH18 **(e+f)** consists of olivine, clinopyroxene (both up to cm-size) and dark-brown chromium-rich spinel. The space in-between the mineral grains is partly filled with nephelinitic groundmass containing phenocrysts; some "pores" contain scoriaceous glass. Spinel lherzolite sample Zinst-1 **(g+h)** consists of olivine, clinopyroxene, orthopyroxene, and dark-brown spinel.

Plate 3
Photographs of thin-sections of amphibole-bearing xenoliths and an amphibole megacryst.
(a) MXZH5: apatite- and amphibole-bearing clinopyroxenite; **(b)** MXZH11: amphibole- and Ti-magnetite-bearing clinopyroxenite, containing also minor titanite (sphene); **(c)** and **(d)** MXZH12, MXZH13: hornblendite samples, consisting mainly of amphibole, which partly overgrows small clinopyroxene grains (poikilitic), as well as of phlogopite and magnetite; **(e)** MXZH33: ilmenite-bearing hornblende-clinopyroxenite; **(f)** MXZH66: amphibole-bearing peridotite consisting of olivine, clinopyroxene and dark-brown spinel; **(g)** MXZH68: hornblendite, consisting only of amphibole and minor magnetite and sulphide inclusion; **(h)** MXZH15: amphibole megacrysts showing inclusion (magnetite and sulphide) trails.

C.3.3   Crustal xenoliths

Crustal xenoliths in the lower unit of the tephra deposit range in size from ash particles up to several decimetre big samples [see *Geissler et al.,* 2004b]. Within the upper unit, their size is up to 10 cm; most samples are coated with the host rock, forming cored bombs. Many samples show primary sedimentary layering (bedding), overprinted by foliation. Main components are quartz and mica (muscovite and biotite); minor constituents are feldspar, garnet, and zircon and others (see Appendix C.ii). Commonly the samples show small grain sizes of the minerals. Samples can be classified by their textures and mineral composition into the following groups: quartzitic (quartz-rich) rocks, phyllitic rocks and mica schists, and feldspar-rich rocks (Plates 4, 5). A transition exists from phyllitic quartzites to quartzitic phyllites/mica schists.

Quartzitic xenoliths show generally an alternated stratification of quartz-rich and mica-rich (mostly muscovite) layers. These rocks have light-grey colours; some samples are whitish. Minor components beside quartz and muscovite are feldspar, biotite, and rounded zircon (sometimes enriched in specific layers/samples; e.g., XKZH58, XKZH61). The phyllitic and mica schist xenoliths are more mica-rich (muscovite, biotite) than the quartzitic samples. They mostly have dark-grey (greenish) colours. Minor components are feldspar, garnet, staurolite, and (?) cordierite.
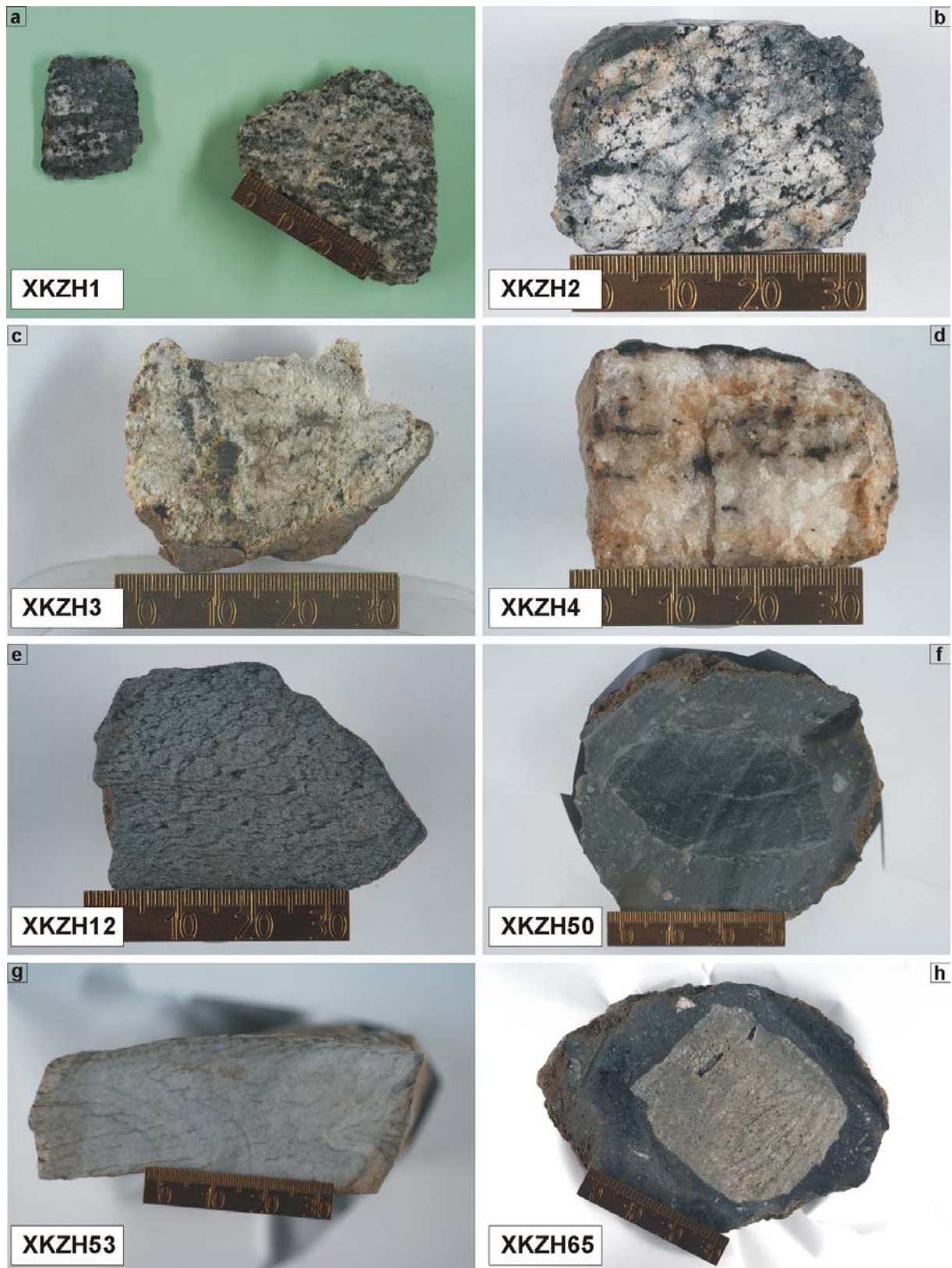
Plate 4
Photographs of typical hand specimen of crustal xenoliths from the Mýtina tephra. **(a)** XKZH1: noritic sample (mainly plagioclase + orthopyroxene ± clinopyroxene) showing weak layering of the main components; **(b)** and **(c)** XKZH2, XKZH3: feldspar rich samples; **(d)** XKZH4: quartz-rich xenolith, probably a fragment of a quartz vein; **(e)** XKZH12: quartzitic mica-schist; **(f)** XKZH50: mica-schist; **(g)** XKZH53: quartzite; **(h)** XKZH65: quartz-feldspar-bearing xenolith, which may belong to meta-tuff layers (within the "Neualbenreuth layers"). (Photographs by E. Gantz, GFZ Potsdam).
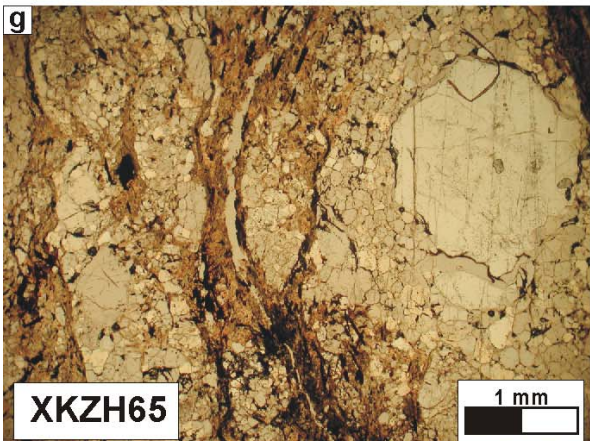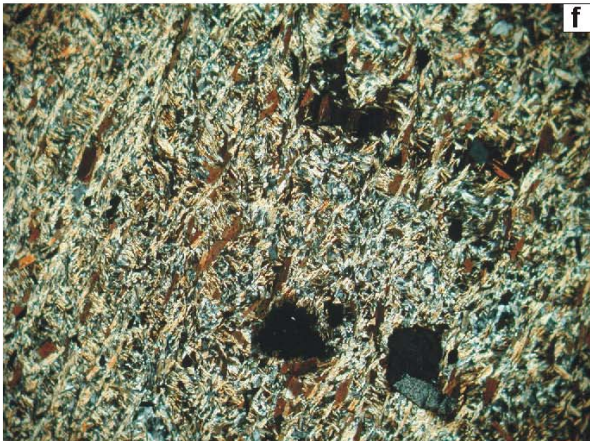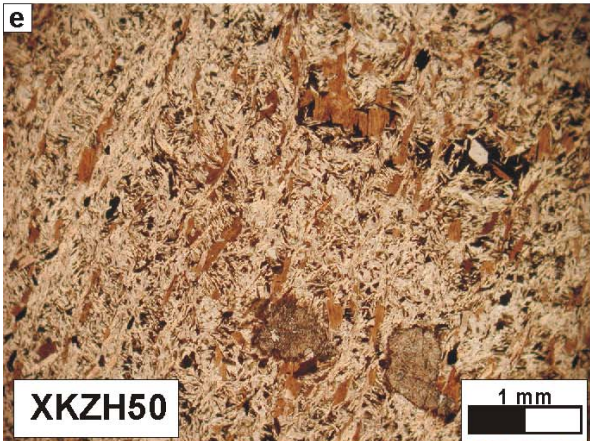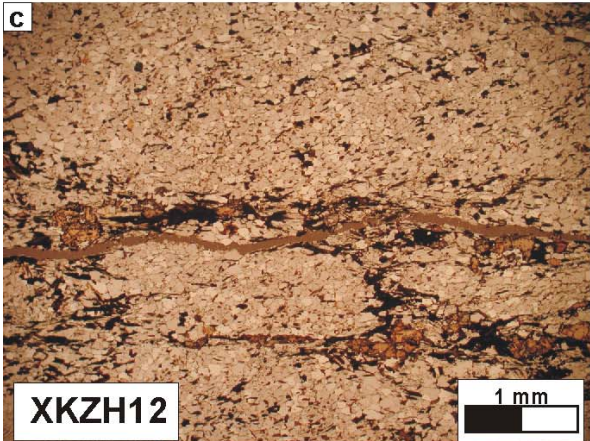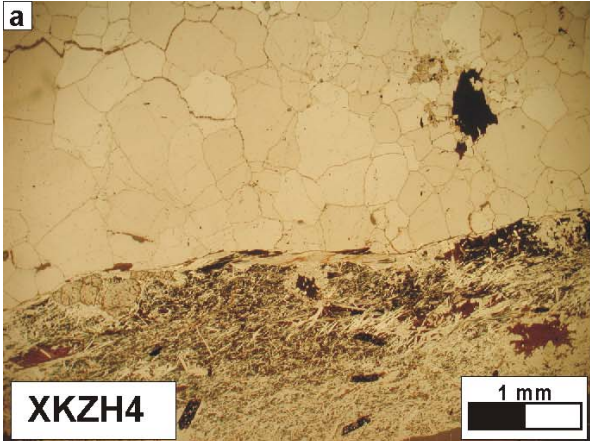
Plate 5
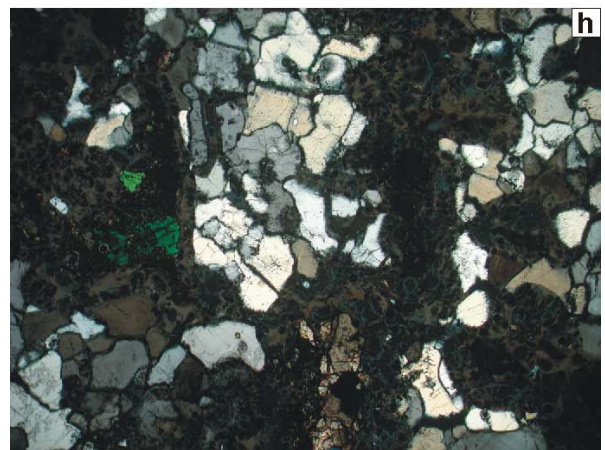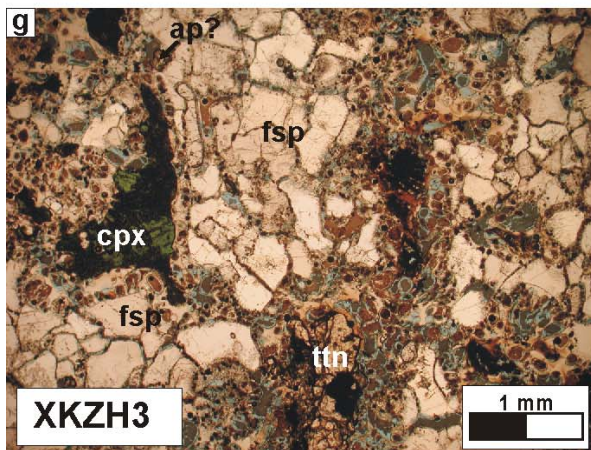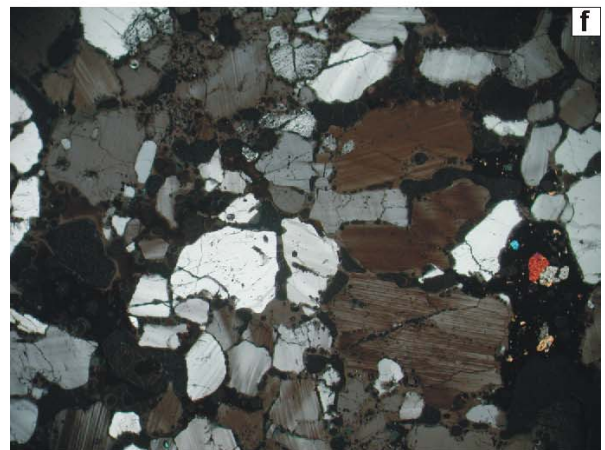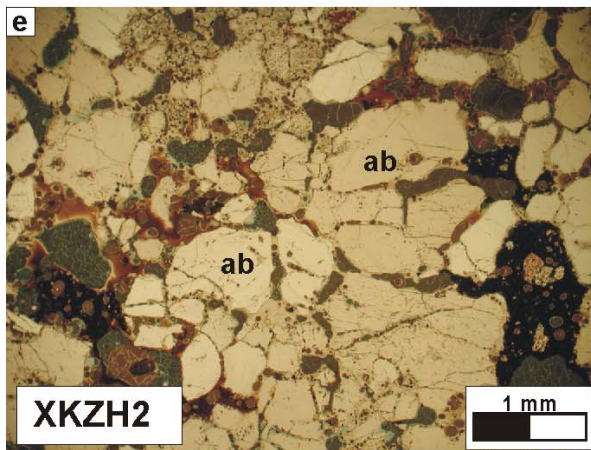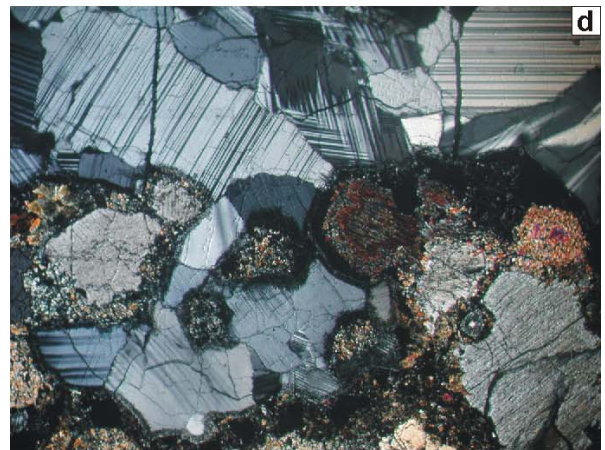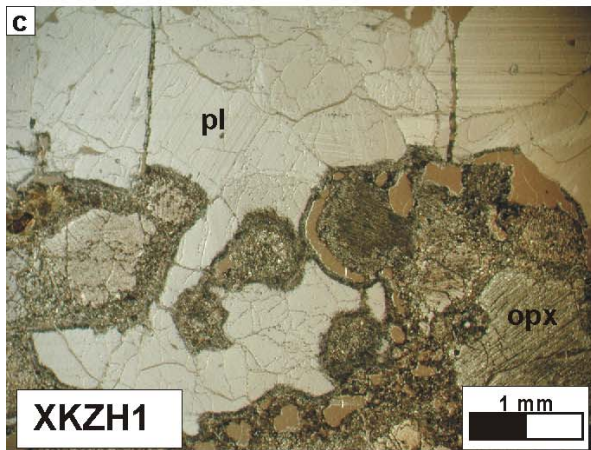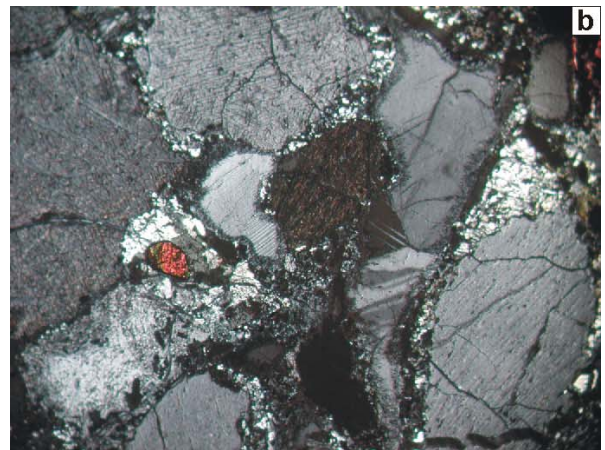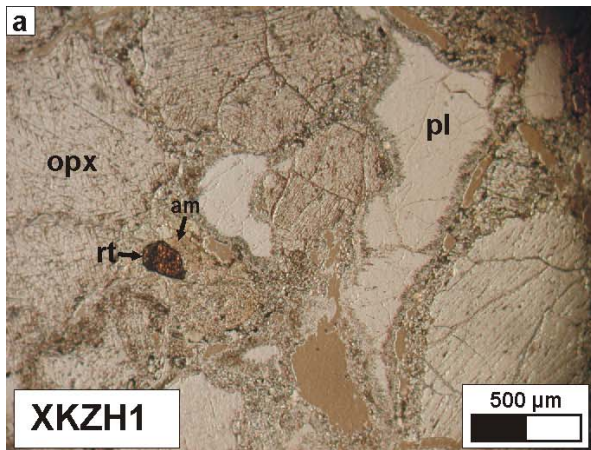
Plate 6

Plate 5
Photographs of thin-sections (left: single, and right: crossed nicols) of typical crustal xenoliths.
Sample XKZH4 **(a+b)** shows a sharp contact between quartzite and garnet-bearing mica schist. XKZH4 might be a fragment of a quartz vein or dike ("Pfahl"), which are common in the area; **(c+d)** XKZH12: garnet- and staurolite-bearing quartzitic mica schist; **(e+f)** XKZH50: garnet-bearing mica schist; **(g+h)** XKZH65: porphyroclastic quartz-feldspar-bearing rock (meta-tuff?).

Plate 6
Photographs of thin-sections (single and crossed nicols) of feldspar-dominated crustal xenoliths.
Noritic sample XKZH1 **(a-d)** consists mainly of plagioclase and orthopyroxene, minor components are amphibole, rutile, brown mica, and fine grained intergrowth of orthopyroxene and clinopyroxene; **(e+f)** XKZH2: glass- (brown) bearing sample mainly composed of albite; contains also minor amounts of zircon and a Nb-Ta-bearing ore [*Kämpf,* personal communication]; **(g+h)** XKZH3: feldspar rich sample, which additionally contains pyroxene (green), zircon (?), apatite, and titanite.
The porous texture of sample XKZH2 and XKZH3 as well as the glass formation in XKZH2 is most probable related to the heating in the host magma, whereas the origin of fine grained orthopyroxene-clinopyroxene intergrowth might be related to previous metamorphic/metasomatic overprinting.

Besides the majority of quartz- and mica-rich crustal xenoliths also light grey more feldspar-rich samples could be found (XKZH1, -2, -3, -6, -65, -66; Plates 4, 6). Three analysed feldspar-rich xenoliths are strongly influenced by heating in the host magma. One of them (XKZH1) shows layering of the major components feldspar and orthopyroxene indicating some metamorphic overprinting of a probable primary magmatic texture. Minor components in sample XKZH1 (Plate 6) are clinopyroxene, dark mica, rutile and amphibole. In the two other analysed feldspar-rich samples (XKZH2, XKZH3) the heating in the host magma resulted into glass formation. This might be an indication for a deeper than uppermost crust origin of these xenoliths (due to a longer residence time in the magma).

Light grey samples XKZH65, XKZH66 (Plates 4, 5) and XKZH6 show coarse feldspar and quartz remnants resting in a (partly re-crystallized) matrix of quartz, feldspar, and mica.

C.4   Data

C.4.1   Whole-rock major and trace element chemistry

Samples were grounded in an agate mill to less than 62 μm and homogenised. Major element oxides and most trace elements were analysed by X-ray fluorescence spectrometry on fused glass pellets on a Siemens SRS 303 spectrometer at the GFZ Potsdam by Dipl.-Krist. Rudolf Naumann. H_2O and CO_2 were determined by IR-spectrometry (LECO CH elemental analyser) or thermal conductivity measurements (vario EL) after decomposition of the rock powder in a 1000°C oxygen stream. FeO was analysed by potentiometric titration using a modification of the Wilson procedure [*Wilson,* 1955]. Trace and Rare Earth (REE) elements were analysed by inductively-coupled plasma mass-spectrometry (ICP-MS) on a Perkin-Elmer/SCIEX Elan 5000 ICP mass-spectrometer at the GFZ Potsdam by Dr. Peter Dulski. For details on ICP-MS sample preparation (mixed acid digestion procedure), calibration, conditions of measurement, and error discussion see *Dulski* [2001].

Table C.II. Whole-rock chemistry of (ultra-) mafic nodules and host rock samples (XRF, ICP-MS).

sample		wehrlites, ol-cpx-aggregates								hbl-pt
		MXZH1	MXZH2	MXZH3	MXZH4	MXZH8	MXZH18	MXZH18D	MXZH67	MXZH66
SiO_2 (wt.%)		47.4	46.2	46.3	43.7	47.5	47.5	47.5	46.0	40.3
TiO_2		0.897	0.534	0.957	0.482	0.741	1.166	1.166	0.704	1.032
Al_2O_3		4.9	3.4	5.1	2.7	4.3	6.5	6.4	3.8	5.2
$Fe_2O_3(t)$		1.77	1.10	2.09	1.66	1.47	2.07	6.31	1.80	2.80
FeO		4.13	5.52	4.39	6.91	4.27	3.81		5.16	10.27
MnO		0.110	0.115	0.117	0.135	0.109	0.116	0.115	0.114	0.166
MgO		22.69	29.48	24.52	35.48	24.69	17.85	17.83	27.03	31.14
CaO		16.36	12.69	14.91	8.80	15.28	17.54	17.54	13.11	6.30
Na_2O		0.52	0.38	0.46	0.26	0.49	0.85	0.86	0.50	0.53
K_2O		0.06	<0,02	0.12	<0,02	0.01	0.24	0.24	0.04	0.47
P_2O_5		0.114	0.042	0.153	0.076	0.073	0.190	0.193	0.075	0.047
H_2O		0.90	0.66	0.85	0.89	0.53	1.04	1.04	0.72	0.76
CO_2		0.26	0.33	0.19	0.37	0.33	0.22	0.22	0.12	0.14
Total		100.11	100.45	100.16	101.46	99.80	99.09	99.41	99.74	100.32
Cs (ppm)	ICP-MS	0.05	< 0.01	0.08	0.02	0.06	0.34		0.03	0.10
Rb	XRF								<10	<10
	ICP-MS	4.7	0.4	6.5	0.7	3.1	19.5		2.2	5.4
Sr	XRF								101	85
	ICP-MS	148	56	181	48	97	255		108	91
Ba	XRF								53	91
	ICP-MS	108	34	199	36	64	215		68	86.3
Zr	XRF								41	35
	ICP-MS	46	19	49	22	33	73		33	26
Nb	XRF									
	ICP-MS								14	10
Ta	ICP-MS								1.2	< 1
Th	ICP-MS	1.03	0.31	1.35	0.51	0.68	2.14		1.02	0.59
U	ICP-MS	0.23	0.07	0.29	0.12	0.13	0.51		0.18	0.15
Pb	ICP-MS	0.43	0.25	0.67	0.39	0.36	0.91		0.57	0.49
V	XRF								160	176
Cr	XRF								3485	2622
Ni	XRF								681	562
Zn	XRF								37	67
Y	XRF								<10	<10
	ICP-MS	6.1	3.6	6.5	3.0	5.1	9.0		4.9	4.2
La	ICP-MS	9.84	3.69	11.9	4.32	6.16	16.9		7.34	4.94
Ce	ICP-MS	21.1	7.98	24.1	9.67	14.1	34.0		16.2	11.0
Pr	ICP-MS	2.73	1.27	3.16	1.36	2.02	4.28		2.08	1.50
Nd	ICP-MS	11.2	5.61	12.4	5.57	8.39	17.0		9.18	6.96
Sm	ICP-MS	2.41	1.33	2.59	1.26	2.04	3.38		1.93	1.57
Eu	ICP-MS	0.75	0.46	0.81	0.40	0.62	1.07		0.60	0.48
Gd	ICP-MS	2.24	1.38	2.32	1.17	1.89	3.15		1.72	1.49
Tb	ICP-MS	0.27	0.18	0.29	0.14	0.24	0.40		0.22	0.19
Dy	ICP-MS	1.46	0.87	1.51	0.77	1.26	2.10		1.17	0.98
Ho	ICP-MS	0.25	0.14	0.26	0.12	0.21	0.36		0.19	0.16
Er	ICP-MS	0.55	0.34	0.60	0.29	0.48	0.86		0.48	0.46
Tm	ICP-MS	0.07	0.04	0.07	0.03	0.05	0.10		0.05	0.04
Yb	ICP-MS	0.46	0.25	0.51	0.25	0.39	0.69		0.32	0.33
Lu	ICP-MS	0.05	0.03	0.06	0.02	0.05	0.08		0.04	0.04
Hf	ICP-MS	1.43	0.71	1.42	0.71	1.16	1.99		1.02	0.97

Table C.II. (continued).

sample		hornblendites, clinopyroxenites					am-X	cpx-X	ol-X	phl-X
		MXZH5	MXZH12	MXZH11	MXZH13	MXZH68	MXZH15	MXZH16	MXZH19	MXZH22
SiO_2 (wt.%)		39.5	39.6	39.2	40.0	40.5	40.8	49.5	39.2	
TiO_2		2.487	3.430	3.846	3.280	3.233	3.131	1.076	0.082	
Al_2O_3		9.8	12.5	6.0	12.6	13.6	14.4	6.6	0.5	
Fe_2O_3(t)		5.44	6.00	11.43	5.28	4.28	2.64	1.95	3.51	
FeO		5.46	6.34	8.55	6.61	5.36	4.84	3.34	15.18	
MnO		0.155	0.128	0.228	0.126	0.097	0.075	0.104	0.226	
MgO		10.79	13.35	10.06	13.28	14.35	15.70	14.88	46.39	
CaO		19.40	12.74	18.88	13.03	11.55	11.56	20.46	0.38	
Na_2O		1.34	1.97	0.76	1.94	2.29	1.96	0.85	<0,1	
K_2O		0.68	1.65	0.06	1.67	1.98	2.21	<0,02	<0,02	
P_2O_5		2.524	0.005	0.111	0.006	0.042	0.031	0.031	0.029	
H_2O		1.53	1.48	0.66	1.20	1.18	1.35	0.80	0.27	
CO_2		0.23	0.24	0.19	0.18	0.09	0.35	0.33	0.14	
Total		99.34	99.44	99.97	99.21	99.11	99.05	99.92	105.91	
Cs (ppm)	ICP-MS	0.67	0.16	0.10	0.22	0.04	0.01	< 0.01	0.03	1.81
Rb	XRF					15				
	ICP-MS	42.0	21.8	8.6	23.8	18.2	14.5	< 0.2	1.0	321
Sr	XRF					321				
	ICP-MS	474	419	240	427	344	282	93	11.3	142
Ba	XRF					254				
	ICP-MS	320	342	107	380	242	185	4.6	12.3	2379
Zr	XRF					73				
	ICP-MS	236	222	201	235	54	37	43	4.4	6.6
Nb	XRF									
	ICP-MS					16				
Ta	ICP-MS					1.8				
Th	ICP-MS	3.05	0.50	1.97	0.56	0.37	0.10	0.08	0.15	0.17
U	ICP-MS	0.73	0.13	0.46	0.14	0.09	0.04	0.02	0.04	0.02
Pb	ICP-MS	1.12	0.67	0.62	0.76	0.60	0.25	0.18	0.21	0.60
V	XRF					365				
Cr	XRF					13				
Ni	XRF					75				
Zn	XRF					35				
Y	XRF					11				
	ICP-MS	17.7	11.0	11.9	11.1	9.4	8.2	8.9	0.45	0.18
La	ICP-MS	33.8	9.02	18.0	9.70	6.93	3.55	2.68	1.14	0.44
Ce	ICP-MS	78.0	28.2	45.4	29.3	20.6	11.8	9.56	2.10	0.86
Pr	ICP-MS	10.6	4.60	6.41	4.83	3.29	2.12	1.86	0.25	0.09
Nd	ICP-MS	43.3	21.2	26.9	22.2	16.3	10.5	9.46	0.87	0.33
Sm	ICP-MS	8.34	4.96	5.39	5.04	3.99	2.86	2.69	0.15	0.06
Eu	ICP-MS	2.51	1.53	1.66	1.59	1.30	0.99	0.95	0.05	< 0.008
Gd	ICP-MS	7.07	4.37	4.57	4.46	3.60	2.89	2.99	0.13	0.04
Tb	ICP-MS	0.82	0.54	0.56	0.55	0.45	0.37	0.40	0.01	< 0.008
Dy	ICP-MS	4.19	2.70	2.90	2.82	2.38	2.01	2.15	0.09	0.04
Ho	ICP-MS	0.69	0.44	0.48	0.46	0.40	0.33	0.36	0.02	0.01
Er	ICP-MS	1.62	1.03	1.15	1.08	0.93	0.80	0.83	0.04	0.02
Tm	ICP-MS	0.20	0.12	0.14	0.13	0.09	0.10	0.10	0.01	< 0.006
Yb	ICP-MS	1.34	0.84	0.96	0.87	0.60	0.63	0.65	0.04	0.03
Lu	ICP-MS	0.16	0.10	0.13	0.10	0.08	0.07	0.07	< 0.009	< 0.009
Hf	ICP-MS	4.26	7.49	6.75	8.07	2.23	1.69	2.17	0.10	0.19

Table C.II. (continued).

sample		host rock (nephelinite)							
		My1	My1-B	My2	My2-B	BK-2	BK-2B	Go-01	Go-02
SiO_2 (wt.%)		40.0	39.8	41.3	41.1	39.9	39.4	41.8	42.0
TiO_2		2.958	2.933	2.898	2.869	2.840	2.906	2.377	2.385
Al_2O_3		11.5	11.4	11.6	11.6	11.2	11.3	12.2	12.2
$Fe_2O_3(t)$		5.58	5.63	5.68	5.39	12.35	7.02	3.45	4.05
FeO		5.26	5.11	5.05	5.27		4.00	7.85	7.41
MnO		0.188	0.187	0.185	0.185	0.210	0.198	0.182	0.182
MgO		13.64	13.70	12.60	12.68	13.05	12.25	11.72	11.93
CaO		12.67	12.54	12.41	12.31	12.69	13.15	11.54	11.35
Na_2O		2.53	2.61	2.30	2.40	3.40	3.47	3.00	3.10
K_2O		1.55	1.53	1.42	1.42	2.11	2.17	1.38	1.29
P_2O_5		0.667	0.724	0.654	0.714	0.740	0.757	0.755	0.751
H_2O		2.21	2.28	2.51	2.75	0.75	1.07	1.80	1.80
CO_2		0.11	0.10	0.11	0.10	0.10	0.17	0.68	0.31
Total		99.38	98.49	99.33	98.78	99.30	97.81	98.75	98.69
Cs (ppm)	ICP-MS	0.91	0.89	2.09	2.03		0.81	1.14	1.03
Rb	XRF	61	59	208	208		58	54	56
	ICP-MS	71	69	246	241	71	64	59	64
Sr	XRF	707	708	681	687		868	842	830
	ICP-MS	759	748	738	724	943	874	916	906
Ba	XRF	780	770	752	738		734	559	569
	ICP-MS	776	761	740	708	678	730	554	542
Zr	XRF	225	220	247	243		259	202	197
	ICP-MS	237	239	242	243	218	269	212	211
Nb	XRF		93		91		105		
	ICP-MS	134	116	73	112		126	109	109
Ta	ICP-MS	9.8	6.7	5.9	6.4		7.3	7.7	12
Th	ICP-MS	8.9	9.0	9.5	9.6	8.9	9.6	7.7	7.6
U	ICP-MS	2.4	2.4	2.4	2.5	2.4	2.8	2.3	2.3
Pb	ICP-MS	2.9	3.1	3.7	4.0		2.7	4.6	4.6
V	XRF	315	320	316	306		308	220	220
Cr	XRF	726	735	586	582		495	317	309
Ni	XRF	249	n.a.	225	n.a.		n.a.	246	255
Zn	XRF	70	72	74	75		76	89	88
Y	XRF	21	22	22	24		23	23	24
	ICP-MS	21	21	23	22	23	24	24	24
La	ICP-MS	68.4	68.3	70.3	68.2		73.9	60.9	60.4
Ce	ICP-MS	131	128	135	129		141	113	112
Pr	ICP-MS	14.8	14.8	15.6	14.7		16.1	12.6	12.5
Nd	ICP-MS	56.2	55.7	59.0	55.6		61.1	47.7	47.6
Sm	ICP-MS	9.61	9.65	10.2	9.66		10.6	8.64	8.58
Eu	ICP-MS	2.92	2.83	2.90	2.77		3.09	2.60	2.61
Gd	ICP-MS	7.69	7.42	8.17	7.73		8.40	7.50	7.37
Tb	ICP-MS	0.97	0.97	1.03	1.00		1.08	1.00	1.01
Dy	ICP-MS	4.94	4.89	5.22	4.98		5.40	5.36	5.36
Ho	ICP-MS	0.81	0.83	0.86	0.84		0.94	0.96	0.93
Er	ICP-MS	2.06	2.05	2.23	2.10		2.32	2.43	2.43
Tm	ICP-MS	0.25	0.26	0.28	0.27		0.28	0.30	0.31
Yb	ICP-MS	1.51	1.51	1.66	1.59		1.73	1.88	1.84
Lu	ICP-MS	0.21	0.20	0.24	0.23		0.25	0.27	0.27
Hf	ICP-MS	5.26	5.35	5.30	5.34		6.10	4.64	4.73

The analytical precision for all methods is better than 10% and was checked against international rock and in-house laboratory standards. The accuracy of ICP-MS measurements is in the range of ±5% [*Dulski,* 2001]. The analyses of Nb and Ta are less accurate due to the unstable behaviour of these elements in solution. The results are listed in Table C.II and Appendix C.ii for mantle and crustal xenoliths, respectively. Figure C.5 and Appendix C.iii show the chondrite (C1)-normalized REE patterns of the investigated samples.
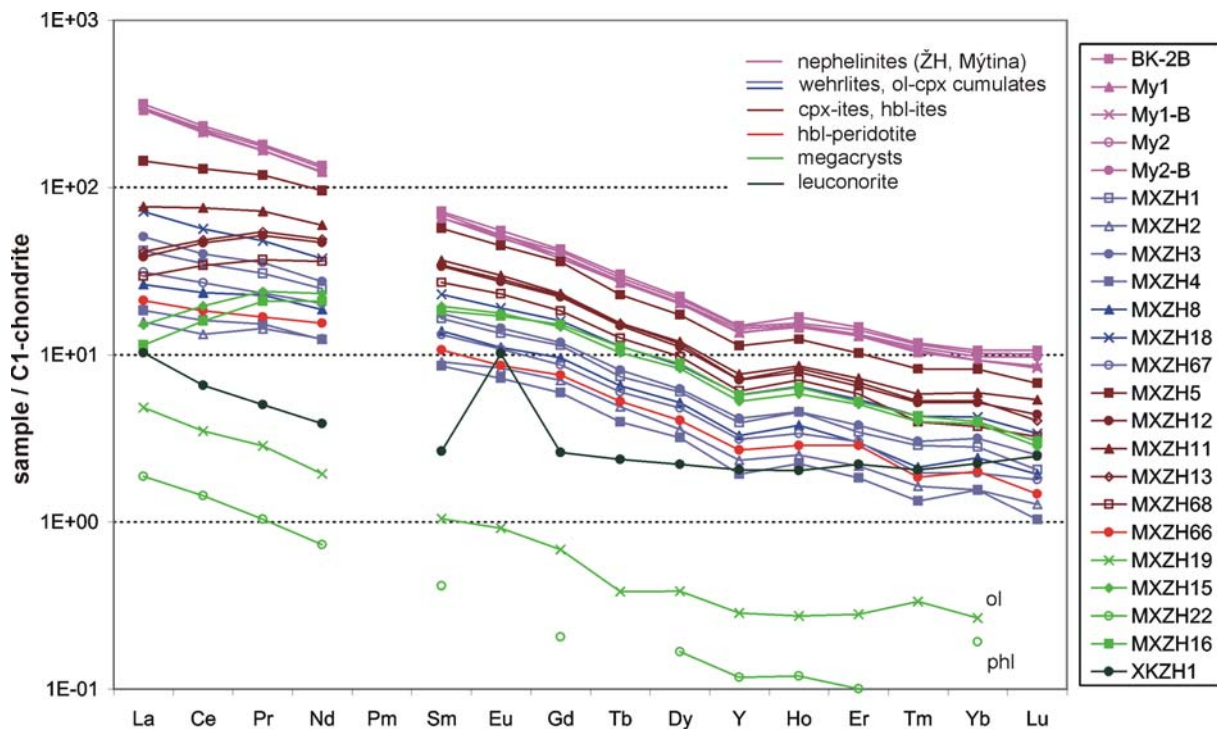
Figure C.5
Chondrite (C1)-normalized REE patterns of host mela-nephelinites and (ultra-) mafic nodules from the tephra deposit in Mýtina (see Table C.II). REE values of C1-chondrites are taken from *Anders and Grevesse* [1989].

C.4.2   Mineral-chemical analyses (EMPA)

Minerals of several mantle xenoliths, megacrysts, and three crustal xenoliths were analysed for their chemical composition. Major and minor elements of minerals (olivine, clinopyroxene, amphibole, phlogopite, spinel, titanite, ilmenite, apatite) were determined with the CAMECA SX50 and CAMECA SX100 microprobes of the GFZ Potsdam, which are equipped with four wave-length dispersive spectrometers, using an acceleration voltage of 15 kV, a beam current of 20 nA, and a beam diameter of 2 µm (for mica, feldspar, and glass analyses 10 µm, because of the higher concentration of diffusion endangered elements like Na, F, K). Counting time for the peak was 20 seconds, and for the background 10 seconds on each side of the peak. Ca in olivine was measured as a trace element (50.2 nA, 15 kV, 300s counting time for peak and background) in selected samples to perform pressure estimations with the olivine-clinopyroxene barometer.

Table C.III. Mineral-chemical composition and structural formulae for peridotites (average and standard deviation; n: number of analyses).

sample	MXZH66				Zinst-1				Go01-1			
	ol	cpx	am	sp	ol	cpx	opx	sp	ol	cpx	opx	sp
n	22	10	10	5	10	10	6	5	3	3	4	3
SiO_2	38.72 ±0.19	49.58 ±0.29	41.72 ±0.17	0.12 ±0.01	40.76 ±0.20	53.48 ±0.23	56.21 ±0.14	0.07 ±0.01	40.88 ±0.08	52.78 ±0.38	55.85 ±0.53	0.02 ±0.01
TiO_2	0.02 ±0.01	1.12 ±0.03	3.24 ±0.05	1.56 ±0.01	0.01 ±0.01	0.32 ±0.03	0.13 ±0.01	0.62 ±0.02	0.01 ±0.01	0.02 ±0.01	0.01 ±0.01	0.01 ±0.01
Al_2O_3	0.04 ±0.01	6.45 ±0.07	14.60 ±0.07	41.61 ±0.07	0.01 ±0.01	3.88 ±0.08	3.65 ±0.03	31.69 ±0.20	0.01 ±0.00	3.90 ±0.53	2.66 ±0.05	40.22 ±0.31
Cr_2O_3	0.01 ±0.02	0.65 ±0.04	0.79 ±0.05	14.27 ±0.09	0.05 ±0.02	1.24 ±0.04	0.79 ±0.03	34.55 ±0.10	0.01 ±0.01	0.95 ±0.22	0.38 ±0.02	26.39 ±0.18
Fe_2O_3				13.56 ±0.43				6.07 ±0.39				5.39 ±0.48
FeO	16.44 ±0.19	5.63 ±0.09	7.21 ±0.15	15.19 ±0.07	8.96 ±0.08	3.00 ±0.05	5.73 ±0.11	11.14 ±0.17	8.99 ±0.07	2.63 ±0.12	6.00 ±0.09	10.38 ±0.31
MgO	44.64 ±0.11	14.86 ±0.07	15.60 ±0.05	15.35 ±0.06	49.87 ±0.25	17.06 ±0.09	33.44 ±0.10	16.90 ±0.10	49.95 ±0.10	16.99 ±0.28	34.17 ±0.14	18.22 ±0.24
MnO	0.23 ±0.03	0.12 ±0.04	0.07 ±0.03	0.17 ±0.03	0.14 ±0.03	0.08 ±0.02	0.14 ±0.03	0.10 ±0.03	0.12 ±0.02	0.09 ±0.03	0.13 ±0.01	0.08 ±0.03
NiO	0.15 ±0.04			0.15 ±0.05	0.41 ±0.04			0.27 ±0.05	0.39 ±0.02			0.22 ±0.03
CaO	0.15 ±0.02	20.74 ±0.17	11.63 ±0.11	0.01 ±0.01	0.09 ±0.02	19.64 ±0.12	0.99 ±0.02	0.02 ±0.02	0.04 ±0.01	21.59 ±0.59	0.51 ±0.02	0.01 ±0.00
BaO												
Na_2O		1.03 ±0.03	2.29 ±0.02			1.43 ±0.05	0.15 ±0.01			0.86 ±0.05	0.05 ±0.01	
K_2O		0.01 ±0.00	2.26 ±0.06			0.00 ±0.01	0.01 ±0.01			0.00 ±0.00	0.00 ±0.00	
P_2O_5												
Cl			0.02 ±0.01									
F			0.07 ±0.03									
H_2O												
Total	100.40 ±0.29	100.18 ±0.39	99.45 ±0.18	101.98 ±0.50	100.30 ±0.42	100.13 ±0.32	101.23 ±0.19	101.42 ±0.19	100.40 ±0.10	99.81 ±0.06	99.76 ±0.54	100.94 ±0.30

Atomic formulae

	ol	cpx	am	sp	ol	cpx	opx	sp	ol	cpx	opx	sp
Si	0.978	1.823	5.974	0.026	0.994	1.931	1.917	0.017	0.996	1.917	1.931	0.005
Ti	0.000	0.031	0.349	0.261	0.000	0.009	0.004	0.107	0.000	0.001	0.00	0.002
Al	0.001	0.280	2.463	10.876	0.000	0.165	0.147	8.547	0.000	0.167	0.109	10.480
Cr	0.000	0.004	0.090	2.502	0.001	0.035	0.021	6.251	0.000	0.027	0.010	4.613
Fe^{3+}				2.262				1.045				0.897
Fe^{2+}	0.347	0.173	0.863	2.817	0.183	0.091	0.164	2.132	0.183	0.080	0.174	1.919
Mg	1.681	0.814	3.329	5.074	1.813	0.918	1.700	5.767	1.813	0.920	1.762	6.003
Mn	0.005	0.019	0.008	0.031	0.003	0.002	0.004	0.019	0.003	0.003	0.004	0.015
Ni	0.003			0.026	0.008			0.049	0.008			0.039
Ca	0.004	0.817	1.784	0.003	0.002	0.759	0.036	0.005	0.001	0.84	0.019	0.003
Ba												
Na		0.074	0.635			0.100	0.010			0.060	0.003	
K		0.000	0.413			0.000	0.000			0.000	0.000	
P												
Total	3.020	4.034	15.907	23.878	3.004	4.011	4.001	23.937	3.004	4.014	4.011	23.976
Ca (trace)	0.0038				0.0020				0.0010			
Cr/(Cr+Al)				0.187				0.422				0.306
Mg/(Mg+Fe)	0.829	0.825	0.794	0.643	0.908	0.910	0.912	0.730	0.908	0.920	0.910	0.758
Fo	82.4				90.3				90.3			
Wo		43.1				40.6	1.9			44.1	1.0	
En		42.9				49.1	88.8			48.4	89.8	
Fs		10.1				5.0	8.7			4.3	9.0	
Ac		3.9				5.4	0.5			3.2	0.2	

Table C.IV. Mineral-chemical composition and structural formulae for clinopyroxenites.

sample	MXZH11				MXZH5					MXZH33		
	cpx	am	mag	ttn	cpx	am	ilm	mag	ap	cpx	am	ilm
n	13	10	13	5	5	5	3	3	5	11	9	8
SiO_2	47.52 ±0.23	40.03 ±0.20	0.04 ±0.02	30.43 ±0.12	47.92 ±0.58	39.76 ±0.16	0.01 ±0.01	0.07 ±0.01	0.30 ±0.02	51.09 ±0.18	39.84 ±0.23	0.02 ±0.01
TiO_2	1.87 ±0.09	2.54 ±0.05	9.78 ±0.15	39.14 ±0.10	1.45 ±0.16	2.36 ±0.02	41.25 ±0.08	9.15 ±0.02	0.01 ±0.01	0.84 ±0.05	2.51 ±0.03	42.09 ±0.29
Al_2O_3	5.84 ±0.11	13.43 ±0.13	2.28 ±0.04	1.00 ±0.02	6.29 ±0.42	14.26 ±0.17	0.31 ±0.02	3.20 ±0.03	0.00 ±0.00	3.56 ±0.09	12.70 ±0.10	0.39 ±0.07
Cr_2O_3	0.01 ±0.01	0.01 ±0.02	0.04 ±0.01	0.02 ±0.02	0.01 ±0.01	0.01 ±0.01	0.02 ±0.01	0.04 ±0.01	0.01 ±0.01	0.01 ±0.01	0.00 ±0.01	0.02 ±0.02
Fe_2O_3			58.07 ±0.30	0.86 ±0.06				59.00 ±0.20				
FeO	9.09 ±0.14	14.38 ±0.19	28.37 ±0.11	0.00 ±0.00	9.60 ±0.09	14.90 ±0.32	54.14 ±0.33	28.88 ±0.53	0.14 ±0.02	6.98 ±0.17	11.71 ±0.11	51.25 ±0.66
MgO	11.29 ±0.08	11.85 ±0.10	1.65 ±0.03	0.00 ±0.00	11.13 ±0.22	11.15 ±0.27	2.46 ±0.12	1.97 ±0.25	0.04 ±0.01	13.35 ±0.11	13.53 ±0.05	3.83 ±0.43
MnO	0.21 ±0.04	0.21 ±0.05	0.72 ±0.04	0.03 ±0.03	0.19 ±0.03	0.19 ±0.02	0.55 ±0.04	0.53 ±0.07	0.05 ±0.01	0.14 ±0.02	0.13 ±0.03	0.41 ±0.03
NiO			0.05 ±0.04	0.03 ±0.02	0.02 ±0.02	0.01 ±0.01	0.03 ±0.02	0.01 ±0.01	0.00 ±0.00			0.04 ±0.03
CaO	22.50 ±0.09	11.88 ±0.08	0.01 ±0.01	28.99 ±0.04	22.66 ±0.09	12.01 ±0.20	0.06 ±0.01	0.03 ±0.02	56.05 ±0.15	23.57 ±0.09	12.04 ±0.10	0.03 ±0.02
BaO												
Na_2O	1.19 ±0.04	2.97 ±0.04		0.04 ±0.01	0.95 ±0.02	2.30 ±0.08			0.11 ±0.02	0.88 ±0.02	2.74 ±0.04	
K_2O	0.01 ±0.01	1.35 ±0.05			0.00 ±0.00	1.69 ±0.02			0.00 ±0.00	0.01 ±0.01	1.48 ±0.03	
P_2O_5				0.13 ±0.02					42.15 ±0.33			
Cl		0.04 ±0.01				0.02 ±0.01			0.17 ±0.01		0.01 ±0.01	
F		0.00 ±0.01		0.14 ±0.03		0.00 ±0.00			0.80 ±0.03		0.00 ±0.00	
H_2O												
Total	99.53 ±0.27	98.68 ±0.26	101.01 ±0.37	100.81 ±0.20	100.22 ±0.28	98.64 ±0.71	98.83 ±0.36	102.86 ±0.56	99.83 ±0.28	100.44 ±0.26	96.70 ±0.31	98.08 ±0.14
Atomic formulae												
Si	1.804	5.978	0.012		1.806	5.949		0.019		1.895	6.009	
Ti	0.053	0.286	2.112		0.041	0.265		1.935		0.024	0.285	
Al	0.262	2.364	0.772		0.280	2.514		1.060		0.156	2.257	
Cr	0.000	0.002	0.008		0.000	0.001		0.008		0.000	0.001	
Fe^{3+}			12.558					12.491				
Fe^{2+}	0.289	1.796	6.819		0.303	1.865		6.793		0.217	1.477	
Mg	0.639	2.637	0.709		0.625	2.486		0.825		0.738	3.042	
Mn	0.007	0.026	0.176		0.006	0.024		0.126		0.004	0.017	
Ni			0.011		0.001	0.001		0.002				
Ca	0.915	1.901	0.002		0.916	1.925		0.009		0.937	1.945	
Ba											0.001	
Na	0.088	0.859			0.069	0.668				0.063	0.801	
K	0.000	0.257			0.000	0.322				0.000	0.285	
P												
Total	4.056	16.106	23.178		4.047	16.021		23.268		4.035	16.119	
Ca (trace)			0.010					0.007				
Cr/(Cr+Al)			0.094				0.07	0.108				0.12
Mg/(Mg+Fe)	0.689	0.595			0.674	0.571				0.773	0.673	
Fo												
Wo	47.2				47.7					47.8		
En	33.0				32.6					37.7		
Fs	15.3				16.1					11.3		
Ac	4.5				3.6					3.2		

Table C.V. Mineral-chemical composition and structural formulae for hornblendites.

sample	MXZH12				MXZH13			MXZH68	
	cpx	am	phl	ilm	mag	cpx	am	ilm	am
n	4	5	10	10	10	5	12	5	10
SiO_2	49.18 ± 0.15	40.87 ± 0.15	37.52 ± 0.12	0.02 ± 0.01	0.08 ± 0.04	50.29 ± 0.19	39.42 ± 0.17	0.02 ± 0.01	41.34 ± 0.16
TiO_2	1.59 ± 0.05	3.06 ± 0.06	3.85 ± 0.03	46.29 ± 0.22	13.95 ± 0.58	1.06 ± 0.03	3.02 ± 0.02	48.93 ± 1.35	3.37 ± 0.04
Al_2O_3	5.02 ± 0.14	13.13 ± 0.05	15.87 ± 0.07	0.27 ± 0.03	4.48 ± 2.90	3.99 ± 0.09	12.76 ± 0.08	0.77 ± 0.05	13.75 ± 0.11
Cr_2O_3	0.01 ± 0.01	0.00 ± 0.00	0.00 ± 0.01	0.02 ± 0.02	0.03 ± 0.01	0.01 ± 0.01	0.01 ± 0.01	0.02 ± 0.01	0.02 ± 0.02
Fe_2O_3					54.04 ± 3.05				
FeO	7.43 ± 0.10	11.81 ± 0.12	11.95 ± 0.13	46.67 ± 0.92	23.75 ± 2.54	6.92 ± 0.11	11.64 ± 0.20	40.51 ± 1.44	9.47 ± 0.15
MgO	12.75 ± 0.06	13.14 ± 0.02	18.17 ± 0.06	4.99 ± 0.64	5.41 ± 1.91	12.98 ± 0.06	13.25 ± 0.06	8.66 ± 0.91	14.39 ± 0.13
MnO	0.15 ± 0.01	0.12 ± 0.03	0.09 ± 0.03	0.58 ± 0.08	0.32 ± 0.07	0.15 ± 0.01	0.13 ± 0.03	0.37 ± 0.05	0.09 ± 0.03
NiO				0.03 ± 0.03	0.03 ± 0.03			0.03 ± 0.04	
CaO	22.83 ± 0.06	11.97 ± 0.09	0.16 ± 0.04	0.02 ± 0.01	0.04 ± 0.04	23.49 ± 0.11	12.05 ± 0.08	0.09 ± 0.02	11.62 ± 0.07
BaO			0.46 ± 0.04				0.02 ± 0.02		
Na_2O	1.03 ± 0.01	2.63 ± 0.02	0.63 ± 0.02			0.93 ± 0.01	2.55 ± 0.04		2.51 ± 0.04
K_2O	0.01 ± 0.00	1.80 ± 0.03	8.36 ± 0.09			0.01 ± 0.00	1.81 ± 0.03		1.97 ± 0.03
P_2O_5									
Cl		0.02 ± 0.00	0.01 ± 0.00				0.02 ± 0.01		0.02 ± 0.01
F		0.00 ± 0.00	0.00 ± 0.00				0.00 ± 0.00		0.02 ± 0.03
H_2O			4.15 ± 0.01						
Total	99.99 ± 0.19	98.54 ± 0.26	101.22 ± 0.27	98.89 ± 0.41	102.13 ± 0.36	99.84 ± 0.44	96.66 ± 0.24	99.40 ± 0.39	98.55 ± 0.24
Atomic formulae									
Si	1.839	6.039	5.419		0.022	1.879	5.961		6.029
Ti	0.045	0.340	0.418		2.836	0.030	0.343		0.370
Al	0.221	2.287	2.701		1.405	0.176	2.274		2.364
Cr	0.001	0.000	0.000		0.006	0.000	0.001		0.002
Fe^{3+}					11.016				
Fe^{2+}	0.233	1.459	1.443		5.388	0.216	1.472		1.155
Mg	0.711	2.894	3.913		2.164	0.723	2.987		3.129
Mn	0.005	0.015	0.011		0.073	0.005	0.017		0.011
Ni					0.006				
Ca	0.915	1.895	0.025		0.011	0.941	1.952		1.815
Ba			0.026				0.001		
Na	0.075	0.753	0.176			0.068	0.748		0.708
K	0.001	0.339	1.539			0.000	0.350		0.367
P									
Total	4.044	16.022	15.670		22.928	4.037	16.105		15.949
Ca (trace)									
Cr/(Cr+Al)									
Mg/(Mg+Fe)	0.754	0.665	0.731	0.16	0.287	0.770	0.670	0.28	0.730
Fo									
Wo	47.2					48.2			
En	36.7					37.0			
Fs	12.2					11.3			
Ac	3.9					3.5			

73

Table C.VI. Mineral-chemical composition and structural formulae for wehrlites and ol-cpx-aggregates (c - core; r - rim composition).

sample	MXZH1			phl	MXZH2				MXZH4		MXZH8	
	ol	cpx1	cpx2		ol1	ol2	cpx1	cpx2	ol	cpx	ol	cpx
n	4	5	6	7	6	4	4	3	9	5	10	8
SiO_2	40.42 ±0.13	51.77 ±0.21	51.24 ±0.34	38.45 ±0.31	40.01 ±0.09	40.28 ±0.06	51.26 ±0.25	52.81 ±0.06	40.37 ±0.12	52.63 ±0.14	40.18 ±0.16	51.27 ±0.26
TiO_2	0.01 ±0.01	0.75 ±0.01	1.09 ±0.08	4.74 ±0.12	0.02 ±0.01	0.01 ±0.01	0.81 ±0.02	0.60 ±0.02	0.01 ±0.01	0.63 ±0.03	0.01 ±0.01	0.64 ±0.04
Al_2O_3	0.04 ±0.01	5.01 ±0.02	6.23 ±0.30	16.99 ±0.21	0.03 ±0.01	0.04 ±0.01	5.28 ±0.03	3.85 ±0.02	0.03 ±0.01	3.91 ±0.09	0.04 ±0.01	4.37 ±0.23
Cr_2O_3	0.04 ±0.01	1.29 ±0.03	0.13 ±0.02	0.09 ±0.04	0.04 ±0.01	0.03 ±0.01	1.47 ±0.03	1.09 ±0.02	0.03 ±0.02	1.13 ±0.03		1.18 ±0.11
Fe_2O_3												
FeO	11.15 ±0.07	3.76 ±0.07	4.55 ±0.12	6.75 ±0.05	11.69 ±0.12	11.21 ±0.12	3.90 ±0.06	3.97 ±0.11	11.67 ±0.13	3.95 ±0.03	11.25 ±0.26	3.64 ±0.12
MgO	48.61 ±0.11	16.23 ±0.09	15.65 ±0.23	20.63 ±0.19	48.20 ±0.20	48.61 ±0.12	15.71 ±0.18	17.06 ±0.10	48.35 ±0.21	16.83 ±0.04	47.93 ±0.16	16.38 ±0.22
MnO	0.17 ±0.01	0.09 ±0.01	0.10 ±0.01	0.03 ±0.02	0.16 ±0.01	0.17 ±0.01	0.08 ±0.02	0.09 ±0.02	0.16 ±0.02	0.10 ±0.03	0.12 ±0.01	0.05 ±0.03
NiO	0.25 ±0.05	0.03 ±0.03	0.01 ±0.02		0.20 ±0.04	0.20 ±0.01	0.02 ±0.02	0.05 ±0.01	0.20 ±0.04	0.03 ±0.03	0.23 ±0.03	
CaO	0.18 ±0.01	20.87 ±0.08	21.05 ±0.12	0.19 ±0.09	0.16 ±0.01	0.17 ±0.01	20.91 ±0.09	20.73 ±0.06	0.17 ±0.01	21.15 ±0.13	0.17 ±0.01	20.46 ±0.21
BaO				0.36 ±0.06								
Na_2O		0.93 ±0.03	0.95 ±0.03	0.49 ±0.02			0.96 ±0.02	0.83 ±0.03		0.86 ±0.02		0.88 ±0.02
K_2O		0.00 ±0.00	0.01 ±0.01	8.56 ±0.38			0.01 ±0.01	0.01 ±0.00		0.01 ±0.01		0.01 ±0.00
P_2O_5												
Cl				0.03 ±0.01								
F				0.00 ±0.00								
H_2O				4.27 ±0.04								
Total	100.88 ±0.16	100.74 ±0.15	101.01 ±0.20	101.56 ±1.10	100.50 ±0.35	100.71 ±0.20	100.41 ±0.50	101.09 ±0.27	101.01 ±0.31	101.23 ±0.23	99.94 ±0.35	98.89 ±0.34
Atomic formulae												
Si	0.990	1.874	1.852	5.392	0.986	0.988	1.865	1.903	0.989	1.897	0.993	1.888
Ti	0.000	0.020	0.029	0.500	0.000	0.000	0.022	0.017	0.000	0.017	0.000	0.018
Al	0.001	0.214	0.265	2.808	0.001	0.001	0.226	0.163	0.001	0.166	0.001	0.190
Cr	0.005	0.037	0.004	0.010	0.001	0.001	0.042	0.031	0.001	0.032		0.035
Fe^{3+}												
Fe^{2+}	0.228	0.114	0.138	0.792	0.241	0.230	0.119	0.120	0.239	0.119	0.233	0.112
Mg	1.774	0.876	0.844	4.313	1.771	1.778	0.852	0.916	1.766	0.905	1.766	0.899
Mn	0.004	0.003	0.003	0.004	0.003	0.003	0.002	0.003	0.003	0.003	0.003	0.002
Ni	0.005	0.001	0.000		0.004	0.004	0.001	0.002	0.004	0.001	0.005	
Ca	0.005	0.809	0.815	0.029	0.004	0.004	0.815	0.801	0.004	0.817	0.005	0.807
Ba				0.020								
Na		0.065	0.067	0.133			0.068	0.058		0.060		0.063
K		0.000	0.000	1.530			0.000	0.000		0.000		0.000
P												
Total	3.012	4.013	4.017	15.530	3.011	3.010	4.012	4.014	3.008	4.017	3.005	4.014
Ca (trace)	0.0045				0.0044	0.0042						
Cr/(Cr+Al)												
Mg/(Mg+Fe)	0.886	0.885	0.860	0.845	0.880	0.885	0.878	0.884	0.881	0.884	0.884	0.889
Fo	88.0				87.5	88.0			87.6		87.8	
Wo		43.4	43.7				43.9	42.2		42.9		42.9
En		46.9	45.2				45.9	48.3		47.5		47.7
Fs		6.2	7.5				6.5	6.5		6.4		6.1
Ac		3.5	3.6				3.7	3.1		3.2		3.3

Table C.VI. (continued).

sample	MXZH18						MXZH61					
	ol1	ol3	cpx1	cpx2-r	cpx2-c	sp	ol-a	ol-b	cpx1-c	cpx1-r	cpx2	sp
n	13	6	14	10	7	10	16	5	11	8	17	5
SiO_2	40.29±0.12	40.13±0.16	51.71±0.32	43.94±1.24	51.94±0.33	0.12±0.07	40.33±0.15	39.54±0.12	52.06±0.12	43.24±1.96	51.12±0.12	0.08±0.01
TiO_2	0.02±0.01	0.02±0.01	0.60±0.04	3.63±0.45	0.58±0.03	1.39±0.03	0.02±0.01	0.03±0.01	0.70±0.02	4.27±0.76	1.01±0.03	1.48±0.03
Al_2O_3	0.04±0.01	0.04±0.01	4.15±0.16	8.45±0.92	3.90±0.04	28.36±0.14	0.04±0.01	0.04±0.01	4.73±0.07	9.05±1.56	6.02±0.06	30.19±0.20
Cr_2O_3	0.07±0.04	0.04±0.02	1.29±0.06	0.05±0.04	1.20±0.02	34.38±0.20	0.03±0.01	0.01±0.01	1.40±0.02	0.04±0.02	0.66±0.12	33.11±0.28
Fe_2O_3						8.35±0.24						8.69±0.11
FeO	10.87±0.09	11.72±0.20	3.54±0.08	7.03±0.32	3.66±0.06	12.25±0.13	12.50±0.55	15.95±0.17	3.71±0.06	7.97±0.55	5.20±0.08	12.56±0.20
MgO	48.27±0.13	47.74±0.23	17.12±0.16	12.56±0.51	17.42±0.13	15.82±0.10	47.93±0.47	45.27±0.13	16.46±0.06	11.57±0.85	15.32±0.05	16.09±0.14
MnO	0.11±0.02	0.13±0.01	0.06±0.03	0.05±0.02	0.07±0.02	0.07±0.02	0.18±0.02	0.22±0.02	0.10±0.02	0.08±0.01	0.11±0.02	0.14±0.02
NiO	0.25±0.04	0.21±0.02				0.17±0.03	0.21±0.04	0.18±0.02	0.04±0.03	0.01±0.02	0.04±0.02	0.17±0.05
CaO	0.16±0.01	0.17±0.01	20.38±0.20	23.06±0.16	20.19±0.05	0.01±0.01	0.17±0.01	0.14±0.01	20.86±0.09	23.92±0.13	20.50±0.09	0.01±0.01
BaO												
Na_2O			0.84±0.03	0.33±0.02	0.84±0.03		0.01±0.01	0.01±0.01	0.91±0.02	0.35±0.04	1.07±0.02	
K_2O			0.01±0.01	0.00±0.00	0.00±0.00		0.00±0.00	0.00±0.00	0.01±0.01	0.01±0.01	0.00±0.01	
P_2O_5							0.01±0.01	0.02±0.02				
Cl												
F												
H_2O												
Total	100.07±0.20	100.19±0.22	99.70±0.36	99.11±0.28	99.81±0.47	100.90±0.36	101.41±0.26	101.41±0.28	100.97±0.17	100.51±0.15	101.05±0.18	102.51±0.16
Atomic formulae												
Si	0.993	0.992	1.888	1.668	1.893	0.028	0.988	0.985	1.879	1.632	1.853	0.019
Ti	0.000	0.000	0.017	0.104	0.016	0.245	0.000	0.001	0.019	0.121	0.027	0.254
Al	0.001	0.001	0.179	0.378	0.168	7.824	0.001	0.001	0.201	0.403	0.257	8.158
Cr	0.001	0.001	0.037	0.002	0.035	6.363	0.001	0.000	0.040	0.001	0.019	6.001
Fe^{3+}						1.471						1.500
Fe^{2+}	0.224	0.242	0.108	0.224	0.111	2.398	0.256	0.332	0.112	0.252	0.158	2.408
Mg	1.774	1.759	0.932	0.711	0.946	5.520	1.751	1.681	0.886	0.651	0.828	5.498
Mn	0.002	0.003	0.002	0.002	0.002	0.014	0.004	0.005	0.003	0.003	0.003	0.027
Ni	0.005	0.004				0.031	0.004	0.004	0.001	0.000	0.001	0.031
Ca	0.004	0.004	0.797	0.938	0.789	0.003	0.004	0.004	0.807	0.968	0.796	0.002
Ba												
Na			0.059	0.024	0.060				0.064	0.026	0.075	
K			0.000	0.000	0.000				0.000	0.000	0.000	
P												
Total	3.005	3.007	4.018	4.051	4.020	23.897	3.010	3.012	4.013	4.057	4.019	23.897
Ca (trace)	0.0039											
Cr/(Cr+Al)						0.449						0.424
Mg/(Mg+Fe)	0.888	0.879	0.896	0.761	0.895	0.697	0.872	0.835	0.888	0.721	0.840	0.695
Fo	88.3	87.4					86.7	83.0				
Wo			42.0	49.4	41.3				43.1	51.0	42.8	
En			49.1	37.4	49.6				47.3	34.3	44.5	
Fs			5.8	11.9	6.0				6.2	13.4	8.7	
Ac			3.1	1.3	3.1				3.4	1.3	4.1	

75

Table C.VI. (continued).

sample	MXZH64				
	ol-a	ol-b	sp	cpx-c	cpx-r
n	17	10	10	25	28
SiO_2	40.47 ± 0.13	39.78 ± 0.18	0.10 ± 0.01	52.29 ± 0.25	42.96 ± 0.73
TiO_2	0.02 ± 0.02	0.02 ± 0.01	1.39 ± 0.03	0.62 ± 0.03	4.03 ± 0.31
Al_2O_3	0.04 ± 0.01	0.04 ± 0.04	27.10 ± 0.26	4.46 ± 0.19	9.67 ± 0.56
Cr_2O_3	0.08 ± 0.06	0.02 ± 0.02	35.36 ± 0.34	1.38 ± 0.07	0.03 ± 0.03
Fe_2O_3			8.51 ± 0.32		
FeO	10.81 ± 0.18	13.17 ± 0.37	12.15 ± 0.29	3.46 ± 0.09	7.56 ± 0.36
MgO	48.42 ± 0.17	46.72 ± 0.38	15.58 ± 0.18	16.34 ± 0.14	11.36 ± 0.40
MnO	0.15 ± 0.03	0.16 ± 0.03	0.12 ± 0.03	0.11 ± 0.03	0.08 ± 0.04
NiO	0.25 ± 0.04	0.18 ± 0.03	0.18 ± 0.04		
CaO	0.16 ± 0.02	0.16 ± 0.01	0.02 ± 0.03	20.93 ± 0.15	23.73 ± 0.14
BaO					
Na_2O	0.03 ± 0.02	0.02 ± 0.02		0.92 ± 0.04	0.41 ± 0.02
K_2O	0.01 ± 0.01	0.01 ± 0.01		0.01 ± 0.01	0.00 ± 0.00
P_2O_5					
Cl					
F					
H_2O					
Total	100.43 ± 0.28	100.26 ± 0.30	100.51 ± 0.41	100.53 ± 0.32	99.83 ± 0.22
Atomic formulae					
Si	0.994	0.989	0.023	1.893	1.629
Ti	0.000	0.000	0.247	0.017	0.115
Al	0.001	0.001	7.543	0.190	0.432
Cr	0.001	0.000	6.604	0.040	0.001
Fe^{3+}			1.513		
Fe^{2+}	0.222	0.274	2.401	0.105	0.240
Mg	1.773	1.732	5.487	0.882	0.642
Mn	0.003	0.003	0.024	0.003	0.002
Ni	0.005	0.004	0.034		
Ca	0.004	0.004	0.005	0.812	0.964
Ba					
Na				0.065	0.030
K				0.000	0.000
P					
Total	3.004	3.009	23.880	4.007	4.055
Ca (trace)	0.0039				
Cr/(Cr+Al)			0.467		
Mg/(Mg+Fe)	0.889	0.863	0.696	0.894	0.728
Fo	88.3	85.9			
Wo				43.5	51.3
En				47.3	34.2
Fs				5.8	12.9
Ac				3.5	1.6

Table C.VII. Chemical composition and structural formulae of olivine megacrysts and associated minerals (c - core; r - rim).

sample	MXZH7	MXZH19			MXZH24					MXZH69	
	ol	ol	ol	cpx-in-gl	ol-a	ol-b	phl1	phl2	cpx-in-gl	ol	phl
n	6 r	10 c	20	6	9 r	10 c	3	5	10	9	5
SiO_2	39.34 ±0.24	39.02 ±0.19	39.16 ±0.09	37.13 ±0.48	39.96 ±0.15	39.11 ±0.17	38.23 ±0.14	38.61 ±0.06	37.95 ±0.41	39.97 ±0.15	38.54 ±0.24
TiO_2	0.02 ±0.01	0.02 ±0.01	0.02 ±0.01	6.59 ±0.14	0.02 ±0.01	0.03 ±0.01	4.70 ±0.03	4.64 ±0.05	6.50 ±0.16	0.03 ±0.01	5.09 ±0.07
Al_2O_3	0.03 ±0.01	0.04 ±0.01	0.03 ±0.01	12.57 ±0.17	0.03 ±0.01	0.04 ±0.01	17.14 ±0.03	17.12 ±0.09	11.86 ±0.28	0.04 ±0.01	17.13 ±0.08
Cr_2O_3	0.03 ±0.02	0.00 ±0.00		0.12 ±0.08	0.03 ±0.02	0.00 ±0.00	0.12 ±0.00	0.84 ±0.15	0.32 ±0.17	0.02 ±0.01	0.56 ±0.02
Fe_2O_3											
FeO	14.24 ±0.18	16.61 ±0.17	16.31 ±0.16	9.13 ±0.19	12.46 ±0.21	16.41 ±0.12	7.21 ±0.25	5.53 ±0.10	8.02 ±0.19	13.12 ±0.80	5.99 ±0.10
MgO	45.70 ±0.23	43.85 ±0.15	43.89 ±0.18	9.01 ±0.22	47.13 ±0.34	43.98 ±0.14	19.99 ±0.03	20.76 ±0.12	10.30 ±0.14	47.14 ±0.56	21.12 ±0.06
MnO	0.22 ±0.03	0.22 ±0.04	0.17 ±0.02	0.08 ±0.02	0.12 ±0.02	0.17 ±0.03	0.05 ±0.02	0.02 ±0.03	0.05 ±0.02	0.17 ±0.02	0.05 ±0.01
NiO	0.16 ±0.03	0.14 ±0.03	0.13 ±0.02		0.14 ±0.02	0.10 ±0.04	0.08 ±0.01	0.14 ±0.02		0.18 ±0.03	
CaO	0.25 ±0.06	0.14 ±0.01	0.14 ±0.01	22.54 ±0.12	0.19 ±0.01	0.16 ±0.01	0.05 ±0.02	0.03 ±0.01	23.05 ±0.14	0.16 ±0.01	0.01 ±0.00
BaO							0.25 ±0.02	0.27 ±0.05			0.30 ±0.04
Na_2O				0.45 ±0.02			0.72 ±0.02	0.45 ±0.02	0.34 ±0.02		0.48 ±0.02
K_2O				0.00 ±0.00			9.09 ±0.13	9.57 ±0.07	0.02 ±0.01		8.89 ±0.06
P_2O_5											
Cl							0.02 ±0.00	0.03 ±0.01			0.02 ±0.01
F							0.00 ±0.00	0.00 ±0.00			0.00 ±0.00
H_2O							4.26 ±0.01	4.30 ±0.01			4.32 ±0.01
Total	100.00 ±0.33	100.03 ±0.38	99.85 ±0.31	97.62 ±0.33	100.07 ±0.28	100.01 ±0.23	101.89 ±0.33	102.28 ±0.21	98.42 ±0.33	100.87 ±0.19	102.49 ±0.32
Atomic formulae											
Si	0.987	0.989	0.992	1.463	0.992	0.990	5.372	5.382	1.477	0.988	5.350
Ti	0.000	0.000	0.000	0.195	0.000	0.000	0.496	0.486	0.190	0.001	0.531
Al	0.001	0.001	0.001	0.584	0.001	0.001	2.839	2.813	0.544	0.001	2.802
Cr	0.001	0.000	0.000	0.004	0.001	0.000	0.013	0.092	0.010	0.000	0.061
Fe^{3+}											
Fe^{2+}	0.299	0.352	0.346	0.301	0.259	0.347	0.847	0.644	0.261	0.271	0.695
Mg	1.709	1.656	1.658	0.529	1.744	1.660	4.189	4.313	0.597	1.737	4.371
Mn	0.005	0.005	0.004	0.003	0.003	0.004	0.006	0.003	0.002	0.004	0.005
Ni	0.003	0.003	0.003		0.003	0.002	0.009	0.016		0.004	
Ca	0.007	0.004	0.004	0.952	0.005	0.004	0.007	0.004	0.961	0.004	0.002
Ba							0.014	0.015			0.016
Na				0.035			0.195	0.120	0.025		0.129
K				0.000			1.630	1.701	0.001		1.575
P											
Total	3.011	3.009	3.011	4.065	3.007	3.009	15.618	15.590	4.069	3.010	15.539
Ca (trace)											
Cr/(Cr+Al)											
Mg/(Mg+Fe)	0.851	0.825	0.827	0.638	0.871	0.827	0.832	0.870	0.696	0.865	0.863
Fo	84.5	82.0	82.3		86.6	82.3				86.0	
Wo				52.3					52.1		
En				29.1					32.3		
Fs				16.7					14.2		
Ac				1.9					1.4		

Table C.VIII. Chemical composition and structural formulae of clinopyroxene megacrysts and associated minerals (HK - analyses by H. Kämpf; c - core; r - rim; s - sector).

sample	MXZH14		MXZH9	MXZH62				EB2				
	cpx-r	cpx-c	cpx-r	cpx-c	cpx-c	cpx-r1	cpx-r2	cpx-old	cpx-r	cpx-s1	cpx-s2	ol
n	5 (HK)	15 (HK)	3	8	2	6	2	2	7	17	20	22
SiO$_2$	46.74±2.30	50.49±0.45	46.76±2.95	51.29±0.15	50.25±0.05	50.76±0.18	42.29±0.33	52.40±0.05	43.52±0.92	50.73±0.18	49.78±0.24	39.24±0.22
TiO$_2$	2.90±0.87	1.03±0.06	2.70±1.08	0.93±0.02	1.27±0.01	1.16±0.02	4.39±0.03	0.66±0.04	3.57±0.29	0.86±0.03	1.05±0.03	0.02±0.01
Al$_2$O$_3$	6.69±1.89	5.95±0.19	6.60±2.26	5.49±0.07	6.58±0.05	6.08±0.03	10.00±0.08	4.36±0.07	8.00±0.95	5.05±0.07	6.18±0.07	0.04±0.02
Cr$_2$O$_3$	0.21±0.11	0.11±0.02	0.20±0.15	0.40±0.01	0.05±0.02	0.07±0.01	0.01±0.00	0.88±0.15	0.02±0.01	0.29±0.02	0.34±0.03	
Fe$_2$O$_3$												
FeO	6.09±0.66	5.63±0.11	6.25±1.24	5.27±0.07	5.91±0.07	5.81±0.10	8.04±0.00	3.50±0.02	7.53±0.24	5.17±0.05	5.31±0.07	14.85±0.50
MgO	13.54±1.18	15.29±0.13	13.36±1.44	15.53±0.09	14.44±0.01	14.83±0.13	11.29±0.16	16.46±0.10	12.03±0.45	15.63±0.07	14.96±0.08	44.85±0.40
MnO	0.07±0.02	0.11±0.04	0.06±0.04	0.14±0.02	0.12±0.01	0.13±0.02	0.09±0.00	0.10±0.00	0.06±0.02	0.09±0.02	0.09±0.02	0.14±0.02
NiO	0.01±0.01	0.02±0.02										0.18±0.03
CaO	23.60±0.12	20.41±0.20	23.68±0.14	20.18±0.08	20.46±0.02	20.57±0.11	23.33±0.04	21.42±0.03	23.31±0.16	20.11±0.08	20.24±0.10	0.14±0.01
BaO												
Na$_2$O	0.37±0.03	1.02±0.03	0.37±0.04	1.02±0.03	1.17±0.00	1.09±0.02	0.42±0.00	0.84±0.02	0.35±0.35	0.93±0.02	1.02±0.04	
K$_2$O	0.00±0.00	0.00±0.00	0.00±0.00	0.00±0.00	0.01±0.01	0.01±0.01	0.00±0.00	0.00±0.00	0.01±0.01	0.01±0.01	0.00±0.00	
P$_2$O$_5$												
Cl												
F												
H$_2$O												
Total	100.21±0.20	100.06±0.51	99.99±0.17	100.25±0.16	100.24±0.08	100.49±0.43	99.85±0.55	100.62±0.13	98.39±0.35	98.86±0.24	98.97±0.27	99.46±0.23
Atomic formulae												
Si	1.740	1.851	1.748	1.871	1.842	1.855	1.607	1.896	1.672	1.877	1.844	0.991
Ti	0.080	0.030	0.076	0.026	0.035	0.032	0.125	0.018	0.103	0.024	0.029	0.000
Al	0.296	0.257	0.292	0.236	0.284	0.262	0.448	0.186	0.362	0.220	0.270	0.001
Cr			0.006	0.012	0.002	0.002	0.000	0.025	0.000	0.008	0.010	
Fe^{3+}												
Fe^{2+}	0.188	0.171	0.196	0.161	0.181	0.177	0.256	0.106	0.242	0.160	0.165	0.314
Mg	0.752	0.832	0.744	0.845	0.789	0.807	0.640	0.888	0.689	0.862	0.826	1.690
Mn			0.002	0.004	0.004	0.004	0.003	0.003	0.002	0.003	0.003	0.003
Ni												0.004
Ca	0.942	0.802	0.949	0.789	0.804	0.805	0.950	0.831	0.960	0.797	0.803	0.004
Ba												
Na	0.028	0.072	0.027	0.072	0.083	0.077	0.031	0.059	0.026	0.067	0.073	
K			0.000	0.000	0.001	0.000	0.000	0.000	0.000	0.000	0.000	
P												
Total	4.026	4.015	4.039	4.015	4.023	4.021	4.059	4.011	4.057	4.018	4.023	3.007
Ca (trace)												
Cr/(Cr+Al)												
Mg/(Mg+Fe)	0.800	0.829	0.792	0.840	0.813	0.820	0.715	0.893	0.740	0.843	0.834	0.843
Fo												83.9
Wo	49.3	42.7	49.5	42.2	43.2	43.0	50.6	44.0	50.0	42.2	43.0	0.2
En	39.4	44.3	38.8	45.2	42.4	43.2	34.0	47.1	35.9	45.6	44.2	84.1
Fs	9.8	9.1	10.3	8.8	9.9	9.7	13.8	5.8	12.7	8.6	8.9	15.8
Ac	1.5	3.8	1.4	3.9	4.5	4.1	1.6	3.1	1.3	3.5	3.9	0.0

78

Table C.VIII. (continued).

sample	EB6		EB7	
	cpx-r	cpx-c	cpx-r	cpx-c
n	5	25	12	13
SiO_2	39.39 ± 0.25	51.59 ± 0.25	45.62 ± 0.90	50.32 ± 0.31
TiO_2	5.93 ± 0.11	0.86 ± 0.03	3.04 ± 0.31	1.05 ± 0.04
Al_2O_3	11.65 ± 0.58	4.82 ± 0.12	6.64 ± 0.87	5.99 ± 0.10
Cr_2O_3	0.01 ± 0.02	0.29 ± 0.02	0.06 ± 0.10	0.28 ± 0.03
Fe_2O_3				
FeO	8.77 ± 0.07	4.17 ± 0.09	6.83 ± 0.49	5.34 ± 0.12
MgO	10.12 ± 0.25	16.23 ± 0.11	12.91 ± 0.54	15.03 ± 0.10
MnO	0.10 ± 0.02	0.09 ± 0.03	0.10 ± 0.02	0.11 ± 0.03
NiO				
CaO	23.38 ± 0.26	21.40 ± 0.10	23.67 ± 0.11	20.23 ± 0.09
BaO				
Na_2O	0.42 ± 0.02	0.82 ± 0.02	0.37 ± 0.03	1.15 ± 0.03
K_2O	0.01 ± 0.00	0.01 ± 0.01	0.00 ± 0.00	0.01 ± 0.01
P_2O_5				
Cl				
F				
H_2O				
Total	99.78 ± 0.27	100.27 ± 0.24	99.23 ± 0.35	99.51 ± 0.33
Atomic formulae				
Si	1.512	1.878	1.728	1.854
Ti	0.171	0.023	0.087	0.029
Al	0.527	0.207	0.297	0.260
Cr	0.000	0.008	0.002	0.008
Fe^{3+}				
Fe^{2+}	0.281	0.127	0.216	0.164
Mg	0.579	0.881	0.729	0.826
Mn	0.003	0.003	0.003	0.004
Ni				
Ca	0.962	0.835	0.961	0.798
Ba				
Na	0.031	0.058	0.027	0.082
K	0.000	0.000	0.000	0.000
P				
Total	4.068	4.020	4.050	4.025
Ca (trace)				
Cr/(Cr+Al)				
Mg/(Mg+Fe)	0.673	0.874	0.771	0.834
Fo				
Wo	51.8	43.9	49.6	42.6
En	31.2	46.3	37.6	44.1
Fs	15.3	6.8	11.3	9.0
Ac	1.7	3.0	1.4	4.4

Table C.IX. Chemical composition and structural formulae of amphibole and mica megacrysts (HK - analyses by H. Kämpf).

sample	EB1 incl. in olivine	MXZH15 rim	core_sulphides	core	MXZH1a	MXZH9	MXZH10 core	rim	MXZH32	near vug	MXZH35	MXZH42
n	41	20	10	10	5	5	6	5	10	2	10	10
SiO_2	41.92 ±0.11	40.52 ±0.36	41.12 ±0.18	41.47 ±0.09	42.05 ±0.02	41.82 ±0.23	41.60 ±0.16	41.74 ±0.08	41.47 ±0.49	41.29 ±0.06	41.66 ±0.33	41.75 ±0.32
TiO_2	3.28 ±0.05	3.26 ±0.05	3.31 ±0.05	3.30 ±0.07	3.49 ±0.06	3.39 ±0.07	3.24 ±0.06	3.26 ±0.05	3.42 ±0.05	3.36 ±0.01	3.27 ±0.03	3.42 ±0.11
Al_2O_3	14.57 ±0.06	14.67 ±0.06	14.62 ±0.08	14.56 ±0.07	13.89 ±0.07	14.32 ±0.07	14.78 ±0.07	14.62 ±0.05	13.80 ±0.09	14.36 ±0.07	14.73 ±0.07	14.22 ±0.24
Cr_2O_3	0.22 ±0.02	0.26 ±0.02	0.11 ±0.02	0.11 ±0.03	0.05 ±0.01	0.06 ±0.02	0.24 ±0.02	0.18 ±0.02	0.01 ±0.01	0.02 ±0.02	0.22 ±0.01	0.06 ±0.02
Fe_2O_3												
FeO	7.37 ±0.10	7.17 ±0.14	7.35 ±0.13	7.62 ±0.12	8.86 ±0.18	7.98 ±0.06	7.38 ±0.13	7.41 ±0.20	8.15 ±0.17	6.74 ±0.14	7.41 ±0.12	7.84 ±0.19
MgO	15.32 ±0.08	15.64 ±0.07	15.65 ±0.05	15.51 ±0.05	14.80 ±0.09	15.20 ±0.07	15.46 ±0.06	15.45 ±0.10	15.40 ±0.10	16.45 ±0.02	15.64 ±0.09	15.37 ±0.13
MnO	0.07 ±0.03	0.08 ±0.04	0.08 ±0.04	0.07 ±0.03	0.08 ±0.03	0.08 ±0.03	0.10 ±0.03	0.09 ±0.03	0.09 ±0.03	0.07 ±0.02	0.07 ±0.03	0.08 ±0.03
NiO	0.04 0.02				0.02 0.02							
CaO	11.53 ±0.06	11.44 ±0.07	11.51 ±0.06	11.46 ±0.12	11.75 ±0.09	11.52 ±0.06	11.59 ±0.09	11.55 ±0.11	11.77 ±0.10	11.71 ±0.07	11.63 ±0.06	11.66 ±0.06
BaO												
Na_2O	2.18 ±0.06	2.24 ±0.03	2.28 ±0.03	2.28 ±0.02	2.43 ±0.04	2.32 ±0.02	2.25 ±0.03	2.25 ±0.03	2.44 ±0.04	2.27 ±0.06	2.29 ±0.03	2.38 ±0.05
K_2O	2.08 ±0.02	2.28 ±0.04	2.22 ±0.04	2.22 ±0.05	1.90 ±0.04	2.18 ±0.02	2.28 ±0.02	2.25 ±0.02	2.07 ±0.04	2.09 ±0.02	2.25 ±0.02	2.19 ±0.09
P_2O_5												
Cl	0.02 ±0.01	0.02 ±0.01	0.02 ±0.01	0.02 ±0.01	0.02 ±0.00	0.02 ±0.01	0.02 ±0.01	0.01 ±0.00	0.01 ±0.01	0.01 ±0.00	0.02 ±0.01	0.02 ±0.01
F	0.00 ±0.00	0.06 ±0.02	0.05 ±0.02	0.04 ±0.02	0.00 ±0.00	0.00 ±0.00	0.04 ±0.04	0.05 ±0.03	0.03 ±0.03	0.09 ±0.03	0.06 ±0.03	0.05 ±0.02
Total	98.61 ±0.23	97.60 ±0.37	98.30 ±0.29	98.63 ±0.21	99.34 ±0.07	98.89 ±0.26	98.95 ±0.17	98.84 ±0.30	98.65 ±0.52	98.41 ±0.05	99.22 ±0.40	99.02 ±0.44

Atomic formulae on the basis of 23 oxygens

	EB1	MXZH15 rim	core_sulphides	core	MXZH1a	MXZH9	MXZH10 core	rim	MXZH32	near vug	MXZH35	MXZH42
Si	6.037	5.916	5.956	5.988	6.056	6.029	5.983	6.006	6.010	5.955	5.976	6.013
Ti	0.356	0.358	0.361	0.358	0.378	0.368	0.351	0.353	0.373	0.364	0.353	0.370
Al	2.473	2.524	2.495	2.477	2.358	2.433	2.506	2.480	2.358	2.441	2.490	2.414
Cr	0.025	0.030	0.013	0.013	0.006	0.007	0.027	0.020	0.002	0.002	0.025	0.007
Fe^{3+}												
Fe^{2+}	0.888	0.876	0.891	0.920	1.067	0.962	0.887	0.892	0.988	0.814	0.889	0.945
Mg	3.288	3.404	3.379	3.338	3.177	3.267	3.314	3.315	3.327	3.537	3.345	3.300
Mn	0.009	0.010	0.010	0.009	0.010	0.010	0.012	0.011	0.011	0.009	0.008	0.010
Ni	0.005				0.002							
Ca	1.780	1.790	1.787	1.772	1.813	1.779	1.786	1.781	1.827	1.809	1.788	1.800
Ba												
Na	0.609	0.634	0.641	0.639	0.680	0.648	0.627	0.627	0.687	0.634	0.636	0.665
K	0.381	0.425	0.410	0.410	0.350	0.400	0.418	0.412	0.383	0.385	0.412	0.402
P												
Total	15.850	15.965	15.942	15.923	15.896	15.904	15.910	15.897	15.964	15.948	15.923	15.925
Cr/(Cr+Al)	0.010	0.012	0.005	0.005	0.002	0.003	0.011	0.008	0.001	0.001	0.010	0.003
Mg/(Mg+Fe)	0.787	0.795	0.791	0.784	0.749	0.773	0.789	0.788	0.771	0.813	0.790	0.777
p - S92 [kbar]	8.8	9.0	8.9	8.8	8.2	8.6	8.9	8.8	8.2	8.6	8.8	8.5
p - Ho87 [kbar]	9.2	9.5	9.3	9.2	8.5	9.0	9.4	9.2	8.5	9.0	9.3	8.9
p - HZ86 [kbar]	8.5	8.8	8.6	8.5	7.9	8.3	8.7	8.6	7.9	8.4	8.6	8.2
p - JR89 [kbar]	7.0	7.2	7.1	7.0	6.5	6.8	7.1	7.0	6.5	6.9	7.1	6.8

S92 - *Schmidt, 1992*; Ho87 - *Hollister et al., 1987*; HZ86 - *Hammarstrom and Zen, 1986*; JR89 - *Johnson and Rutherford, 1989*.

Table C.IX. (continued).

sample	MXZH39		MXZH21	
	core	rim	phl	
n	20	10	11	11 (HK)
SiO$_2$	41.54 ± 0.21	41.55 ± 0.13	37.74 ± 0.32	37.30 ± 0.39
TiO$_2$	3.32 ± 0.03	3.28 ± 0.03	4.25 ± 0.06	4.23 ± 0.05
Al$_2$O$_3$	14.51 ± 0.06	14.53 ± 0.08	16.93 ± 0.25	16.72 ± 0.18
Cr$_2$O$_3$	0.30 ± 0.02	0.22 ± 0.02	0.03 ± 0.02	
Fe$_2$O$_3$				
FeO	7.22 ± 0.15	7.19 ± 0.14	7.54 ± 0.14	7.39 ± 0.19
MgO	15.48 ± 0.08	15.51 ± 0.08	19.12 ± 0.24	19.31 ± 0.17
MnO	0.08 ± 0.03	0.09 ± 0.02		0.05 ± 0.02
NiO				
CaO	11.52 ± 0.10	11.51 ± 0.05	0.14 ± 0.12	0.03 ± 0.03
BaO			0.13 ± 0.02	*0.33 ± 0.09*
Na$_2$O	2.28 ± 0.03	2.26 ± 0.02	0.67 ± 0.05	0.67 ± 0.03
K$_2$O	2.19 ± 0.05	2.20 ± 0.03	8.59 ± 0.54	8.98 ± 0.14
P$_2$O$_5$			0.00 ± 0.00	0.02 ± 0.02
Cl	0.02 ± 0.01	0.02 ± 0.01	0.02 ± 0.01	0.02 ± 0.01
F	0.05 ± 0.02	0.06 ± 0.04	0.00 ± 0.00	0.00 ± 0.00
Total	98.48 ± 0.29	98.40 ± 0.18	95.17 ± 0.54	95.05 ± 0.82
Atomic formulae on the basis of 23 oxygens				
Si	5.997	6.001		
Ti	0.360	0.357		
Al	2.470	2.473		
Cr	0.035	0.026		
Fe^{3+}				
Fe^{2+}	0.872	0.868		
Mg	3.331	3.340		
Mn	0.010	0.011		
Ni				
Ca	1.783	1.782		
Ba				
Na	0.639	0.633		
K	0.403	0.406		
P				
Total	15.898	15.896		
Cr/(Cr+Al)	0.014	0.010		
Mg/(Mg+Fe)	0.793	0.794	0.819	0.823
p - S92 [kbar]	8.7	8.8		
p - Ho87 [kbar]	9.2	9.2		
p - HZ86 [kbar]	8.5	8.5		
p - JR89 [kbar]	7.0	7.0		

Table C.X. Chemical composition and structural formulae of groundmass (gm) minerals (c- core; r - rim).

sample	MXZH2 ol-gm 1 r	MXZH2 ol-gm 4 c	MXZH18 ol-gm 7	MXZH9 ol-gm 8	MXZH8 ol-gm1 9 c	MXZH8 ol-gm1 6 r	EB2 ol-gm2 8	EB2 ol-gm 4	MXZH64 ol-gm 3	MXZH69 ol-gm 3 c	MXZH17 ol-gm 2 r	MXZH17 ol-gm 1	sp(ol) 1
SiO_2	39.81	40.50 ±0.06	40.52 ±0.11	40.50 ±0.14	39.94 ±0.41	39.48 ±0.22	39.06 ±0.20	39.61 ±0.10	39.30 ±0.18	40.18 ±0.09	39.42 ±0.03	40.44	0.11
TiO_2	0.04	0.01 ±0.00	0.02 ±0.01	0.01 ±0.01	0.02 ±0.01	0.04 ±0.02	0.03 ±0.02	0.02 ±0.01	0.03 ±0.01	0.02 ±0.01	0.03 ±0.01	0.01	1.40
Al_2O_3	0.04	0.04 ±0.00	0.04 ±0.01	0.04 ±0.01	0.04 ±0.02	0.03 ±0.01	0.20 ±0.27	0.03 ±0.01	0.02 ±0.01	0.04 ±0.01	0.02 ±0.00	0.03	29.17
Cr_2O_3	0.04	0.04 ±0.01	0.06 ±0.03	0.08 ±0.02					0.03 ±0.02	0.04 ±0.01	0.02 ±0.01	0.06	33.66
Fe_2O_3													9.02
FeO	14.32	10.91 ±0.11	10.04 ±0.34	10.05 ±0.09	10.39 ±0.56	12.87 ±0.40	13.60 ±0.24	13.54 ±0.19	13.25 ±0.39	11.11 ±0.08	13.98 ±0.02	11.24	11.84
MgO	46.46	48.78 ±0.07	48.76 ±0.07	48.95 ±0.05	48.34 ±0.64	46.29 ±0.36	45.38 ±0.41	45.69 ±0.22	45.34 ±0.24	48.70 ±0.08	46.01 ±0.10	48.43	16.28
MnO	0.27	0.16 ±0.02	0.11 ±0.02	0.16 ±0.03	0.11 ±0.02	0.16 ±0.03	0.14 ±0.02	0.16 ±0.01	0.31 ±0.15	0.15 ±0.01	0.27 ±0.01	0.20	0.09
NiO	0.04	0.24 ±0.02	0.32 ±0.05	0.37 ±0.03	0.31 ±0.04	0.14 ±0.05	0.15 ±0.03	0.13 ±0.03	0.14 ±0.11	0.24 ±0.02	0.09 ±0.01	0.24	0.22
CaO	0.35	0.18 ±0.01	0.17 ±0.04	0.14 ±0.01	0.19 ±0.02	0.31 ±0.12	0.22 ±0.03	0.24 ±0.03	0.43 ±0.11	0.18 ±0.01	0.35 ±0.00	0.17	0.01
BaO													
Na_2O													
K_2O													
P_2O_5													
Cl													
F													
H_2O													
Total	101.37	100.85 ±0.11	100.04 ±0.25	100.29 ±0.20	99.33 ±0.77	99.32 ±0.40	98.77 ±0.35	99.42 ±0.35	98.89 ±0.55	100.66 ±0.20	100.20 ±0.09	100.83	101.79
Atomic formulae													
Si	0.985	0.990	0.995	0.993	0.991	0.990	0.989	0.995	0.993	0.986	0.986	0.991	0.026
Ti	0.001	0.000	0.000	0.000	0.000	0.001	0.001	0.000	0.001	0.000	0.001	0.000	0.244
Al	0.001	0.001	0.001	0.001	0.001	0.001	0.006	0.001	0.001	0.001	0.001	0.001	7.944
Cr	0.001	0.001	0.001	0.001						0.001		0.001	6.149
Fe^{3+}													1.568
Fe^{2+}	0.296	0.223	0.206	0.206	0.216	0.270	0.288	0.284	0.280	0.228	0.292	0.231	2.287
Mg	1.713	1.778	1.786	1.789	1.787	1.731	1.713	1.711	1.709	1.782	1.715	1.770	5.608
Mn	0.006	0.003	0.002	0.003	0.002	0.003	0.003	0.003	0.007	0.003	0.006	0.004	0.017
Ni	0.001	0.005	0.006	0.007	0.006	0.003	0.003	0.003	0.003	0.005	0.002	0.005	0.040
Ca	0.009	0.005	0.004	0.004	0.005	0.008	0.006	0.007	0.012	0.005	0.010	0.005	0.003
Ba													
Na													
K													
P													
Total	3.012	3.007	3.003	3.005	3.008	3.008	3.008	3.004	3.005	3.011	3.012	3.007	23.886
Ca (trace)													
Cr/(Cr+Al)													0.436
Mg/(Mg+Fe)	0.853	0.889	0.896	0.897	0.892	0.865	0.856	0.857	0.859	0.887	0.854	0.885	0.710
Fo	84.6	88.3	89.1	89.0	88.6	85.9	85.1	85.2	85.0	88.1	84.7	87.9	
Wo													
En													
Fs													
Ac													

Table C.X. (continued).

sample	MXZH8		MXZH24		MXZH69	EB1	EB5	MXZH64	MXZH17	MXZH69
	cpx-gm	cpx-gm	cpx-gm	cpx-gm	cpx-gm	cpx-gm	cpx-gm	mag-gm	sp-gm	sp-gm
n	9 c	4 r	11 c	4 r	1	6	4	1	1	2
SiO_2	45.59 ± 0.42	39.14 ± 1.48	49.57 ± 0.44	44.86 ± 2.57	39.82	38.30 ± 0.83	41.75 ± 0.78	3.32	0.10	0.09 ± 0.00
TiO_2	2.88 ± 0.07	5.69 ± 0.68	1.05 ± 0.04	3.08 ± 0.74	5.58	6.18 ± 0.32	4.83 ± 0.54	10.99	1.16	1.42 ± 0.02
Al_2O_3	6.29 ± 0.25	11.28 ± 1.24	6.07 ± 0.05	7.23 ± 1.87	11.66	11.97 ± 0.48	9.66 ± 0.57	6.48	25.24	30.28 ± 0.12
Cr_2O_3	0.03 ± 0.02	0.16 ± 0.16	0.05 ± 0.02	0.08 ± 0.11	0.01	0.00 ± 0.01	0.23 ± 0.14	0.13	40.82	33.05 ± 0.21
Fe_2O_3								48.33	7.16	8.43 ± 0.14
FeO	7.11 ± 0.14	8.21 ± 0.44	5.57 ± 0.06	6.83 ± 1.02	8.68	8.75 ± 0.38	7.72 ± 0.55	21.89	11.85	12.40 ± 0.13
MgO	12.99 ± 0.15	10.38 ± 0.68	15.21 ± 0.11	13.08 ± 1.18	10.33	9.75 ± 0.26	11.31 ± 0.37	4.61	16.04	16.12 ± 0.09
MnO	0.08 ± 0.02	0.06 ± 0.01	0.08 ± 0.02	0.05 ± 0.02	0.09	0.07 ± 0.02	0.06 ± 0.02	1.18	0.14	0.10 ± 0.02
NiO					0.02			0.12	0.28	0.23 ± 0.02
CaO	23.16 ± 0.14	22.95 ± 0.21	20.28 ± 0.09	23.47 ± 0.13	23.45	22.91 ± 0.08	23.51 ± 0.11	1.40	0.00	0.00 ± 0.00
BaO										
Na_2O	0.35 ± 0.02	0.40 ± 0.02	1.07 ± 0.03	0.35 ± 0.04	0.36	0.40 ± 0.01	0.41 ± 0.01			
K_2O	0.01 ± 0.01	0.00 ± 0.00	0.01 ± 0.01	0.00 ± 0.00	0.04	0.01 ± 0.01	0.01 ± 0.01			
P_2O_5										
Cl										
F										
H_2O										
Total	98.48 ± 0.23	98.27 ± 0.67	98.96 ± 0.47	99.03 ± 0.35	100.02	98.36 ± 0.32	99.49 ± 0.38	98.45	102.78	102.11 ± 0.22
Atomic formulae										
Si	1.740	1.522	1.839	1.703	1.523	1.493	1.595	0.904	0.024	0.022
Ti	0.083	0.167	0.029	0.088	0.160	0.181	0.139	2.253	0.203	0.245
Al	0.283	0.517	0.265	0.325	0.526	0.550	0.435	2.083	6.936	8.204
Cr	0.001	0.005	0.002	0.002	0.000	0.000	0.007	0.027	7.525	6.005
Fe^{3+}								9.913	1.256	1.458
Fe^{2+}	0.227	0.267	0.173	0.217	0.278	0.285	0.247	4.989	2.310	2.383
Mg	0.739	0.602	0.841	0.740	0.589	0.567	0.644	1.872	5.575	5.523
Mn	0.002	0.002	0.003	0.002	0.003	0.003	0.002	0.273	0.028	0.019
Ni					0.000			0.026	0.053	0.042
Ca	0.947	0.956	0.806	0.955	0.961	0.957	0.962	0.410	0.000	0.001
Ba										
Na	0.026	0.030	0.077	0.026	0.027	0.030	0.030			
K	0.000	0.000	0.000	0.000	0.002	0.000	0.001			
P										
Total	4.048	4.067	4.036	4.058		4.066	4.061	22.750	23.910	23.900
Ca (trace)										
Cr/(Cr+Al)								0.013	0.520	0.423
Mg/(Mg+Fe)	0.765	0.693	0.830	0.773	0.679	0.665	0.723	0.273	0.707	0.699
Fo										
Wo	48.8	51.5	42.4	49.3	51.7	52.0	51.0			
En	38.1	32.4	44.3	38.2	31.7	30.8	34.2			
Fs	11.8	14.5	9.2	11.3	15.1	15.6	13.2			
Ac	1.3	1.6	4.1	1.3	1.5	1.6	1.6			

Table C.XI. Chemical composition of glass (gl) and groundmass (gm) in xenoliths.

sample	MXZH8			MXZH18		MXZH61		MXZH62	MXZH24		MXZH69	EB1
	glass1	glass2	gm3	glass1	glass2	glass	glass	glass1	glass1	glass2	glass	glass rim
n	10	7	9	15	5	9	1	1	6	10	6	15
SiO_2	39.40 ± 0.63	41.09 ± 1.38	40.53	40.28 ± 0.10	39.98 ± 0.68	40.97 ± 0.23	38.04	48.03	41.43 ± 0.45	40.99 ± 0.25	42.42 ± 0.69	41.71 ± 0.88
TiO_2	3.49 ± 0.17	4.23 ± 0.47	2.38	3.28 ± 0.06	3.22 ± 0.08	3.29 ± 0.09	0.11	0.83	3.63 ± 0.07	3.65 ± 0.08	3.39 ± 0.23	3.19 ± 0.25
Al_2O_3	14.20 ± 0.16	11.67 ± 0.47	13.87	13.26 ± 0.08	14.98 ± 0.23	15.43 ± 0.23	34.45	21.98	15.29 ± 0.27	15.24 ± 0.10	16.34 ± 0.34	16.52 ± 0.35
Cr_2O_3	0.01 0.01	0.01 ± 0.01	0.00			0.01 ± 0.01	0.03	0.00	0.00 0.01	0.01 0.01	0.03 ± 0.02	0.01 0.01
Fe_2O_3												
FeO	10.65 ± 0.85	13.55 ± 1.32	9.79	10.26 ± 0.14	10.36 ± 0.28	10.85 ± 0.54	0.85	8.22	9.68 ± 0.29	9.93 ± 0.21	9.10 ± 0.40	10.17 ± 1.08
MgO	0.74 ± 0.06	1.05 ± 0.15	0.56	5.08 ± 0.09	4.08 ± 0.18	4.95 ± 0.41	0.38	3.33	5.74 ± 0.08	5.81 ± 0.09	4.54 ± 0.38	0.79 ± 0.09
MnO	0.16 ± 0.02	0.19 ± 0.02	0.18	0.15 ± 0.03	0.17 ± 0.02	0.23 ± 0.02	0.02	0.27	0.19 ± 0.02	0.19 ± 0.03	0.21 ± 0.03	0.17 ± 0.02
NiO						0.01 ± 0.01	0.02	0.00	0.02 0.01	0.00 0.00	0.02 0.02	
CaO	15.99 ± 0.47	14.85 ± 0.73	16.57	17.42 ± 0.15	14.10 ± 0.78	15.03 ± 0.23	6.06	4.37	15.30 ± 0.39	16.01 ± 0.14	13.86 ± 0.53	13.40 ± 1.19
BaO	0.05 ± 0.02	0.01 ± 0.02	0.64	0.09 ± 0.02	0.12 ± 0.04	0.17 ± 0.02	0.04	0.16	0.20 ± 0.02	0.18 ± 0.03	0.16 0.06	0.02 ± 0.04
Na_2O	3.65 ± 0.15	0.49 ± 0.05	6.83	2.97 ± 0.07	2.57 ± 0.46	3.95 ± 0.07	6.18	5.92	3.61 ± 0.06	3.79 ± 0.03	4.07 ± 1.40	6.20 ± 0.87
K_2O	3.74 ± 0.22	0.28 ± 0.10	1.85	4.70 ± 0.14	6.24 ± 0.67	4.60 ± 0.09	4.03	4.33	3.70 ± 0.11	3.68 ± 0.04	4.71 ± 1.46	2.12 ± 0.50
P_2O_5	1.15 ± 0.06	1.27 ± 0.12	1.31	0.98 ± 0.06	1.16 ± 0.06	1.34 ± 0.06	0.55	0.73	0.96 ± 0.06	1.00 ± 0.06	1.01 0.09	1.51 ± 0.06
Cl	0.12 ± 0.01	0.01 ± 0.01	0.05	0.27 ± 0.01	0.35 ± 0.02	0.36 ± 0.01	1.67	0.50	0.28 ± 0.01	0.27 ± 0.01	0.30 0.04	0.06 ± 0.04
F	0.01 ± 0.01	0.00 ± 0.00	0.00	0.00 ± 0.01	0.24 ± 0.14	0.01 ± 0.02	0.00	0.07	0.03 ± 0.02	0.00 ± 0.01	0.02 0.05	0.00 ± 0.00
SrO	0.00 ± 0.00	0.00 ± 0.00	0.45									0.06 ± 0.04
S	0.06 0.02	0.02 ± 0.01	0.13									
Total	93.39 ± 0.36	88.71 ± 0.71	95.11	98.68 ± 0.25	97.39 ± 1.60	101.09 ± 0.38	92.04	98.58	99.98 ± 0.20	100.71 ± 0.40	100.13 ± 1.08	95.93 ± 0.80

Atomic formulae

Si, Ti, Al, Cr, Fe3+, Fe2+, Mg, Mn, Ni, Ca, Ba, Na, K, P, Total

	MXZH8			MXZH18		MXZH61		MXZH62	MXZH24		MXZH69	EB1
Ca (trace)												
Cr/(Cr+Al)												
Mg/(Mg+Fe)	0.110	0.121	0.093	0.469	0.413	0.449	0.442	0.419	0.514	0.511	0.471	0.122
Fo												
Wo												
En												
Fs												
Ac												

Table C.XII. Chemical composition and structural formulae of olivine crystals from Železná Hůrka.

sample	EB5-olivines					EB1	
	ol9-core	ol9-rim	sp-in-ol9	ol4-core	ol4-rim	ol-core	ol-rim
n	38	1	3	8	5	36	11
SiO_2	40.43 ± 0.14	39.75	0.10 ± 0.02	38.77 ± 0.18	39.52 ± 0.23	39.15 ± 0.13	39.80 ± 0.07
TiO_2	0.01 ± 0.01	0.05	1.38 ± 0.01	0.03 ± 0.01	0.03 ± 0.02	0.02 ± 0.02	0.02 ± 0.01
Al_2O_3	0.04 ± 0.01	0.04	22.65 ± 0.22	0.04 ± 0.01	0.04 ± 0.01	0.04 ± 0.01	0.04 ± 0.01
Cr_2O_3	0.06 ± 0.01	0.04	41.32 ± 0.26	0.01 ± 0.01	0.02 ± 0.02		
Fe_2O_3			8.33 ± 0.10				
FeO	10.57 ± 0.11	14.24	12.36 ± 0.07	17.12 ± 0.22	13.83 ± 0.35	16.23 ± 0.09	13.53 ± 0.19
MgO	48.87 ± 0.16	45.83	15.27 ± 0.08	43.61 ± 0.09	46.04 ± 0.19	43.85 ± 0.10	45.76 ± 0.21
MnO	0.15 ± 0.02	0.22	0.10 ± 0.01	0.24 ± 0.02	0.20 ± 0.02	0.16 ± 0.02	0.15 ± 0.02
NiO	0.28 ± 0.02	0.13	0.17 ± 0.02	0.09 ± 0.03	0.12 ± 0.05	0.13 ± 0.02	0.13 ± 0.04
CaO	0.17 ± 0.01	0.33	0.01 ± 0.01	0.15 ± 0.01	0.25 ± 0.08	0.14 ± 0.01	0.26 ± 0.08
BaO							
Na_2O							
K_2O							
P_2O_5							
Cl							
F							
H_2O							
Total	100.59 ± 0.25	100.62	101.69 ± 0.24	100.05 ± 0.31	100.05 ± 0.20	99.71 ± 0.17	99.70 ± 0.28
Atomic formulae							
Si	0.991	0.990	0.025	0.985	0.988	0.993	0.996
Ti	0.000	0.001	0.248	0.000	0.001	0.000	0.000
Al	0.001	0.001	6.369	0.001	0.001	0.001	0.001
Cr	0.001	0.001	7.792	0.000	0.000		
Fe^{3+}			1.495				
Fe^{2+}	0.217	0.297	2.466	0.364	0.289	0.344	0.283
Mg	1.785	1.702	5.431	1.652	1.717	1.658	1.708
Mn	0.003	0.005	0.020	0.005	0.004	0.003	0.003
Ni	0.005	0.003	0.033	0.002	0.002	0.003	0.003
Ca	0.005	0.009	0.002	0.004	0.007	0.004	0.007
Ba							
Na							
K							
P							
Total	3.007	3.008	23.881	3.014	3.011	3.006	3.002
Ca (trace)							
Cr/(Cr+Al)			0.550				
Mg/(Mg+Fe)	0.892	0.852	0.688	0.820	0.856	0.828	0.858
Fo	88.6	84.5		81.5	85.0	82.4	85.2
Wo							
En							
Fs							
Ac							

Table C.XIII. Mineral-chemical composition and structural formulae for feldspar rich rocks (c - core, r - rim, i - intergrowth).

sample	XKZH1								XKZH2			
	fsp	opx-r	opx-c	opx-i	cpx-i	am	phl	rt	fsp	glass	glass	mag
n	5	8	4	2	4	4	4	4	4	3	4	1
SiO_2	54.05±0.30	53.66±0.22	53.93±0.22	53.95±0.07	51.87±0.86	45.50±0.87	38.46±0.25	0.01±0.01	67.79±0.19	68.36±0.83	58.35±0.99	0.55
TiO_2	0.04±0.04	0.08±0.01	0.10±0.01	0.38±0.01	0.71±0.24	1.65±0.02	4.84±0.08	100.68±0.37	0.01±0.01	0.46±0.09	0.52±0.28	11.45
Al_2O_3	29.83±0.16	2.42±0.07	2.56±0.08	4.28±0.34	4.17±1.22	11.52±0.24	16.35±0.05	0.03±0.02	20.80±0.01	21.51±0.07	20.54±0.09	8.72
Cr_2O_3		0.03±0.02	0.07±0.02	0.16±0.01	0.14±0.07	0.05±0.02	0.04±0.03	0.06±0.02		0.01±0.01	0.01±0.01	0.06
Fe_2O_3												48.25
FeO	0.08±0.04	17.81±0.14	17.89±0.27	12.87±1.00	7.36±0.66	10.33±0.19	11.13±0.23	0.42±0.29	0.06±0.03	4.35±0.52	4.00±0.52	24.74
MgO	0.01±0.01	25.89±0.12	25.61±0.07	27.89±0.94	15.99±0.82	15.33±0.18	16.58±0.25	0.06±0.09	0.00±0.00	0.78±0.09	0.70±0.11	3.60
MnO	0.01±0.01	0.38±0.05	0.38±0.03	0.19±0.02	0.16±0.02	0.13±0.03	0.05±0.04	0.00±0.00	0.00±0.01	0.29±0.04	0.30±0.06	1.87
NiO				0.03±0.02	0.05±0.03					0.01±0.01	0.00±0.01	0.00
CaO	12.02±0.05	0.37±0.03	0.51±0.05	1.56±0.06	19.33±0.81	11.24±0.08	0.07±0.03	0.01±0.01	1.26±0.03	0.93±0.06	0.99±0.12	0.03
BaO	0.02±0.01						0.23±0.07		0.02±0.01	0.06±0.00	0.08±0.01	
Na_2O	5.13±0.08	0.01±0.00	0.03±0.00	0.05±0.00	0.55±0.10	1.96±0.06	0.80±0.06		10.88±0.08	2.70±0.22	8.70±0.06	
K_2O	0.18±0.01	0.01±0.01	0.00±0.00			0.55±0.02	7.82±0.57		1.06±0.03	1.15±0.04	3.66±0.05	
P_2O_5										0.06±0.05		
Cl						0.02±0.00	0.01±0.01			0.03±0.01	0.08±0.02	
F						0.00±0.00	0.00±0.00			0.00±0.00	0.00±0.00	
H_2O							4.17±0.02					
SrO									0.08±0.03			
ZnO											0.00±0.00	0.33
Total	101.36±0.44	100.66±0.40	101.06±0.36	99.97±0.31	100.09±1.00	98.25±1.30	96.38±0.96	101.27±0.19	101.95±0.24	100.70±0.28	97.91±0.36	99.60
Atomic formulae												
Si	2.416	1.940	1.942	1.899	1.900	6.549	5.525		2.931			
Ti	0.001	0.002	0.003	0.010	0.020	0.179	0.523		0.000			
Al	1.572	0.103	0.108	0.178	0.180	1.954	2.768		1.060			
Cr		0.001	0.002	0.005	0.004	0.005	0.005					
Fe^{3+}												
Fe^{2+}	0.003	0.538	0.539	0.379	0.226	1.243	1.337		0.002			
Mg	0.000	1.395	1.375	1.463	0.873	3.289	3.550		0.000			
Mn	0.000	0.012	0.012	0.006	0.005	0.015	0.006		0.000			
Ni				0.001	0.001							
Ca	0.576	0.014	0.020	0.059	0.759	1.734	0.011		0.058			
Ba	0.000	0.000	0.002				0.013		0.000			
Na	0.444	0.000	0.000	0.004	0.039	0.547	0.223		0.912			
K	0.010	0.001				0.101	1.433		0.059			
P												
Total	5.024	4.006	4.002	4.001	4.007	15.614	15.392		5.022			
Ca (trace)												
Cr/(Cr+Al)												
Mg/(Mg+Fe)		0.722	0.718	0.794	0.795	0.726	0.726			0.242	0.237	0.206
Fo												
Wo or An	55.9	0.7	1.0	3.1	39.9				5.6			
En or Ab	43.1	71.2	70.6	76.6	45.9				88.7			
Fs or Or	1.0	28.1	28.3	20.1	12.1				5.7			
Ac		0.0	0.1	0.2	2.1							

Table C.XIII. (continued).

sample	XKZH3 cpx	fsp1	fsp2	ttn	ap
n	3	4	2	8	3
SiO_2	52.18 ± 0.18	67.49 ± 0.19	68.38 ± 0.19	30.60 ± 0.25	0.27 ± 0.03
TiO_2	0.19 ± 0.00	0.01 ± 0.02	0.01 ± 0.00	37.80 ± 0.87	0.00 ± 0.01
Al_2O_3	1.65 ± 0.06	19.26 ± 0.08	20.02 ± 0.06	1.34 ± 0.21	0.01 ± 0.01
Cr_2O_3	0.03 ± 0.01			0.03 ± 0.02	0.01 ± 0.01
Fe_2O_3				2.03 ± 0.41	
FeO	17.18 ± 0.03	0.12 ± 0.02	0.16 ± 0.00	0.01 ± 0.02	0.02 ± 0.01
MgO	7.48 ± 0.05	0.00 ± 0.00	0.00 ± 0.00	0.09 ± 0.02	0.00 ± 0.00
MnO	0.56 ± 0.01	0.01 ± 0.01	0.01 ± 0.01	0.02 ± 0.03	0.05 ± 0.01
NiO					0.01 ± 0.01
CaO	16.21 ± 0.04	0.31 ± 0.02	0.56 ± 0.03	28.14 ± 0.29	55.94 ± 0.11
BaO		0.36 ± 0.04	0.03 ± 0.01	0.00 ± 0.00	0.03 ± 0.02
Na_2O	4.76 ± 0.08	7.35 ± 0.03	11.17 ± 0.12	0.13 ± 0.04	0.28 ± 0.02
K_2O	0.01 ± 0.00	6.23 ± 0.05	1.21 ± 0.01	0.00 ± 0.00	0.00 ± 0.01
P_2O_5				0.02 ± 0.02	35.57 ± 0.67
Cl				0.01 ± 0.01	0.01 ± 0.01
F				0.38 ± 0.17	3.56 ± 0.02
H_2O	SrO 0.12 ± 0.01	0.12 ± 0.01	0.11 ± 0.01		
Total	100.25 ± 0.23	101.25 ± 0.29	101.68 ± 0.34	100.45 ± 0.74	94.27 ± 0.61
Atomic formulae					
Si	2.012	2.987	2.964		
Ti	0.005	0.000	0.000		
Al	0.075	1.005	1.023		
Cr	0.001				
Fe^{3+}					
Fe^{2+}	0.554	0.005	0.006		
Mg	0.430	0.000	0.000		
Mn	0.018	0.000	0.001		
Ni					
Ca	0.670	0.015	0.026		
Ba		0.006	0.001		
Na	0.356	0.630	0.939		
K	0.000	0.352	0.067		
P					
Total	4.122	4.999	5.025		
Ca (trace)					
Cr/(Cr+Al)	0.437				
Mg/(Mg+Fe)					
Fo					
Wo or An	33.0	1.5	2.5		
En or Ab	21.2	63.2	91.0		
Fs or Or	28.2	35.3	6.5		
Ac	17.6				

87

The amount of Fe^{3+} in spinel was calculated from stoichiometry by the algorithm in the CAMECA software. Natural and synthetic standards (Smithsonian Standards; Astimex Scientific Limited) were used for calibration. To test the degree of equilibration between and within mineral grains (intra-grain heterogeneity), a large number of point analyses and profiles were performed. The consistency of the data set was checked by repeated measurements for some samples. The accuracy of microprobe analyses is in the range of 0.05 to 0.2 wt.%. The matrix correction was done by the algorithm that is implemented in the software of the CAMECA microprobes (PAP algorithm; *Pouchou and Pichoir,* 1984). The results of the microprobe measurements are listed in Tables C.III to C.XIII.

Olivine analyses

The investigated olivines have forsterite contents between 0.82 and 0.88 (Tables C.III, C.IV, C.VII, C.X, C.XII) and differ from olivines in spinel lherzolites (0.90 to 0.91) from nearby localities in NE-Bavaria [*Huckenholz and Kunzmann,* 1993; own data], the Rhön [*Franz et al.,* 1997], and the Elbe Zone [*Medaris et al.,* 1997; *Kramer and Seifert,* 2000; own data]. Normal and reversed zoning of Mg and Fe could be observed in many of the investigated grains. CaO contents are relatively high in the analysed olivines from Mýtina (wehrlitic samples: 0.17 wt.%; megacrysts cores and MXZH66: 0.15 wt.%; phenocryst cores: 0.18 wt.%) comparable to olivines from Železná Hůrka (0.14 to 0.17 wt.%), whereas olivines in spinel lherzolites have lower CaO contents (Zinst-1: 0.09 wt.%; Go01-1: 0.04 wt.%). Rims of phenocrysts and megacrysts have CaO contents > 0.25 wt.%, but analyses may be influenced by the so-called phase boundary fluorescence effect.

Clinopyroxene analyses

Analysed clinopyroxenes can be classified as chromian or aluminian diopsides and augites, according to *Morimoto* [1988] (Tables C.III-C.VI, C.VIII, C.X, C.XII; Figure C.6). Cr-rich clinopyroxenes commonly belong to the spinel lherzolites, wehrlites or olivine-clinopyroxene-spinel cumulates. The composition of groundmass clinopyroxenes and rims is titanian aluminian diopsidic (up to > 6 wt.% TiO_2; up to 12 wt.% Al_2O_3). The Cr-content of clinopyroxenes within wehrlites (e.g., MXZH1) is highly variable, indicating magmatic/metasomatic overprinting of the samples.

Amphibole analyses

The investigated amphiboles (polycrystalline and megacrysts) are Fe-, Ti-rich calcic amphiboles (potassian titanian pargasites, according to *Leake et al.* [1978, 1997]; Tables C.III-C.V, C.IX, C.XIII). They show widespread K_2O/Na_2O ratios (composite samples 0.5 to 1.0; megacrysts 0.8 to 1.0). Mg/(Mg+Fe) values are 0.67 for clinopyroxene-hornblendites, 0.73 for hornblendite, 0.57 to 0.6 for hornblende-clinopyroxenites, and 0.79 for hbl-peridotite. Mg/(Mg+Fe) values of analysed amphibole megacrysts are close to 0.8. The TiO_2 content is about 2.5 wt.% in clinopyroxenites, > 3 wt.% in hornblendites as well as in sample MXZH66. TiO_2 content of megacrysts is 3.3 to 3.4 wt.%. Al_2O_3

varies between 12.7 wt.% (MXZH33) and 14.6 wt.% (MXZH66) for xenoliths, and between 13.8 and 14.7 wt.% for megacrysts. Only amphibole in sample MXZH66 (0.8 wt.%) and amphibole megacrysts (0 to 0.3 wt.%) contain significant amounts of Cr_2O_3.

A Fe^{3+}/Fe^{2+} ratio of 0.5 was determined for amphibole megacryst MXZH15 from the whole-rock chemistry (Table C.II). This sample and hornblendite sample MXZH68 also contain rounded Ni, Co, Pt and Cu bearing magnetite-sulphide inclusions (average sulphide analyses: 57.7 wt.% Fe, 38.7 wt.% S, 3.3 wt.% Ni, 0.2 wt.% Co, up to 4 wt.% Cu, up to 0.7 wt.% Pt; pyrrhotite). Such sulphide inclusions are common in metasomatized mantle xenoliths [e.g., *Shaw,* 1997] and may result from the immiscibility of sulphide liquids with the magma [*Deer et al.,* 1963].

Amphibole in the crustal xenolith XKZH1 has lower TiO_2 (1.65 wt.%), Al_2O_3 (11.5 wt.%) and K_2O (0.55 wt.%) than amphiboles in the other analysed (ultra-) mafic samples.

Phlogopite analyses

Micas, occurring as megacrysts and within xenoliths, are Ti-rich phlogopites (3.8 to 4.8 wt.% TiO_2, 18 to > 20 wt.% MgO; Tables C.V-C.VII, C.IX) [see also *Seifert and Kämpf*, 1994].
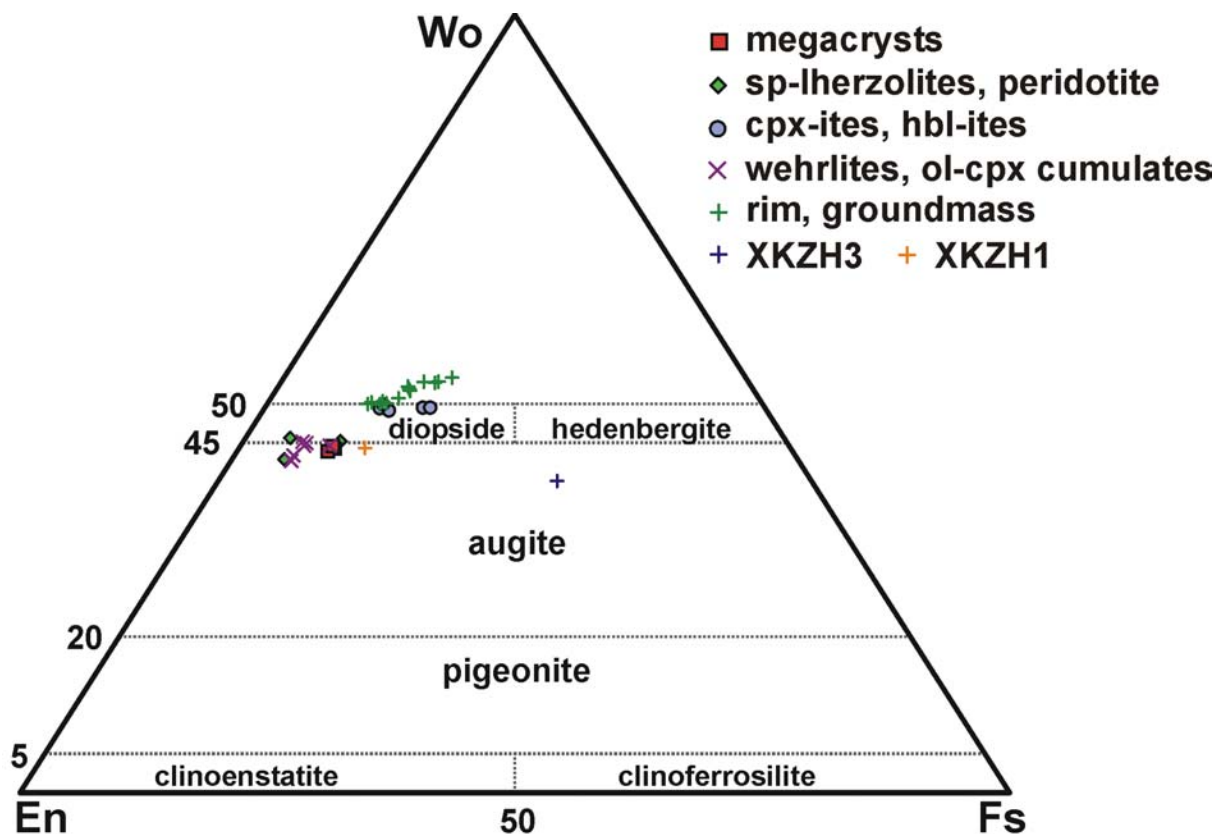
Figure C.6
Ternary classification diagram for clinopyroxenes [after *Morimoto,* 1988]. Cr-rich clinopyroxenes of spinel lherzolites, peridotite, wehrlites, olivine-clinopyroxene-spinel cumulates, and clinopyroxene in XKZH1 plot close to the augite-diopside boundary. Clinopyroxenes within clinopyroxenites and hornblendites can be classified as diopsides. Clinopyroxene rims and groundmass crystals plot above the 50% Wollastonite line due to very high Al and Ti contents. Sample XKZH3 contains Na-rich augitic clinopyroxene (aegirine-augite).

C.5 Interpretation of the petrological data

C.5.1 Composition and origin of xenoliths and megacrysts

Already in the 19th century, there was a controversy on the origin of the ultramafic nodules (mantle xenoliths) and megacrysts from Mýtina, whether they are true xenoliths or cumulates that crystallized in the host magma. Whereas *Reuss* [1852] argued that the olivine, amphibole, and augite nodules are evidence for a previous basaltic activity and that they were partly re-melted or became scoria-like, *Proft* [1894] favoured the early crystallization in the basaltic host magma.

C.5.1.1 Mantle xenoliths and cumulates

The magmatic textures of most ultramafic nodules indicate the crystallization from a melt not long before the entrainment into the host magma; otherwise textural equilibration and development of metamorphic fabric would be expected [*Best*, 2003]. The mineral chemistry (relatively low Mg content of olivine, low Cr_2O_3 contents of clinopyroxenes, high TiO_2 contents of diopsidic clinopyroxenes and amphiboles, widespread K_2O/Na_2O ratios of amphiboles) as well as the occurrence of titaniferous micas let me argue that the majority of the investigated samples are directly related to alkaline magmatism, associated with incompatible element enrichment of peridotite wall-rocks in the immediate vicinity of frozen conduits [see *Wilkinson and Le'Maitre,* 1987; *Witt and Seck,* 1989]. According to *Huckenholz et al.* [1992], amphiboles crystallized from basaltic magmas have a "convex-up shaped" Eu and Sm anomaly in the C1-normalized REE pattern; and amphiboles in veins, small dikes or selvages have lower mg-values and overlap for Na, K, Ti with megacrysts. The REE C1-normalized patterns of the analysed amphibole-bearing xenoliths (LREE enriched convex-upward; Figure C.5) resample that of vein amphiboles from ultramafic Alpine massifs and xenoliths, as compiled by *Downes* [2001], supporting the interpretation of a magmatic origin.

Pargasites within sample MXZH66 (mg 0.8, 0.5-0.8 wt.% Cr_2O_3) show some similarities to amphiboles of secondary origin, which commonly occur interstitially in the olivine-orthopyroxene-clinopyroxene-spinel matrix of peridotites (mg 0.82-0.94, >1 wt% Cr_2O_3; see *Huckenholz et al.,* [1993]). MXZH66 might represent a sample from near a hornblendite vein; such veins are widely observed in ultramafic Alpine massifs [e.g., Lherz massif, French Pyrenees; *McPherson et al.,* 1996; *Woodland et al.,* 1996; *Zanetti et al.,* 1996; *Fabries et al.,* 2001].

Some wehrlitic samples containing Cr-bearing diopside and olivine (Fo 88) and showing cumulus textures are possibly related to alkaline metasomatism (by alkaline-carbonatitic melts) of the uppermost mantle (see below). Generally, samples similar to the analysed (meta-) cumulates,

pyroxenites and hornblendites are also reported from the North Hessian Depression, the Eifel, the Urach and the Hegau volcanic fields [e.g., *Becker,* 1977; *Vinx and Jung,* 1977; *Mengel et al.,* 1991].

C.5.1.2   Megacrysts – high pressure precipitates or fragments of pegmatites or dikes ?

According to *Irving* [1984] and *Schulze* [1987], basaltic megacrysts can be divided into two groups: Group A, including aluminian augite, olivine, kaersutitic amphibole, may have been crystallized from the host basalts or similar magmas; and Group B, including Ti-rich mica, apatite, ilmenite, is considered to represent (pegmatitic) xenocrysts, belonging originally to more evolved magmas (possibly related to the host) intruded to shallower depths prior to the host magma [*Schulze,* 1987]. *Righter and Carmichael* [1993] argued that large, unzoned, inclusion-free megacrysts cannot have grown from the basalt host during ascent, because that would require unreasonable large growth and diffusion rates. According to *Righter and Carmichael* [1993], the unzoned nature of many megacrysts indicate a slow crystallization in magma chambers or as pegmatites. The growth of 1-cm crystals may last thousands of years, which requires long-lived magma chambers. In such reservoirs with stable temperature-pressure conditions close to mineral liquidus, small crystals of a specified mineral may dissolve and large crystals grow by the process of textural coarsening [e.g., *Higgins and Roberge,* 2003]. Arguments for a xenocryst origin of megacrysts are the fragmented or irregular edges in contact with the host basalt; some coarse xenocrysts show also fracturing [*Righter and Carmichael*, 1993]. Shape, composition and size indicate derivation from disaggregated gabbroic, pyroxenitic, wehrlitic dikes and pegmatites. Some coarse subhedral crystals could be real phenocrysts [*Righter and Carmichael*, 1993]. Furthermore, isotopic studies can be useful to clarify the relationship between megacrysts and the host rock [see *Schulze, 1987*].

Most of the olivine megacrysts from Mýtina show a narrow range in chemical composition of mineral cores (Fo 82 to 83; see Table C.VII). The core composition of megacrysts differs strongly from core analyses of the magnesium rich phenocrysts in the host rock (Fo 88 to 89; Table C.X). Towards the rim many megacrysts are more magnesian (Fo 85 to 86) indicating changing chemical conditions [see *Kämpf et al.,* 1993], magmatic overprinting (diffusion), or further crystallization in the host magma. This rim composition of olivine megacrysts is similar to that of olivine crystals (both pheno- and xenocrysts) from the Železná Hůrka scoria (see Table C.XII). Generally, the existence of large melt inclusion can be interpreted as an effect of fast crystallization (skeletal growth) in a magma reservoir, but it cannot be excluded that this porosity is also an effect of magmatic resorption due to melt infiltration. The different core compositions of most phenocrysts and megacrysts from the Mýtina tephra let me argue, that they at least did not crystallize in one single magma chamber. Maybe the less magnesian megacrysts are related to shallower reservoirs.

Most single clinopyroxene megacrysts, sampled from the Mýtina tephra and the Železná Hůrka scoria, can be classified as aluminian augites (see Table C.VIII; Figure C.6). However, also large chromian diopside crystals occur in olivine-clinopyroxene-spinel aggregates (MXZH61, MXZH64). Narrow rims are always titanian diopsidic in composition, similar to Ti-rich diopside phenocrysts in the host rock. Aluminian augites are the most likely candidates for high-pressure phenocrysts [*Schulze*, 1987]. The equilibrium composition (with host melt) depends strongly on p-T conditions. For a primary origin of some clinopyroxene-megacrysts as phenocrysts argue the fact that they grew on smaller crystals (e.g., MXZH62: chromian augite xenocryst; EB2: olivine xenocryst). In the ternary Wo-En-Fs diagram (Figure C.6) aluminian augite megacrysts plot close the clinopyroxenes (chromian augites to diopsides) from wehrlitic samples and olivine-clinopyroxene cumulates.

The chemical composition of amphibole megacrysts from the Mýtina tephra is similar to that of amphiboles in clinopyroxenites and hornblendites (Tables C.IX and C.III-C.V). All samples can be classified as titanian pargasites [*Leake,* 1978, 1997], however Al and Cr contents vary between samples. Ti-rich amphibole is a near liquidus phase in alkali basaltic systems [e.g., *Allen et al.,* 1975] and could represent deep-seated phenocrysts.

The coarse grain size of Ti-rich ferromagnesian micas (phlogopite), which are relatively uncommon as megacrysts in alkali basalts [according to *Schulze*; 1987], may indicate their origin as phenocrysts.

C.5.1.3   Crustal rocks

Sample XKZH1 could be a rare fragment of feldspar-rich meta-intrusive rocks noritic in composition. Similar rock types (charnockitic, noritic, gabbroic), which might be related to magmatic intrusions into the lower crust, were described as xenoliths from the Elbe Zone and the Česke středohoři Mts. by *Opletal* [1967], *Kramer* [1988], *Opletal and Vrána* [1989], and *Kramer and Seifert,* [2000]. However, the ages of these rocks and therefore the times of intrusion are unknown. Sample XKZH1 shows weak metamorphic layering, which constrains an older age and implies that the samples are not directly related to the Tertiary-Quaternary volcanic/magmatic episode.

Upper crustal xenoliths (quartzites, phyllites, and mica schists) are most probably fragments of the uppermost kilometre(s) of the crust in the area around Mýtina. According to *Richter and Stettner* [1993] and *Fiala and Vejnar* [2004], the uppermost crust in the vicinity of Mýtina consists of an Upper Cambrian to Ordovician alternated stratification of quartzites and phyllites or mica schists (Figure C.7). *Lapp and Weber* [1992] described a similar metagreywacke-phyllite-unit (about 250 m thick) from a core drilled near Neualbenreuth (south of Mýtina). Assuming no thin-skinned tectonic

stacking and the eruption of the tephra from the Železná Hůrka vent, which is located within the Cambrian mica schist units [cb; see *Bayerisches Geologisches Landesamt,* 1998], the samples should not originate from the stratigraphical higher Frauenbach and Phycoden units. The REE pattern of XKZH60 (pronounced negative Eu anomaly; see Appendix C.iii) shows similarities to the "muscovite gneisses" of the Erzgebirge. The magmatic protoliths of these gneisses were probably derived from high-silica per-aluminous rhyolites [see *Mingram et al.,* 2004].
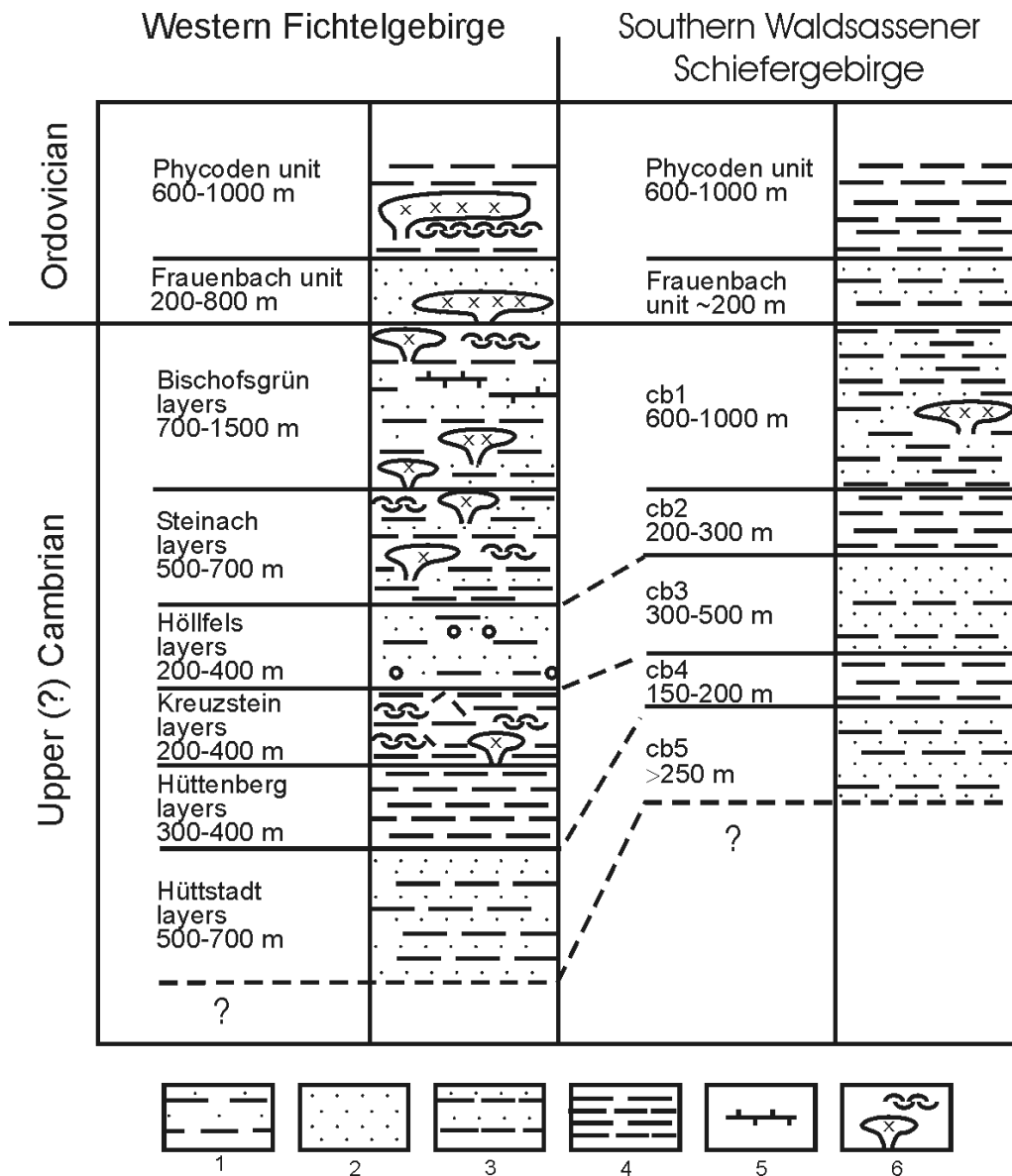
Figure C.7
Lithostratigraphical section of the uppermost crust in the vicinity of Neualbenreuth (southern Waldsassener Schiefergebirge) in comparison to the western Fichtelgebirge [from *Richter and Stettner,* 1993].
1 – shales and phyllites with silty layers; 2 – quartzites, quartzitic schists; 3 – alternated stratification quartzites/phyllites or mica schists; 4 – phyllite and mica schist; 5 – carbonate and calc-silicate intercalations; 6 – acid volcanics (tuffs, ignimbrites).
MXZH6, MXZH65, and MXZH66 (Plates 4, 5) might be samples from acid meta-tuffs, which belong to the "Neualbenreuth layers" in cb1 [*Richter and Stettner,* 1993]. Zircon enriched samples (e.g., XKZH51, 58, 59, 61 with Zr values >1000 ppm, see Appendix C.ii) might belong to zircon rich layers (placer like) in cb3. *Richter and Stettner* [1993] described zircon rich quartzite layers in the Frauenbach and the cb3 (cb5?) units.

C.5.2   Depth origin of xenoliths (geothermobarometry)

Geobarometric estimations for lower crust and upper mantle samples were performed because they may report more or less the conditions close to their formation or metamorphic overprinting at the present depth level. The results of the geothermobarometric calculations for the different types of (ultra-) mafic nodules (cumulates, hornblendites and megacrysts) are shown in Figure C.8 (amphiboles) and listed in Table C.XIV. No geothermobarometric calculations were carried out for upper crustal xenoliths in this study.

Different mineral pairs within one sample record sometimes different pressure-temperature conditions, which may be related to the formation, cooling history, or to later overprinting of the mineral assemblage. Now, I try to interpret the p-T estimates calculated for different samples and mineral pairs from the Mýtina ultramafic xenolith suite (Table C.XIV). However, this give only some constraints on the true pressure-temperature conditions, because the geothermobarometers based on inter-crystalline exchange of elements also show complex dependences on element concentrations.

Magma temperature (olivine-spinel and phlogopite-glass thermometry)

The olivine-spinel thermometers are strongly sensitive to sub-solidus reactions, however from spinel inclusion in olivine phenocrysts it should be possible to estimate the temperature during crystallization of the mineral pair. Values of about 1100°C and 1170°C can be calculated for spinel inclusions within olivine phenocrysts (samples EB5-9, MXZH17) using the geothermometric formulation of *Ballhaus et all.* [1991] and *O'Neill and Wall* [1987], respectively. Because of the fast undercooling during ascent and eruption, I think that sub-solidus reactions did not take place and these values can be assumed to be the temperature of the magma (liquidus). A similar temperature range (1130 to 1150°C) was estimated using the phlogopite-glass geothermometer of *Righter and Carmichael* [1996] for samples MXZH24 and MXZH69. A temperature of 1140°C can be estimated for the combination MXZH21 (phlogopite megacryst) and My1 (nephelinite).

Hbl-peridotite (p-T; MXZH66)

For the amphibole-bearing peridotite xenolith MXZH66 two pressure (depth) estimates were obtained. Using the Al/Ti diagram proposed by *Ernst and Liu* [1998] a pressure of 8 to 9 kbar (30 km depth) and a temperature of 960°C is indicated (Figure C.8a). Using the formulation of *Huckenholz et al.* [1993], the pressure estimate is about 15 kbar (50 km). The discrepancy in pressure estimates might be related to disequilibrium between the mineral phases (post-entrainment modification) or the fact that some assumptions of one of the geobarometers are not fulfilled. Maybe the elevated Cr (and Fe^{3+}?) content of the amphibole makes the sample not suitable to plot it in the Al-Ti diagram, or at least enforce some corrections before plotting. Because the clinopyroxene barometer of *Nimis and Ulmer* [1998] also gives values around 15 kbar (for a olivine-spinel temperature of 1060°C), I prefer this pressure

estimate. Temperatures calculated with the olivine-spinel thermometers of *Ballhaus et all.* [1991] and *O'Neill and Wall* [1987] are 950°C and 1060°C, respectively.

Hbl-clinopyroxenites and cpx-hornblendites, amphibole megacrysts (p-T)

The pressure-temperature conditions of formation of the amphibole-bearing samples (clinopyroxenites, hornblendites), including the amphibole megacrysts were estimated using the Al/Ti plot of *Ernst and Liu* [1998]. The polycrystalline samples plot almost all in a narrow p-T range (see Figure C.8a) of 6 to 8 kbar (22 to 29 km) and 900 to 970°C, only the apatite-bearing sample MXZH5 as well as sample MXZH66 show higher pressures of up to 10 kbar (about 35 km). The amphibole megacrysts plot between 7 and 10 kbar (25 to 35 km) at a very narrow temperature range around 970°C (Figure C.8b).

Figure C.8
Results from the Al-Ti amphibole thermobarometry [*Ernst and Liu,* 1998] **(a)** for amphibole-bearing xenoliths and **(b)** megacrysts.

Table C.XIV. p-T estimates of selected (ultra-) mafic nodules (xenoliths and cumulates) from the Mýtina tephra and the Železná Hůrka scoria cone using different geothermobarometers. Two spinel lherzolite samples from the Elbe Zone (Saxony) and from NE-Bavaria are included for comparison. For the clinopyroxene barometry [NU: *Nimis and Ulmer*, 1998; *Nimis*, 1999] T_{cpxbar} = (1000–1150)°C was used, if no other temperature constraints were available. T=1150°C was used for wehrlites (MXZH1, -2, -4) and ol-cpx cumulates (MXZH18, -64) and the olivine-clinopyroxene barometer [KB: *Köhler and Brey*, 1990]. At T=1130°C, pressure estimates for samples MXZH18 and MXZH64 coincide (10 to 11 kbar) using clinopyroxene and olivine-clinopyroxene barometry.

sample	rock type	temperature [°C]							pressure [kbar]				T_{cpxbar} °C	$p_{max}(sp)$
		ol-sp R1979	ol-sp B1991	ol-sp NW1987	hbl E1998	opx BK1990	2px BKN	phl-gl RC1996	cpx-hbl H1992	hbl E1998	ol-cpx KB	cpxbar NU1998		N81
Železná Hůrka														
EB1	ol-megacryst + am				960							p(BH)		
EB5-ol9	ol-phenocryst + sp	1180	1090	1160						8.9				29
Mýtina														
XKZH1	norite (primary)				805	810(r)..870(c)								
	norite (secondary?)					*1125*	970						p(BA)	
MXZH66	hbl-peridotite	1290	950	1060	960				6	6	?	4?	1060..960	24
MXZH5	hbl-clinopyroxenite				900				15	8.9		15..20	1000..900	
MXZH11	hbl-clinopyroxenite				900				12	9.5..10		7.5..12.5	1000..900	
MXZH33	hbl-clinopyroxenite				900				11	7.5..8		7.5..12.5	1000..900	
MXZH12	cpx-hornblendite				930..970				5	6.7		5..10	970..930	
MXZH13	cpx-hornblendite				930				10	5.6		9..11	970..930	
MXZH68	hornblendite				970				8	6.7		7.5..9.5		
MXZH1	wehrlite										10	10..18	1150..1000	
MXZH2	wehrlite										10..11	10..18	1150..1000	
MXZH4	wehrlite										(11)	7..15	1150..1000	
MXZH8	ol-cpx-cumulate											9..17	1150..1000	
MXZH18	ol-cpx-cumulate + sp	1170	1040	1110							13 (10)	11..14	1110..1050	27
MXZH64	ol-cpx-cumulate + sp	1180	1060	1120							13 (10)	11..14	1120..1060	27
MXZH61	ol-cpx-cumulate + sp	1300	1100	1190								10..12	1150..1100	27
MXZH17 (gm)	ol-phenocryst + sp	1270	1100	1170										27
MXZH24	ol-megacryst + phl, gl, cpx							1150				1..3	1150..1100	
	cpx-phenocryst (GM)											11..13	1150..1100	
MXZH69	ol-megacryst							1130						
MXZH21 + My1	phlogopite + nephelinite							1140						
sp-lherzolites														
Zinst-1	sp-lherzolite	1060	960	1000		1080	1105				21	16..21	1100..1000	25
Go01-1	sp-lherzolite (harzburgite)	1070	900	920		920	980				19	17..20	980..920	27

B1991 – *Ballhaus et al.*: 1991; BKN, BK1990 – *Brey and Köhler*, 1990; E1998 – *Ernst and Liu*, 1998; H1992 – *Huckenholz et al.*, 1992; KB – *Köhler and Brey*, 1990; NU1998 – *Nimis and Ulmer*, 1998; NW1987 – *O'Neill and Wall*, 1987; R1979 – *Roeder et al.*, 1979; RC1996 – *Righter and Carmichael*, 1996; N81 – *O'Neill*, 1981 (without Fe^{2+} correction).

Pressures calculated with the formulation of *Huckenholz et al.* [1993] give slightly higher pressure estimates between 5/8 and 12 kbar (22/29 to 40 km) for the clinopyroxene-amphibole-bearing samples. The differences between pressure estimates from both methods are within the given uncertainties. A comparison with experimental partitioning data for Ti, Ho, Lu, Sr between amphibole and basanitic melt from *Adam and Green* [1994] indicates the crystallization of amphibole megacryst MXZH15 at pressures above 1 GPa, assuming that the nephelinite sample My1 represents also the melt composition in the magma reservoir.

The relatively high temperatures obtained for the amphibole-bearing samples, possibly originating from near the crust-mantle boundary, are most probably crystallization (magmatic) temperatures. These values are valid for small dikes or intrusion at the time of their formation and do not necessarily represent temperatures valid for the crust-mantle transition and lower crust on the regional scale. If the amphibole megacrysts would be high-pressure precipitates of the host melt, then the p-T estimates provide constraints for the depth and temperatures of the palaeo-magma reservoirs near the crust-mantle boundary. The rounding of most amphibole megacrysts might be an effect of the upward transport (decompression) in a hotter and reactive melt.

Wehrlites, olivine-clinopyroxene aggregates and clinopyroxene-megacrysts (p-T)
For most wehrlitic samples (MXZH1, -2, -4), olivine-clinopyroxene aggregates (MXZH18, -64), and clinopyroxene megacrysts and phenocrysts (groundmass crystal in MXZH24), depths of origin of 29 to 38 km (8 to 11 kbar) could be estimated using the olivine-clinopyroxene barometer of *Köhler and Brey* [1990] and the clinopyroxene barometer of *Nimis and Ulmer* [1998]. However, both barometers are strongly temperature sensitive. Assuming a temperature of 1150°C, the estimates from both calibrations are more or less the same. This high temperature value (near liquidus) indicates that most samples are somehow related to the host magma or at least to the same Late Cainozoic magmatic activity. A comparison with experimental partitioning data for Ti and Ho between clinopyroxene and basanitic melt from *Adam and Green* [1994] indicates the crystallization of amphibole megacryst MXZH16 at pressures above 1 GPa, assuming that the nephelinite sample My1 represents also the melt composition in the magma reservoir.

Spinel lherzolites
The commonly applied geothermobarometers for spinel lherzolitic samples were tested on samples Go01-1 and Zinst-1, which are included in this study for comparison reasons.
The harzburgitic sample Go01-1 from the Elbe Zone was equilibrated at a pressure of about 19 kbar (more than 60 km depth), according to the formulation of *Köhler and Brey* [1990]. Temperature values (olivine-spinel, two-pyroxene) range from 920 to 980°C, depending on the formulation used. For the pressure calculation the temperature estimate from the two-pyroxene thermometer of *Brey and Köhler*

[1990] was used. The temperature estimate is closer to values reported from the eastern Erzgebirge than to values from the Elbe Zone [*Kramer and Seifert,* 2000]; the sample locality is close to the boundary of both areas.

A pressure of 21 kbar (approximately 70 km depth) was estimated for the sample from Zinst, NE-Bavaria. Calculated temperatures are in the range of 1000 to 1100°C, close to estimates from nearby localities (see references in section A.3.3, Table A.1).

Noritic xenolith (XKZH1)

For the noritic xenolith, depth and temperature estimation was possible using the Al/Ti-in-amphibole plot of Ernst and Liu [1998]. The sample plots at about 6 kbar (about 22 km) and 800°C (see Figure C.8a). An identical temperature (800°C) could be obtained using the Ca-in-orthopyroxene thermometer of *Brey and Köhler* [1990] and rim composition of the orthopyroxene close to the analysed amphibole. The core composition gives values of 860°C. This difference between rim and core might be related to cooling (after intrusion or during tectonic uplift) or a post-intrusion overprinting at lower temperatures. Temperatures between 700-900°C were also reported by *Mengel* [1990] for mafic and noritic granulites from the North Hessian Depression, which are interpreted as high-grade equivalents of subduction-related volcanics and cumulates.

Higher temperature values (970°C/1125°C) were obtained using analyses from areas of orthopyroxene-clinopyroxene intergrowth using two different formulations of *Brey and Köhler* [1990]. Because both temperature values differ strongly, the analysed minerals might not be in equilibrium. This may be an effect of magmatic overprinting (heating) of the sample in the host magma, or may be related to an earlier metasomatic event.

C.5.3   p-T data and regional geotherms

The p-T estimates for xenoliths can generally provide constraints on the recent thermal structure of the deep crust and uppermost mantle. As shown in Figure C.9, most analysed samples plot close to the alkaline province geotherm [*Jones et al.,* 1983], that means above proposed regional geotherms [*Čermák,* 1994] derived from surface heat-flow studies.

Moho temperatures, calculated from regional surface heat flow data differs from 450°C up to 750°C [see *Förster et al.,* 2003]. The problem in extrapolating the regional surface heat-flow data to depth is the strong influence of high-radioactive, heat-producing granitic rocks in the upper crust. Therefore, it is difficult to estimate the regional Moho heat-flow and temperatures [*Förster and Förster,* 2000]. However, from the p-T xenolith data, which is so far available for the area under investigation, it is impossible to construct a regional xenolith geotherm to get better constraints on the recent or at least Late Cainozoic thermal structure of the lower crust and upper mantle.
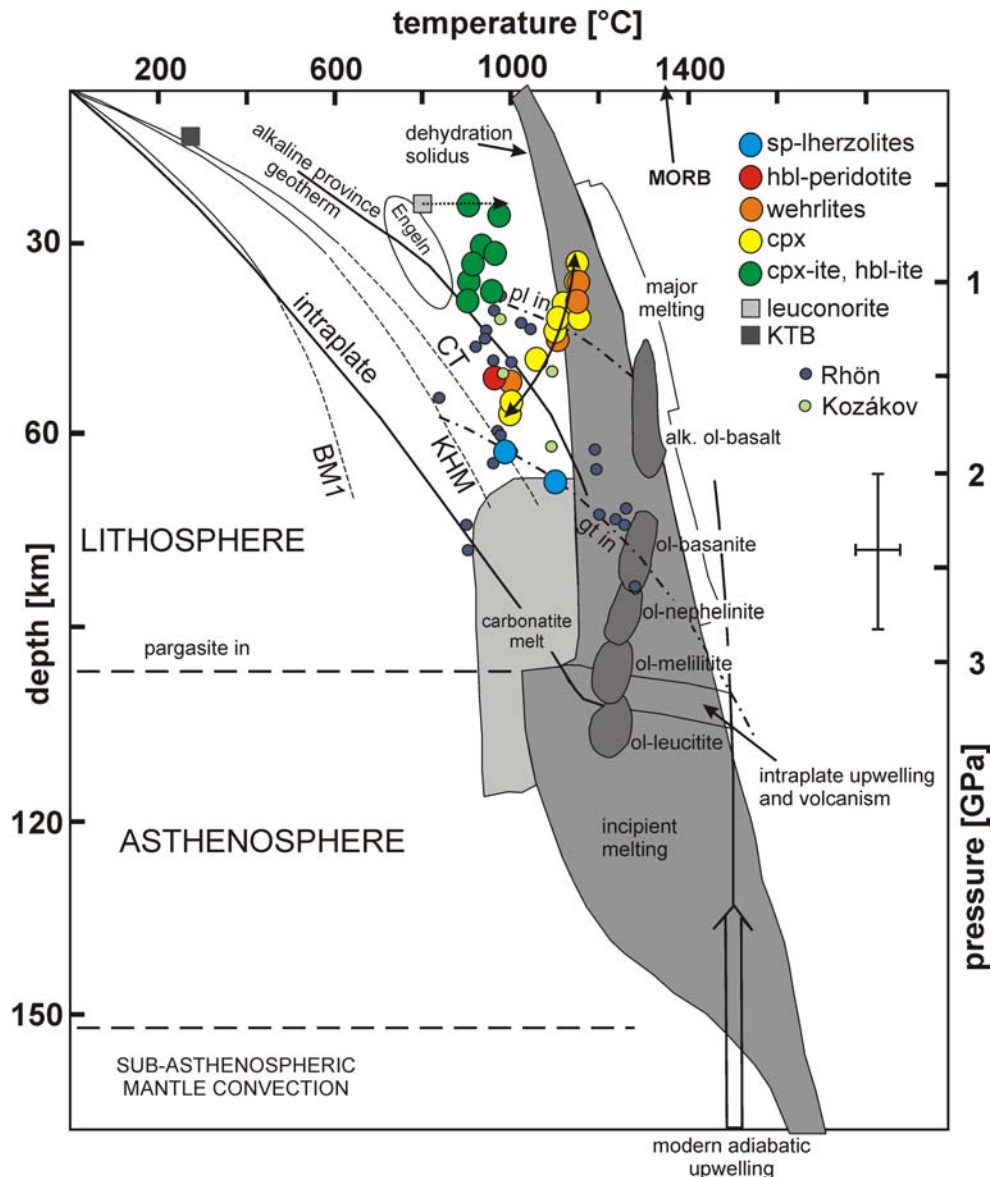
Figure C.9
Results of p-T calculations plotted into a diagram of *Green and Falloon* [1998]. The alkaline province geotherm [*Jones et al.,* 1983], regional geotherms (BM1 -Bohemian Massif minimum, KHM - Krušne Hory Mts., CT - Cretaceous Basin; *Čermák,* 1994), and one KTB-value [*Clauser et al.,* 1997] are included. The p-T field for granulite-facies metabasite ejecta from Engeln (Eifel, Germany) is shown for comparison with sample XKZH1 [adopted from *Jones et al.,* 1983; data from *Okrusch et al.,* 1979]. p-T estimates from the Rhön and the Kozákov are adopted from *Franz et al.* [1997] and *Medaris et al.* [1997], respectively.
Wilson and Downes [1992] described the frequently occurring/widespread melilite nephelinites as most likely candidates for primary melts from the asthenosphere/basal lithosphere. According to *Wilson et al.* [1995], melt coexisting with lherzolitic rocks at T >1025°C and pressures in the garnet stability field is in composition similar to ol-melilitite, whereas at lower pressures in the spinel stability field, silicate melt resamples ol-nephelinites.

C.6   Petrological indications for processes at the crust-mantle boundary

The p-T estimates indicate a depth origin of ultramafic nodules within the lower crust and uppermost mantle (approximately 20 to 50 km, with a maximum at 30 to 35 km). No orthopyroxene-bearing spinel-lherzolitic xenoliths could be found in the Quaternary volcanics; such xenoliths are thought to represent normal lithospheric upper mantle beneath Central Europe. The results indicate that possibly

large parts of the uppermost mantle beneath NW-Bohemia might be affected by mantle metasomatism around 0.3 Ma (due to infiltration of alkaline melts), which resulted in a mantle composition dominated by olivine and clinopyroxene (±amphibole, ±phlogopite).

The amphibole-rich nodules from about 20 to 35/40 km depth could represent fragments of magmatic dikes within the uppermost mantle and lower crust, which may be a more widespread phenomenon in the study area. According to *Barclay and Carmichael* [2004], isobaric crystallization of amphibole (hornblende) in a subduction related hornblende-basaltic melt near the base of the crust can influence the magma's capacity to flow (viscosity). And once amphibole crystallizes, the magma's ascent might be retarded by its high crystallinity. As *Barclay and Carmichael* [2004] pointed out, great proportions of basaltic bulk composition can crystallize as amphibole (as can be also seen in the similar chemical compositions of the pargasites and the nephelinitic host rock from Mýtina), and therefore most magma intrusions may stop in the lowermost crust due to cooling (freezing) by the surrounding "cold" crust. Maybe the uppermost mantle and lowermost crust beneath the western Eger Rift experienced many intrusions of small amounts of alkaline melt during the late Tertiary and Quaternary; only very few of these melts reached the surface.

The content and distribution of REEs in the nephelinitic host rock of the Mýtina tephra and from the Železná Hůrka scoria cone (Figure C.5) can be interpreted in terms of low percentage (approximately 1 %) of partial melting in a garnet-bearing source [according to *Rollinson,* 1993]. However, 1 % partial melt may be the amount of melt in the source region (90 to 100km depth?); more than 1 % could be present in the ponding region in the uppermost mantle (25 to 50 km depth), where it may form magma reservoirs. High "porosity", which can be observed in some ultramafic nodules, may indicate that this samples originate as "wall rock" of magma chambers, as discussed by *Tait* [1988] or may represent itself parts of a sponge-like magma reservoir.

Origin of CO_2 – related to alkaline-carbonatitic mantle metasomatism ?

According to *Green and Falloon* [1998], olivine-nephelinitic to olivine-melilitic melts originate at depths of about 90 to 100 km in a garnet-bearing source region (asthenosphere). Garnet remains in the residuum (might be inferred from the REE pattern). The ascending melts crystallize amphibole and phlogopite. This modal metasomatism of garnet/spinel lherzolite might leave carbonatitic residual melts, which react with enstatite and spinel to form olivine + (diopside + jadeite) + chromite + CO_2. The metasomatic lithosphere becomes enriched in clinopyroxene, illustrated by the formation of wehrlites (olivine + clinopyroxene + apatite + chromite) [see also *Yaxley et al.,* 1991, *Rudnick et al.,* 1993]. The CO_2 is released and migrates to the surface. This might be a possible scenario for the study area as well. However, up to now there are no further indications for the involvement of carbonatitic melts, as for instance carbonate inclusions in olivine and clinopyroxene or carbonate globules in silicate glass as observed by *Seifert and Thomas* [1995] in samples from the Elbe Zone, Germany.

D   Synthesis

In this chapter, I aim at a joint interpretation of the results obtained in this study by seismic and petrological investigations, and to discuss these results together with results from different previous geoscientific studies in the area (including seismicity, gas-geochemistry, and seismic studies). Finally, a process-orientated model of the system crust-uppermost mantle beneath the earthquake swarm region and intraplate CO_2 degassing field is presented.

D.1   A seismic and petrologic model of the crust-mantle transition and the origin of the "6 s phase"

To relate results from seismic studies to petrology, it is necessary to compare seismic velocity-depth profiles with velocity values of regionally occurring rocks, which can be measured on hand specimen in the laboratory or calculated from the modal (mineral) composition of rocks [e.g., *O'Reilly et al.,* 1990; *James et al.,* 2004]. Unfortunately, the xenoliths from Mýtina are too small to measure seismic velocities directly. So, the elastic properties can only be estimated comparing the xenoliths to published data of rock samples of similar mineralogy or by calculation from the modal composition. Pressure estimates on xenoliths and temperatures from geotherms can be used to correct the elastic parameters (seismic velocities) for conditions in their primary depth in the lower crust or uppermost mantle (at the crust-mantle boundary). In Figure D.1 the results from the receiver function study and the petrologic and geobarometric studies on xenoliths from the Mýtina tephra are combined.

D.1.1   Relating seismic velocities to petrology

D.1.1.1   Upper and middle crust

Regional P-wave seismic velocity models published in literature (see Figure B.9) let me argue that most of the upper and middle crust is composed of meta-sedimentary, granitic, and granulitic rocks comparable to rocks at the surface in the western and northern Bohemian Massif. This concurs with the petrophysical interpretation of the MVE90 and GRANU95 seismic profiles by *Mueller* [1995], *DEKORP and Orogenic Processes Working Groups* [1999], and *Krawczyk et al.* [2000]. Further arguments come from the KTB deep drill hole where similar rocks were cored down to nine kilometres [*Emmermann and Lauterjung,* 1997], which is one third of the crustal thickness in the region. Seismic velocities of typical crustal rocks are compiled by *Christensen and Money* [1995] and *Rudnick and Fountain* [1995].

D.1.1.2   Lower crust and uppermost mantle

Laboratory elastic parameter (seismic velocity) studies for lower crust and upper mantle rocks are rare, especially for hydrous mantle minerals. Previous compilations of elastic parameters and their dependence on pressure and temperature conditions valid for the crust-mantle boundary were published, e.g., by *Christensen* [1989] and *Mechie et al.* [1994b]. More recently, compilations were published by *Shaocheng Ji et al.* [2002] and *Hacker and Abers* [2004]. However, some of the necessary mineral elastic parameters were still calculated from similar minerals instead of directly measured [see *Hacker and Abers*, 2004]. To get an idea of probable seismic velocities in the upper mantle of the study area, seismic velocities of hypothetic rocks similar to the analysed ultramafic nodules (Table D.I) were calculated using the Excel-workbook provided by *Hacker and Abers* [2004]. The results using this workbook are similar to the velocity calculations using the elastic parameter values given by *Mechie et al.* [1994b] (see Appendix D.i).

At pressure-temperature conditions at the crust-mantle boundary (1.0 GPa, 650°C; extrapolation of the CT-geotherm published by *Čermák* [1994]) clinopyroxenites (v_s 4.2 km/s, v_p 7.5 km/s) and hornblendites (v_s 4 km/s, v_p 7.1 km/s) have 5 to 12 % lower seismic velocities than spinel lherzolites (v_s 4.6 km/s, v_p 8.1 km/s). Wehrlites have 2 to 3 % lower seismic velocities (v_s 4.5 km/s, v_p 7.9 km/s). Assuming lower temperatures (550°C), seismic velocities would increase by 0.05 km/s. At 2.0 GPa and 1000°C (extrapolation of the CT-geotherm published by *Čermák* [1994]) seismic velocities are reduced by about 0.1 km/s in comparison to the values at 1.0 GPa and 650°C. For the noritic sample seismic velocities were calculated at 0.6 GPa and 600°C (v_s 3.8 km/s, v_p 6.8 km/s).

D.1.2   The origin of the "6 s phase"

Considering all available information, it is possible to discuss the origin of the observed "6 s phase" in the receiver function study. As it is evident from receiver function modelling (Figures B.15, D.1) the origin of the "6 s phase" could be in the crust or mantle or both. As it is already mentioned above, no further move-out with epicentral distance can be observed; indicating that this converted phase might be of upper mantle origin. The independent observation of the converter at the same location at different stations (coherent stacking at upper mantle depths) may also be an argument for this interpretation. However, from the receiver functions alone I cannot favour model b or model e (Figure B.15b, e) at the moment. Both might be geological reasonable and fit the observed data very well.

Table D.I. Seismic velocities for hypothetic mantle assemblages beneath the swarm-earthquake region Vogtland/NW-Bohemia at specified pressure and temperature conditions. Temperatures of about 650°C near the Moho (1 GPa) and 1000°C at 2 GPa were assumed, according to the extrapolation of the CT-geotherm published by *Čermák* [1994]. The composition of the selected rocks is close to the composition of the ultramafic nodules analysed in this study. For the calculation the Excel-workbook of *Hacker and Abers* [2004] was used. Parameters for minerals were calculated from the mineral end-member values.

vol.%	norite	hbl-ite	cpx-hbl-ite	cpx-ite	wehrlite	wehrlite	hbl-peridotite	hbl-peridotite	sp-lherzolite 1	sp-lherzolite 1	sp-lherzolite 2	sp-lherzolite 2	dunite	dunite	pyrolite	harzburgite	lhz W	eclogite
alpha quartz																		6.0
high albite	24.0																	
anorthite	31.0																	
orthoclase																		
sanidine																		
almandine															2.1	0.7	5.2	18.0
grossular															1.1	0.5	2.2	13.0
pyrope															10.8	5.4	14.3	11.0
forsterite					44.5	44.5	49.8	49.8	60.0	60.0	76.0	76.0	91.0	91.0	54.5	61.7	51.4	
fayalite					5.0	5.0	10.2	10.2	6.0	6.0	8.0	8.0	9.0	9.0	6.7	5.4	5.7	
enstatite	26.3								16.4	16.4	9.6	9.6			14.7	16.8	1.1	
ferrosilite	10.2								1.6	1.6	1.0	1.0			1.5	1.6	0.1	4.0
diopside	6.3		36.0	75.0	44.1	44.1	8.2	8.2	13.7	13.7	4.6	4.6			7.4	6.7	18.0	24.0
hedenbergite	1.8		12.0	25.0	5.5	5.5	1.8	1.8	1.4	1.4	0.4	0.4					2.0	2.0
jadeite																		18.0
pargasite		100.0	47.0				25.0	25.0							1.2	1.2		
phlogopite	0.5		3.0															
muscovite																		
spinel					1.0	1.0	5.0	5.0	1.0	1.0	0.5	0.5						2.0
hercynite																		2.0
magnetite			2.0															
Sum	100.0	100.0	100.0	100.0	100.0	100.0	100.0	100.0	100.0	100.0	100.0	100.0	100.0	100.0	100.0	100.0	100.0	100.0
p (GPa)	0.6	1.0	1.0	1.0	1.0	2.0	1.0	1.5	2.0	1.0	1.0	2.0	1.0	2.0	1.0	2.0	2.0	1.0
T (°C)	600	650	650	650	650	1000	650	800	1000	650	650	1000	650	1000	650	1000	1000	650
Physical properties calculated with Hashin-Shtrikman average:																		
H_2O (wt%)	0.0	2.2	1.2	0.0	0.0	0.0	0.6	0.6	0.0	0.0	0.0	0.0	0.0	0.0	0.0	0.0	0.0	0.1
rho (g/cm3)	3.0	3.1	3.2	3.3	3.3	3.3	3.3	3.3	3.3	3.3	3.3	3.3	3.3	3.3	3.3	3.3	3.4	3.5
V_p (km/s)	6.77	7.12	7.23	7.52	7.87	7.77	7.79	7.76	7.70	7.98	7.86	7.96	8.07	8.17	7.99	7.97	8.06	7.95
V_s (km/s)	3.75	4.01	4.04	4.19	4.45	4.35	4.40	4.36	4.30	4.57	4.46	4.51	4.56	4.67	4.52	4.53	4.52	4.53
K (GPa)	81	89	98	110	117	115	115	115	114	117	116	119	122	124	122	119	127	126
G (GPa)	42	49	52	58	65	64	63	61	61	69	65	67	68	72	68	67	69	72
Poissons	0.28	0.27	0.27	0.28	0.27	0.27	0.27	0.27	0.27	0.26	0.26	0.26	0.26	0.26	0.27	0.26	0.27	0.26
v_p/v_s	1.80	1.78	1.79	1.80	1.77	1.77	1.78	1.79	1.79	1.75	1.76	1.77	1.77	1.75	1.77	1.76	1.78	1.75

D.1.2.1   Arguments for an upper mantle origin of the "6 s phase"

Further indications for local seismic discontinuities in the uppermost mantle beneath the Vogtland/NW-Bohemia region came from reflection seismic profiling. *Tomek et al.* [1997] detected three mantle reflectors (MR) at depths of 35 (MR$_1$), 42 (MR$_2$, box P in Figure B.14a), and 56 km (MR$_3$, box L in Figure B.14a) along the 9HR seismic profile (see Figure A.5). Reflector M$_1$ at about 32 km depth could also be interpreted to be of subcrustal origin. Unfortunately, it is not possible to interpret polarities of these reflections [*Tomek*, personal communication]. Reflection MR$_3$ argues for a local sharp discontinuity in the uppermost mantle instead of the gradient zone modelled in Figure B.15e. In case of a very local discontinuity no multiple converted phases could be observed.

Subcrustal lithospheric seismic discontinuities were previously found worldwide in a wide variety of tectonic settings [cf., *Hales*, 1969; *Ginzburg et al.*, 1979; *Keller et al.*, 1994; *Bostock*, 1999; *Ascencio et al.*, 2003; *Rost and Williams*, 2003]. Discussed causes of such discontinuities include spinel-to-garnet transition, compositional differences due to differentiation processes or the presence of partial melt, anisotropic layers with preferred orientation of olivine crystals, and relic subduction zone eclogitized oceanic crust.

Assuming that model e explains the "6 s phase", the piercing points of the analysed rays at 50 km depth were plotted (Figures B.14a, 15e) together with the results of the gas mapping of *Weinlich et al.* [1999] (see Figure A.4a). Interpreting the "6 s phase" as being of uppermost mantle origin, the distribution of red points in Figure B.14a marks more or less the areas with relatively reduced seismic velocities in the uppermost mantle above a converter. If the "6 s phase" is associated with upper mantle structure the average velocity reduction in the uppermost mantle above the converter might be up to 8 % ($v_p/v_s = 1.79$) or 5 % for v_p and 11.5 % for v_s ($v_p/v_s = 1.92$), respectively, relative to a "normal" upper mantle P-wave velocity of 8.0 km/s ($v_p/v_s = 1.79$). This could indicate the presence of 3 to 5 % melt or fluids in the uppermost mantle [according to *Faul et al.*, 1994]. Even less melt might be present using the values for velocity reduction obtained by *Hammond and Humphreys* [2000].

As discussed by *Glahn et al.* [1992], water-bearing minerals like phlogopite and amphibole can lower the seismic velocities in the uppermost mantle significantly. Up to now, orthopyroxene-bearing xenoliths could not be found in the Quaternary volcanics of the investigated area. The most common mantle xenoliths are wehrlites and clinopyroxenites characterizing the uppermost mantle beneath the study area as metasomatic. Some of them contain also significant amounts of amphibole. These rock types can have more than 5 % lower seismic velocities than normal upper mantle rocks lherzolitic-harzburgitic in composition (see Table D.I). This could explain at least some of the assumed velocity reduction. The higher seismic velocities beneath the discontinuity might represent "normal" upper mantle rocks or slightly depleted rocks (harzburgites/dunites) in the source region of alkaline magmas.
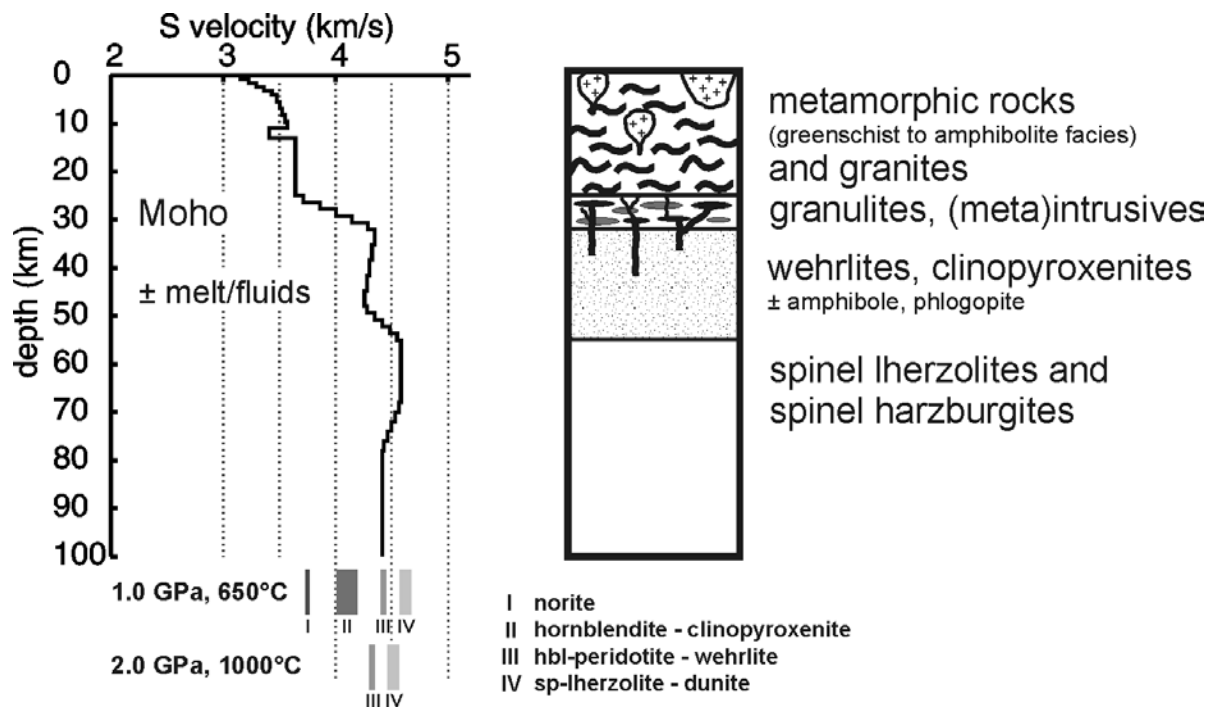
Figure D.1
Model of the Pleistocene lithosphere beneath the Železná Hůrka area. Left: Proposed present-day shear wave velocity model beneath NW-Bohemia for the area of the "6 s phase" (see Figure B.14). Also shown are the ranges of shear wave velocities for different (ultra-) mafic rock types at different temperature-pressure conditions. Temperatures of about 650°C near the Moho (1 GPa) and 1000°C at 2 GPa were assumed, according to the extrapolation of the CT-geotherm published by *Čermák* [1994]. For the calculation of the seismic velocities of rocks the Excel-workbook of *Hacker and Abers* [2004] was used (see Table D.I).
It should be pointed out, that it is not possible to derive true velocity-depth profiles using receiver functions alone, however the velocity difference across seismic discontinuities is more or less well resolved. Therefore, the comparison of the velocity-depth profile and the shear wave velocities calculated for different rock types should not be over-interpreted.
Right: Petrological crustal section derived from the xenolith study and local surface geology.

The assumption on the presence of partial melts in the uppermost mantle above the converter concur with the observed isotope signatures of the CO_2-dominated gas exhalations in the western Eger Rift [*Weinlich et al.,* 1999]. The gas escape centres with helium isotope signatures of the subcontinental lithospheric mantle (^{3}He/^{4}He ratios up to 5.9 Ra in the Cheb Basin) [*Bräuer et al.,* 2004] as well as the position of the Quaternary scoria cones of Komorní Hůrka and Železná Hůrka overlap with the position of the local converter/reflector in the depth of approximately 50 to 60 km (Figures A.5, B.14) [see also *Tomek et al.,* 1997].

The observed seismic converter/reflector at about 50 to 60 km depth might also be explained as related to the spinel lherzolite-garnet lherzolite transition as discussed by *O'Reilly and Griffin* [1985] for the uppermost mantle of southeastern Australia. Further constraints for a sharp seismic discontinuity in that depth range came from a study of *Webb and Wood* [1986], who showed that the transition might occur over a pressure interval of only about 2 kbar (6 km). However, up to now no garnet-bearing upper mantle xenoliths are reported from the Eger Rift area and the spinel stability field might be

expanded down to about 90 km [*Franz et al.,* 1997; *Medaris et al.,* 1999]. Therefore, I favour the interpretation that the seismic discontinuity is related to the base of a metasomatic uppermost mantle containing a few percent of melts.

As mentioned above, seismic discontinuities in the uppermost mantle could be related to the boundary between two layers with differently oriented seismic anisotropy. Seismic anisotropy in the upper mantle is indicated by SKS and P residua studies [e.g., *Bormann et al.,* 1996; *Plenefisch et al.,* 2001; *Babuška and Plomerová,* 2001]. But the observation of the „6 s phase" does not show clear dependence on the back-azimuth of analysed events. Also no coherent signals in the T-components could be identified in the present dataset. Such signals would indicate anisotropic seismic properties in the studied depth interval. Possibly, the existence of anisotropic layers could be proved or disproved with a more extended database [see also *Christensen et al.,* 2001].

Finally, the observed conversions might be caused by eclogites, representing material possibly subducted during the Variscan convergence. But up to now no eclogite xenoliths could be identified, but the possibility of their existence cannot be ruled out definitively. Further detailed studies on the lateral extension and possible depth variations of the converter/reflector might help to solve this question.

D.1.2.2   Arguments for a crustal origin of the "6 s phase"

There are also arguments for a possible discontinuity at the base of the upper crust (model in Figure B.15b). The nature of the seismicity in the investigated area indicates a fluid-rich seismogenic crust. The earthquake swarms are commonly interpreted as fluid-triggered seismicity [*Špičak et al.,* 1999; *Dahm et al.,* 2000; *Špičak and Horálek,* 2001; *Horálek et al.,* 2002; *Plenefisch et al.,* 2003; *Vavryčuk,* 2002; *Fischer and Horálek,* 2003]. *Weise et al.* [2001] calculated the CO_2 volume of crustal origin, released by seismically induced micro-fracturing in December 1994 to be between 9.3×10^{10} and 0.1×10^{10} l. Fluid traps in the seismogenic upper crust are of local dimension and possibly spot-like distributed [*Behr et al.,* 1994; *Boušková et al.,* 2003; *Parotidis et al.,* 2003]. Furthermore, the rareness of CO_2 exhalations directly in the epicentral area of Nový Kostel could be explained with permeability barriers, capping the hydraulic system. Mantle-derived fluids may be trapped in the crustal segment below such a barrier [*Bräuer et al.,* 2003].

Because of geochemical evidences and indications from reflection seismic profiling, a combination of both velocity models b and e with half the amplitudes of each anomalous layer might also be plausible (Figures B.15f, D.1).

D.2   The structure of the crust and the subcrustal mantle beneath

 the western Eger (Ohře) Rift – towards a process orientated model

The observed anomaly at the Moho level and the local indications for a seismic converter/reflector at about 50 to 60 km depth concur with the distribution of the CO_2 emanation centres and the Quaternary volcanoes at the surface, as well as with the main swarm-earthquake activity in the upper crust of the Vogtland/NW-Bohemia area. Therefore, I believe that all these observations are somehow interrelated by an active zone of mantle melting and magmatic underplating, associated with recent extensional tectonics, which may be illustrated by Figure D.2.

The helium isotopic signature of several CO_2 vents at the surface reaches up to 5.9 Ra. This is an evidence for the origin of the CO_2-dominated gas phase from subcontinental lithospheric mantle (SCLM) according to *Gautheron and Moreira* [2002] and *Bräuer et al.* [2004]. CO_2 and other volatile components (e.g. Ar, H_2O, N_2, Ne) are included in the partial melting process of the upper mantle (at approximately 90 to 100 km depth). There need to be no difference between transport of the CO_2 (and other volatiles) and the magma transport in the upper mantle. *Weinlich et al.* [1999] evaluated the composition of the magmas in the uppermost mantle of the working area and calculated the magmatically dissolved CO_2 portion. Results of thermobarometric studies on melt and carbon dioxide inclusions in Saxon Tertiary alkalibasaltic volcanics and peridotite xenoliths [*Thomas*, 1992] argues, that the formation of a CO_2-dominated gas phase (the separation of CO_2 from the melt) starts in the depth range of 30 to 21 km. Further studies on fluid inclusions in upper mantle derived rocks indicate that a free gas phase can exist at least up to 1.2 to 1.4 kbar and maybe down to 70 km [cf., *Pasteris,* 1987; *Andersen and Neumann,* 2001]. So I conclude, CO_2 with SCLM-signature at surface is directly linked to magmatic processes and the melt reservoir(s) in the uppermost mantle, or as discussed above to metasomatic processes in the uppermost mantle (also related to alkaline magmatism).

The structural (seismic) and petrological (xenoliths) results of this study in combination with the geochemical and isotope evidence from previous investigations enable to find a link for mantle-crust interaction processes at different depths (Figure D.2). From bottom to top I try to relate a number of features to presently active magmatic underplating processes overprinting the Cainozoic Eger Rift environment.

Asthenospheric up-welling beneath the western Eger Rift area is indicated by different studies [*Rajkes and Bonjer,* 1983; *Faber et al.,* 1986; *Plomerová and Babuška,* 1988; *Plešinger et al., 1994; Passier and Snieder;* 1996; *Plomerová et al.,* 1998; *Babuška and Plomerová,* 2001]. An **isolated subcrustal seismic converter/reflector** exists at a depth of approximately 50 to 60 km ["6 s phase", *this study*; *Tomek et al.,* 1997], which can be interpreted as the base of a zone of a highly metasomatic

mantle (containing wehrlites, clinopyroxenites, amphibole-peridotites) infiltrated by melts (magma/fluid reservoirs). Besides that, the position of a **local scale Moho updoming** from about 31 in the surroundings to 27 km in the centre (NNW-SSE extension of 40 km) overlaps with a presently active **CO_2 mantle-degassing field** showing clear upper mantle derived helium portions [*Weinlich et al.,* 1999, 2003; *Geissler et al.,* 2004a]. Decreased sub-Moho P-wave velocities of 7.6 to 7.7 km/s [*Giese,* 1976; *Hemmann,* 2002; *Hemmann et al.,* 2003] together with local observations of **weak or absent Moho conversions** [*this study*] point to a complex transition zone rather than a sharp velocity contrast at the crust-mantle boundary. Thermal and magmatic overprinting of the crust-mantle boundary in this region with small intrusions into the lower crust might cause a locally complex and broad Moho transition zone. As it is assumed by different authors [e.g., *McKenzie,* 1984; *Furlong and Fountain,* 1986; *Mengel and Kern,* 1991], the crust-mantle boundary acts as a barrier for ascending mafic magmas (ponding region). I suppose, the observed seismic Moho beneath the region is a relatively young feature. **Increased reflectivity in the lower crust** northeast of the KTB and beneath the Vogtland area [*Trappe and Wever,* 1990; *Behr et al.,* 1994; *Bleibinhaus et al.,* 2003] may be interpreted as low angle shear zones partly filled with fluids and/or small magmatic intrusions (hornblendite and clinopyroxenite sills/dikes) or partial melting [cf., *Matthews,* 1986; *Wever and Meissner,* 1987; *Vanderhaege and Teyssier,* 1997]. A decreased thickness of seismogenic (brittle) upper crust and repeated occurrence of **earthquake swarms** are observed above the Moho updoming and the local converters in the subcrustal mantle [*Horálek et al.,* 2000b, *this study*], which can be interpreted as rheological effects related to CO_2-dominated fluids. "Secondary phases" are observed in some local NW-Bohemia seismograms [*Boušková et al.,* 2003], which may originate at short distances from the hypocentres and are possibly caused by **spot-like low velocity zones** at the base of the upper crust filled with fluids.

The compilation of all results of previous and this studies indicates a systematic mantle/crust coupling maybe by the emplacement of mafic magmas near the base of the continental crust beneath the western Eger Rift. From bottom to top the following sub-processes can be distinguished (Figure D.2):

(1) release of CO_2-dominated fluid/magma from isolated crystallizing melt-reservoirs and/or metasomatic reactions in the depth range of 60 to 30 km; (2) active Moho updoming from about 31 to 27 km caused by thinning of the ductile lower crust at low angle shear zones as a consequence of magma/fluid/heat transport; (3) intrusion of alkaline melts into the lower crust forming dikes and sills (hornblendites, clinopyroxenites); (4) separation of CO_2 from such melts at 29 to 21 km depths and channel-like CO_2 transport through the crust; (5) occurrence of fluid triggered seismicity (earthquake swarms) in the depth range of 15 to 6 km which is caused by high pore fluid pressure in local captured upper crustal environment; (6) permeability of the upper crust beneath the area under investigation enable high permanent CO_2 transport through the upper crust.

This process is known under the term "magmatic underplating" in literature [*Furlong and Fountain*, 1986; *Griffin and O'Reilly*, 1987; *Cox*, 1993]. Geological, geophysical, and geochemical evidence suggest that magmatic underplating in extensional tectonic regimes is a first order process in the formation, growth, and modification of the oceanic and continental crust [cf., *Griffin and O'Reilly*, 1987; *O´Nions and Oxburgh*, 1988; *Jarchow et al.*, 1993; *Hansteen et al.*, 1998; *Grevemeyer and Flueh*, 2000; *Sachs and Hansteen*, 2000]. Seismic detecting of active magmatic underplating is clearly illustrated by the mid-ocean ridge magma additions [e.g., *Detrick et al.*, 1987; *Garmany*, 1989; *Caress et al.*, 1995]. Examples from the continental crust are rare in the literature [*Jarchow et al.*, 1993].
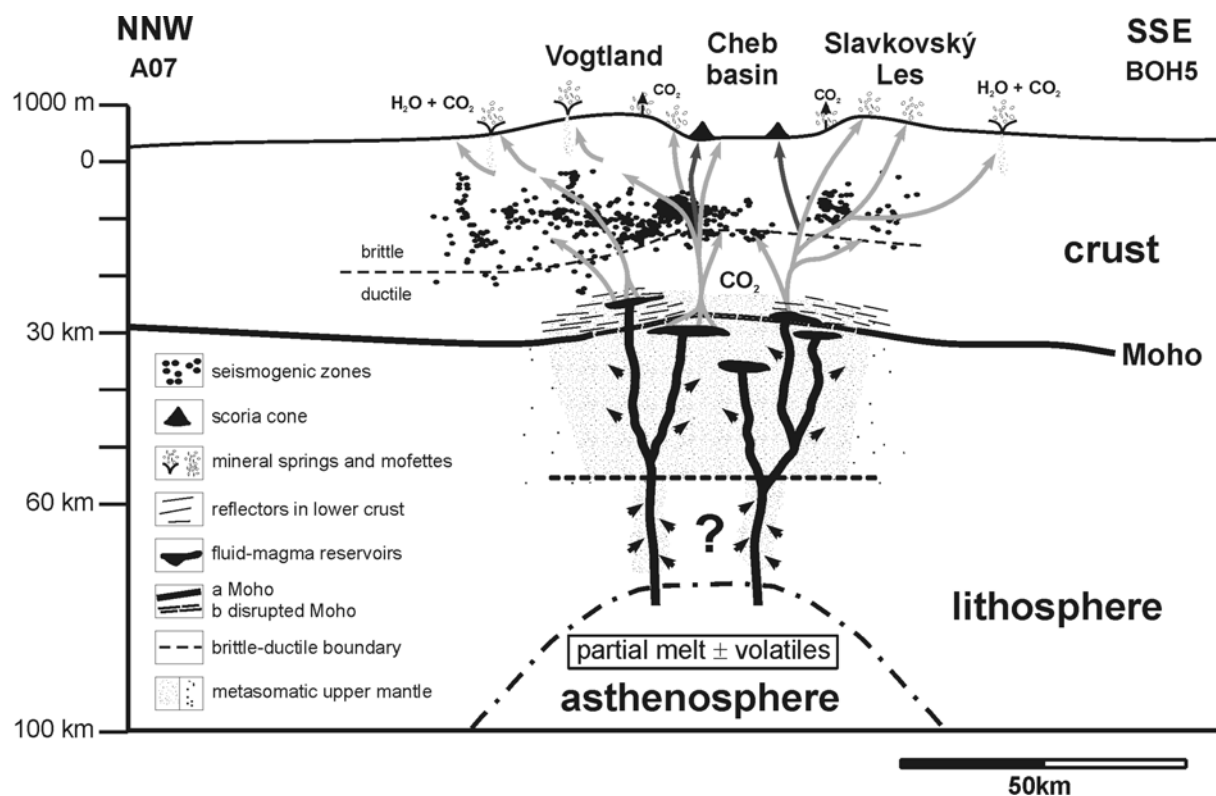
Figure D.2
Cartoon illustrating the asthenosphere-lithosphere interaction in the Vogtland/NW-Bohemia region.
The results of former studies [*Trappe and Wever*, 1990; *Tomek et al.*, 1997; *Vrána et al.*, 1997; *Babuška and Plomerová*, 2001; *Weinlich et al.*, 1999, 2003; *Horálek et al.*, 2000; *Bräuer et al.*, 2003, 2004] and the seismic and petrological results of this study were compiled. Black channels mark uprising CO_2 dissolved in melts; grey channels mark the CO_2/fluid transport through crust.
Observed converted phases at 6 seconds delay time might be caused by a thin low-velocity layer at the base of the seismogenic zone or at the base of a zone in the upper mantle with reduced seismic velocities. Reduced delay times of weak or lacking Moho conversions beneath the western Eger Rift points to overprinting of the crust-mantle boundary by magmatic and tectonic processes. Increased reflectivity within the lower crust and reduced thickness of the brittle upper crust possibly indicate that the discussed processes also affect the lower crust. Most of the seismic swarm activity is concentrated under the Vogtland area, whereas very little activity was detected in the other high CO_2 discharge zone in the Slavkovský Les area. This could be caused by the local crustal geology (Vogtland: interbedding of metasediments and metabasites / permeability barriers in seismogenic zones [*Bräuer et al.*, 2003]; Slavkovský Les: block of metabasites + granites) or differences in the local stress field.

E   Conclusions and open questions

The detailed mapping of the crust-mantle boundary in the western Eger Rift was done using Ps receiver functions with a higher lateral resolution than it is possible by refraction seismic studies. The lithospheric structural features observed in this study are of local dimension. Only due to a dense spacing of seismic stations and sufficiently long recording times of medium- to broadband stations it was possible to resolve them. Crustal and Moho arrivals could also be observed studying the data from the permanent triggered short-period networks in NW-Bohemia, but it was not possible to invert these data for Moho depth and v_p/v_s ratios due to missing crustal multiples.

The cause of some low average crustal v_p/v_s ratios (1.63 to 1.67) in the study area remains unsolved. The interpretation of v_p/v_s ratios needs further effort, the application of laboratory measurements to in-situ conditions, especially.

Using teleseismic receiver functions a local "6 s phases" was detected underneath the area of CO_2 emanations and Quaternary volcanism, which could be interpreted as caused by a converter at about 50 to 60 km depth and/or a low velocity zone in the middle crust. Previously, a reflector was detected by reflection seismic studies at 55 km depth [*Tomek et al.,* 1997]. New wide-angle seismic data also show a local reflector at this depth range [*Hrubcova,* personal communication]. More seismic data, detailed analysis, as well as more petro- and mineral-physical data are needed to clarify the extend and the nature of this probable local seismic upper mantle discontinuity.

New, more detailed results can be obtained from running active and passive seismic investigations in the area. The huge data set of the BOHEMA project 2000-2003 (including receiver function, tomography and anisotropy studies) is already under investigation [*Babuška et al.,* 2003]. Further detailed velocity information at least for the crust can be expected from wide-angle seismic experiments, which were carried out recently, namely CELEBRATION-2000 and SUDETES-2003 [*Guterch et al.,* 2003]. A synopsis of the results from passive seismic investigations, wide-angle seismic experiments, and the re-processing of the deep-seismic profile 9HR would be very useful to improve the location and identification of velocity contrasts of the seismic discontinuities.

The existence of a mantle finger like proposed under the French Massif Central and the Eifel, Germany, could not be proved or denied in this study. However, the apparent deepening of the '410' beneath the study area might indicate for the presence of lower seismic velocities in the upper mantle than in the IASP91 reference model.

The xenolith study showed that most of the analysed samples are cumulates of alkaline melts or fragments of a metasomatic upper mantle; no orthopyroxene-bearing spinel-lherzolitic xenoliths were found in the Quaternary volcanics up to now. Geothermobarometric estimates for most samples indicate a depth of origin of about 25 to 40 km. This depth range might be the intrusion level for the

alkaline melts in the past and also presently, since there are still exhalations of gases with upper mantle isotope signatures (C, He, N) at the surface in the area under study [*Bräuer et al.*, 2004].

Calculated equilibrium or crystallization temperatures are higher than indicated by the extrapolation of regional geotherms derived from surface heat flow studies. Hornblendite and clinopyroxenite samples could be fragments of small magmatic intrusions into the uppermost mantle and lower crust (dikes and sills), which could cause local scale thermal and magmatic overprinting of the Moho as, indicated by the receiver function study. However, the studied xenolith suite and available p-T data from the broader region do not allow making better constraints (xenolith geotherm) on the overall thermal structure in the lower crust and uppermost mantle so far. Further studies on xenoliths from Tertiary and Quaternary volcanics (including p-T, isotope, and fluid/melt inclusion studies) are necessary for the construction of a regional xenolith geotherm and the understanding of the Tertiary to Quaternary evolution of the upper mantle and lower crust.

There are a lot of further questions related to the possible existence of and processes related to a covered deep-seated magmatic activity beneath the swarm-earthquake region and CO_2 degassing field. There is a massive need for the identification of seismic reflections/conversion related to fluids in the lower crust and uppermost mantle in the existing and new seismic data. Further fluid inclusion studies could help to identify the depth level of separation of CO_2 from melts. The question if the alkaline melts play a direct role in the hypocentres of swarm-earthquakes as supposed by *Špičák et al.* [1999] can possibly be solved by improved seismological and noble gas isotope observations or as a final stage deep drilling. Very interesting would be the study of seismicity related to possible fluid movements in the middle and lower crust. Maybe a new sensitive seismic network with still better signal-to-noise ratio than the existing ones (seismometers in boreholes?) can shed some light on deep low-magnitude seismicity. Assuming that magmatic activity has been going on since the Tertiary but at least since 0.3 to 0.5 Ma, there should be a thermal signal somewhere in the crust. To find signals of this probable thermal perturbation heat flow studies in one or more deep boreholes are necessary.

In this work, a first compilation of seismic, petrological [*this study*], seismological, and gas-geochemical results [*from literature*] was done, which might point to a local scale active magmatic addition to the base of the continental crust in a rift environment. CO_2-rich gases (fluids) rising from melts at the crust-mantle boundary to the Earth's surface influence the seismicity of the upper crust. The combination of these different geoscientific methods has a high potential for the detection and evaluation of deep covered magmatic/fluid activity within continental rift areas. The observations should be confirmed by additional measurements in Vogtland/NW-Bohemia as well as in other volcanic fields of Western and Central Europe (e.g., the French Massif Central, the Eifel, and the Jeseniky volcanic fields).

Acknowledgements

References

Adam, J. and T.H. Green, The effects of pressure and temperature on the partitioning of Ti, Sr and REE between amphibole, clinopyroxene and basanitic melts, *Chem. Geol., 117,* 219-233, 1994.

Aichele, H., Interpretation refraktionsseismischer Messungen im Gebiet des Fränkisch-Schwäbischen Jura, *Doctoral thesis, 105p.*, Stuttgart, 1976.

Alinaghi, A., G. Bock, R. Kind, W. Hanka, K. Wylegalla, TOR and SVEKALAPKO Working Groups, Receiver function analysis of the crust and upper mantle from the North German Basin to the Archaen Baltic Shield, *Geophys. J. Int., 155,* 641-652, 2003.

Allen, J.C., A.L. Boettcher, and G. Marland, Amphiboles in andesite and basalts: I. Stability as a function of P-T-fO$_2$, *Am. Min., 60,* 1069-1085, 1975.

Anders, E. and N. Grevesse, Abundances of the elements: Meteoric and solar. *Geochimica et Cosmochimica Acta, 53,* 197-214, 1989.

Anderson, T. and E.-R. Neumann, Fluid inclusions in mantle xenoliths, *Lithos, 55*, 301-320, 2001.

Ascencio, E., J.H. Knapp, T.J. Owens, and G. Helffrich, Mapping fine-scale heterogeneities within the continental mantle lithosphere beneath Scotland: Combining active- and passive-source seismology, *Geology, 31(6),* 477-480, 2003.

Babuška, V. and J. Plomerová, Subcrustal lithosphere around the Saxothuringian-Moldanubian Suture Zone - a model derived from anisotropy of seismic wave velocities, *Tectonophysics, 332*, 185-199, 2001.

Babuška V., J. Plomerová, and BOHEMA working group, Seismic Experiment Searches for Active Magmatic Source in Deep Lithosphere, Central Europe, *EOS Transactions, 84(40),* 409, 416-417, 2003.

Bachmann, G.H., M. Müller, and K. Weggen, Evolution of the Molasse Basin (Germany, Switzerland), *Tectonophysics, 137,* 77-92, 1987.

Baldridge, W.S., G.R. Keller, V. Haak, E. Wendlandt, G.R. Jiraček, and K.H. Olsen, The Rio Grande Rift; in *Continental rifts: evolution, structure, tectonics, Developments in Geotectonics, vol. 25,* edited by K.H. Olsen, 233-275, Elsevier, 1995.

Ballhaus, C., R.F. Berry, and D.H. Green, High pressure experimental calibration of the olivine-orthopyroxene-spinel oxygen geobarometer: implications for the oxidation state of the upper mantle, *Contrib. Mineral. Petrol., 107,* 27-40, 1991.

Bankwitz, P., G. Schneider, H. Kämpf, and E. Bankwitz, Structural characteristics of epicentral areas in Central Europe: Study case Cheb Basin (Czech Republic), *J. Geodyn.*, 35, 5-32, 2003a.

Bankwitz, P., E. Bankwitz, K. Bräuer, H. Kämpf, and M. Störr, Deformation structures in Plio- and Pleistocene sediments (NW Bohemia, Central Europe), *Geol. Soc. Spec. Pub., London, 216,* 73-93, 2003b.

Barclay, J. and I.S.E. Carmichael, A Hornblende Basalt from Western Mexico: Water-saturated Phase Relations Constrain a Pressure-Temperature Window of Eruptibility, *J. Petrol., 45(3),* 485-506, 2004.

Bayerisches Geologisches Landesamt, Geologie von Bayern, CD-ROM, Bayerisches Geologisches Landesamt, München, 1998.

Becker, H.J., Pyroxenites and hornblendites from the maar-type volcanoes of the Westeifel, Federal Republic of Germany, *Contrib. Mineral. Petrol., 65,* 45-52, 1977.

Behr, H.-J., H.-J. Dürbaum, and P. Bankwitz (Editors), Crustal structure of the Saxothuringian Zone: Results of the deep seismic profile MVE-90(East), *Z. geol. Wiss., 22(6),* 647-769, 1994.

Best, M.G., Igneous and metamorphic petrology, Blackwell Science, Oxford, 2003.

Bleibinhaus, F., D. Stich, M. Simon, and H. Gebrande, New results from amplitude preserving prestack depth migration of the Münchberg/Vogtland segment of the MVE deep seismic survey, *J. Geodyn., 35*, 33-43, 2003.

Blundy, J.D. and T.J.B. Holland, Calcic amphibole equilibria and a new amphibole-plagioclase geothermometer, *Contrib. Mineral. Petrol., 104,* 208-224, 1990.

Bormann, P. (Ed.), Monitoring and analysis of the earthquake swarm 1985/86 in the region Vogtland/Western Bohemia, *ZIPE-Veröff., Nr. 110*, 282 p., Zentralinstitut für Physik der Erde, Potsdam, 1989.

Bormann, P, P., Bankwitz, W. Conrad, and Ch. Oelsner, Crustal structure and development in Central Europe. *Gerlands Beitr. Geophysik, 98/5,* 353-367, Leipzig, 1989.

Bormann, P., G. Grünthal, R. Kind, and H. Montag, Upper mantle anisotropy beneath Central Europe from SKS wave splitting: effects of absolute plate motion and lithosphere-asthenosphere boundary topography?, *J. Geodyn., 22 (1/2),* 11-32, 1996.

Bostock, M.G., Seismic imaging of lithospheric discontinuities and continental evolution, *Lithos, 48*, 1-16, 1999.

Boušková, A., J. Horálek, T. Fischer, and Z. Hudová, Time and Space Variations of Local Seismic Signals in the NW-Bohemia/Vogtland Swarm Region, *Geophys. Research Abstracts, Vol. 5,* 08495, 2003.

Boušková, A., T. Fischer, J. Horálek, and Z. Hudová, Seismic activity after 2000 swarm and new results in the Western Bohemia/Vogtland area, *Geolines, 17,* 25, 2004.

References

Braile, L.W., B. Wang, C.R. Daudt, G.R. Keller, and J.P. Patel, Modeling the 2-D seismic velocity structure across the Kenya rift, in *Crustal and upper mantle structure of the Kenya rift*, edited by C. Prodehl, G.R. Keller and M.A. Khan, *Tectonophysics, 236,* 179-200, 1994.

Bräuer, K., H. Kämpf, G. Strauch, and S.M. Weise, Isotopic evidence (^{3}He/^{4}He, ^{13}C$_{CO2}$) of fluid-triggered intraplate seismicity, *J. Geophys. Res., 108(B2),* 2070, doi: 10.1029/2002JB002077, 2003.

Bräuer, K., H. Kämpf, S. Niedermann, G. Strauch, and S.M. Weise, Evidence for a nitrogen flux directly derived from the European subcontinental mantle in the western Eger Rift, Central Europe, *Geochim. Cosmochim. Acta, 68,* 4935-4947, 2004.

Brey, G.P. and T. Köhler, Geothermometry in Four-phase Lherzolites II. New Thermobarometers, and Practical Assesment of Existing Thermobarometers, *J. Petrol., 31(6),* 1353-1378, 1990.

Caress, D.W., M.K. McNutt, R.S. Detrik, and J.C. Mutter, Seismic imaging of hotspot related crustal underplating beneath the Marquesas Island, *Nature, 373,* 600-603, 1995.

Christensen, N.I., Poisson's ratio and crustal seismology, *J. Geophys. Res., 101(B2),* 3,139-3,156, 1996.

Christensen, N.I., Section VI – Seismic velocities, in *Practical Handbook of Physical Properties of Rocks and Minerals,* edited by I.S.E. Carmichael, 430-546, CRC press, Cleveland Ohio, 1989.

Christensen, N.I. and W.D. Mooney, Seismic velocity structure and composition of the continental crust: A global view, *J. Geoph. Res., 100(B7),* 9761-9788, 1995.

Christensen, N.I., L.G. Medaris Jr., H.F. Wang, and E. Jelínek, Depth variation of seismic anisotropy and petrology in central European lithosphere: A tectonothermal synthesis from spinel lherzolite, *J. Geophys. Res., 106(B1),* 645-664, 2001.

Čermák, V., Results of Heat Flow Studies in Czechoslovakia, in *Crustal Structure of the Bohemian Massif and the West Carpathians, Exploration of the Deep Continental Crust,* edited by V. Bucha, and M. Blížkovský, 85-120, Springer-Verlag Berlin Heidelberg New York, 1994.

Chevrot, S., Vinnik, L.P., and J.-P. Montagner, Global-scale analysis of the mantle Pds phases, *J. Geophys. Res., 104(B9),* 20,203-20,219, 1999.

Clauser, C., P. Giese, E. Huenges, T. Kohl, H. Lehmann, L. Rybach, J. Safanda, H. Wilhelm, K. Windloff, and G. Zoth, The thermal regime of the crystalline continental crust: Implications from the KTB, *J. Geophys. Res., 102(B8),* 18,417-18,441, 1997.

Cox, K.G., Continental magmatic underplating, *Phil. Trans. R. Soc. Lond., A 342,* 155-166, 1993.

Credner, H., Die vogtländischen Erdbebenschwärme während der Zeit des Juli und August 1900, *Ber. ü. Verh. Kgl. Sächs. Ges. Wiss. Leipzig*, 52, 153-177, 1900.

Dahm, T., J. Horálek, and J. Šílený, Comparison of absolute and relative moment tensor solutions for the January 1997 West Bohemia earthquake swarm, *Studia geoph. et geod., 44(2),* 233-250, 2000.

Deer, W.A., R.A. Howie, and J. Zussmann, Rock-forming minerals vol. 5: Non-Silicates, Longmans, Green and Co Ltd, London, 371 p, 1963.

Deer, W.A., R.A. Howie, and J. Zussmann, An Introduction to the Rock-Forming Minerals – 2nd edition, Longman Scientific & Technical, Burnt Mill, Harlow, 1992.

DEKORP Research Group, Results of the DEKORP 4/KTB Oberpfalz deep seismic reflection investigations, *J. Geophys., 62,* 69-101, 1988.

DEKORP Research Group (B), The deep seismic reflection profiles DEKORP 3/MVE-90, *Z. für geol. Wiss., 22(6),* 623-825, 1994.

DEKORP and Orogenic Processes Working Groups, Structure of the Saxonian granulites: geological and geophysical constraints on the exhumation of high-pressure/high-temperature rocks in the mid-European Variscan belt, *Tectonics, 18(5),* 756-773, 1999.

Detrik, R.S., P. Buhl, E. Vera, J. Mutter, J. Orcutt, J. Madsen, and T. Brocher, Multi-channel seismic imaging of a crustal magma chamber along the East Pacific Rise, *Nature, 326,* 35-41, 1987.

Dezes, P. and P.A. Ziegler, Depth of the European Moho, http://comp1.geol.unibas.ch, 2002.

Dezes, P., S.M. Schmid, and P.A. Ziegler, Evolution of the European Cenozoic Rift System: interaction of the Alpine and Pyrenean orogens with their foreland lithosphere, *Tectonophysics, 389,* 1-33, 2004.

Downes, H., The nature of the lower continental crust of Europe: petrological and geochemical evidence from xenoliths, *Phys. Earth Planet. Inter., 79,* 195-218, 1993.

Downes, H., Formation and Modification of the Shallow Sub-continental Lithospheric Mantle: a Review of Geochemical Evidence from Ultramafic Xenolith Suites and Tectonically Emplaced Ultramafic Massifs of Western and Central Europe, *J. Petrol., 4,* 233-250, 2001.

Dulski, P., Reference Materials for Geochemical Studies: New Analytical Data by ICP-MS and Critical Discussion of Reference Values, *Geostandards Newsletter, 25(1),* 87-125, 2001.

Dziewonski, A.M. and D.L. Anderson, Preliminary reference Earth model, *Phys. Earth Planet. Inter., 25,* 297-356, 1981.

Emmermann, R. and J. Lauterjung, The German Continental Deep Drilling Program KTB: Overview and major results, *J. Geophys. Res., 102,* 18,179-18,201, 1997.

Enderle, U., K. Schuster, C. Prodehl, A. Schulze, and J. Bribach, The refraction seismic experiment GRANU95 in the Saxothuringian belt, SE-Germany, *Geophys. J. Int., 133,* 245-259, 1998.

Ernst, W.G. and J. Liu, Experimental phase-equilibrium study of Al- and Ti-contents of calcic amphibole in MORB – A semiquantitative thermobarometer, *Am. Min., 83,* 952-969, 1998.

Faber, S., J. Plomerová, and V. Babuška, Deep-seated lateral variations beneath the GRF array inferred from mislocation patterns and P residuals, *J. Geophys., 60,* 139-148, 1986.

Fabries, J., Spinel-olivine geothermometry in peridotites from ultramafic complexes, *Contrib. Mineral. Petrol., 69,* 329-336, 1979.

Fabries, J., J.-P. Lorand, and M. Guiraud, Petrogenesis of the amphibole-rich veins from the Lherz orogenic lherzolite massif (Eastern Pyrenees, France): a case study for the origin of the orthopyroxene-bearing amphibole pyroxenites in the lithospheric mantle, *Contrib. Mineral. Petrol., 140,* 383-403, 2001.

Faul, U.H., D.R. Toomey, and H.S. Waff, Intergranular basaltic melt is distributed in thin, elongated inclusions, *Geoph. Res. Lett., 21(1),* 29-32, 1994.

Fei, Y., J. van Orman, J. Li, W. van Westrenem, C. Sanloup, W. Minarik, K. Hirose, T. Komabayashi, M. Walter, and K. Funakoshi, Experimentally determined postspinel transformation boundary in Mg2SiO4 using MgO as internal pressure standard and its geophysical implications, *J. Geophys. Res., 109,* B02305, doi:10.1029/2003JB002552, 2004.

Ferrucci, F., A. Hirn, G. De Natale, J. Virieux, and L. Mirabile, P-SV Conversions at a Shallow Boundary Beneath Campi Flegrei Caldera (Italy): Evidence for the Magma chamber, *J. Geoph. Res. 97(B11),* 15,351-15,359, 1992.

Fiala, J. and Z. Vejnar, The Cheb-Dyleň Crystalline Unit, relations to the Moldanubian Zone, *in Geological model of Western Bohemia related to the KTB borehole in Germany,* edited by S. Vrána and V. Štědrá, *J. Geol. Sci., Geology, 47,* 56-57, 1997.

Fiala, J. and Z. Vejnar, The lithology, geochemistry, and metamorphic gradation of the crystalline basement of the Cheb (Eger) Tertiary Basin, Saxothuringian Unit, *Bull. Geosciences, 79(1),* 41-52, 2004.

Fischer, T. and J. Horálek, Space-time distribution of earthquake swarms in the principal focal zone of the NW-Bohemian/Vogtland seismoactive region: period 1985-2001, *J. Geodyn., 35,* 125-144, 2003.

Förster A. and H.-J. Förster, Crustal composition and mantle heat flow: Implications from surface heat flow and radiogenic heat production in the Variscan Erzgebirge (Germany), *J. Geophys. Res., 105(B12),* 27,917-27,938, 2000.

Förster, A., H.-J. Förster, and D. Stromeyer, An internally consistent present-day thermo-petrological model of the Erzgebirge crust (ext. abstr): Intern. Conf. Geology without Frontiers, Czech and Slovak Geological Societies, *J. Czech Geol. Soc., 48, 1-1,* 49-50, 2003.

Franz, L. and W. Seifert, Basement studies in a continental suture zone – Xenoliths from the Mid-German Crystalline Rise (Rhön area, Mid-European Variscides), *N. Jb. Miner. Abh., 173(3),* 263-303, 1998.

Franz, L., W. Seifert, and W. Kramer, Thermal evolution of the mantle underneath the Mid-German Crystalline Rise: Evidence from mantle xenoliths from the Rhön area (Central Germany). *Mineral. Petrol., 61,* 1-25, 1997.

Frey, F.A. and M. Prinz, Ultramafic inclusions from San Carlos, Arizona: petrologic and geochemical data bearing on their petrogenesis, *Earth Planet. Sci. Lett., 38,* 129-176, 1978.

Furlong, K. and D.M. Fountain, Continental Crustal Underplating: Thermal Considerations And Seismic-Petrologic Consequences, *J. Geoph. Res., 91(B8),* 8285-8294, 1986.

Garmany, J., Accumulations of melt at the base of young oceanic crust, *Nature, 340,* 628-632, 1989.

Gautheron, C. and A. Moreira, Helium signature of the subcontinental lithospheric mantle, *Earth Planet. Sci. Lett., 199,* 39-47, 2002.

Geissler, W.H., H. Kämpf, R. Kind, K. Bräuer, K. Klinge, T. Plenefisch, J. Horálek, J. Zednik, and V. Nehybka, Seismic location of a CO2 source in the upper mantle of the western Eger rift, Central Europe, *Tectonics, subm,* 2004a.

Geissler, W.H., H. Kämpf, P. Bankwitz, E. Bankwitz, Das quartäre Tephra-Tuff-Vorkommen von Mýtina (Südrand des westlichen Eger-Grabens/Tschechische Republik): Indikationen für Ausbruchs- und Deformationsprozesse, *Z. Geol. Wiss. 32(1),* 31-54, 2004b.

Giese, P., Results of the Generalized Interpretation of the Deep-Seismic Sounding Data, in *Explosion Seismology in Central Europe - Data and Results*, edited by P. Giese, C. Prodehl, and A. Stein, *Crustal and Upper Mantle Structure in Europe, No. 1*, 201-214, Springer Verlag Berlin Heidelberg New York, 1976.

Giese, P., Main Features of Geophysical Structures in Central Europe, in *Pre-Permian Geology of Central and Eastern Europe,* edited by R.D. Dallmeyer, W. Franke, and K. Weber, pp. 7-25, Springer-Verlag Berlin Heidelberg, 1995.

Ginzburg, A., J. Makris, K. Fuchs, B. Perathoner, and C. Prodehl, Detailed structure of the crust and upper mantle along the Jordan-Dead Sea Rift, *J. Geophys. Res., 84,* 5605-5612, 1979.

Glahn, A., P.M. Sachs, and U. Achauer, A teleseismic and petrologic study of the crust and upper mantle beneath the geothermal anomaly Urach/SW-Germany, *Phys. Earth Planet. Interior, 69,* 176-206, 1992.

Goes, S., W. Spakman, and H. Bijwaard, A Lower Mantle Source for Central European Volcanism, *Science, 286,* 1928-1930, 1999.

References

Gossler, J., R. Kind, S.V. Sobolev, H. Kämpf, K. Wylegalla, M. Stiller, and TOR Working Group, Major crustal features from the Harz Mountains to the Baltic Shield derived from receiver functions. *Tectonophysics, 314(1-3),* 321-333, 1999.

Granet, M., M. Wilson, and U. Achauer, Imaging a mantle plume beneath the Massif Central (France), *Earth Planet Sci. Lett., 136,* 281-296, 1995.

Gray, A.L., Inductively Coupled Plasma Source Mass Spectrometry, in *Inorganic Mass Spectrometry*, edited by F. Adams, R. Gijbel, and R. Van Grieken, pp. 257-300, Wiley-Interscience, New York, 1988.

Green, D.H. and T.J. Falloon, Pyrolite: A Ringwood Concept and Its Current Expression, in *The Earth's Mantle – Composition, Structure and Evolution*, edited by I. Jackson, pp. 311-378, Cambridge University Press, Cambridge-New York-Melbourne, 1998.

Grevemeyer, I. and E.R. Flueh, Crustal underplating and its implications for subsidence and state of isostasy along the Ninetyeast Ridge hotspot trail, *Geophys. J. Int. , 142,* 643-649, 2000.

Griesshaber, E., R.K. O´Nions, and E.R. Oxburgh, Helium and carbon isotope systematics in crustal fluids from the Eifel, the Rhine Graben and Black Forest, F.R.G., *Chem. Geol., 99,* 213-235, 1992.

Griffin, W.L. and S.Y. O'Reilly, The composition of the lower crust and the nature of the continental Moho – xenolith evidence, in *Mantle Xenoliths,* edited by P.H. Nixon, 413-430, John Wiley & Sons Ltd., 1987.

Guterch, A., M. Grad, A. Špičák, E. Brueckl, E. Hegedus, G.R. Keller, H. Thybo, CELEBRATION 2000, ALP 2002, SUDETES 2003 Working Groups, An overview of recent seismic refraction experiments in Central Europe, *Stud. Geophys. Geod., 47,* 651-657, 2003.

Hacker, B.R. and G.A. Abers, Subduction Factory 3: An Excel worksheet and macro for calculating the densities, seismic wave speeds, and H2O contents of minerals and rocks at pressure and temperature, *Geochem. Geophys. Geosyst. G3, 5(1),* Q01005, doi:10.1029/2003GC000614, 2004.

Hales, A.L., A seismic discontinuity in the lithosphere, *Earth Planet. Sci. Lett., 7,* 44-46, 1969.

Hammarstrom, J.M., and E-an Zen, Aluminum in hornblende: an empirical igneous geobarometer, *Am. Min., 71,* 1297-1313, 1986.

Hammond, W.C. and E.D. Humphreys, Upper mantle seismic wave velocity: Effects of realistic partial melt geometries, *J. Geophys. Res., 105(B5),* 10,975-10,986, 2000.

Hansteen, T.H., A. Klügel, and H.-U. Schmincke, Multi-stage magma ascent beneath the Canary Islands: evidence from fluid inclusions, *Contrib. Mineral. Petrol., 132,* 48-64, 1998.

Hegner, E. and T.W. Vennemann, Role of fluids in the origin of Tertiary European intraplate volcanism: Evidence from O, H, and Sr isotopes melilitites, *Geology, 25(11),* 1035-1038, 1997.

Hegner, E. and A. Kröner, Review of Nd isotopic data and xenocrystic and detrital zircon ages from the pre-Variscan basement in the eastern Bohemian Massif: speculations on palinspastic reconstructions, in *Orogenic Processes: Quantification and Modeling in the Variscan Belt,* edited by W. Franke, V. Haak, O. Oncken and D. Tanner, *Spec. Publ. Geol. Soc. London, 179*, 113-129, 2000.

Helffrich, G.R. and B.J. Wood, The Earths mantle, *Nature, 412,* 501-507, 2001.

Helz, R.T., Phase relation and composition of amphiboles produced in studies of the melting behavior of rocks, in *Amphiboles,* edited by H. Ribbe, *Reviews in Mineralogy, 9B,* 279-353, Mineral. Soc. Amer., 1982.

Hemmann, A., Relativrelokalisierung von Erdbebenschwärmen in der Saxothuringischen Seismotektonischen Province, *Doctoral Thesis*, University of Jena, 2002.

Hemmann, A. and H. Kämpf, Seismicity in the central part of the Naab-Pritzwalk-Rostock lineament, related to mantle fluid activity ? *Geophys. Research Abstracts, Vol. 4,* EGS02-A-05193, 2002.

Hemmann, A., T. Meier, G. Jentzsch, and A. Ziegert, Similarity of waveforms and relative relocation of the earthquake swarm 1997/98 near Werdau, *J. Geodyn., 35,* 191-208, 2003.

Higgins, M.D. and J. Roberge, Crystal Size Distribution of Plagioclase and Amphibole from Soufriere Hills Volcano, Montserrat: Evidence for Dynamic Crystallization-Textural Coarsening Cycles, *J. Petrol., 44,* 1401-1411, 2003.

Holbrook, W.S., D. Gajewski, A. Kramer, and C. Prodehl, An interpretation of Wide-Angle Compressional and Shear Wave Data in Southwest Germany: Poisson's Ratio and Petrological Implications, *J. Geophys. Res., 93,* 12,081-12,106, 1988.

Holland, T., and J. Blundy, Non-ideal interactions in calcic amphiboles and their bearing on amphibole-plagioclase thermometry, *Contrib. Mineral. Petrol., 116,* 433-447, 1994.

Hollister, L.S., G.C. Grissom, E.K. Peters, H.W. Stowell, and V.B. Sisson, Confirmation of the empirical correlation of Al in hornblende with pressure of solidification of calc-alkaline plutons, *Am. Min., 72,* 231-239, 1987.

Horálek, J., J. Šílený, T. Fischer, A. Slancová, and A. Boušková, The scenario of the January 1997 West Bohemia Earthquake Swarm, *Studia geoph. et geod., 44(4),* 491-521, 2000a.

Horálek, J., T. Fischer, A. Boušková, and P. Jedlička, Western Bohemia/Vogtland region in the light of the WEBNET network, *Studia geoph. et geod., 44(2),* 107-125, 2000b.

Horálek, J., J. Šílený, and T. Fischer, Moment tensors of the January 1997 earthquake swarm in NW Bohemia (Czech Republic): double-couple vs. non-double-couple events, *Tectonophysics, 356,* 65-85, 2002.

Huckenholz, H.G. and T. Noussinanos, Evaluation of temperature and pressure conditions in alkalibasalts and their peridotite xenoliths in NE Bavaria, Western Germany, *N. Jb. Min. Abh., 129,* 139-159, 1977.

Huckenholz, H.G. and T. Kunzmann, Tertiärer Vulkanismus im bayerischen Teil des Egergrabens und des mesozoischen Vorlandes, *Beih. z. Eur. J. Mineral., 5(2),* 1-34, 1993.

Huckenholz, H.G., M.C. Gilbert, and T. Kunzmann, Stability and phase relations of calcic amphiboles crystallized from magnesio-hastingsite compositions in the 1 to 45 kbar pressure range, *N. Jb. Min. Abh., 164,* 229-268, 1992.

Illies, H.J., Intraplate tectonics in stable Europe as related to plate tectonic on the Alpine system, *Geol. Rundsch., 64(3),* 677-699, 1975.

Irvine, T.N., Chromian spinel as a petrogenetic indicator. I. Theory, *Can. J. Earth Sci., 2,* 648-72, 1965.

Irving, A.J., Megacrysts from the Newer Basalts and other basaltic rocks of southeastern Australia, *Geol. Soc. Am. Bull., 85,* 1503-1514, 1974.

Jackson, E.D., Chemical variation in coexisting chromite and olivine in the chromitite zones of the Stillwater complex, *Econ. Geol. Mon., 4,* 41-71, 1969.

James, D.E., F.R. Boyd, D. Schutt, D.R. Bell, and R.W. Carlson, Xenolith constraints on seismic velocities in the upper mantle beneath southern Africa, *Geochem. Geophys. Geosyst. G3, 5(1),* Q01002, doi:10.1029/2003GC000551, 2004.

Janský, J., J. Horálek, J. Málek, and A. Boušková, Homogenous Velocity Models of the West Bohemian Swarm Region Obtained by Grid Search, *Studia geoph. et geod., 44(2),* 158-174, 2000.

Jarchow, C.M., G.A. Thompson, R.D. Catchings, and W.D. Mooney, Seismic Evidence for Active Magmatic Underplating Beneath the Basin and Range Province, Western United States, *J. Geophys. Res., 93,* 22,095-22,108, 1993.

Jones, A.P., J.V. Smith, J.B. Dawson, and E.C. Hansen, Metamorphism, partial melting and K-metasomatism of garnet-scapolite-kyanite granulite xenoliths from Lashaine, Tanzania, *J. Geol., 91,* 143-165, 1983.

Johnson, R.W. (ed.), Intraplate Volcanism in Eastern Australia and New Zealand, Cambridge University Press, Cambridge-New York-Port Chester-Melbourne-Sydney, 394 p., 1989.

Johnson, M.C. and M.J. Rutherford, Experimental calibration of the aluminium-in-hornblende geobarometer with application to Long Valley caldera (California) volcanic rocks, *Geology, 17,* 837-841, 1989.

Kämpf, H., M. Malkovsky, and F.H. Weinlich, Vulkanismus – Mineralwässer – Seismizität im Bereich der Marienbader Störungszone, in *Münchberger Gneismasse und ihr geologischer Rahmen,* edited by H. Kämpf, P. Bankwitz, and E. Bielefeld, 1. Jahrestagung der Gesellschaft für Geowissenschaften, Falkenstein, Oktober 1992, pp. 127-155, 1992.

Kämpf, H., Vogtland earthquake swarms and their relation to reflection seismic indications, in *Crustal structure of the Saxothuringian Zone: Results of deep seismic profile MVE-90 (East),* edited by H.-J. Behr, H.-J. Dürbaum, and P. Bankwitz, *Z. geol. Wiss., 22,* 696-700, 1994.

Kämpf, H., W. Seifert, and M. Ziemann, Mantel-Kruste-Wechselwirkungen im Bereich der Marienbader Störungszone, Teil 1: Neue Ergebnisse zum quartären Vulkanismus in NW-Böhmen, *Z. geol. Wiss., 21,* 117-134, 1993.

Kämpf, H., W. Seifert, and P. Dulski, Mantle and crustal xenoliths from the Quaternary volcano Železná Hůrka, western Eger rift, in *Magmatism and Rift Basin evolution,* edited by J. Ulrych, V. Cajz, and J. Adamovic, IGCP 369 workshop, Czech Republic, Liblice, September 7-11, 1998, excursion guide and abstract volume, p 74, 1998.

Kämpf, H., K. Bräuer, G. Strauch, and S.M. Weise, Indications for an Active Magma Chamber in the Upper Mantle Below the Western Eger Graben, Czech Republic, *EOS, 1999 Spring Meeting,* V52A-03 (abstract), 1999a.

Kämpf, H., W. Geissler, H.-J. Müller, and M. Uhlig, Quantitative characterization of microscopic porous networks in Quaternary upper mantle xenoliths of western Eger Rift, Czech Republic, in *Workshop on fluids and fractures in the lithosphere, Nancy, 26-27 March 1999, abstracts,* edited by M. Lespinasse and J.-L. Vigneresse, 84, 1999b.

Katsura, T., H. Yamada, O. Nishikawa, M. Song, A. Kubo, T. Shinmei, S. Yokoshi, Y. Aizawa, T. Yoshino, M.J. Walter, and E. Ito, Olivine-wadsleyite transition in the system $(Mg,Fe)_2SiO_4$, *J. Geophys. Res., 109,* B02209, doi:10.1029/2003JB002438, 2004.

Keller, G.R., J. Mechie, L.W. Braile, W.D. Mooney, and C. Prodehl, Seismic structure of the uppermost mantle beneath the Kenya rift, in *Crustal and Upper Mantle Structure of the Kenya Rift,* edited by C. Prodehl, G.R. Keller, and M.A. Khan, *Tectonophysics, 236,* 210-216, 1994.

Kennett, B.L.N. (Ed.), IASPEI 1991 Seismological tables, Research School of Earth Sciences, Australian National Univ., Canberra, 1991.

Kennett, B.L.N. and E.R. Engdahl, Traveltimes for global earthquake location and phase identification, *Geophys. J. Int., 105,* 429-465, 1991.

Kind, R., The reflectivity method for different source and receiver structures and comparison with GRF data, *J. Geophys., 58,* 146-152, 1985.

References

Kind, R. and L.P. Vinnik, The upper-mantle discontinuities underneath the GRF array from P-to-S converted phases, *J. Geophys., 62,* 138-147, 1988.

Kind R., G.L. Kosarev, and N.V. Petersen, Receiver functions at the Stations of the German Regional Seismic Network (GRSN), *Geophys. J. Int., 121,* 191-202, 1995.

Kind, R., X. Yuan, J. Saul, D. Nelson, S.V. Sobolev, J. Mechie, W. Zhao, G. Kosarev, J. Ni, U. Achauer, and M. Jiang, Seismic images of crust and upper mantle beneath Tibet: Evidence for Eurasian plate subduction, *Science 298,* 1219-1221, 2002.

Klein, C. and C.S. Hurlbut Jr., Manual of mineralogy, 21st ed, after J.D. Dana, John Wiley & Sons, New York, 1993.

Klinge, K., T. Plenefisch, and K. Stammler, The earthquake swarm 2000 in the region Vogtland/NW-Bohemia - Earthquake recording at German Stations and temporal distribution of events, *J. Geodyn., 35,* 83-96, 2003.

Knett, J., Das Erzgebirgische Schwarmbeben zu Hartenberg vom 1. Jänner bis Feber 1824, Sitzungsber. Deutsch. Naturwiss.- med. Ver. Böhmen, *Lotus Prag N.F., 19,* 167-191, 1899.

Knothe, C., Die Struktur der Erdkruste Mittel- und Südosteuropas nach Angaben der Tiefenseismik, *Geodätisch geophysikalische Veröffentlichungen, NKGG, Reihe III, 27,* 59-68, 1972.

Koch, U. and J. Heinicke, Hydrological pre- and co-seismic effects of the latest Vogtland-NW Bohemian swarmquake period (August to December 2000), *J. Geodyn., 35,* 107-123, 2003.

Köhler, T.P. and G.P. Brey, Calcium exchange between olivine and clinopyroxene calibrated as a geothermobarometer for natural peridotites from 2 to 60 kbar with applications, *Geochim. Cosmochim. Acta, 54,* 2375-2388, 1990.

Köhler, W., H. Grosser, and P. Bormann, Investigation of plane solutions, spectra and focal processes, in *Monitoring and Analysis of the Earthquake swarm 1985/86 in the Region Vogtland/Western Bohemia,* edited by P. Bormann, *ZIPE-Veröff., Nr. 110,* 165-193, Zentralinstitut für Physik der Erde, Potsdam, 1989

Kosarev, G., R. Kind, S.V. Sobolev, X. Yuan, W. Hanka, and S. Oreshin, Seismic Evidence for a Detached Indian Lithospheric Mantle Beneath Tibet, *Science, 283,* 1306-1309, 1999.

Krawczyk, C.M., Stein, E., Choi, S., Oettinger, G, Schuster, K., Götze, H.-J., Haak, V., Oncken, O., Prodehl, C. und A. Schulze, Geophysical constraints on exhumation mechanism of high-pressure rocks: the Saxo-Thuringian case between the Franconian Line and Elbe Zone, in *Orogenic Processes: Quantification and Modelling in the Variscan Belt,* edited by W. Franke, V. Oncken, and D. Tanner, *Geological Society, London Special Publications, 179,* 303-322, 2000.

Kramer, W., Magmengenetische Aspekte der Lithosphärenentwicklung, *Schriftenreihe für Geologische Wissenschaften (Series in Geological Sciences), 26,* 136 p., Akademie-Verlag, Berlin, 1988.

Kramer, W. and W. Seifert, Mafische Xenolithe und Magmatite im östlichen Saxothuringikum und westlichen Lugikum: Ein Beitrag zum Krustenbau und zur regionalen Geologie, *Z. geol. Wiss. 28(1/2),* 133-156, 2000.

Kretz, R., Symbols for rock-forming minerals, *Am. Min., 68,* 277-279, 1983.

Krüger, F. and M. Weber, The effect of low-velocity sediments on the mislocation vectors of the GRF array, *Geophys. J. Int., 108,* 387-393, 1992.

Kuno, H. and K.I. Aoki, Chemistry of ultramafic nodules and their bearing on the origin of basaltic magmas, *Phys. Earth Planet. Int., 3,* 273-301, 1970.

Langston, C.A., Structure Under Mount Rainier, Washington, Inferred From Teleseismic Body Waves, *J. Geophys. Res., 84(B9),* 4,749-4,762, 1979.

Lapp, M. and K. Weber, Postkinematische Alteration von Metagrauwacken und Phylliten der Bohrung Neualbenreuth, *KTB-Report 92-4,* 241-250, 1992.

Le Bas, M.J., Nephelinites and carbonatites, in *Alkaline igneous rocks*, edited by J.G. Fitton and B.G.J. Upton, *Geol. Soc. Spec. Pub., 30,* 53-83, London, 1987.

Le Bas, M.J., R.W. Le Maitre, and A.R. Woolley, The construction of the total alkali-silica chemical classification of volcanic rocks, *Mineral. Petrol., 46,* 1-22, 1992.

Lebedev, S., S. Chevrot, and R.D. van der Hilst, Seismic evidence for Olivine Phase Changes at the 410- and 660-Kilometer Discontinuities, *Science,* 296, 1300-1302, 2002.

Le Maitre, R.W. (ed.), A classification of igneous rocks and glossary terms, Blackwell Scientific Publications, Oxford London Edinburgh Boston Melbourne, 193 p., 1989.

Leake, B.E., Nomenclature of amphiboles, *Am. Min., 63,* 1023-1052, 1978.

Leake, B.E., Nomenclature of amphiboles – Report of the Subcommittee on Amphiboles of the International Mineralogical Association Commission on New Minerals and Mineral Names, *Eur. J. Mineral., 9,* 623-651, 1997.

Lehrberger, G., A. Saurle, and U. Hartmann, Anwendung des SAR-DGM bei der tektonischen Interpretation des Moldanubikums am Westrand der Böhmischen Masse, *Geol. Bav., 107,* 269-280, 2003.

Li, X., R. Kind, K. Priestley, S.V. Sobolev, F. Tilmann, X. Yuan, and M. Weber, Mapping the Hawaiian plume conduit with converted seismic waves, *Nature, 405,* 938-941, 2000a.

Li, X., S.V. Sobolev, R. Kind, X. Yuan, and C. Estabrook, A detailed receiver function image of the upper mantle discontinuities in the Japan subduction zone, *Earth Planet. Sci. Lett., 183,* 527-541, 2000b.

Li, X., R. Kind, and X. Yuan, Seismic study of upper mantle and transition zone beneath hotspots, *Phys. Earth Planet. Inter. 136*, 79-92, 2003a.

Li, X., G. Bock, A. Vafidis, R. Kind, H.-P. Harjes, W. Hanka, K. Wylegalla, M. van der Meijde, and X. Yuan, Receiver function study of the Hellenic subduction zone: imaging crustal thickness variations and the oceanic Moho of the descending African lithosphere, *Geophys. J. Int., 155,* 733-748, 2003b.

Lindsley, D.H ., Pyroxene thermometry, *Am. Min., 68,* 477-493, 1983.

Linnemann, U., M. Gehmlich, M. Tichomirova, B. Buschmann, L. Nasdala, P. Jonas, H. Lützner, and K. Bombach, From Cadomian subduction to Early Paleozoic rifting: the evolution of Saxo-Thuringia at the margin of Gondwana in the light of single zircon geochronology and basin development (central European Variscides, Germany), in *Orogenic Processes: Quantification and Modelling in the Variscan Belt.* edited by W. Franke, V. Haak, O. Oncken, and D. Tanner*, Spec. Publ. Geol. Soc. London, 179,* 131-153, 2000.

Lippoldt, H.J., K-Ar Age Determinations and correlation of tertiary volcanic activity in Central Europe, *Geol. Jb., D52,* 119-141, 1982.

Lloyd, F.E., Upper mantle metasomatism beneath a continental rift: clinopyroxenes in alkalic alkalic mafic lavas and nodules from southwest Uganda, *Mineral. Mag., 44,* 315-323, 1981

Lloyd, F.E., Characterization of mantle metasomatic fluids in spinel lherzolites and clinopyroxenites from the West Eifel and South Uganda, in *Mantle metasomatism,* edited by M.A. Menzies and C.J. Hawkesworth, Academic Press, London, pp 91-120, 1987.

Lloyd, F.E. and D.K. Bailey, Light element metasomatism of the continental mantle: the evidence and the consequences, *Phys. Chem. Earth, 9,* 389-416, 1975

Lüschen, E., S. Sobolov, U. Werner, W. Söllner, K. Fuchs, B. Gurevich, and P. Hubral, Fluid Reservoir (?) beneath the KTB Drillbit indicated by seismic shear-wave observations, *Geoph. Res. Lett., 20(10),* 923-926, 1993.

Maccregor, I.D., The effect of CaO, Cr_2O_3, Fe_2O_3 and Al_2O_3 on the stability of spinel and garnet peridotites, *Phys. Earth Planet. Interiors, 3,* 372-377, 1970.

Málek, J., J. Janský, and J. Horálek, Layered Velocity Models of the Western Bohemian Region, *Studia geoph. et geod., 44(4),* 475-490, 2000.

Málek, J., M. Broz, T. Fischer, J. Horálek, P. Hrubcova, J. Janský, O. Novotny, and B. Ruzek, Seismic measurements along short profiles in western Bohemia during the Celebration 2000 experiment, *Acta Montana IRSM AS CR, Series A, No. 18(121)*, 15-28, 2001.

Malkovsky, M., Saxonische Tektonik der Böhmischen Masse, *Geol. Rundschau, 65,* 127-143, 1976.

Marty, B., R.K. O´Nions, E.R. Oxburgh, D. Martel, and S. Lombardi, Helium isotopes in Alpine regions, *Tectonophysics, 206,* 71-78, 1992

Matthews, D. H., Seismic reflections from lower crust around Britain, in *The Nature of the Lower Continental Crust,* edited by J. Dawson, D. Carswell, J. Hall, and K. Wedepohl, pp 11-21, Blackwell Oxford, 1986.

Matthews, A., C. Fouillac, R. Hill, R.K. O´Nions, and E.R. Oxburgh, Mantle-derived volatiles in continental crust: The Massif Central of France*, Earth Planet Sci. Lett., 85,* 117-128, 1987.

May, F., Quantifizierung des CO_2-Flusses zur Abbildung magmatischer Prozesse im Untergrund der Westeifel, 170 p., Shaker Verlag, Aachen, 2002.

Mayerová, M., Z. Nakladalová, I. Ibrmajer, and M. Fejfar, Construction of the Moho Discontinuity Map, in *Crustal Structure of the Bohemian Massif and the West Carpathians,* edited by V. Bucha and M. Blížkovský, *Exploration of the Deep Continental Crust,* pp 20-21, Springer-Verlag Berlin Heidelberg New York, 1994.

McKenzie, D., A possible mechanism for epirogenetic uplift, *Nature, 307,* 616-618, 1984.

McLennann, S.M., Rare earth elements in sedimentary rocks: Influence of provenance and sedimentary processes, in *Geochemistry and Mineralogy of Rare Earth Elements,* edited by B.R. Lipin and G.A. McKay, p 169-200, Mineral. Soc. Am., Washington, DC, 1989.

McPherson, E., M.F. Thirlwall, I.J. Parkinson, M.A. Menzies, J.L. Bodinier, A. Woodland, and G. Bussod, Geochemistry of metasomatism adjacent to amphibole-bearing veins in the Lherz peridotite massif, *Chem. Geol., 134,* 134-157, 1996.

Mechie, J., G.R. Keller, C. Prodehl, S. Gaciri, L.W. Braile, W.D. Mooney, D. Gajewski, and K.-J. Sandmeier, Crustal structure beneath the Kenya Rift from axial profile data, in *Crustal and upper mantle structure of the Kenya rift*, edited by C. Prodehl, G.R. Keller, and M.A. Khan, *Tectonophysics, 236,* 179-200, 1994a.

Mechie, J., K. Fuchs, and R. Altherr, The relationship between seismic velocity, mineral composition, temperature and pressure in the upper mantle – with an application to the Kenya rift and its eastern flank, in *Crustal and upper mantle structure of the Kenya rift*, edited by C. Prodehl, G.R. Keller, and M.A. Khan, *Tectonophysics, 236,* 453-464, 1994b.

Medaris, L.G., J.H. Fournelle, H.F. Wang, and E. Jelinek, Thermobarometry and reconstructed chemical compositions of spinel-pyroxene symplectites: evidence for pre-existing garnet in lherzolite xenoliths from Czech Neogene lavas, *Russ. Geol. Geoph., 38(1),* 260-268, 1997.

References

Medaris, L.G., H.F. Wang, J.H. Fournelle, J.H. Zimmer, and E. Jelinek, A cautionary tale of spinel peridotite thermobarometry: an example from xenoliths of Kozakov volcano, Czech Republic, *Geolines, 9,* 92-96, 1999.

Mengel, K, Crustal xenoliths from Tertiary volcanics of the Northern Hessian Depression. Petrological and chemical evolution, *Contrib. Mineral. Petrol., 104,* 8-26, 1990.

Mengel, K. and H. Kern, Evolution of the petrological and seismic Moho – Implications for the continental crust/mantle boundary, *Terra Nova, 4,* 109-123, 1991.

Mengel, K., P.M. Sachs, H.G. Stosch, G. Wörner, and G. Loock, Crustal xenoliths from Cenozoic volcanic fields of West Germany: Implications for structure and composition of the continental crust, *Tectonophysics, 195,* 271-289, 1991.

Menzies, M.A., and J.L. Bodinier, Growth of the European lithospheric mantle – dependence of upper-mantle peridotite facies and chemical heterogeneity on tectonics and age, *Phys. Earth Planet. Int., 79,* 219-240, 1993.

Merle, O., and L. Michon, The formation of the West European rift: A new model as exemplified by the Massif Central, *Bull. Soc. Geol. France, t. 172, No. 2,* pp. 213-221, 2001.

Mingram, B., A. Kröner, E. Hegner, and O. Krentz, Zircon ages, geochemistry, and Nd isotopic systematics of pre-Variscan orthogneisses from the Erzgebirge, Saxony (Germany), and geodynamic interpretation, *Int. J. Earth Sci. (Geol. Rundsch.), 93,* 706-727, 2004.

Morimoto, N., Nomenclature of Pyroxenes, *Mineral. Petrol., 39,* 55-76, 1988.

Mueller, H.J., Modelling the lower crust by simulation of the in situ conditions: an example from the Saxon Erzgebirge, *Phys. Earth Planet. Inter., 92,* 3-15, 1995.

Neunhöfer, H., The Catalogue of the Vogtland/Western Bohemia Earthquakes and VOCATUS as an Auxiliary Code, *Stud. Geophys. Geod., 44(4),* 549-555, 2000.

Neunhöfer H. and T. Meier, Seismicity in the Vogtland/western Bohemia earthquake region between 1962 and 1998, *Stud. Geophys. Geod., 48,* 539-562, 2004.

Nimis, P., A clinopyroxene geobarometer for basaltic systems based on crystal-structure modeling, *Contrib. Mineral. Petrol., 121,* 115-125, 1995.

Nimis, P., Clinopyroxene geobarometry of magmatic rocks. Part 2. Structural geobarometers for basic to acid, tholeiitic and mildly alkaline magmatic systems, *Contrib. Mineral. Petrol., 135,* 62-74, 1999.

Nimis, P. and P. Ulmer, Clinopyroxene geobarometry of magmatic rocks Part 1: An expanded structural geobarometer for anhydrous and hydrous, basic and ultrabasic systems, *Contrib. Mineral. Petrol., 133,* 122-135, 1998.

Okrusch, M., B. Schröeder, and A. Schnüttgen, Granulite-facies metabasite ejecta in the Laacher See area, Eifel, West Germany, *Lithos, 12,* 251-270, 1979.

O'Neill, H.S.C., The transition between spinel lherzolite and garnet lherzolite, and its use as a geobarometer, *Contrib. Mineral. Petrol., 77,* 185-194, 1981.

O'Neill, H.S.C. and V.J. Wall, The Olivine-Orthopyroxene-Spinel Oxygen Geobarometer, the Nickel Precipitation Curve, and the Oxygen Fugacity of the Earth's Upper Mantle, *J. Petrol., 28(6),* 1169-1191, 1987.

O´Nions, R.K. and E.R. Oxburgh, Helium, volatile fluxes and the development of continental crust, *Earth Planet. Sci. Lett., 90,* 331-347, 1988.

O´Nions, R.K., E. Griesshaber, and E.R. Oxburgh, Rocks that are too hot to handle, *Nature, 341,* 391, 1989.

Opletal, M., Předběžná zpráva o nálezu xenolitů charnockitických hornin v čedičových horninách Českeho středohoři, *Čas. Mineral. Geol., 12/3,* 301-303, 1967.

Opletal, M. and S. Vrána, Charnockite xenoliths in the Tertiary volcanites of the České středohoři Mts., northern Bohemia, *Sbor. Geol. Ved Geologie, 44,* 51-78, 1989.

O'Reilly, S.Y. and W.L. Griffin, A xenolith-derived geotherm for southeastern Australia and its geophysical implications, *Tectonophysics, 111,* 41-63, 1985.

O'Reilly, S.Y., I. Jackson, and C. Bezant, Equilibration temperatures and elastic wave velocities for upper mantle rocks from eastern Australia: implications for the interpretation of seismological models, *Tectonophysics, 185,* 67-82, 1990.

O'Reilly, S.Y., D. Chen, W.L. Griffin, and G.C. Ryan, Minor elements in olivine from spinel lherzolite xenoliths: implications for thermobarometry, *Mineral. Mag., 61,* 257-269, 1997.

Otten, M.T., The origin of brown hornblende in the Artfjället gabbro and dolerites, *Contrib. Mineral. Petrol, 86,* 189-199, 1984.

Parotidis, M., E. Rothert, and S.A. Shapiro, Pore-pressure diffusion : A possible triggering mechanism for the earthquake swarms 2000 in Vogtland/NW-Bohemia, central Europe, *Geoph. Res. Lett., 30(20),* 2075, doi:10.1029/2003GL018110, 2003.

Passier, M.L. and R.K. Snieder, Correlation between shear wave upper mantle structure and tectonic surface expressions: Application to central and southern Germany, *J. Geophys. Res.,101,* 25,293-25,304, 1996.

Pasteris, J.D., Fluid inclusions in mantle xenoliths, in *Mantle xenoliths,* edited by P.H. Nixon, pp. 691-707, Wiley, Chichester, 1987.

Pearson, D.G., D. Canil, and S.B. Shirey, Chapter 7 – Mantle samples included in volcanic rocks: xenoliths and diamonds, in *Treatise On Geochemistry: Vol. 2, The Mantle,* edited by R.W. Carlson, pp. 171-277, Elsevier, New York, 2004.

Petersen, N.L., L. Vinnik, G. Kosarev, R. Kind, S. Oreshin, and K. Stammler, Sharpness of the mantle discontinuities, *Geophys. Res. Lett., 20,* 859-862, 1993.

Plenefisch, T. and K. Klinge, Temporal variations of focal mechanisms in the Nový Kostel focal zone (Vogtland/NW-Bohemia) - Comparison of the swarms 1985/86, 1994, 1997 and 2000, *J. Geodyn.,* 35, 145-156, 2003.

Plenefisch, T., K. Klinge, and R. Kind, Upper mantle anisotropy at the transition zone of the Saxothuringicum and Moldanubicum in southeast Germany revealed by shear wave splitting, *Geophys. J. Int., 144,* 309-319, 2001.

Plešinger, A., H. Neunhöfer, and E. Wielandt, Deep Structure of the Bohemian Massif from Phase Velocities of Seismic Surface Waves, in *Crustal Structure of the Bohemian Massif and the West Carpathians, Exploration of the Deep Continental Crust*, edited by V. Bucha, and M. Blížkovský, pp. 53-62, Springer-Verlag Berlin Heidelberg New York, 1994.

Plomerová, J. and V. Babuška, Lithospheric thickness in the contact zone of the Moldanubicum and Saxothuringicum in central Europe, *Phys. Earth Planet. Int., 51,* 159-165, 1988.

Plomerová, J., V. Babuška, J. Sileny, and J. Horalek, Seismic Anisotropy and Velocity Variations in the Mantle beneath the Saxothuringicum-Moldanubicum Contact in Central Europe, *Pure appl. geophys.*, 151, 365-394, 1998.

Pouchou, J.L. and F. Pichoir, A new model for quantitative X-ray microanalysis, Part I. Applications to the analyses of homogenous samples, *Rech. Aerosp., 3,* 13-38, 1984.

Prodehl, C., S. Mueller, A. Glahn, M. Gutscher, and V. Haak, Lithospheric cross sections of the European Central rift system, in *Geodynamics of Rifting, Volume I. Case history studies on rifts: Europe and Asia,* edited by P.A. Ziegler, *Tectonophysics, 208,* 113-138, 1992.

Prodehl, C., S. Müller, and V. Haak, The European Cenozoic rift system, in *Continental rifts: evolution, structure, tectonics*, edited by K.H. Olsen, Developments in *Geotectonics, 25,* 133-212, Elsevier, 1995.

Proft, E., Kammerbühl und Eisenbühl, die Schichtvulkane des Egerer Beckens, *Jahrb. Geol. Reichsanstalt Wien, 44,* 25-85, Wien, 1894.

Rajkes, S. and K.-P. Bonjer, Large-Scale Mantle Heterogeneities Beneath the Rhenish Massif and its Vicinity from Teleseismic P-Residuals Measurements, in *Plateau Uplift. The Rhenish Shield - A Case History*, edited by K. Fuchs, K. von Gehlen, H. Mälzer, H. Murawski, and A. Semmel, 315-331, Springer-Verlag Berlin Heidelberg, 1983.

Regenauer-Lieb, K., Dilatant plasticity applied to Alpine collison: ductile void growth in the intraplate area beneath the Eifel volcanic field, *J. Geodynamics, 27,* 1-21, 1999.

Renno, A.D., B.R. Hacker, and K.P. Stanek, An Early Cretaceous (126 Ma) ultramafic alkaline lamprophyre from the Quarry Klunst (Ebersbach, Lusatia, Germany), *Z. geol. Wiss., 31(1),* 31-36, 2003.

Reuss, A.E., Die geologischen Verhältnisse des Egerer Bezirks und des Ascher Gebietes in Böhmen, *Abh. Geol. Reichsanstalt Wien, 1,* 1-73, Wien, 1852.

Richter, P. and G. Stettner, Lithologische und geochemische Profilierung im Kambroordovizium des südlichen Waldsassener Schiefergebirges, *Geol. Bavarica, 98,*175-217, 1993.

Righter, K. and I.S.E. Carmichael, Mega-xenocrysts in alkali olivine basalts: Fragments of disrupted mantle assemblages, *Am. Min., 78,* 1230-1245, 1993.

Righter, K. and I.S.E. Carmichael, Phase equilibria of phlogopite lamprophyres from western Mexico: biotite-liquid equilibria and p-T estimates for biotite-bearing igneous rocks, *Contrib. Min. Petrol., 123,* 1-21, 1996.

Ritter, J.R.R., M. Jordan, U.R. Christensen, and U. Achauer, A mantle plume below the Eifel volcanic fields, Germany, *Earth Planet. Sci. Lett., 186,* 7-14, 2001.

Roeder, P.L., I.H. Campbell, and H.E. Jamieson, A Re-Evaluation of the Olivine-Spinel Geothermometer, *Contrib. Mineral. Petrol. 68,* 325-334, 1979.

Röllig, G., M. Viehweg, and N. Reuter, The ultramafic lamprophyres and carbonatites of Delitzsch/GDR, *Z. Angew. Geol., 36,* 49-54, 1990.

Rollinson, H.R., Using Geochemical Data: Evaluation, Presentation, Interpretation, Longman Scientific & Technical, Burnt Mill, Harlow, 1993.

Rößler, D., G. Rümpker, and F. Krüger, Ambiguos Moment Tensors and Radiation Patterns in Anisotropic Media with Applications to Modeling of Earthquake Mechanism in W-Bohemia, *Studia geoph. et geodet., 48(1),* 233-250, 2004.

Rost, S. and Q. Williams, Seismic detection of sublithospheric plume head residue beneath the Pitcairn hot-spot chain, *Earth Planet. Sci. Lett., 209,* 71-83, 2003.

Rudnick, R.L. and D.M. Fountain, Nature and Composition of the Continental Crust: A Lower Crustal Perspective, *Rev. Geoph., 33,* 267-309, 1995.

References

Rudnick, R.L., W.F. McDonough, and B.W. Chappell, Carbonatite metasomatism in the northern Tanzanian upper mantle: petrographic and geochemical characteristics, *Earth Planet. Sci. Lett., 114,* 463-475, 1993.

Sachs, P.M. and T.H. Hansteen, Pleistocene underplating and metasomatism of the Lower Continental crust: a xenolith study, *J. Pet., 41,* 331-356, 2000.

Schmidt, M.W., Amphibole composition in tonalite as a function of pressure: an experimental calibration of the Al-in-hornblende barometer, *Contrib. Mineral. Petrol., 110,* 304-310, 1992.

Schmoll, J., R. Bittner, H.-J. Dürbaum, T. Heinrichs, R. Meißner, C. Reichert, T. Rühl, and H. Wiederhold, Oberpfalz Deep Seismic Reflection Survey and Velocity Studies, in *The German Continental Deep Drilling Program (KTB),* edited by R. Emmermann and J. Wohlenberg, *Exploration of the Deep Continental Crust,* pp. 363-383, Springer Verlag, 1989.

Schulze A. and E. Lück, Some results of deep seismic investigations in East Germany, *Phys. Earth Planet. Inter., 69,* 231-238, 1992.

Schulze, D.J., Megacrysts from alkalic volcanic rocks, in *Mantle Xenoliths,* edited by P.H. Nixon, pp. 433-451, John Wiley & Sons Ltd., 1987.

Seifert, W. and H. Kämpf, Ba-enrichment in phlogopite of a nephelinite from Bohemia, *Eur. J. Mineral., 6,* 497-502, 1994.

Seifert, W. and R. Thomas, Silicate-carbonate Immiscibility: A Melt Inclusion Study of Olivine Melilitite and Wehrlite Xenoliths im Tephrite from the Elbe Zone, Germany, *Chem. Erde, 55,* 263-279, 1995.

Seifert, W.,H. Kämpf, and J. Wasternack, Compositional variation in apatite, phlogopite and other accessory minerals of the ultramafic Delitzsch complex, Germany: implication for cooling history of carbonatites, *Lithos, 53,* 81-100, 2000.

Shaocheng Ji, Qin Wang, Bin Xia, Handbook of Seismic Properties of Minerals, Rocks and Ores, Polytechnic International Press, Montreal, 630 p., 2002.

Shaw, C.S.J., Origin of Sulfide blebs in variably metasomatized mantle xenoliths, Quaternary West Eifel volcanic field, Germany, *Can. Min., 35,* 1453-1463, 1997.

Shearer, P.M., Constraints on Upper Mantle Discontinuities From Observations of Long-Period Reflected and Converted Phases, *J. Geophys. Res., 96(B11),* 18,147-18,182, 1991.

Shearer, P.M., Upper mantle discontinuities, in Earth's deep interior: Mineral Physics and Tomography – From the Atomic to the Global Scale, *AGU Geophys. Monograph, 117,* 115-131, 2000.

Spear, F.S., An experimental study of hornblende stability and compositional variability in amphibolite, *Am. J. Science, 281,* 697-734, 1981.

Špičák, A., J. Horálek, A. Bouškova, Č. Tomek and J. Vanek, Magma intrusions and earthquake swarm occurrence in the Western part of the Bohemian Massif, *Studia geoph. et geod., 43,* 87-106, 1999.

Špičák, A. and J. Horálek, Possible role of fluids in the process of earthquake swarm generation in the West Bohemia/Vogtland seismoactive region, *Tectonophysics, 336,* 151-161, 2001.

Špičáková, L., D. Uličný, and G. Koudelková, Tectonosedimentary Evolution of the Cheb Basin (NW Bohemia, Czech Republic) between Late Oligocene and Pliocene: A Preliminary Note, *Studia geoph. et geod., 44(4),* 556-580, 2000.

Stackebrandt, W. and H.J. Franzke, Alpidic Reactivation of the Variscan Consolidated Lithosphere – The Activity of some Fracture Zones in Central Europe, *Z. geol. Wiss., 17(7),* 699-712, 1989.

Stammler, K., R. Kind, N. Petersen, G. Kosarev, L. Vinnik, and L. Qiyuan, The upper mantle discontinuities: correlated or anticorrelated?, *Geophys. Res. Lett., 19,* 1563-1566, 1992.

Stammler, K, SeismicHandler: programmable multichannel data handler for interactive and automatic processing of seismological analyses, *Comp. Geosci., 19,* 135-140, 1993.

Strößenreuther, U., Die Struktur der Erdkruste am Südwest-Rand der Böhmischen Masse, abgeleitet aus refraktionsseismischen Messungen der Jahre 1970 und 1978/79, *Doctoral Thesis,* Ludwig-Maximilian-University Munich, 1982.

Švancara, J., I. Gnojek, F. Hubatka, and K. Dědáček, Geophysical Field Pattern in the West Bohemian Geodynamic Active Area, *Studia geoph. et geod., 44(2),* 307-326, 2000.

SZGRF-Seismologisches Zentralobservatorium Gräfenberg, Erlangen, SZGRF Vogtland Bulletin 1994-1997, http://www.szgrf.bgr.de/bul_vogt_szgrf.html.

Tait, S.R., Samples from the crystallizing boundary layer of a zoned magma chamber, *Contrib. Mineral. Petrol., 100,* 470-483, 1988.

Tanner, D.C., J.H. Behrmann, O. Oncken, and K. Weber, Three-dimensional retro-modelling of transpression on a linked fault system: the Upper Cretaceous deformation on the western border of the Bohemian Massif, Germany, in: *Continental Transpressional and Transtensional Tectonics,* edited by R.E. Holdsworth and J.F. Dewey, *Geological Society London Special Publications, 135,* 275-287, 1998.

Tillmanns, M., M. Simon, A. Zitzelsberger, and H. Gebrande, Neue Seismographien aus dem Umfeld der Kontinentalen Tiefbohrung (KTB), Oberpfalz, *Geologica Bavarica, 101,* 291-314, 1996.

Thomas, R., Results of investigations on melt inclusions in various magmatic rocks from the northern border of the Bohemian Massif, in *Proceedings of the 1st International Conference on the Bohemian Massif, Prague, Czechoslovakia, Sept. 26-Oct. 3, 1988,* edited by Z. Kukal, 298-306, Czech Geological Surv., Prague, 1992.

Todt W. and H.J. Lippolt, K-Ar Altersbestimmung an Vulkaniten bekannter paläomagnetischer Feldrichtung, I. Oberpfalz und Oberfranken, *J. Geophys., 41,* 43-61, 1975.

Tomek, Č., V. Dvořáková, and S. Vrána, Geological interpretation of the 9HR and 503M seismic profiles in Western Bohemia, *in Geological model of Western Bohemia related to the KTB borehole in Germany,* edited by S. Vrána and V. Štědrá, *J. Geol. Sci., Geology, 47,* 43-50, 1997.

Trappe, H. and T. Wever, Seismic evidence of increased tectonothermal activity near the Oberpfalz deep continental drilling location (SE Germany), *Geologische Rundschau, 79/3,* 649-658, 1990.

Ulrych, J. and E. Pivec, Age-related Contrasting Alkaline Volcanic Series in North Bohemia, *Chem. Erde, 57,* 311-336, 1997.

Ulrych, J., E. Pivec, M. Lang, V. Kropáček, and K. Balogh, Cenozoic intraplate volcanic rock series of the Bohemian Massif: a review, in *Proceedings IGCP No. 369/2a Magmatism and Rift Basin Evolution, Liblice 1998,* edited by J. Ulrych, V. Cajz, and J. Adamovic, *Geolines, 9,* 123-133, 1999.

Ulrych, J., E. Pivec, P. Povondra, and J. Rutšek, Upper-mantle xenoliths in melilitic rocks of the Osečná Complex, North Bohemia, *J. Czech Geol. Soc., 45/1-2,* 79-93, 2000.

Ulrych, J., F.E. Lloyd, and K. Balogh, Age Relations and Geochemical Constraints of Cenozoic Alkaline Volcanic Series in W Bohemia: A Review, *Geolines, 15*, 168-180, 2003.

Vanderhaege, O. and C. Teyssier, Formation of the Shuswap metamorphic complex during late-orogenic collapse of the Canadian Cordillera: Role of ductile thinning and partial melting of the mid- to lower crust, *Geodynamica Acta, 10,* 41-58, 1997.

Vavryčuk, V., Inversion for parameters of tensile earthquakes, *J. Geophys. Res., 106,* 16,339-16,355, 2001.

Vavryčuk, V., Non-double-couple earthquakes of 1997 January in West Bohemia, Czech Republic: Evidence for tensile faulting, *Geophys. J. Int., 149*, 364-373, 2002.

Vinnik, L.P., Detection of waves converted from P to SV in the mantle, *Phys. Earth Planet. Inter., 15,* 39-45, 1977.

Vinnik, L.P., V.G. Krishna, R. Kind, P. Bormann, and K. Stammler, Shear wave splitting in the records of the German Regional Seismic Network, *Geoph. Res. Lett., 21(6),* 457-460, 1994.

Vinx, R. and D. Jung, Pargasitic-kaersutitic amphibole from a basanitic diatreme at the Rosenberg, north of Kassel (North Germany), *Contrib. Mineral. Petrol., 65,* 135-142, 1977.

Vokurka, K. and P. Povondra, Geothermometry and Geobarometry of Lherzolite Nodules from Kozakov, NE Bohemia, Czechoslovakia, *Acta Univ. Carol., 4,* 261-272, 1983.

Vrána, S., J. Cháb, and V. Štědrá, Main results of the project, *in Geological model of Western Bohemia related to the KTB borehole in Germany,* edited by S. Vrána and V. Štědrá, *J. Geol. Sci., Geology, 47,* 43-50, 1997.

Wagner, G.A., D.A. Coyle, J. Duyster, F. Henjes-Kunst, A. Peterek, B. Schröder, B. Stöckhert, K. Wemmer, G. Zulauf, H. Ahrendt, R. Bischoff, E. Hejl, J. Jacobs, D. Menzel, Nand Lal, P. Van den haute, C. Vercoutere, and B. Welzel, Post-Variscan thermal and tectonic evolution of the KTB site and its surroundings, *J. Geophys. Res., 102(B8),* 18,221-18,232, 1997.

Wagner, G.A., K. Gögen, R. Jonckheere, I. Wagner, and C. Woda, Dating of Quaternary volcanoes Komorni Hůrka (Kammerbühl) and Železna Hůrka (Eisenbühl), Czech Republic, by TL, ESR, alpha-recoil and fission track chronometry, *Z. geol. Wiss., 30(3),* 191-200, 2002.

Webb, S.A. and B.J. Wood, Spinel-pyroxene-garnet relationships and their dependence on Cr/Al ratio. *Contrib. Mineral. Petrol., 92,* 471-480, 1986.

Weinlich, F.H., K. Bräuer, H. Kämpf, G. Strauch, J. Tesař, and S.M. Weise, An active subcontinental mantle volatile system in the western Eger rift, Central Europe: Gas flux, isotopic (He, C, and N) and compositional fingerprints, *Geochim. Cosmochim. Acta., 63,* 3,653-3,671, 1999.

Weinlich, F.H., K. Bräuer, H. Kämpf, G. Strauch, J. Tesař, and S.M. Weise, Gas Flux and Tectonic Structure in the Western Eger Rift, Karlovy Vary – Oberpfalz and Oberfranken, Bavaria, *Geolines, 15*, 181-187, 2003.

Weise, S.M., K. Bräuer, H. Kämpf, G. Strauch and U. Koch, Transport of mantle volatiles through the crust traced by seismically released fluids: a natural experiment in the earthquake swarm area Vogtland/NW Bohemia, Central Europe, *Tectonophysics, 336,* 137-150, 2001.

Wells, P.R.A., Pyroxene Thermometry in Simple and Complex Systems, *Contr. Mineral. Petrol., 62,* 129-139, 1977.

Wessels, P. and W.H.F. Smith, New, improved version of Generic Mapping Tools released, *EOS Trans. Am. Geophys. Union, 79,* 579, 1998.

Wever, T. and R. Meissner, About the nature of reflections from the lower continental crust, *Ann. Geophys., 5B*, 349-352, 1987.

Wilkinson, J.F.G. and R.W. Le'Maitre, Upper Mantle Amphiboles and Micas and TiO2, K2O, and P2O5 Abundances and 100 Mg/(Mg+Fe^{2+}) Ratios of Common Basalts and Andesites: Implications for Modal Mantle Metasomatism and Undepleted Mantle Compositions, *J. Petrol., 28,* 37-73, 1987.

Wilshire, H.G. and N.J. Trask, Structural and textural relationships of amphibole and phlogopite in peridotite inclusions, Dish Hill, California, *Am. Min., 56,* 240-255, 1971.

Wilson, A.D., A new method for the determination of ferrous iron in rocks and minerals, *Bull. Geol. Surv. G.B., 9,* 56-58, 1955.

125

References

Wilson, C.K., C.H. Jones, and H. Gilbert, Single-chamber silicic magma system inferred from shear wave discontinuities of the crust and uppermost mantle, Coso geothermal area, California, *J. Geoph. Res., 108(B5),* 2226, doi:10.1029/2002JB001798, 2003.

Wilson, M. and H. Downes, Tertiary-Quaternary Extension-Related Alkaline Magmatism in Western and Central Europe, *J. Petrology, 32,* 811-849, 1991.

Wilson, M. and H. Downes, Mafic alkaline magmatism associated with the European Cenozoic rift system, *Tectonophysics, 208,* 173-182, 1992.

Wilson, M., J.M. Rosenbaum, and E.A. Dunworth, Melilitites: partial melts of the thermal boundary layer?, *Contrib. Mineral. Petrol., 119*, 181-196, 1995.

Wimmenauer, W., The alkaline province of Central Europe and France, in *The Alkaline Rocks*, edited by H. Sörensen, John Wiley & Sons, London, pp. 238-271,1974.

Wirth, W., T. Plenefisch, K. Klinge, and K. Stammler, Focal Mechanisms and Stress Field in the Region Vogtland/NW-Bohemia, *Studia Geoph. Geod., 44(2),* 126-141, 2000.

Witt, G. and H.A. Seck, Origin of amphibole in recrystallized and porphyroclastic mantle xenoliths from the Rhensih Massif: implications for the nature of mantle metasomatism, *Earth Planet. Sci. Lett., 91,* 317-340, 1989.

Witt-Eickschen, G. and G. Kramm, Mantle upwelling and metasomatism beneath Central Europe: geochemical and isotopic constraints from mantle xenoliths from the Rhön (Germany), *J. Petrol., 38,* 479-493, 1997.

Wones, D.R. and M.C. Gilbert, Amphiboles in the igneous environment, in *Amphiboles*, edited by H. Ribbe, *Reviews in Mineralogy, 9B,* pp. 355-390, Mineral. Soc. Amer., 1981.

Woodland, A.B., J. Kornprobst, E. McPherson, J.-L. Bodinier, and M.A. Menzies, Metasomatic interactions in the lithospheric mantle: petrologic evidence from the Lherz massif, French Pyrenees, *Chem. Geol., 134,* 83-112, 1996.

Yaxley, G.M., A.J. Crawford, and D.H. Green, Evidence for carbonatite metasomatism and magmatism in spinel peridotite xenoliths from W. Victoria, Australia, *Earth Planet. Sci. Lett., 107,* 305-317, 1991.

Yuan, X., J. Ni, R. Kind, J. Mechie, and E. Sandvol, Lithospheric and upper mantle structure of southern Tibet from a seismological passive source experiment, *J. Geophys. Res., 102(B12),* 27,491-27,500, 1997.

Yuan, X., S.V. Sobolev, R. Kind, O. Oncken, G. Bock, G. Asch, B. Schurr, F. Graeber, A. Rudloff, W. Hanka, K. Wylegalla, R. Tibi, Ch. Haberland, A. Rietbrock, P. Giese, P. Wigger, P. Röwer, G. Zandt, S. Beck, T. Wallace, M. Pardo, and D. Comte, Subduction and collision processes in the Central Andes constrained by converted seismic phases, *Nature, 408,* 958-961, 2000.

Yuan, X., S.V. Sobolev, and R. Kind, Moho topography in the central Andes an its geodynamic implications, *Earth Planet. Sci. Letters, 199*, 389-402, 2002.

Zandt, G. and Ammon, C.J., Continental crust composition constrained by measurements of crustal Poisson's ratio, *Nature, 374,* 152-154, 1995.

Zandt, G., S.C. Myers, and T.C. Wallace, Crust and mantle structure across the Basin and Range-Colorado Plateau boundary at 37°N latitude and implications for Cenozoic extensional mechanism, *J. Geophys. Res., 100(B6),* 10,529-10,548, 1995.

Zanetti, A., R. Vannucci, P. Bottazzi, R. Oberti, and L. Ottolini, Infiltration metasomatism at Lherz as monitored by systematic ion-microprobe investigations close to a hornblendite vein, *Chem. Geol., 134,* 113-133, 1996.

Zhu, L. and H. Kanamori, Moho depth variation in southern California from teleseismic receiver functions, *J. Geophys. Res., 105(B2),* 2,969-2,980, 2000.

Zeyen, H., O. Novak, M. Landes, C. Prodehl, L. Driad, and A. Hirn, Refraction-seismic investigations of the northern Massif Central (France), *Tectonophysics, 275*, 9-117, 1997.

Ziegler, P.A., European Cenozoic rift system, *Tectonophysics, 208,* 91-111, 1992.

Zimanowski, B., Fragmentationsprozesse beim explosiven Vulkanismus in der Westeifel, *PhD thesis*, Univ. Mainz, 251 p., Mainz, 1986.

Zulauf, G. and J. Duyster, Faults and veins in the superdeep well KTB: constraints on the amount of Alpine intra-plate thrusting and stacking of Variscan basement (Bohemian Massif, Germany), *Geol. Rundsch., 86, Suppl,* S28-S33, 1997a.

Zulauf, G. and J. Duyster, Supracrustal intraplate thickening of Variscan basement due to Alpine foreland compression: Results from the superdeep well KTB (Bohemian Massif, Germany), *Tectonics, 16(5),* 730-743, 1997b.

Zussmann, J. (ed.), Physical methods in determinative mineralogy, 2.ed., Academic Press, London, 720 p., 1977.

Erklärung

Hiermit erkläre ich an Eides statt, dass ich die vorliegende Arbeit selbständig angefertigt habe und keine weiteren außer den angegebenen Quellen und Hilfsmitteln verwendet habe.

Potsdam, 16. Dezember 2004

Wolfram H. Geißler

Appendices

Appendix B.i. **(a)** Input seismic velocity model for reflectivity method.
IASP91 reference model [*Kennett and Engdahl,* 1991].

depth [km]	v_p [km/s]	v_s [km/s]	rho [g/cm^3]	Q_p	Q_s	n (layers)
0	5.8	3.36	2.8	1350	600	0
10	5.8	3.36	2.8	1350	600	1
20	5.8	3.36	2.8	1350	600	1
20	6.5	3.75	3	1350	600	0
35	6.5	3.75	3	1350	600	1
35	8.04	4.47	3.38	1350	600	0
71	8.044	4.483	3.37688	1447	600	4
120	8.05	4.5	3.37091	195	80	8
171	8.192	4.51	3.3671	195	80	5
210	8.3	4.518	3.4	195	80	5
210	8.3	4.522	3.4	362	143	0
271	8.523	4.628	3.46264	365	143	6
371	8.888	4.802	3.51639	370	143	10
410	9.03	4.87	3.54325	372	143	5
410	9.36	5.07	3.72378	366	143	0
450	9.494	5.1548	3.78678	365	143	8
500	9.662	5.2608	3.8498	364	143	8
550	9.83	5.3668	3.91282	363	143	8
600	9.9984	5.4728	3.97584	362	143	8
635	10.116	5.547	3.98399	362	143	6
660	10.2	5.6	3.99214	362	143	6
660	10.79	5.95	4.38071	759	312	0
721	10.9521	6.1083	4.41241	744	312	10
771	11.0756	6.218	4.44316	730	312	8
871	11.2506	6.2929	4.50372	737	312	15
971	11.4172	6.3635	4.56307	743	312	15
1071	11.5761	6.4302	4.62129	750	312	15
1271	11.8732	6.5532	4.7346	761	312	30
1471	12.1469	6.6643	4.84422	770	312	30
1671	12.402	6.7663	4.95073	779	312	30
1871	12.6435	6.8617	5.05469	788	312	30
2071	12.8764	6.9532	5.15669	795	312	30
2271	13.1055	7.0434	5.25729	803	312	30
2471	13.3359	7.1348	5.35706	811	312	30
2571	13.4531	7.1819	5.40681	815	312	15
2671	13.5725	7.2302	5.45657	819	312	15
2771	13.6636	7.2722	5.50642	823	312	15
2871	13.6866	7.297	5.55641	826	312	15
2889	13.6908	7.3015	5.56645	826	312	6
2889	8.009	0.2	9.915	57822	100	0
2971	8.15	0.2	10.043	57822	100	15
3071	8.317	0.2	10.195	57822	100	15
3171	8.477	0.2	10.34	57822	100	15
3271	8.63	0.2	10.478	57822	100	15
3371	8.777	0.2	10.611	57822	100	15
3471	8.917	0.2	10.738	57822	100	15
3571	9.05	0.2	10.859	57822	100	15
3671	9.176	0.2	10.974	57822	100	15
3771	9.295	0.2	11.084	57822	100	15
3871	9.408	0.2	11.189	57822	100	15
3971	9.514	0.2	11.288	57822	100	15
4071	9.614	0.2	11.383	57822	100	15
4171	9.706	0.2	11.473	57822	100	15
4271	9.792	0.2	11.558	57822	100	15
4371	9.871	0.2	11.639	57822	100	15
4471	9.944	0.2	11.716	57822	100	15
4571	10.009	0.2	11.789	57822	100	15
4671	10.068	0.2	11.857	57822	100	15
4771	10.12	0.2	11.922	57822	100	15
4871	10.166	0.2	11.984	57822	100	15
4971	10.204	0.2	12.042	57822	100	15
5071	10.236	0.2	12.096	57822	100	15
5153.9	10.258	0.2	12.703	57822	100	15
5153.9	10.971	3.439	12.703	633	100	0
5171	10.976	3.442	12.703	633	100	15
5271	10.999	3.462	12.753	626	100	15
5371	11.02	3.479	12.798	621	100	15
5471	11.039	3.496	12.834	617	100	15
5571	11.056	3.51	12.875	614	100	15
5671	11.071	3.523	12.907	611	100	15
5771	11.085	3.534	12.935	608	100	15
5871	11.096	3.543	12.959	606	100	15
5971	11.105	3.551	12.978	604	100	15

Appendix B.i. **(b)** Input seismic velocity model (BM3A) for reflectivity method.

depth [km]	v_p [km/s]	v_s [km/s]	rho [g/cm³]	Q_p	Q_s	n (layers)
0	5.4	3.12	2.6	1350	600	5
4	6	3.47	2.7	1350	600	5
11	6.2	3.58	2.8	1350	600	5
13	6.3	3.64	2.8	1350	600	5
25	6.3	3.64	2.8	1350	600	5
34	8	4.47	3	1350	600	5
71	8.044	4.483	3.37688	1447	600	4
71	7.785	4.21	3.37091	195	80	0
100	7.785	4.21	3.37091	195	80	8
120	7.785	4.21	3.37091	195	80	8
171	7.785	4.21	3.3671	195	80	5
210	7.785	4.21	3.3671	195	80	5
210	8.3	4.522	3.4	362	143	0
271	8.523	4.628	3.46264	365	143	6
371	8.888	4.802	3.51639	370	143	10
410	9.03	4.87	3.54325	372	143	5
410	9.36	5.07	3.72378	366	143	0
450	9.494	5.1548	3.78678	365	143	8
500	9.662	5.2608	3.8498	364	143	8
550	9.83	5.3668	3.91282	363	143	8
600	9.9984	5.4728	3.97584	362	143	8
635	10.116	5.547	3.98399	362	143	6
660	10.2	5.6	3.99214	362	143	6
660	10.79	5.95	4.38071	759	312	0
721	10.9521	6.1083	4.41241	744	312	10
771	11.0756	6.218	4.44316	730	312	8
871	11.2506	6.2929	4.50372	737	312	15
971	11.4172	6.3635	4.56307	743	312	15
1071	11.5761	6.4302	4.62129	750	312	15
1271	11.8732	6.5532	4.7346	761	312	30
1471	12.1469	6.6643	4.84422	770	312	30
1671	12.402	6.7663	4.95073	779	312	30
1871	12.6435	6.8617	5.05469	788	312	30
2071	12.8764	6.9532	5.15669	795	312	30
2271	13.1055	7.0434	5.25729	803	312	30
2471	13.3359	7.1348	5.35706	811	312	30
2571	13.4531	7.1819	5.40681	815	312	15
2671	13.5725	7.2302	5.45657	819	312	15
2771	13.6636	7.2722	5.50642	823	312	15
2871	13.6866	7.297	5.55641	826	312	15
2889	13.6908	7.3015	5.56645	826	312	6
2889	8.009	0.2	9.915	57822	100	0
2971	8.15	0.2	10.043	57822	100	15
3071	8.317	0.2	10.195	57822	100	15
3171	8.477	0.2	10.34	57822	100	15
3271	8.63	0.2	10.478	57822	100	15
3371	8.777	0.2	10.611	57822	100	15
3471	8.917	0.2	10.738	57822	100	15
3571	9.05	0.2	10.859	57822	100	15
3671	9.176	0.2	10.974	57822	100	15
3771	9.295	0.2	11.084	57822	100	15
3871	9.408	0.2	11.189	57822	100	15
3971	9.514	0.2	11.288	57822	100	15
4071	9.614	0.2	11.383	57822	100	15
4171	9.706	0.2	11.473	57822	100	15
4271	9.792	0.2	11.558	57822	100	15
4371	9.871	0.2	11.639	57822	100	15
4471	9.944	0.2	11.716	57822	100	15
4571	10.009	0.2	11.789	57822	100	15
4671	10.068	0.2	11.857	57822	100	15
4771	10.12	0.2	11.922	57822	100	15
4871	10.166	0.2	11.984	57822	100	15
4971	10.204	0.2	12.042	57822	100	15
5071	10.236	0.2	12.096	57822	100	15
5153.9	10.258	0.2	12.703	57822	100	15
5153.9	10.971	3.439	12.703	633	100	0
5171	10.976	3.442	12.703	633	100	15
5271	10.999	3.462	12.753	626	100	15
5371	11.02	3.479	12.798	621	100	15
5471	11.039	3.496	12.834	617	100	15
5571	11.056	3.51	12.875	614	100	15
5671	11.071	3.523	12.907	611	100	15
5771	11.085	3.534	12.935	608	100	15
5871	11.096	3.543	12.959	606	100	15
5971	11.105	3.551	12.978	604	100	15

Appendix B.ii. Velocity models used for forward modelling (Figure B.10).

a) Gräfenberg - *Aichele* [1976]

depth [km]	v_p [km/s]	v_p/v_s ratio	n (layers)
0	4.0	1.73	5
1	5.6	1.73	5
3	5.8	1.73	5
6	5.9	1.73	5
6	5.5	1.73	0
12.5	5.5	1.73	5
12.5	6.3	1.73	0
14.5	6.3	1.73	5
20	6.4	1.73	5
23	6.9	1.73	5
32	7.2	1.73	5
33	7.2	1.73	5
33	8.2	1.76	0
50	8.3	1.76	5
100	8.3	1.76	1

d) MOKH - *Plešinger et al.* [1994]

depth [km]	v_p [km/s]	v_p/v_s ratio	n (layers)
0	5.9	1.73	3
6.5	5.9	1.73	5
6.7	6.5	1.73	5
22.5	6.5	1.73	5
23	6.6	1.73	5
32	6.6	1.73	5
32	8.1	1.79	0
55	8.1	1.79	5
55	7.8	1.79	0
140	7.8	1.79	5
140	8.2	1.79	0

b) GRANU95-shotpoint F - *Enderle et al.* [1998]

depth [km]	v_p [km/s]	v_p/v_s ratio	n (layers)
0	5.3	1.73	3
0.5	5.3	1.73	5
0.5	5.8	1.73	0
2	5.8	1.73	5
2	6.4	1.73	0
5	6.5	1.73	5
5	6.4	1.73	0
15.5	6.4	1.73	5
15.5	6.4	1.73	0
24.5	6.4	1.73	5
24.5	7.0	1.73	0
32.7	7.1	1.73	5
32.7	8.0	1.73	0
100	8.0	1.79	1

e) W-Bohemian Massif - *Strößenreuther* [1982]

depth [km]	v_p [km/s]	v_p/v_s ratio	n (layers)
0	5.5	1.73	3
2	5.8	1.73	5
4	6.0	1.73	5
11	6.1	1.73	5
11	5.8	1.73	0
13.5	5.8	1.73	5
15.5	6.4	1.73	5
15.5	6.1	1.73	0
23	6.2	1.73	5
27	6.7	1.73	5
29	6.8	1.73	5
30	7.2	1.73	5
33	7.3	1.73	5
33	8.1	1.79	0
40	8.2	1.79	5
100	8.2	1.79	1

c) Vogtland - *Köhler et al.* [1989]

depth [km]	v_p [km/s]	v_p/v_s ratio	n (layers)
0	5.0	1.73	5
1	5.6	1.73	5
3	6.0	1.73	5
17	6.3	1.73	5
32	7.1	1.73	5
32	8.0	1.79	0
40	8.2	1.79	5
100	8.2	1.79	1

f) Vogtland - *Schulze and Lück* [1992]

depth [km]	v_p [km/s]	v_p/v_s ratio	n (layers)
0	4.8	1.73	5
3.5	6.0	1.73	5
8	6.2	1.73	5
8	5.9	1.73	0
17.5	5.9	1.73	5
17.5	6.4	1.73	0
25	6.8	1.73	5
30	8.0	1.79	5
100	8.0	1.79	1

Appendix B.ii. (continued).

g) MVE90 CMP1 - *Behr et al.* [1994]

depth [km]	v_p [km/s]	v_p/v_s ratio	n (layers)
0	5.4	1.73	3
1	5.9	1.73	5
2	6.0	1.73	5
2	5.6	1.73	0
5	6.9	1.73	5
6	7.0	1.73	5
6	6.2	1.73	0
13	6.3	1.73	5
13	5.5	1.73	0
14	6.7	1.73	3
14.5	6.9	1.73	3
14.5	6.5	1.73	0
30	6.6	1.73	5
30	7.0	1.73	0
32	7.4	1.73	5
32	7.8	1.79	0
35	8.0	1.79	5
100	8.0	1.79	1

h) MVE90 CMP2 - *Behr et al.* [1994]

depth [km]	v_p [km/s]	v_p/v_s ratio	n (layers)
0	5.4	1.73	5
3	5.9	1.73	5
6	6.1	1.73	5
14	5.8	1.73	5
14	6.5	1.73	0
15	7.1	1.73	5
15	6.0	1.73	0
16.5	7.2	1.73	5
16.5	6.1	1.73	0
25	6.6	1.73	5
32	7.2	1.73	5
32	8.0	1.79	0
35	8.0	1.79	5
100	8.0	1.79	1

i) KTB MN - *Schmoll et al.* [1989]

depth [km]	v_p [km/s]	v_p/v_s ratio	n (layers)
0	4.9	1.73	3
1.5	5.7	1.73	5
3.5	5.8	1.73	5
4	6.0	1.73	5
6	6.1	1.73	5
6	5.7	1.73	0
9.5	5.8	1.73	5
9.5	6.0	1.73	0
12	6.2	1.73	5
15.5	6.2	1.73	5
19	6.9	1.73	5
19	6.3	1.73	0
25	6.3	1.73	5
25	6.7	1.73	0
29.5	7.1	1.73	5
29.5	6.2	1.73	0
32	6.4	1.73	5
32	8.1	1.79	0
36	8.2	1.79	5
100	8.2	1.79	1

Appendix B.iii. Velocity models used for forward modelling (Figure B.14).

a)

depth [km]	v_p [km/s]	v_p/v_s ratio	n (layers)
0	5.4	1.73	5
4	6.0	1.73	5
15	6.2	1.73	5
23	6.2	1.73	5
25	6.2	1.73	5
34	8.0	1.79	5
34	8.0	1.79	0
100	8.0	1.79	1

d)

depth [km]	v_p [km/s]	v_p/v_s ratio	n (layers)
0	5.4	1.73	5
4	6.0	1.73	5
5	6.0	1.73	5
15	6.2	1.73	5
23	6.2	1.73	5
25	6.2	1.73	5
33	8.0	1.79	5
40	8.0	1.79	5
43	7.3	1.95	5
48	7.3	1.95	5
49	8.2	1.79	5
100	8.2	1.79	1

b)

depth [km]	v_p [km/s]	v_p/v_s ratio	n (layers)
0	5.4	1.73	5
4	6.0	1.73	5
11	6.2	1.73	5
11	5.7	1.73	0
13	5.7	1.73	5
13	6.3	1.73	0
25	6.3	1.73	5
34	8.0	1.79	5
34	8.0	1.79	0
35	8.0	1.79	5
100	8.0	1.79	1

e)

depth [km]	v_p [km/s]	v_p/v_s ratio	n (layers)
0	5.4	1.73	5
4	6.0	1.73	5
5	6.0	1.73	5
15	6.2	1.73	5
23	6.2	1.73	5
25	6.2	1.73	5
32	7.6	1.79	5
48	7.3	1.79	5
55	8.2	1.79	5
68	8.2	1.79	5
78	7.6	1.79	5
100	7.6	1.79	5

c)

depth [km]	v_p [km/s]	v_p/v_s ratio	n (layers)
0	5.4	1.73	5
4	6.0	1.73	5
7.5	6.2	1.73	5
7.5	7.0	1.73	0
10.5	7.0	1.73	5
10.5	6.2	1.73	0
25	6.3	1.73	5
34	8.0	1.79	5
34	8.0	1.79	0
35	8.0	1.79	5
100	8.0	1.79	1

f)

depth [km]	v_p [km/s]	v_p/v_s ratio	n (layers)
0	5.4	1.73	5
4	6.0	1.73	5
11	6.2	1.73	5
11	5.9	1.73	0
13	5.9	1.73	5
13	6.3	1.73	0
23	6.3	1.73	5
25	6.3	1.73	5
32	7.8	1.79	5
48	7.6	1.79	5
55	8.2	1.79	5
68	8.2	1.79	5
78	7.9	1.79	5
100	7.9	1.79	5

Appendix C.i. Whole-rock chemistry (XRF) of the tephra profile Mýtina.

sample	nephelinite					country rock			Mýtina-lower unit								
	My1	My1-B	My2	My2-B	BK-2B	UF-B1	UF-B2	My-base	UT3	UT4	UT5	UT7	UT9	UT10	UT11	UT14	UT20
depth (cm)								420	390	380	370	350	330	320	310	280	220
SiO_2 (wt.%)	40.0	39.8	41.3	41.1	39.4	65.6	61.3	65.4	60.1	58.9	58.5	58.5	59.0	59.0	59.0	57.3	57.5
TiO_2	2.96	2.93	2.90	2.87	2.91	0.96	0.94	1.06	1.30	1.32	1.30	1.39	1.43	1.47	1.47	1.61	1.63
Al_2O_3	11.5	11.4	11.6	11.6	11.3	16.4	19.8	18.0	17.9	18.2	18.6	17.5	17.1	17.0	16.4	15.9	15.8
$Fe_2O_3(t)$	5.58	5.63	5.68	5.39	7.02	3.32	2.21	6.81	4.37	4.52	4.17	4.50	4.26	4.57	4.05	4.38	4.35
FeO	5.26	5.11	5.05	5.27	4.00	3.64	4.21		3.04	3.20	3.53	3.29	3.40	3.20	3.55	3.60	3.67
MnO	0.19	0.19	0.19	0.19	0.20	0.09	0.05	0.02	0.08	0.09	0.09	0.09	0.09	0.10	0.10	0.11	0.11
MgO	13.64	13.70	12.60	12.68	12.25	1.59	1.59	0.50	2.64	2.88	2.87	3.29	3.50	3.67	4.04	4.94	4.99
CaO	12.67	12.54	12.41	12.31	13.15	0.26	0.28	0.22	1.21	1.55	1.44	2.04	2.31	2.51	3.04	4.06	4.07
Na_2O	2.53	2.61	2.30	2.40	3.47	0.95	1.07	0.15	0.90	0.93	0.96	0.90	0.87	0.85	0.82	0.82	0.78
K_2O	1.55	1.53	1.42	1.42	2.17	3.02	4.16	3.46	3.36	3.38	3.46	3.17	3.10	3.03	2.84	2.60	2.47
P_2O_5	0.67	0.72	0.65	0.71	0.76	0.14	0.15	0.13	0.22	0.23	0.23	0.25	0.25	0.26	0.28	0.33	0.34
H_2O	2.21	2.28	2.51	2.75	1.07	3.96	4.09	4.82	4.91	4.95	5.00	4.81	4.62	4.48	4.31	4.35	4.35
CO_2	0.11	0.10	0.11	0.10	0.17	0.06	0.13	0.36	0.12	0.09	0.11	0.10	0.09	0.10	0.08	0.11	0.13
Total	99.38	98.49	99.33	98.78	97.81	99.95	99.93	100.93	100.11	100.22	100.18	99.92	100.00	100.23	100.02	100.11	100.11
Ba (ppm)	780	770	752	738	734	508	638	557	751	777	836	860	1010	1004	703	713	592
Cr	726	735	586	582	495	73	87		147	158	149	174	189	184	192	230	235
Nb		93		91	105	14	16		32	32	31	37	38	37	36	43	44
Rb	61	59	208	208	58	153	193	174	152	156	161	146	151	150	131	119	121
Sr	707	708	681	687	868	79	109	78	135	154	156	185	209	219	184	229	217
V	315	320	316	306	308	103	119		131	142	136	130	134	135	146	167	165
Y	21	22	22	24	23	41	40	29	39	38	35	38	32	30	33	33	32
Zn	70	72	74	75	76	98	83		101	105	105	104	104	106	102	96	94
Zr	225	220	247	243	259	422	216	178	310	286	292	284	282	289	274	273	288

Appendix C.i. (continued).

sample	Mýtina-lower unit			Mýtina-upper unit										
	UT21a	UT21b	UT22	OT1	OT2	OT3	OT4	OT5	OT6	OT7	OT8	OT9	OT10	OT26
depth (cm)	212	208	200	175	165	155	145	135	125	115	105	95	85	160
SiO_2 (wt.%)	55.9	55.4	55.8	49.3	50.5	46.7	50.6	51.2	52.6	48.3	50.9	45.3	49.6	49.4
TiO_2	1.68	1.53	1.66	2.24	2.22	2.16	2.21	2.09	2.12	2.34	2.22	2.50	2.06	2.21
Al_2O_3	16.4	18.4	16.5	14.1	14.0	13.5	14.5	14.2	13.0	13.8	13.9	13.4	15.4	14.2
$Fe_2O_3(t)$	4.50	5.09	4.71	6.12	5.95	5.73	5.88	5.86	5.76	6.47	6.23	6.16	7.00	6.33
FeO	3.76	3.32	3.60	3.74	3.72	4.65	3.70	3.65	3.56	3.81	3.49	4.17	3.48	3.62
MnO	0.11	0.09	0.11	0.15	0.15	0.16	0.15	0.14	0.15	0.16	0.15	0.16	0.15	0.15
MgO	5.15	3.32	4.98	9.48	9.21	12.32	8.66	9.20	9.21	10.60	9.41	12.14	8.41	9.98
CaO	4.33	2.35	4.02	7.12	7.06	7.34	6.50	6.45	6.91	7.47	6.77	8.70	5.52	6.83
Na_2O	0.80	0.83	0.76	0.73	0.69	1.00	0.72	0.84	0.74	0.66	0.68	0.80	0.66	0.79
K_2O	2.56	3.03	2.55	1.58	1.57	1.69	1.82	1.61	1.42	1.37	1.43	1.26	1.73	1.61
P_2O_5	0.35	0.30	0.34	0.47	0.45	0.46	0.43	0.42	0.45	0.48	0.45	0.48	0.42	0.46
H_2O	4.56	5.79	4.82	4.61	4.42	3.94	4.22	4.17	4.03	4.46	4.39	4.34	5.07	4.31
CO_2	0.12	0.24	0.16	0.21	0.18	0.16	0.18	0.20	0.20	0.24	0.24	0.44	0.56	0.22
Total	100.17	99.76	100.10	99.90	100.06	99.84	99.63	100.12	100.09	100.18	100.18	99.86	100.13	100.03
Ba (ppm)	635	714	666	784	770	834	793	753	746	817	797	765	789	806
Cr	247	179	235	444	432	430	410	441	432	522	456	676	390	484
Nb	45	50	47	67	63	64	63	59	65	69	70	69	61	66
Rb	121	155	125	88	88	113	105	90	98	76	77	61	91	101
Sr	224	170	212	362	366	419	351	349	377	380	359	389	299	372
V	174	181	172	233	226	221	223	223	218	244	223	280	217	223
Y	33	37	34	27	27	26	32	28	25	27	27	26	31	30
Zn	93	98	95	87	88	88	87	87	81	87	85	76	96	88
Zr	287	293	286	251	268	224	269	234	236	247	256	225	231	246

Appendix C.ii. Whole-rock chemistry of crustal xenoliths (XRF, ICP-MS).

sample		quartzitic rocks								
		XKZH4	XKZH8	XKZH5	XKZH53	XKZH64	XKZH6	XKZH54	XKZH55	XKZH58
SiO_2 (wt.%)		100.4	93.1	90.6	89.1	90.4	86.3	85.4	88.7	85.6
TiO_2		0.011	0.418	0.273	0.307	0.191	0.085	0.146	0.124	0.713
Al_2O_3		0.4	3.2	4.5	6.1	3.5	8.4	9.1	5.1	6.2
$Fe_2O_3(t)$		0.14	2.15	2.16	0.51	1.01	1.41	0.43	1.21	2.97
MnO		0.002	0.018	0.064	0.003	0.024	0.026	<0.004	0.027	0.016
MgO		<0,04	0.09	0.27	0.20	0.18	0.26	0.22	0.14	0.31
CaO		0.07	0.19	0.32	0.10	0.15	0.56	0.11	0.12	0.18
Na_2O		<0,1	<0,1	0.63	<0.1	0.82	1.07	<0.1	0.79	<0.1
K_2O		<0,2	0.64	0.86	1.94	0.37	1.31	2.83	2.32	2.42
P_2O_5		0.017	0.085	0.137	0.054	0.031	0.092	0.053	0.042	0.106
H_2O		0.40	1.13	0.77	1.02	0.58	1.05	1.20	0.71	0.91
CO_2		0.22	0.14	0.12	0.06	0.04	0.16	0.07	0.09	0.08
Total		101.66	101.16	100.70	99.33	97.29	100.72	99.48	99.34	99.46
Cs (ppm)	ICP-MS	0.12	1.19	3.8	2.2	0.74	1.28	2.4	1.69	5.5
Rb	XRF				64	17		93	94	85
	ICP-MS	1.8	33	66	64	22	37	89	95	87
Sr	XRF				10	94		12	116	61
	ICP-MS	2.7	90	143	12	92	161	14	111	63
Ba	XRF				348	160		497	604	486
	ICP-MS	7.8	1342	205	322	141	657	463	555	459
$Zr^{1)}$	XRF				791	337		119	105	1409
	ICP-MS	4.7	276	247	202	68	15	29	36	396
Nb	ICP-MS				7.6	5.7		2.7	4.9	23
Ta	ICP-MS				< 1	< 1		< 1	< 1	3
Th	ICP-MS	0.39	22	12.3	9.9	4.3	1.47	1.7	2.7	37
U	ICP-MS	0.08	2.0	1.6	1.8	0.73	0.35	0.29	0.60	5.5
Pb	ICP-MS	0.61	4.7	4.8	2.3	4.5	22	3.9	15	24
V	XRF				<10	<10		<10	10	33
Cr	XRF				<10	<10		<10	<10	20
Ni	XRF				<10	<10		<10	<10	<10
Zn	XRF				<10	17		<10	27	16
Y	XRF				16	10		<10	<10	42
	ICP-MS	0.29	23	10.5	9.8	5.5	3.3	3.3	6.4	30
La	ICP-MS	0.30	29.6	24.9	18.5	12.7	2.56	7.26	12.7	41.1
Ce	ICP-MS	0.97	62.8	52.7	39.8	27.7	8.69	13.0	30.3	126
Pr	ICP-MS	0.07	7.19	5.73	4.47	2.75	0.59	1.37	2.75	9.98
Nd	ICP-MS	0.32	26.3	19.4	17.4	9.87	2.29	4.74	10.2	35.9
Sm	ICP-MS	0.14	5.26	3.51	3.33	1.73	0.54	0.91	1.90	6.95
Eu	ICP-MS	0.03	0.89	0.68	0.63	0.37	0.39	0.52	0.36	0.98
Gd	ICP-MS	0.11	5.09	2.71	2.86	1.44	0.60	0.73	1.54	5.96
Tb	ICP-MS	0.01	0.75	0.38	0.39	0.19	0.10	0.10	0.21	0.92
Dy	ICP-MS	0.07	4.17	1.92	2.09	1.17	0.58	0.62	1.22	5.55
Ho	ICP-MS	0.01	0.80	0.36	0.34	0.19	0.12	0.11	0.22	1.13
Er	ICP-MS	0.03	2.25	1.01	1.01	0.58	0.34	0.34	0.65	3.41
Tm	ICP-MS	< 0.006	0.34	0.15	0.13	0.08	0.05	0.04	0.08	0.50
Yb	ICP-MS	0.04	2.34	1.10	0.90	0.58	0.35	0.34	0.58	3.52
Lu	ICP-MS	< 0.02	0.34	0.17	0.15	0.08	0.05	0.05	0.08	0.55
Hf	ICP-MS	0.14	8.20	6.82	5.59	1.85	0.45	0.77	0.99	11.5
microscopy		qtz	qtz-m	qtz-m fsp-zrn glass?	qtz-m		qtz-m fsp	qtz-m fsp	qtz fsp?	qtz-m-o zrn

[1)] Discrepancy in Zr (Hf, Th) contents probably due to incomplete decomposition of refractory minerals (ICP-MS).

Appendix C.ii. (continued).

sample		quartzitic rocks								
		XKZH75	XKZH7	XKZH11	XKZH12	XKZH13	XKZH14	XKZH16	XKZH51	XKZH59
SiO_2 (wt.%)		86.4	82.8	83.9	81.4	81.7	79.4	83.6	82.3	84.9
TiO_2		0.517	0.092	0.657	0.780	0.783	0.215	0.650	0.679	1.024
Al_2O_3		5.6	11.0	8.8	8.9	8.4	12.4	8.0	8.2	6.1
$Fe_2O_3(t)$		4.14	0.71	3.14	4.63	4.22	3.39	2.54	3.60	3.66
MnO		0.034	0.005	0.029	0.025	0.027	0.037	0.032	0.027	0.033
MgO		0.43	0.16	0.19	0.57	0.62	0.64	0.60	0.54	0.32
CaO		0.22	0.30	0.21	0.26	0.16	0.38	0.30	0.17	0.25
Na_2O		0.68	2.26	<0,1	1.10	<0,1	<0,1	<0,1	<0.1	<0.1
K_2O		0.55	1.99	1.76	1.50	3.12	2.02	2.78	2.68	2.01
P_2O_5		0.070	0.156	0.091	0.093	0.091	0.130	0.093	0.091	0.127
H_2O		1.28	0.86	2.36	1.24	1.49	2.31	1.53	1.43	1.02
CO_2		0.07	0.14	0.25	0.09	0.16	0.15	0.23	0.12	0.09
Total		99.91	100.47	101.39	100.59	100.77	101.07	100.36	99.77	99.57
Cs (ppm)	ICP-MS	2.23	1.53	2.02	9.06	6.13	4.54		6.05	2.6
Rb	XRF	31							100	56
	ICP-MS	35	55	51	95	118	68		102	64
Sr	XRF	35							45	70
	ICP-MS	38	49	62	43	56	123		47	71
Ba	XRF	171							514	512
	ICP-MS	161	382	547	350	479	748		476	462
Zr	XRF	695							1063	2304
	ICP-MS	206	18	536	483	947	41		438	476
Nb	ICP-MS	15							22	33
Ta	ICP-MS	2							3	4
Th	ICP-MS	15	1.8	25	25	43	4.0		29	59
U	ICP-MS	2.6	0.53	3.8	4.4	5.6	1.20		4.3	7.4
Pb	ICP-MS	6	10.6	20	6.6	22	17		14	33
V	XRF	36							34	43
Cr	XRF	16							27	29
Ni	XRF	12							15	28
Zn	XRF	59							31	30
Y	XRF	30							37	63
	ICP-MS	20	7.5	36	36	40	15		29	43
La	ICP-MS	37.7	9.82	46.6	53.7	46.8	12.0		49.4	69.1
Ce	ICP-MS	77.0	18.0	99.7	112	133	26.4		108	174
Pr	ICP-MS	8.76	2.06	11.4	13.4	11.6	2.90		11.9	16.1
Nd	ICP-MS	32.4	7.33	40.7	47.9	40.6	10.9		44.0	60.1
Sm	ICP-MS	5.74	1.42	7.95	8.95	7.74	2.59		8.15	11.4
Eu	ICP-MS	1.13	0.83	1.32	1.50	1.09	0.66		1.19	1.45
Gd	ICP-MS	4.83	1.40	7.29	7.47	6.76	3.22		6.70	9.90
Tb	ICP-MS	0.69	0.22	1.07	1.09	1.05	0.49		0.94	1.40
Dy	ICP-MS	3.89	1.34	6.32	6.33	6.47	2.88		5.71	8.16
Ho	ICP-MS	0.73	0.26	1.25	1.25	1.34	0.54		1.09	1.53
Er	ICP-MS	2.15	0.72	3.66	3.66	4.14	1.50		3.24	4.59
Tm	ICP-MS	0.30	0.10	0.55	0.55	0.66	0.21		0.45	0.66
Yb	ICP-MS	2.07	0.67	3.81	3.84	4.67	1.38		3.22	4.48
Lu	ICP-MS	0.30	0.08	0.56	0.57	0.72	0.19		0.48	0.69
Hf	ICP-MS	5.91	0.52	14.3	13.3	24.9	1.25		12.4	13.8
microscopy		qtz-m		qtz-m	qtz-m-mag	qtz-m-mag		qtz-m-mag	qtz-m	qtz-m-o
				zrn?		ms-bt?		ms-bt?		ms-bt?
		fsp?		melt?	grt-st	zrn-am?				zrn

sample		quartzitic rocks				norite	phyllites, mica shists			
		XKZH61	XKZH70	XKZH65	XKZH 66	XKZH1	XKZH10	XKZH67	XKZH62	XKZH69
SiO_2 (wt.%)		83.6	84.3	82.6	83.3	52.2	55.2	57.4	59.9	61.0
TiO_2		0.796	0.524	0.206	0.138	0.281	1.467	1.128	1.093	1.067
Al_2O_3		7.2	6.0	8.6	9.4	21.6	24.7	21.8	21.8	20.2
Fe_2O_3(t)		3.15	4.08	1.23	1.25	5.30	7.47	7.71	6.44	6.16
MnO		0.014	0.075	0.014	0.010	0.091	0.083	0.067	0.046	0.049
MgO		0.37	0.52	0.33	0.39	7.19	1.80	1.60	1.21	1.40
CaO		0.18	0.29	0.35	0.39	9.51	0.42	0.32	0.34	0.33
Na_2O		<0.1	0.64	1.38	1.15	3.00	1.53	1.12	1.52	1.71
K_2O		2.68	1.47	1.82	1.15	0.14	4.48	4.34	4.58	4.09
P_2O_5		0.105	0.121	0.085	0.191	0.027	0.159	0.089	0.117	0.123
H_2O		1.16	1.40	0.96	1.50	0.64	2.75	4.58	3.03	3.98
CO_2		0.08	0.05	0.06	0.13	0.07	0.48	0.05	0.29	0.12
Total		99.34	99.50	97.65	99.04	100.05	100.54	100.21	100.34	100.28
Cs (ppm)	ICP-MS	3.9	12.9	1.1	0.76	0.0	10.2	12.6	12.7	10.2
Rb	XRF	81	90	44	28			215	196	188
	ICP-MS	85	90	44	29	2	136	204	196	198
Sr	XRF	81	87	77	81			144	168	123
	ICP-MS	84	85	70	78	446	129	130	163	123
Ba	XRF	584	252	1011	474			947	784	965
	ICP-MS	573	225	930	434	155	790	853	756	880
Zr	XRF	1727	800	54	52			233	285	279
	ICP-MS	492	437	27	20	6.6	226	182	189	199
Nb	ICP-MS	26	16	7	5			30	30	30
Ta	ICP-MS	4	2	< 1	< 1			4	7	5
Th	ICP-MS	43	17	2.1	2.1	0.05	20	19	21	20
U	ICP-MS	5.7	2.8	0.54	0.64	0.03	3.2	2.7	3.6	3.3
Pb	ICP-MS	22	33	12.4	5.3	1.12	36	23	28	20
V	XRF	42	32	17	13			126	137	109
Cr	XRF	25	23	21	<10			94	90	84
Ni	XRF	<10	13	12	<10			43	31	32
Zn	XRF	23	72	20	14			131	85	87
Y	XRF	60	35	<10	<10			40	42	41
	ICP-MS	43	28	6.0	7.6	3.20	37	32	31	32
La	ICP-MS	65.1	30.5	7.42	11.2	2.41	55.6	54.4	63.3	59.9
Ce	ICP-MS	146	78.4	15.7	19.3	3.96	121	107	126	120
Pr	ICP-MS	15.4	7.07	1.65	2.17	0.45	13.9	12.6	15.1	14.0
Nd	ICP-MS	56.7	26.3	6.22	7.68	1.75	50.0	46.1	55.2	52.3
Sm	ICP-MS	11.0	5.21	1.28	1.58	0.39	9.55	8.45	10.29	9.67
Eu	ICP-MS	1.59	1.00	0.61	0.78	0.57	1.82	1.72	2.02	1.80
Gd	ICP-MS	9.53	5.42	1.30	1.48	0.51	8.20	7.00	8.40	8.01
Tb	ICP-MS	1.38	0.85	0.18	0.23	0.09	1.19	1.03	1.14	1.09
Dy	ICP-MS	8.16	5.19	1.14	1.45	0.54	6.97	6.27	6.28	6.27
Ho	ICP-MS	1.56	1.01	0.21	0.26	0.11	1.36	1.20	1.17	1.17
Er	ICP-MS	4.57	3.02	0.66	0.77	0.35	3.87	3.69	3.47	3.50
Tm	ICP-MS	0.65	0.42	0.09	0.10	0.05	0.56	0.52	0.48	0.49
Yb	ICP-MS	4.48	2.81	0.58	0.64	0.36	3.95	3.43	3.29	3.14
Lu	ICP-MS	0.66	0.42	0.07	0.08	0.06	0.56	0.50	0.50	0.50
Hf	ICP-MS	15.0	11.5	0.74	0.63	0.23	6.37	5.34	5.65	5.92
microscopy		qtz-m-mag ms-bt zrn	qtz-m-o	qtz-m-fsp ms mag	qtz-m-fsp ms mag	fsp-opx phl-cpx-rt mag	m-qtz-mag	m-qtz-mag crd?	m-qtz-mag	m-qtz-mag crd?

Appendix C.ii. (continued).

sample		phyllites, mica shists						mica shists		?
		XKZH17	XKZH19	XKZH56	XKZH57	XKZH 68	XKZH63	XKZH50	XKZH52	XKZH60
SiO_2 (wt.%)		60.6	70.9	68.9	65.6	74.5	76.3	43.2	41.6	71.5
TiO_2		1.093	0.704	0.799	1.054	0.923	0.840	1.432	1.477	0.261
Al_2O_3		21.6	13.8	13.8	19.3	12.9	10.1	32.0	31.2	17.0
Fe_2O_3(t)		6.54	7.17	7.98	5.52	6.68	6.51	9.23	9.07	1.80
MnO		0.060	0.049	0.044	0.050	0.085	0.066	0.069	0.122	0.011
MgO		0.86	1.48	1.67	0.70	0.74	1.18	1.56	2.02	0.57
CaO		0.35	0.26	0.30	0.31	0.29	0.29	0.39	0.25	0.24
Na_2O		1.24	0.63	2.13	1.68	0.63	0.82	1.33	0.54	<0.1
K_2O		4.22	2.44	2.37	3.10	1.13	1.42	6.63	7.59	5.81
P_2O_5		0.096	0.071	0.074	0.084	0.074	0.074	0.073	0.059	0.136
H_2O		3.90	3.28	2.11	2.81	2.48	2.54	3.92	6.39	2.10
CO_2		0.37	0.17	0.16	0.18	0.06	0.05	0.15	0.07	0.08
Total		100.93	100.95	100.36	100.36	100.52	100.20	99.99	100.33	99.54
Cs (ppm)	ICP-MS	7.4	13.3	11.7	5.8	2.6	5.8	14.4	16.9	10.7
Rb	XRF			164	117	51	96	256	323	295
	ICP-MS	161	158	175	120	50	101	254	269	298
Sr	XRF			117	142	92	69	196	189	41
	ICP-MS	119	100	114	141	90	70	190	168	42
Ba	XRF			428	627	436	571	2079	1371	912
	ICP-MS	694	669	378	569	387	492	1866	1176	881
Zr	XRF			243	281	537	495	263	291	188
	ICP-MS	216	161	107	151	170	210	207	254	104
Nb	ICP-MS			24	31	27	23	45	42	17
Ta	ICP-MS			5	5	4	3	9	7	4
Th	ICP-MS	18	12	15	18	19	18	25	23	15
U	ICP-MS	2.7	2.4	2.4	3.2	3.3	3.6	3.7	3.4	6.5
Pb	ICP-MS	31	17	18	18	6	7	59	28	10
V	XRF			72	108	76	58	204	205	10
Cr	XRF			55	74	48	41	128	135	<10
Ni	XRF			32	28	27	25	40	57	<10
Zn	XRF			121	88	86	113	104	148	40
Y	XRF			29	40	43	39	52	46	45
	ICP-MS	33	27	20	26	25	30	33	33	30
La	ICP-MS	47.0	34.3	39.6	53.9	51.8	49.0	80.4	64.6	12.1
Ce	ICP-MS	97.1	68.1	80.6	108	104	98.8	159	130	53.2
Pr	ICP-MS	11.5	8.39	9.37	12.7	11.9	11.5	18.4	15.4	3.29
Nd	ICP-MS	41.1	30.1	34.2	47.3	44.1	42.2	68.6	58.0	12.6
Sm	ICP-MS	7.74	5.94	6.38	8.63	7.71	7.54	12.3	10.1	3.18
Eu	ICP-MS	1.57	1.22	1.20	1.69	1.46	1.46	2.30	1.97	0.19
Gd	ICP-MS	6.66	5.20	5.01	6.89	6.38	6.31	9.48	7.57	3.52
Tb	ICP-MS	0.99	0.75	0.67	0.94	0.88	0.96	1.20	1.13	0.73
Dy	ICP-MS	5.90	4.65	3.92	5.38	4.89	5.60	6.74	6.82	4.99
Ho	ICP-MS	1.18	0.93	0.71	1.00	0.92	1.06	1.27	1.32	1.08
Er	ICP-MS	3.44	2.68	2.12	2.94	2.69	3.09	3.60	3.89	3.52
Tm	ICP-MS	0.51	0.42	0.32	0.39	0.37	0.43	0.51	0.56	0.54
Yb	ICP-MS	3.53	2.72	2.06	2.72	2.59	3.02	3.46	3.88	3.58
Lu	ICP-MS	0.51	0.41	0.32	0.40	0.37	0.43	0.52	0.59	0.50
Hf	ICP-MS	6.13	4.55	3.13	4.47	4.94	6.17	5.85	7.08	3.67
microscopy		m-qtz-mag	qtz-m-mag	qtz-m-mag	qtz-m-mag	qtz-m	qtz-m	m-grt-qtz-mag	m-qtz-mag	qtz-m
		ms	ms-bt?	ms-bt?				(ms-bt-chl)	crd?	ms-bt?
		crd?-pm		fsp?			fsp?	zrn-crd?	hbl?	fsp?

Appendix C.iii. **(a)** Chondrite (C1)-normalised REE patterns of crustal xenoliths from the tephra deposit in Mýtina. REE values of C1-chondrites taken from *Anders and Grevesse* [1989].
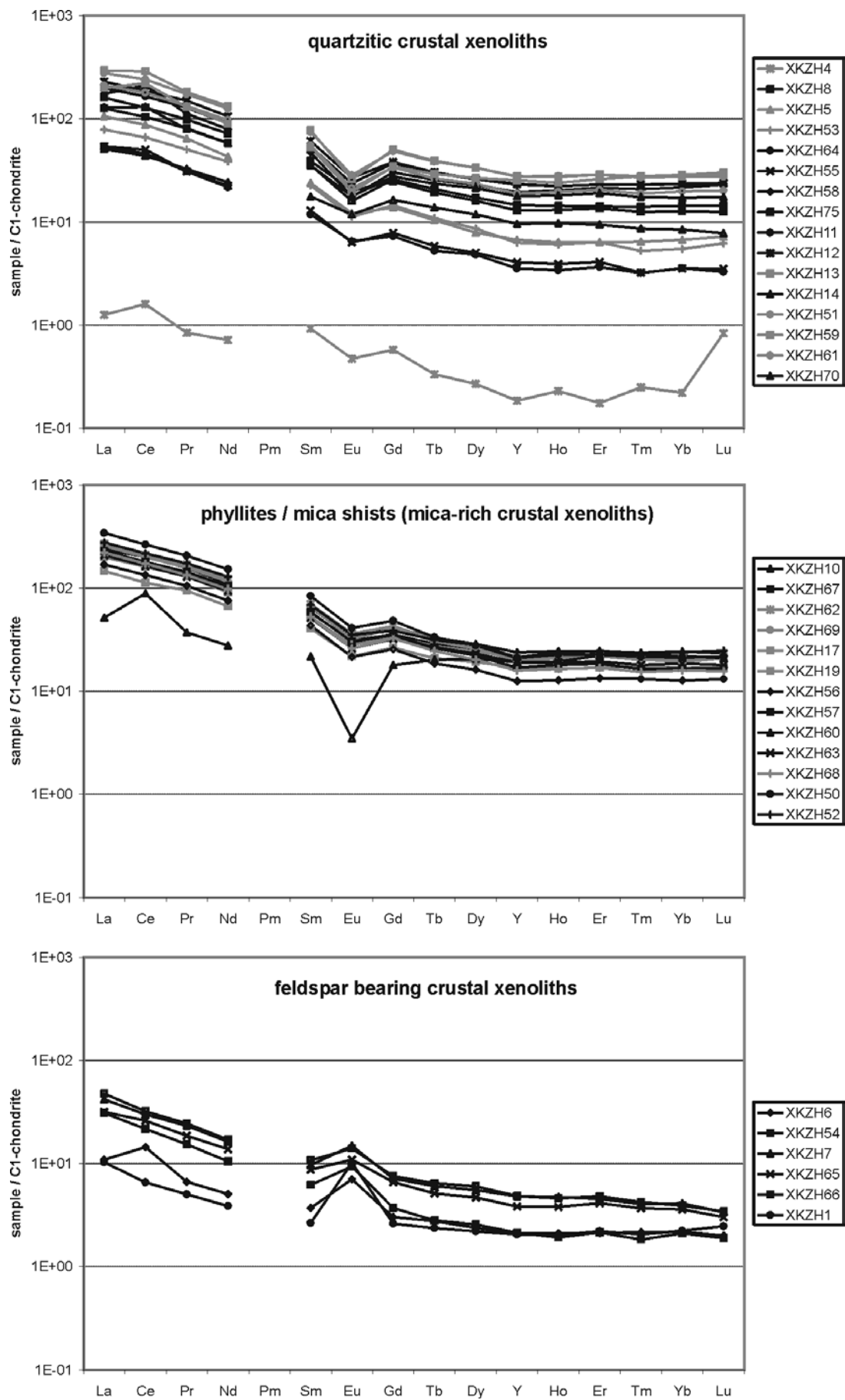
Appendix C.iii. **(b)** Post-Archean Australian Shale (PAAS)-normalised REE patterns of crustal xenoliths from the tephra deposit in Mýtina. REE values of PAAS taken from *McLennann* [1989].
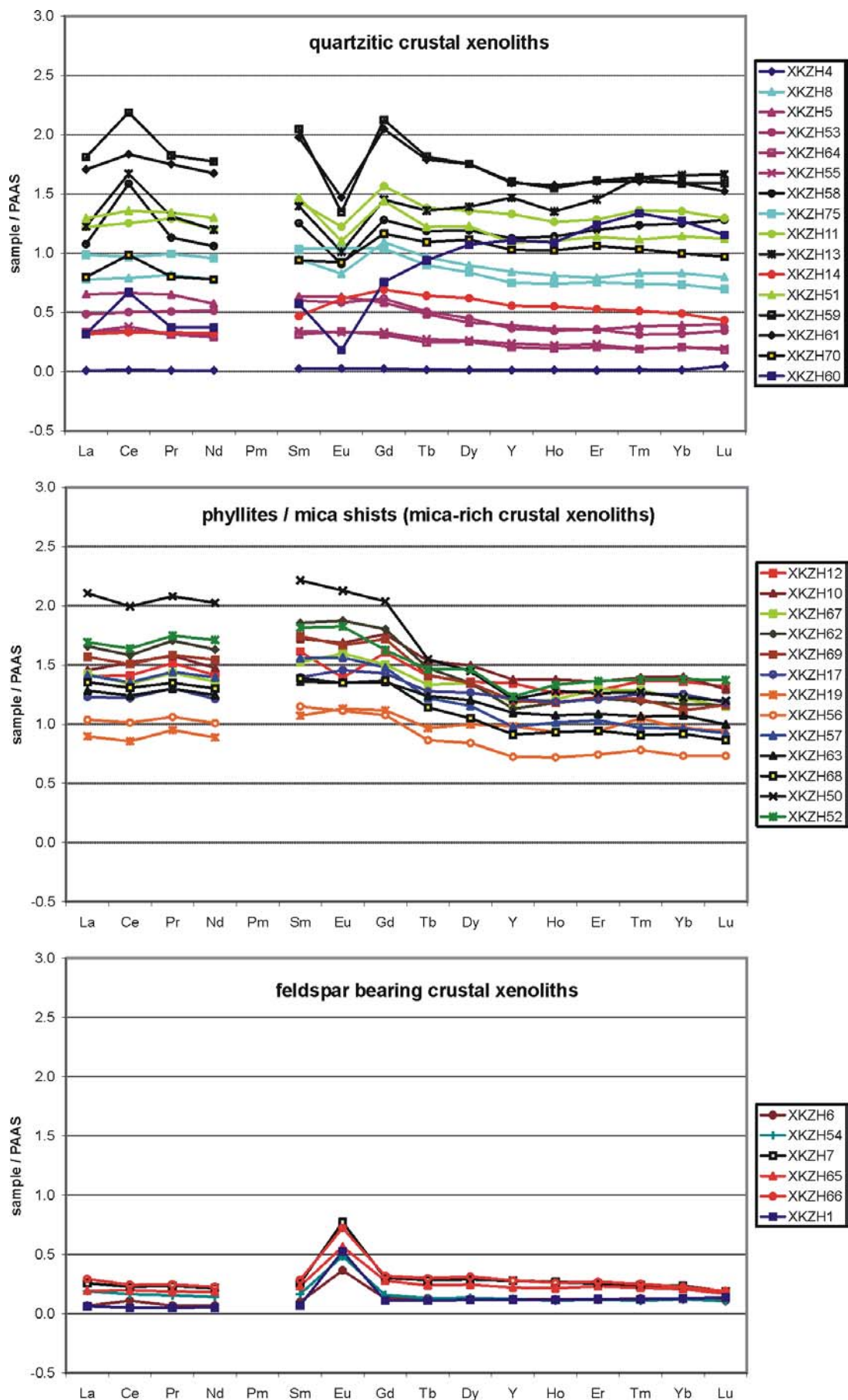
Appendix C.iv. Pressure estimates from clinopyroxenes, calculated with the Excel-worksheet of *Nimis* [1999]. Due to uncertainties in estimating temperatures, pressure was calculated for two different temperature values.

Sample	P(BA) kbar	Temp (°C)	P(BH) kbar	Temp (°C)	P(BH) kbar
peridotites					
MXZH66	7	960	20	1058	15
		1100	13	1150	12
Zinst-1	9	1000	21	1100	16
Go01-1	6	920	20	980	17
wehrlites, ol-cpx cumulates					
MXZH1	7	1000	18	1150	10
MXZH2-cpx1	7	1000	18	1150	10
MXZH2-cpx2	5	1000	15	1150	8
MXZH4	5	1000	15	1150	7
MXZH8	6	1000	17	1150	9
MXZH18-cpx1	6	1050	14	1110	11
MXZH18-cpx2-c	6	1050	14	1110	11
MXZH18-cpx2-r	0	1050	5	1110	2
MXZH61-cpx1-c	6	1100	12	1150	10
MXZH61-cpx1-r	-1	1050	3	1100	0
MXZH61-cpx2	8	1100	14	1150	12
MXZH64-c	6	1060	14	1120	11
MXZH64-r	0	1060	5	1150	1
clinopyroxenites, hornblendites					
MXZH11	0	900	12	1000	7
MXZH5	0	900	13	1000	8
MXZH33	-1	900	10	1000	5
MXZH12	1	930	11	970	9
MXZH13	-1	930	9	1000	6
megacrysts					
MXZH9	7	1000	18	1150	11
MXZH14	7	1000	18	1150	11
MXZH16	8	1000	19	1150	12
MXZH62-cpxold	6	1000	16	1150	8
MXZH62-cpx	8	1000	19	1150	12
MXZH62-cpx-r1	7	1000	18	1150	11
MXZH62-cpx-r2	0	1000	8	1150	1
EB2-cpx-s1	6	1000	17	1150	9
EB2-cpx-s2	7	1000	19	1150	11
EB7	8	1000	19	1150	12
EB6	5	1000	15	1150	8
groundmass					
MXZH8-gm-c	-2	1000	4	1150	-2
MXZH24-gm-c	7	1100	13	1150	11
MXZH24-gm-r	-1	1000	6	1150	-1
MXZH24-glass	-1	1000	7	1150	0
crust xenoliths					
XKZH1	4	800	23	1150	5
XKZH3	5	1000	17	1150	10

Appendix C.v. Results of two-pyroxene geothermometry [*Brey and Köhler,* 1990].

	Go01-1		Zinst-1		XKZH1					
	cpx	opx	cpx	opx	opx-r		opx-c		cpx	opx-x
Si	1.917	1.931	1.931	1.917		1.940		1.942	1.846	1.914
Ti	0.001	0.00	0.009	0.004		0.002		0.003	0.039	0.010
Al	0.167	0.109	0.165	0.147		0.103		0.108	0.247	0.162
Cr	0.027	0.010	0.035	0.021		0.001		0.002	0.005	0.003
Fe^{3+}										
Fe^{2+}	0.080	0.174	0.091	0.164		0.538		0.539	0.229	0.414
Mg	0.920	1.762	0.918	1.700		1.395		1.375	0.788	1.426
Mn	0.003	0.004	0.002	0.004		0.012		0.012	0.004	0.004
Ni										
Ca	0.84	0.019	0.759	0.036		0.014		0.020	0.812	0.057
Ba										
Na	0.060	0.003	0.100	0.010		0.000		0.002	0.045	0.008
K	0.000	0.000	0.000	0.000		0.001		0.000	0.001	0.000
P										
Total	4.014	4.011	4.011	4.001	0.000	4.006	0.000	4.002	4.014	3.998
Mg/(Mg+Fe)	0.92	0.91	0.91	0.91		0.72		0.72	0.77	0.78
K_D	0.109		0.162		1.015		1.020		0.159	
p (kbar)	19		21		6		6		6	
	T (K)	T (°C)	T (K)	T (°C)	T (K)	T (°C)	T (K)	T (°C)	T (K)	T (°C)
Ca-in-opx	1195	922	1351	1078	1081	808	1139	866	1398	1125
BKN	1257	984	1378	1105					1239	966
Na-in-cpxopx	1276	1003	1444	1171					1555	1282

Appendix C.vi. Results of olivine-spinel geothermometry.

	Go01-1		Zinst-1		MXZH66		MXZH18		MXZH64		MXZH61		MXZH17		EB5-9		MXZH69-gm	
	ol	sp	ol	sp	ol	sp	ol	sp	ol	sp	ol	sp	ol	sp	ol	sp	ol	sp
Si	0.996	0.00	0.994	0.02	0.978	0.03	0.993	0.03	0.994	0.02	0.988	0.02	0.991	0.03	0.991	0.02	0.986	0.02
Ti	0.000	0.00	0.000	0.11	0.000	0.26	0.000	0.24	0.000	0.25	0.000	0.25	0.000	0.24	0.000	0.25	0.000	0.25
Al	0.000	10.48	0.000	8.55	0.001	10.88	0.001	7.82	0.001	7.54	0.001	8.16	0.001	7.94	0.001	6.37	0.001	8.20
Cr	0.000	4.61	0.001	6.25	0.000	2.50	0.001	6.36	0.001	6.60	0.001	6.00	0.001	6.15	0.001	7.79	0.001	6.01
Fe^{3+}		0.90		1.04		2.26		1.47		1.51		1.50		1.57		1.49		1.46
Fe^{2+}	0.183	1.92	0.183	2.13	0.347	2.82	0.224	2.40	0.222	2.40	0.256	2.41	0.231	2.29	0.217	2.47	0.228	2.38
Mg	1.813	6.00	1.813	5.77	1.681	5.07	1.774	5.52	1.773	5.49	1.751	5.50	1.770	5.61	1.785	5.43	1.782	5.52
Mn	0.003	0.01	0.003	0.02	0.005	0.03	0.002	0.01	0.003	0.02	0.004	0.03	0.004	0.02	0.003	0.02	0.003	0.02
Ni	0.008	0.04	0.008	0.05	0.003	0.03	0.005	0.03	0.005	0.03	0.004	0.03	0.005	0.04	0.005	0.03	0.005	0.04
Ca	0.001	0.00	0.002	0.00	0.004	0.00	0.004	0.00	0.004	0.01	0.004	0.00	0.005	0.00	0.005	0.00	0.005	0.00
Ba																		
Na																		
K																		
P																		
Total	3.004	23.976	3.004	23.937	3.020	23.878	3.005	23.897	3.004	23.880	3.010	23.897	3.007	23.886	3.007	23.881	3.011	23.900
$Mg/(Mg+Fe^{2+})$	0.908	0.758	0.908	0.730	0.829	0.643	0.888	0.697	0.889	0.696	0.872	0.695	0.885	0.710	0.892	0.688	0.887	0.699
X_{Mg}/X_{Fe}	9.905	3.128	9.922	2.705	4.842	1.801	7.911	2.302	7.986	2.286	6.837	2.283	7.677	2.452	8.240	2.202	7.814	2.318
CaO/MgO																		
Cr/(Cr+Al)		0.306		0.422		0.187		0.449		0.467		0.424		0.436		0.550		0.423
$Cr/(Cr+Al+Fe^{3+})$		0.288		0.395		0.160		0.406		0.422		0.383		0.393		0.498		0.383
$Al/(Cr+Al+Fe^{3+})$		0.655		0.540		0.695		0.500		0.482		0.521		0.507		0.407		0.524
$Fe^{3+}/(Cr+Al+Fe^{3+})$		0.056		0.066		0.145		0.094		0.097		0.096		0.100		0.095		0.093
$K_D(Mg/Fe^{2+})$	3.166		3.668		2.688		3.437		3.494		2.995		3.131		3.741		3.371	

	Go01-1		Zinst-1		MXZH66		MXZH18		MXZH64		MXZH61		MXZH17		EB5-9		MXZH69-gm	
p (kbar)	19		21		15		10		10		10		10		10		10	
	T (K)	T (°C)	T (K)	T (°C)	T (K)	T (°C)	T (K)	T (°C)	T (K)	T (°C)	T (K)	T (°C)	T (K)	T (°C)	T (K)	T (°C)	T (K)	T (°C)
Roeder et al. [1979]	1339	1066	1328	1055	1563	1290	1445	1172	1449	1176	1575	1302	1543	1270	1456	1183	1439	1166
Ballhaus et al., [1991]	1170	897	1236	963	1219	946	1317	1044	1329	1056	1374	1101	1375	1102	1364	1091	1302	1029
O'Neill and Wall [1987]	1196	923	1276	1003	1331	1058	1381	1108	1393	1120	1459	1186	1443	1170	1435	1162	1364	1091
Fabries [1979]																		
Irvine [1965]	$KD_0=$ 2.530		$KD_0=$ 2.817		$KD_0=$ 1.507		$KD_0=$ 2.360		$KD_0=$ 2.374		$KD_0=$ 2.042		$KD_0=$ 2.098		$KD_0=$ 2.554		$KD_0=$ 2.323	
	1268	995	1298	1025	1589	1316	1414	1141	1422	1149	1498	1225	1485	1212	1431	1158	1406	1133
Roeder et al. [1979]	$KD_0=$ 2.830		$KD_0=$ 3.215		$KD_0=$ 2.013		$KD_0=$ 2.848		$KD_0=$ 2.880		$KD_0=$ 2.473		$KD_0=$ 2.563		$KD_0=$ 3.091		$KD_0=$ 2.798	
	1202	929	1228	955	1295	1022	1301	1028	1307	1034	1366	1093	1351	1078	1326	1053	1292	1019
O'Neill [1981] - p_{max}	25		27		24		27		27		27		27		29		27	

Appendix C.vii. Results of olivine-clinopyroxene geobarometry [*Köhler and Brey, 1990*]. Temperatures were calculated with different geothermometers [BKN - *Brey and Köhler, 1990*; NW1987 - *O'Neill and Wall, 1987*; R1979 - *Roeder et al., 1979*] or assumed (T=1150°C).

	Go01-1 ol	Go01-1 cpx	Zinst-1 ol	Zinst-1 cpx	MXZH66 ol	MXZH66 cpx	MXZH1 ol	MXZH1 cpx	MXZH2 ol1	MXZH2 cpx1	MXZH2 ol2	MXZH2 cpx2	MXZH4 ol1	MXZH4 cpx1	MXZH18 ol	MXZH18 cpx	MXZH64 ol	MXZH64 cpx
Si	0.996	1.917	0.994	1.93	0.978	1.82	0.990	1.87	0.986	1.87	0.988	1.90	0.989	1.90	0.993	1.89	0.994	1.89
Ti	0.000	0.001	0.000	0.01	0.000	0.03	0.000	0.02	0.000	0.02	0.000	0.02	0.000	0.02	0.000	0.02	0.000	0.02
Al	0.000	0.167	0.000	0.17	0.001	0.28	0.001	0.21	0.001	0.23	0.001	0.16	0.001	0.17	0.001	0.18	0.001	0.19
Cr	0.000	0.027	0.001	0.04	0.000	0.00	0.005	0.04	0.001	0.04	0.001	0.03	0.001	0.03	0.001	0.04	0.001	0.04
Fe^{3+}																		
Fe^{2+}	0.183	0.080	0.183	0.09	0.347	0.17	0.228	0.11	0.241	0.12	0.230	0.12	0.239	0.12	0.224	0.11	0.222	0.10
Mg	1.813	0.920	1.813	0.92	1.681	0.81	1.774	0.88	1.771	0.85	1.778	0.92	1.766	0.90	1.774	0.93	1.773	0.88
Mn	0.003	0.003	0.003	0.00	0.005	0.02	0.004	0.00	0.003	0.00	0.003	0.00	0.003	0.00	0.002	0.00	0.003	0.00
Ni	0.008		0.008		0.003		0.005	0.0008	0.004	0.0005	0.004	0.00167	0.004	0.0012	0.005		0.005	
Ca	0.001	0.840	0.002	0.76	0.004	0.82	0.005	0.81	0.004	0.82	0.004	0.80	0.004	0.82	0.004	0.80	0.004	0.81
Ba																		
Na		0.060		0.10		0.07		0.07		0.07		0.06		0.06		0.06	0.002	0.06
K		0.000		0.00		0.00		0.00		0.00		0.00		0.00		0.00	0.000	0.00
P																		
Total	3.004	4.014	3.004	4.011	3.020	4.034	3.012	4.013	3.011	4.012	3.010	4.014	3.008	4.017	3.005	4.018	3.005	4.007
Ca (trace)	0.0010		0.0020		0.0038		0.0045		0.0044		0.0042		0.0044[*]		0.0039		0.0039	
Mg/(Mg+Fe)	0.91	0.92	0.91	0.91	0.83	0.82	0.89	0.89	0.88	0.88	0.89	0.88	0.88	0.88	0.89	0.90	0.89	0.89
X_{Mg}/X_{Fe}	9.90		9.92		4.84		7.77		7.35		7.73		7.38		7.91		7.99	
D_{Ca}	0.0012		0.0026		0.0047		0.0055		0.0054		0.0053		0.0054		0.0049		0.0048	
	T (K)	p (kbar)	T (K)	p (kbar)	T (K)	p (kbar)	T (K)	p (kbar)	T (K)	p (kbar)	T (K)	p (kbar)	T (K)	p (kbar)	T (K)	p (kbar)	T (K)	p (kbar)
BKN or assumed	1257	19	1378	21	1423	14	1423	10	1423	10	1423	11	1423	11	1423	13	1423	13
NW1987	1196	8	1276	4	1331	-1									1381	6	1393	9
R1979	1339	34	1328	12	1563	37									1445	16	1449	18
Fo	90.3		90.3		82.4		88.0		87.5		88.0		87.6		88.3		88.3	
Wo		44.1		40.6		43.1		43.4		43.9		42.2		42.9		42.0		43.5
En		48.4		49.1		42.9		46.9		45.9		48.3		47.5		49.1		47.3
Fs		4.3		5.0		10.1		6.2		6.5		6.5		6.4		5.8		5.8
Ac		3.2		5.4		3.9		3.5		3.7		3.1		3.2		3.1		3.5

[*] – value taken from MXZH2

Appendix C.viii. Results of (clinopyroxene-) amphibole geobarometry.

	MXZH66 cpx	MXZH66 am	MXZH11 cpx	MXZH11 am	MXZH5 cpx	MXZH5 am	MXZH33 cpx	MXZH33 am	MXZH12 cpx	MXZH12 am	MXZH13 cpx	MXZH13 am	XKZH1 cpx	XKZH1 am
Si	1.823	5.974	1.804	5.978	1.806	5.949	1.895	6.009	1.839	6.039	1.879	5.961	1.846	6.549
Ti	0.031	0.349	0.053	0.286	0.041	0.265	0.024	0.285	0.045	0.340	0.030	0.343	0.039	0.179
Al	0.280	2.463	0.262	2.364	0.280	2.514	0.156	2.257	0.221	2.287	0.176	2.274	0.247	1.954
Cr	0.004	0.090	0.000	0.002	0.000	0.001	0.000	0.001	0.001	0.000	0.000	0.001	0.005	0.005
Fe^{3+}														
Fe^{2+}	0.173	0.863	0.289	1.796	0.303	1.865	0.217	1.477	0.233	1.459	0.216	1.472	0.229	1.243
Mg	0.814	3.329	0.639	2.637	0.625	2.486	0.738	3.042	0.711	2.894	0.723	2.987	0.788	3.289
Mn	0.019	0.008	0.007	0.026	0.006	0.024	0.004	0.017	0.005	0.015	0.005	0.017	0.004	0.015
Ni					0.001	0.001								
Ca	0.817	1.784	0.915	1.901	0.916	1.925	0.937	1.945	0.915	1.895	0.941	1.952	0.812	1.734
Ba								0.001				0.001		
Na	0.074	0.635	0.088	0.859	0.069	0.668	0.063	0.801	0.075	0.753	0.068	0.748	0.045	0.547
K	0.000	0.413	0.000	0.257	0.000	0.322	0.000	0.285	0.001	0.339	0.000	0.350	0.001	0.101
P														
Total	4.034	15.907	4.056	16.106	4.047	16.021	3.005	16.119	4.044	16.022	4.037	16.105	4.014	15.614
$Mg/(Mg+Fe^{2+})$	0.825	0.794	0.689	0.595	0.674	0.571	0.773	0.673	0.754	0.665	0.770	0.670	0.775	0.726

p (kbar)

	MXZH66	MXZH11	MXZH5	MXZH33	MXZH12	MXZH13	XKZH1
Huckenholz et al., 1992	**15**	**11**	**12**	**5**	**10**	**8**	**6**
Schmidt, 1992	9	8	9	8	8	8	6
Hollister et al., 1987	9	9	9	8	8	8	6
Hammarstrom and Zen, 1986	8	8	9	7	8	8	6
Johnson and Rutherford, 1989	7	7	7	6	6	6	5

XAb 0.43
XAn 0.56

$P_{Schmidt}$ (kbar) 6

T (°C)
HB1 - *Holland and Blundy, 1994* 812
HB2 - *Holland and Blundy, 1994* 837
BH - *Blundy and Holland, 1990* 847

Appendix C.ix. p-T estimates for phlogopite-glass pairs after *Righter and Carmichael* [1996].

sample	MXZH24				MXZH69		MXZH21	My1
n	phl1	glass1	phl2	glass2	phl	glass	phl	ON
SiO_2	38.23	41.43	38.61	40.99	38.54	42.42	37.74	39.87
TiO_2	4.70	3.63	4.64	3.65	5.09	3.39	4.25	2.95
Al_2O_3	17.14	15.29	17.12	15.24	17.13	16.34	16.93	11.43
Cr_2O_3	0.12	0.00	0.84	0.01	0.56	0.03	0.03	
Fe_2O_3								5.60
FeO	7.21	9.68	5.53	9.93	5.99	9.10	7.54	5.19
MgO	19.99	5.74	20.76	5.81	21.12	4.54	19.12	13.67
MnO	0.05	0.19	0.02	0.19	0.05	0.21		0.19
NiO	0.08	0.02	0.14	0.00		0.02		
CaO	0.05	15.30	0.03	16.01	0.01	13.86	0.14	12.61
BaO	0.25	0.20	0.27	0.18	0.30	0.16	0.13	0.08
Na_2O	0.72	3.61	0.45	3.79	0.48	4.07	0.67	2.57
K_2O	9.09	3.70	9.57	3.68	8.89	4.71	8.59	1.54
P_2O_5		0.96		1.00		1.01	0.00	0.70
Cl	0.02	0.28	0.03	0.27	0.02	0.30	0.02	
F	0.00	0.03	0.00	0.00	0.00	0.02	0.00	
H_2O	4.26		4.30		4.32			2.25
Total	101.89	99.98	102.28	100.71	102.49	100.13	95.17	98.62
TiO_2/TiO_2		1.295		1.270		1.501		1.443
BaO/BaO		1.287		1.549		1.931		1.723
T (K)		1424		1426		1407		1412
T (°C)		1151		1153		1134		1139
p (kbar) - a $_{H2O}$ =1		8		6		4		6

Appendix C.x. Density measurements on xenolith hand specimen using the weigh method.

sample	mass [g]			density [g/cm³]			volume [cm³]		porosity [%]
	dry sample	dipped in H$_2$O	H$_2$O saturated	fluid	bulk sample	sample matrix	sample	pore space	
mantle									
MXZH 67[1]	24.80	17.80	25.50	1.0000	3.22	3.54	7.70	0.70	9.1
MXZH 27[2]	77.60	52.50	80.30	1.0000	2.79	3.09	27.80	2.70	9.7
MXZH 32[2]	50.40	34.20	50.90	1.0000	3.02	3.11	16.70	0.50	3.0
MXZH 1[3]	82.05	57.03	87.68	0.9989	2.67	3.28	30.69	5.64	18.4
MXZH 2[3]	15.94	11.12	16.77	0.9989	2.82	3.30	5.66	0.83	14.7
MXZH 3[3]	31.62	21.74	33.72	0.9989	2.64	3.20	11.99	2.10	17.5
MXZH 4[3]	36.86	25.77	39.31	0.9989	2.72	3.32	13.55	2.45	18.1
MXZH 8[3]	20.60	14.25	22.09	0.9989	2.62	3.24	7.85	1.50	19.1
MXZH 19[3]	101.17	71.07	105.38	0.9989	2.95	3.36	34.35	4.22	12.3
crust									
XKZH 5[2]	23.70	14.50	23.90	1.0000	2.52	2.58	9.40	0.20	2.1
XKZH 12[2]	66.80	42.40	67.30	1.0000	2.68	2.74	24.90	0.50	2.0
XKZH 52[2]	343.30	222.70	347.50	1.0000	2.75	2.85	124.80	4.20	3.4
XKZH 53[2]	255.60	159.50	257.20	1.0000	2.62	2.66	97.70	1.60	1.6
XKZH 54[2]	347.10	217.70	349.60	1.0000	2.63	2.68	131.90	2.50	1.9
XKZH 55[2]	159.00	98.90	160.50	1.0000	2.58	2.65	61.60	1.50	2.4
XKZH 56[2]	51.90	33.00	52.50	1.0000	2.66	2.75	19.50	0.60	3.1
XKZH 58[2]	178.70	112.90	181.30	1.0000	2.61	2.72	68.40	2.60	3.8
XKZH 59[1]	10.70	6.70	10.90	1.0000	2.55	2.68	4.20	0.20	4.8
XKZH 60[2]	94.10	59.50	96.00	1.0000	2.58	2.72	36.50	1.90	5.2
XKZH 62[2]	80.70	51.30	81.60	1.0000	2.66	2.74	30.30	0.90	3.0
XKZH 63[2]	217.70	137.20	219.10	1.0000	2.66	2.70	81.90	1.40	1.7
XKZH 67[2]	203.00	128.90	205.10	1.0000	2.66	2.74	76.20	2.10	2.8
XKZH 69[2]	156.50	99.10	158.70	1.0000	2.63	2.73	59.60	2.20	3.7
XKZH 70[2]	257.20	162.00	260.30	1.0000	2.62	2.70	98.30	3.10	3.2
XKZH 75[2]	73.90	46.60	74.80	1.0000	2.62	2.71	28.20	0.90	3.2

[1] analyses by T. Schläfke

[2] analyses by C. Cunow and I. Schüler

[3] analyses by C. Karger

Appendix D.i. Elastic properties of mantle minerals, calculations after *Mechie et al.* [1994]. (STP: surface temperature-pressure conditions).

	STP						1.0 GPa 650 °C						2.0 GPa 1000 °C					
	r_0 g/cm^3	v_p km/s	v_s km/s	v_p/v_s	K_s kbar	G kbar	r g/cm^3	v_p km/s	v_s km/s	v_p/v_s	K_s kbar	G kbar	r g/cm^3	v_p km/s	v_s km/s	v_p/v_s	K_s kbar	G kbar
olivine	3.34	8.37	4.86	1.72	129	79	3.31	8.15	4.67	1.75	124	72	3.31	8.08	4.58	1.76	123	70
orthopyroxene	3.28	7.87	4.77	1.65	104	75	3.26	7.70	4.61	1.67	101	69	3.27	7.67	4.55	1.69	102	68
clinopyroxene	3.32	7.81	4.48	1.75	114	66	3.29	7.63	4.33	1.76	110	62	3.29	7.58	4.26	1.78	110	60
spinel	3.62	9.91	5.64	1.76	202	115	3.60	9.76	5.50	1.77	198	109	3.60	9.70	5.42	1.79	197	106
jadeite	3.32	8.76	5.03	1.74	143	84	3.29	8.54	4.84	1.76	137	77	3.29	8.46	4.76	1.78	136	74
garnet																		
pyrop/almandin	3.71	8.95	4.97	1.80	175	92	3.68	8.75	4.85	1.80	166	87	3.68	8.67	4.79	1.81	164	84
grossular	3.60	9.25	5.38	1.72	169	104	3.57	9.04	5.18	1.74	164	96	3.56	8.96	5.09	1.76	163	92
plagioclase (An60)		6.69						6.74						6.85				
amphibole		6.92						7.24						7.62				

Lebenslauf (Curriculum Vitae)

Persönliche Daten

Name: Wolfram Hartmut Geißler
Geburtstag: 10.10.1975
Geburtsort: Dresden

Schulbesuch und Studium

1982-84	Polytechnische Oberschule (POS) „Friedrich Schiller" Pirna
1984-90	POS „Alfred Vater" Pirna-Copitz, Klasse mit erweitertem Russischunterricht
1990-94	Spezialschule math.- naturw.- techn. Richtung „Friedrich Engels" Riesa (ab 1991 Werner- Heisenberg- Schule, ab 1992 Gymnasium)
06/1994	Allgemeine Hochschulreife (Abitur)
1995-1997	Studienfach Geophysik, TU Bergakademie Freiberg
08/1997	Vordiplom Geophysik
1997-1998	Studium an der Staatl. Akademie für Erdöl u. Erdgas I.M. Gubkin, Moskau
02/1998	Aufnahme in die Studienstiftung des Deutschen Volkes
1998-2001	Fortsetzung des Studiums an der TU Bergakademie Freiberg
2000-2001	Anfertigung der Diplomarbeit über das Thema „Marine seismische Untersuchungen am nördlichen Kontinentalrand von Svalbard (Spitzbergen)", Alfred-Wegener-Institut für Meeres- und Polarforschung Bremerhaven
05/2001	Diplom Geophysik
2002-2004	Anfertigung der Dissertation als Stipendiat der Studienstiftung des Deutschen Volkes, Geoforschungszentrum Potsdam/Freie Universität Berlin

Berufserfahrung, Praktika

1994/95	Zivildienst im Kreiskrankenhaus Pirna
08/1998	Praktikum am Geoforschungszentrum Potsdam
1998-2001	studentische Hilfskraft am Geoforschungszentrum Potsdam und am Institut für Geophysik, TU Bergakademie Freiberg
01-03/2000	Expedition ANT-XVII/2 mit „FS Polarstern"
06-12/2001	wissenschaftliche Hilfskraft am Geoforschungszentrum Potsdam
2003	Mitorganisation und Teilnahme am internationalen Weitwinkelseismischen Experiment SUDETES-2003
11/2004	Forschungsaufenthalt am Geophysikalischen Institut der Polnischen Akademie der Wissenschaften, Warschau